

**Transmission electron microscopy
of $\text{In}_x\text{Ga}_{1-x}\text{N}_y\text{As}_{1-y}$ nanostructures
using ab-initio structure factors
for strain-relaxed supercells**

Knut Müller

Bibliografische Information der *Deutschen Nationalbibliothek*

Die Deutsche Nationalbibliothek verzeichnet diese Publikation in der Deutschen Nationalbibliografie; detaillierte bibliografische Daten sind im Internet über <<http://dnb.ddb.de>> abrufbar.

ISBN: 978-3-86664-959-0

Zugl.: Bremen, Univ., Diss., 2011

Dissertation, Universität Bremen

Dieses Werk ist urheberrechtlich geschützt.

Alle Rechte, auch die der Übersetzung, des Nachdruckes und der Vervielfältigung des Buches, oder Teilen daraus, vorbehalten. Kein Teil des Werkes darf ohne schriftliche Genehmigung des Verlages in irgendeiner Form reproduziert oder unter Verwendung elektronischer Systeme verarbeitet, vervielfältigt oder verbreitet werden.

Die Wiedergabe von Gebrauchsnamen, Warenbezeichnungen, usw. in diesem Werk berechtigt auch ohne besondere Kennzeichnung nicht zu der Annahme, dass solche Namen im Sinne der Warenzeichen- und Markenschutz-Gesetzgebung als frei zu betrachten wären und daher von jedermann benutzt werden dürfen.

This document is protected by copyright law.

No part of this document may be reproduced in any form by any means without prior written authorization of the publisher.

Alle Rechte vorbehalten | all rights reserved

© Mensch und Buch Verlag 2011

Choriner Str. 85 - 10119 Berlin

verlag@menschundbuch.de – www.menschundbuch.de

Transmission electron microscopy of
 $\text{In}_x\text{Ga}_{1-x}\text{N}_y\text{As}_{1-y}$ nanostructures using ab-initio
structure factors for strain-relaxed supercells

Knut Müller

Bibliografische Information der *Deutschen Nationalbibliothek*

Die Deutsche Nationalbibliothek verzeichnet diese Publikation in der Deutschen Nationalbibliografie; detaillierte bibliografische Daten sind im Internet über <<http://dnb.ddb.de>> abrufbar.

ISBN: 978-3-86664-959-0

Zugl.: Bremen, Univ., Diss., 2011

Dissertation, Universität Bremen

Dieses Werk ist urheberrechtlich geschützt.

Alle Rechte, auch die der Übersetzung, des Nachdruckes und der Vervielfältigung des Buches, oder Teilen daraus, vorbehalten. Kein Teil des Werkes darf ohne schriftliche Genehmigung des Verlages in irgendeiner Form reproduziert oder unter Verwendung elektronischer Systeme verarbeitet, vervielfältigt oder verbreitet werden.

Die Wiedergabe von Gebrauchsnamen, Warenbezeichnungen, usw. in diesem Werk berechtigt auch ohne besondere Kennzeichnung nicht zu der Annahme, dass solche Namen im Sinne der Warenzeichen- und Markenschutz-Gesetzgebung als frei zu betrachten wären und daher von jedermann benutzt werden dürfen.

This document is protected by copyright law.

No part of this document may be reproduced in any form by any means without prior written authorization of the publisher.

Alle Rechte vorbehalten | all rights reserved

© Mensch und Buch Verlag 2011

Choriner Str. 85 - 10119 Berlin

verlag@menschundbuch.de – www.menschundbuch.de

Transmission electron microscopy of
 $\text{In}_x\text{Ga}_{1-x}\text{N}_y\text{As}_{1-y}$ nanostructures using ab-initio
structure factors for strain-relaxed supercells

Vom Fachbereich Physik und Elektrotechnik der
Universität Bremen genehmigte Dissertation.

Vorgelegt von

Dipl. Phys. Knut Müller

aus Burghasungen

zur Erlangung des akademischen Grades

Doktor der Naturwissenschaften (Dr. rer. nat.).



Begutachtung:

1. Prof. Dr. Andreas Rosenauer

2. Prof. Dr. Dagmar Gerthsen

Promotionskolloquium: 23. März 2011,
Bremen (Germany)

Die umseitige Figur trägt den Titel **Walking For Science**.
Knut Müller 1998
Wilhelm-Filchner-Gesamtschule, Wolfhagen

Abstract

This thesis reports on theoretical, methodical and experimental studies concerning scattering and structural properties of $\text{In}_x\text{Ga}_{1-x}\text{N}_y\text{As}_{1-y}$ using transmission electron microscopy (TEM).

First, theoretical concepts to describe electron scattering at real crystals including the effects of bonding and static atomic displacements (SAD) are considered. The approach of modified atomic scattering amplitudes (MASA), which uses density functional theory (DFT) to model bonding in an atomistic manner, is exploited to calculate composition-dependent MASA for InGaNAs. Valence force field (VFF) calculations are applied to determine SAD caused by atom size effects. Huang scattering caused by SAD is shown to pile up in the vicinity of Bragg peaks, contrary to the smooth background caused by thermal diffuse scattering (TDS). In simulation studies it is demonstrated that Huang scattering leads to significant attenuation of Bragg beam amplitudes, for which additional absorptive form factors can be defined that are added as an imaginary part to atomic scattering amplitudes (ASA).

The reliability of VFF strain relaxation is verified by full DFT calculations of residual forces for supercells with 216 atoms. It is found that atomic forces after VFF relaxation do not exceed 10 mRy/Bohr, which translates to a maximum error of 2.58 pm for SAD. Furthermore, results for composition-dependent structure factors calculated by full DFT and atomistic models are compared. This confirms that SAD affect structure factor amplitudes and phases drastically and exhibits that the MASA approach in combination with SAD obtained by VFF meets the full DFT results most accurately. Thus it is possible to account for both bonding and SAD in large supercells containing 10^6 atoms by modelling bonding via MASA and calculating SAD by VFF.

Second, structure factors for GaAs and InAs are measured by parallel and convergent beam electron diffraction (PBED and CBED) to verify the MASA approach. The PBED method was implemented in Bloch wave routines embedded in a least-squares refinement that allows for a refinement of structure factors, Debye-Waller factors, specimen thickness and -orientation. The method is based on extraction of integrated Bragg intensities from electron spot diffraction patterns. Errors in PBED are estimated from the application to simulated diffraction patterns with TDS background, and rules for the recognition of reasonable initial refinement conditions are derived. Then, PBED is applied to the measurement of the 200 structure factors of GaAs and InAs. Conversion to X-ray structure factors yields $X_{200}^{\text{GaAs}} = -6.366 \pm 0.015$ and $X_{200}^{\text{InAs}} = 53.687 \pm 0.110$, respectively. By CBED, $X_{200}^{\text{GaAs}} = -6.350 \pm 0.015$ is measured. All results agree with each other and with expectations from the MASA concept inside the error margins, whereas isolated atom ASA must be rejected. Additionally, Debye-Waller factors for GaAs have been refined to $B_{\text{Ga}} = 0.275 \pm 0.003 \text{ \AA}^2$ and $B_{\text{As}} = 0.242 \pm 0.003 \text{ \AA}^2$ at 99 K using PBED.

Third, above theoretical scattering data is used in composition measurements in InGaNAs solar cell and laser structures via TEM lattice fringe imaging. Lattice strain and chemically sensitive 200 fringe contrast are measured from a single image and compared

with simulations based on elasticity theory and the Bloch wave approach. First, a two-beam lattice fringe image formed by beams 000 and 200 is used to investigate the effect of bonding and SAD on composition quantification in $\text{In}_{0.08}\text{Ga}_{0.92}\text{N}_{0.03}\text{As}_{0.97}$. In particular, neglect of bonding results in a relative error of 25% for the In content, whereas SAD have small impact. Second, a three-beam imaging technique is developed that utilises beams 000, 200 and 220, for which an L-shaped objective aperture was inserted into an FEI Titan 80/300 microscope. By decomposition of the image into 220 and 020 fringe images, artefacts due to nonlinear imaging are circumvented. Imaging conditions that minimise errors induced by inaccurately known specimen thickness are derived. Bloch wave simulations of reference 200 fringe contrast include structure factors adapted for chemical bonding, SAD, and diffuse losses due to SAD and TDS. As a main application, the three-beam method is applied to $\text{In}_{0.28}\text{Ga}_{0.72}\text{N}_{0.025}\text{As}_{0.975}$ before and after thermal annealing. Dissolution of In-rich islands and N-rich clusters and formation of a homogeneously thick quantum well with nearly constant stoichiometry is found. The increase by a factor of 20 and blue-shift of 60 meV of the photoluminescence peak are finally interpreted by means of the TEM results.

Contents

1	Introduction	1
	Survey of research on InGaNAs	2
	TEM methodology	3
	Spectroscopic methods	5
	Scanning transmission electron microscopy (STEM)	6
	Conventional TEM	7
	Structure of this thesis	9
2	Electron scattering theory	11
2.1	Introduction	11
	Survey of literature	12
2.2	Scattering potential of single atoms	13
2.3	Scattering potential of ideal crystals	15
	2.3.1 The structure factor	15
	2.3.2 Isolated atom approximation	17
	2.3.3 Density functional theory	18
	2.3.4 The WIEN2K code	21
	2.3.5 Chemical bonding	24
	Modified atomic scattering amplitudes	27
	Compositional dependence	30
2.4	Bloch wave approach	31
2.5	Multislice approach	35
2.6	Scattering potential of real crystals	36
	2.6.1 Thermal diffuse scattering	37
	2.6.2 Calculation of static atomic displacements	41
	2.6.3 Huang scattering	43
	2.6.4 Absorptive form factors for Huang scattering	45
2.7	Discussion	46
	2.7.1 General remarks	46
	2.7.2 Significance of MASA	47
	2.7.3 Significance of SAD	47
2.8	Summary and conclusions	48
3	Measurement of structure factors and Debye parameters by electron diffraction	51
3.1	Introduction	51
	Outline of electron diffraction techniques	52
3.2	Experimental	55

3.2.1	PBED pattern acquisition	55
3.2.2	CBED pattern acquisition	56
3.3	Parallel beam electron diffraction	56
3.3.1	Description of the method	56
	The Bloch wave refinement routine Bloch4TEM	57
	Practical considerations	59
	Estimation of systematic errors	60
	Ambiguity of refinement results	63
3.3.2	Measurement of the 200 potential for GaAs	66
	Estimation of initial thicknesses for the refinement	66
	Refinement results for the 200 potential	67
	Behaviour of the 400 crystal potential	69
3.3.3	Measurement of the 200 potential for InAs	70
3.3.4	Measurement of Debye parameters for GaAs	71
3.4	Convergent beam electron diffraction	73
3.4.1	Methodical summary	73
3.4.2	Refinement preconditions	74
	Polarity of GaAs	74
	Acceleration voltage of the TEM	75
	Debye parameters of GaAs	77
	Initial thicknesses	77
3.4.3	Measurement of the 200 potential for GaAs	77
3.5	Discussion	80
3.5.1	Validity of the PBED test results	80
3.5.2	Methodological aspects	80
3.5.3	Discussion of the results for the 200 potentials	82
	GaAs	82
	InAs	85
	Relevance of charge density (difference) maps	85
3.5.4	Discussion of Debye parameters for GaAs	86
	Side note to quantitative STEM	87
3.6	Summary and conclusions	88
4	Effects of bonding and static atomic displacements on composition quantification in $\text{In}_x\text{Ga}_{1-x}\text{N}_y\text{As}_{1-y}$	91
4.1	Introduction	91
4.2	Valence force field and first-principles calculations	93
4.2.1	Minimisation of strain energy	94
4.2.2	Density functional theory results	94
	Residual forces	94
	Structure factors	96
4.3	Experimental composition quantification in InGaNAs	100
4.3.1	Methodical summary	100
	Strain state analysis	100
	Composition evaluation by lattice fringe analysis (CELFA)	102
	Application to an experimental image	102
4.3.2	Simulation of reference data	103
4.3.3	Composition maps and profiles	105

4.4	Discussion	107
4.4.1	Modelling of scattering properties	107
	Relevance for structure factors	107
	Side note to quantitative STEM	108
4.4.2	Methodical aspects	110
4.4.3	Composition profiles	111
4.5	Summary and conclusions	112
5	Atomic scale annealing effects on InGaNAs studied by TEM three-beam imaging	115
5.1	Introduction	115
5.2	Experimental	117
5.3	Description of the method	118
5.3.1	Nonlinear imaging	118
5.3.2	Three-beam imaging	121
5.3.3	Simulation of reference data and optimised imaging conditions . . .	123
5.4	Results for the low-indium regime	127
5.5	Annealing effects in $\text{In}_{0.28}\text{Ga}_{0.72}\text{N}_{0.025}\text{As}_{0.975}$	129
5.6	Discussion	132
5.6.1	Composition mapping	132
5.6.2	Annealing effects	134
5.7	Summary and conclusions	136
6	Comprehensive discussion	139
6.1	Discussion of the present work	139
6.2	Prospects	141
	List of acronyms	143
	Bibliography	145
	Selected publications	155
	Danksagung (Acknowledgement)	157

Chapter 1

Introduction

One main characteristic of modern societies is the necessity of communication as a social, economic or scientific event. Of at least comparable importance is the global exigency to find sustainable solutions for the power supply of industrial countries. In both fields, communication and power supply, technology comprising semiconductor nanostructures constitutes an essential part in form of optoelectronic devices, such as light emitting or laser diodes and solar cells, respectively. Macroscopically observable properties of these devices, that is, photoluminescence spectra of light emitting diodes and absorption spectra of solar cells, are governed by structural properties at atomic scale. In this respect, local chemical composition, as well as interatomic bond lengths and -types in semiconductor crystals play a central role. However, although contemporary techniques for crystal growth, such as metal organic vapour phase epitaxy (MOVPE) and molecular beam epitaxy (MBE), can be used to fabricate nearly perfect crystals with unprecedented quality, formation of quantum layers exhibiting the intended local composition remains a problem. This is not only due to the statistical nature of epitaxial growth, but also because of near-surface kinetics involving, e.g., segregation or island formation. At this point it becomes obvious that transmission electron microscopy (TEM) of semiconductor nanostructures plays a key role as to atomic layer characterisation, since modern microscopes allow for imaging with sub-Ångström resolution.

Even though the briefness of the above paragraph demonstrates the close connection between important technical applications and high-resolution TEM (HRTEM), it is by far insufficient to motivate active microscopic research from this attitude alone. The reader of this work will notice quickly that contemporary TEM is a close interplay between experiment and theory, which only together make a measurement. In other words, present-day TEM aims for congruence between simulated and recorded data. This is the point where electron microscopy extends its role of being pure feedback to device engineering towards basic solid state research, because simulation of electron interaction with a crystal requires knowledge of fundamental solid state properties, such as lattice dynamics, electron density or static atomic displacements (SAD) caused by point defects. Accordingly, derivation and modelling of appropriate scattering potentials has gained new interest, especially by virtue of efficient density functional theory (DFT) codes [1] and continuously rising computing power. In this way, TEM is particularly a discipline which probes not only crystal properties at atomic scale, but also the reliability of ab-initio or empirical concepts in solid state physics.

This thesis deals with transmission electron microscopy of quaternary $\text{In}_x\text{Ga}_{1-x}\text{N}_y\text{As}_{1-y}$ solar cell and laser structures buried in GaAs, aiming at the de-

velopment of a HRTEM method to measure both local indium and local nitrogen content simultaneously. Methodically, the main challenge consists in the extraction of two sources of information from a single TEM recording. In this way, the author intends to allow for substantial answers to questions concerning local stoichiometry of InGaNAs layers in view of possible (anti-) correlations between the atomic-scale indium and nitrogen distributions. This means an important extension of existing TEM methods that either superpose two TEM micrographs showing different regions of a specimen [2], or work with a ternary InGaAs standard assuming that the indium distribution is invariant with respect to nitrogen incorporation [3], or combine TEM with a different method, e.g., Rutherford backscattering [4]. The presented methodical work for composition quantification is closely related to the application point of view, as mentioned at the beginning.

As stated above, experiments are to be interpreted by means of simulations, which require reliable electron scattering factors. Even for binary GaAs, isolated atom (low-order) structure factors commonly used are inaccurate because they are significantly altered by electron redistributions due to chemical bonding [5, 6]. Density functional theory can be used to quickly solve this problem for ideal crystals where small unit cells are sufficient. Beyond that, indium- and especially nitrogen impurities are of drastic different size, compared to gallium and arsenic atoms on the host sublattices, causing strong local strain fields which lead to SAD [7, 8]. The fact that treatment of SAD requires large cells containing about 10^6 atoms, whereas ab-initio study of bonding is restricted to several hundreds of atoms, efficient modelling of bonding effects on scattering factors is needed, e.g., via modified atomic scattering amplitudes (MASA [9]) obtained from DFT. Consequently, approximately two thirds of the results of this work concern the derivation and verification of appropriate scattering data for InGaNAs including bonding and SAD, before this scattering data is exploited for composition quantification in this material. The effort spent on scattering data hence stems from a more basic interest in solid state properties, since accurate scattering factors are important not only for composition quantification but for all simulations at least in the field of TEM.

Let us now briefly collect some concrete aspects on the InGaNAs material system and TEM methodology, so as to facilitate reading of the following chapters.

Survey of research on InGaNAs

As to telecommunication, optical loss spectra of quartz fibres principally show two minima with losses below 1 dB/km in the near infrared region at wavelengths of 1.3 and 1.55 μm , called “telecom windows”. The former window is loss-limited, meaning that dispersion is very low, so that it is suitable for high transmission rates over short distances below about 10 km. The latter exhibits lowest loss and is hence attractive for telecommunication over long distances. That InGaNAs is a promising material system for such applications becomes obvious from Fig. 1.1, where the bandgaps of all possible binary and ternary InGaNAs components are plotted versus their lattice parameters using data from Refs. [10, 11]. Starting from the well-established $\text{In}_x\text{Ga}_{1-x}\text{As}$ system represented by the black graph, we see that the telecom windows shown in grey correspond to indium contents of $x \approx 0.41$ and $x \approx 0.55$, which can hardly be achieved practically due to strong compressive strain in such layers. However, contrary to InGaAs, the blue and red curves in Fig. 1.1 exhibit that nitride compounds cause immense bandgap bowing while inducing tensile strain. Hence, incorporation of nitrogen in $\text{In}_x\text{Ga}_{1-x}\text{As}$ is not only suitable for lattice-matched growth

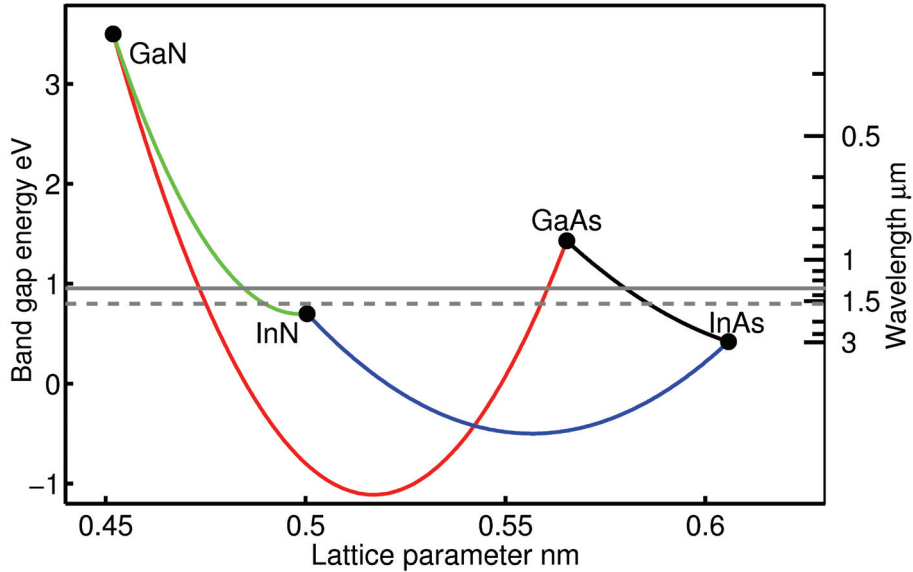


Figure 1.1: Energy gap and wavelength versus lattice parameter for binary zinc blende compounds involved in InGaNAs (black dots) and bandgap bowing graphs for the corresponding ternary alloys. Transmission windows of optical fibres are shown in grey.

of $\text{In}_{0.08}\text{Ga}_{0.92}\text{N}_{0.03}\text{As}_{0.97}$ solar cells with 1 eV bandgap, but can principally also be used for the epitaxy of $\text{In}_{0.28}\text{Ga}_{0.72}\text{N}_{y \approx 0.02}\text{As}_{1-y}$ laser diodes whose emission meets the telecom windows.

As to dilute nitrides, successful epitaxy of ternary $\text{GaN}_y\text{As}_{1-y}/\text{GaAs}$ layers by Weyers and Sato in 1992 [12] offered the perspective for the growth of $\text{In}_x\text{Ga}_{1-x}\text{N}_y\text{As}_{1-y}/\text{GaAs}$ quaternary heterostructures, which was achieved by Kondow [13] et al. a few years later. It was quickly noticed that as-grown samples produced by both MBE and MOVPE indeed exhibit room temperature photoluminescence (PL) near the desired wavelength of, e.g., 1.3 μm , but that PL peaks are relatively weak and broad [13, 14, 15]. Concerning the optical performance, satisfying PL intensity and peak widths have since then been obtained after thermal annealing, but unfortunately the spectral position shifted several tens of nanometres towards smaller wavelengths, depending on annealing temperature and stabilising atmosphere [16, 15, 17, 18, 19]. In order to explain this blue shift, researchers additionally focus on structural characteristics of InGaNAs before and after annealing. In particular, the role of nitrogen as an impurity of drastically different size than atoms at the host lattice is considered, since it was shown by simulations of Neugebauer et al. [10] that drastic bandgap bowing and a miscibility gap between GaAs and GaN can be attributed to this size effect. For $\text{In}_x\text{Ga}_{1-x}\text{N}_y\text{As}_{1-y}$, it was questioned by Kim and Zunger [20] whether this material is to be thought of as InAs+GaN or as InN+GaAs. Subsequent measurements have then frequently been interpreted by accompanying studies of the coordination of nitrogen in $\text{In}_x\text{Ga}_{1-x}\text{N}_y\text{As}_{1-y}$ [21, 22, 16], or by long-range ordering of indium and nitrogen [23, 17].

TEM methodology

Modern TEM is rather a collective term for spectroscopic, diffraction and imaging methods than just the electron-optical counterpart of light microscopy. Since spectroscopic methods usually reveal the most characteristic signature of atomic species involved, it

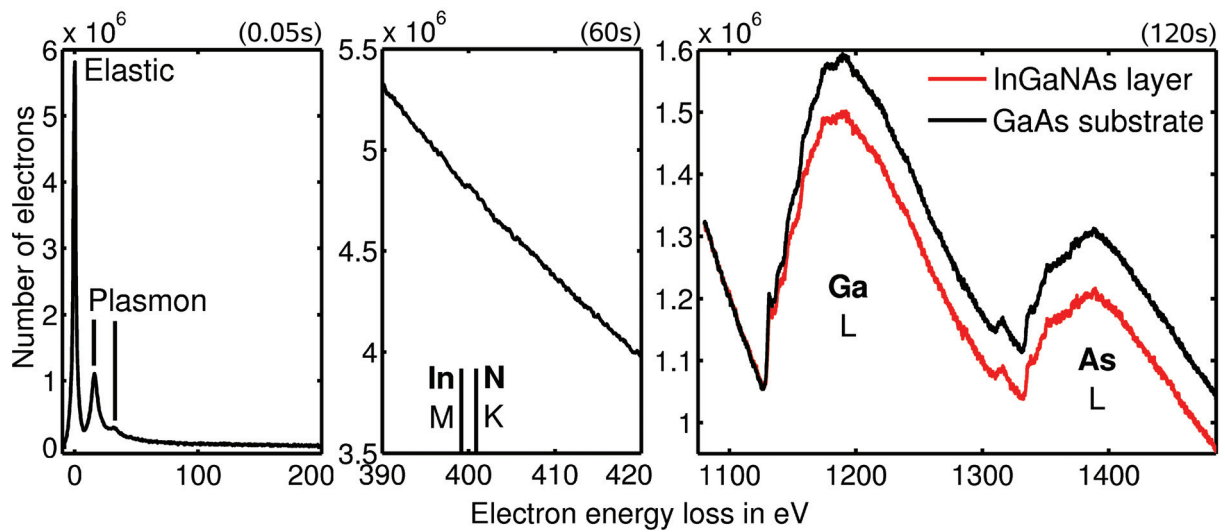


Figure 1.2: EELS spectra recorded in different spectral windows using a Gatan imaging filter mounted at a Titan 80/300 facility, which was operated at 300 kV. The electron beam was focused into an $\text{In}_{0.28}\text{Ga}_{0.72}\text{N}_{0.015}\text{As}_{0.985}$ layer. Integration times are given top of each figure. The black spectrum on the right was taken in the GaAs substrate.

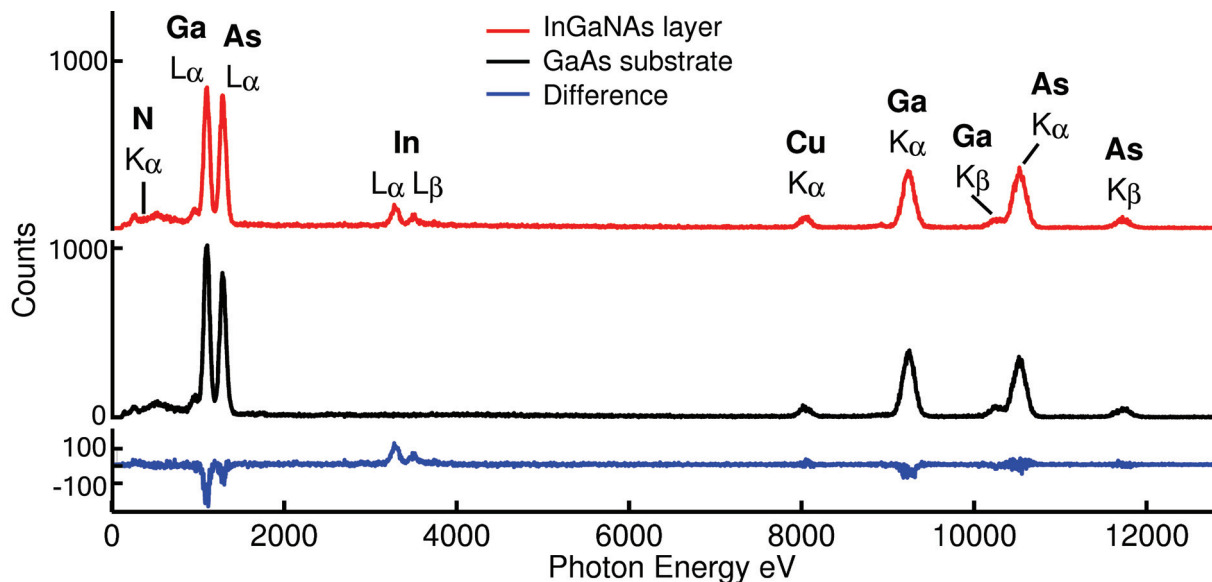


Figure 1.3: EDX spectra of the $\text{In}_{0.28}\text{Ga}_{0.72}\text{N}_{0.015}\text{As}_{0.985}$ layer (red) and of pure GaAs substrate regions taken at a Titan 80/300 facility at 300 kV. The blue curve corresponds to the subtraction of the substrate spectrum from that of the layer.

is briefly shown in the following that both electron energy loss spectroscopy (EELS) and energy dispersive X-ray (EDX) analysis are problematic for atomic-scale composition quantification in $\text{In}_x\text{Ga}_{1-x}\text{N}_y\text{As}_{1-y}$, contrary to scanning TEM (STEM) and conventional TEM. In all of the following cases, the same $\text{In}_{0.28}\text{Ga}_{0.72}\text{N}_{0.015}\text{As}_{0.985}$ layer was investigated.

Spectroscopic methods

Primary electrons may be scattered elastically and inelastically during propagation through the TEM specimen. During an inelastic scattering event, energy may be transferred to electrons in the specimen via excitation of plasmons, or by electronic excitation and ionisation of atoms.

Using a post-column Gatan imaging filter, which essentially disperses electrons of different velocity by a magnetic field, EELS spectra shown in Fig. 1.2 have been recorded at a Titan 80/300 facility operated at 300 kV. In particular, the primary beam was focused into the $\text{In}_{0.28}\text{Ga}_{0.72}\text{N}_{0.015}\text{As}_{0.985}$ quantum well using settings for the electron gun and condenser system that provide highest intensity of the primary electron beam. The low-loss part of the EELS spectrum depicted on the left of Fig. 1.2 exhibits that most of the scattered electrons suffered no energy loss (elastic or zero-loss peak) or were scattered at plasmons. In the centre of Fig. 1.2, we see the spectral range of both the nitrogen K-edge and the indium M-edge. These are not only too close together for a separate analysis, but also provide very weak signal. Additionally, the visible small peak is to be attributed rather to nitrogen than to indium, whose M-edge is known to be very broad [24]. Thus we find that quantification of both indium and nitrogen from their characteristic edges is hardly possible due to the low nitrogen content and the shape of the indium M-edge. It is also worth noting that the spectrum was recorded for 60 s with the beam focused at one point, making atomically resolved mapping of both edges impossible. The same holds for the gallium L- and arsenic L-edges depicted on the right of Fig. 1.2, having been recorded for 120 s. Although the two edges clearly overlap in part, significant characteristic signal is observed. Furthermore, the red graph corresponds to a region inside the quantum well, whereas the black one was taken in a GaAs substrate region, indirectly indicating the presence of indium and nitrogen. Principally, this part of the EELS spectrum contains a lot of information: First, for thin specimen, the integrated edge signal is proportional to the amount of the respective element. Second, the clearly visible near-edge fine structure is sensitive to the nearest neighbour type and coordination. Using advanced modelling of EELS edges [25], investigation of the overall composition or mean coordination appears realistic, but again atomically resolved indium and nitrogen mapping will be very difficult due to the low probability for scattering events with high energy losses.

The same $\text{In}_{0.28}\text{Ga}_{0.72}\text{N}_{0.015}\text{As}_{0.985}$ quantum well has been studied with EDX, which exploits the characteristic X-ray emission originating from a recombination of electrons to vacant low-energy electronic states. Using settings optimised for maximum primary beam intensity again, EDX spectra in Fig. 1.3 have been integrated over 300 s inside the quantum well (red) and inside GaAs (black). The characteristic signature of InGaAs is clearly visible in the form of K- and L-lines, whereas the K-line of nitrogen does not extend significantly over the background as can be seen from the difference of both spectra shown in blue. Consequently, measurement of indium content appears realistic here, whereas EDX exhibits low sensitivity to small amounts of nitrogen. Nevertheless, indirect quantification of the latter could be possible by evaluating the arsenic signal, but this is hindered by the finite width of the adjacent gallium peak. Still, the extremely long

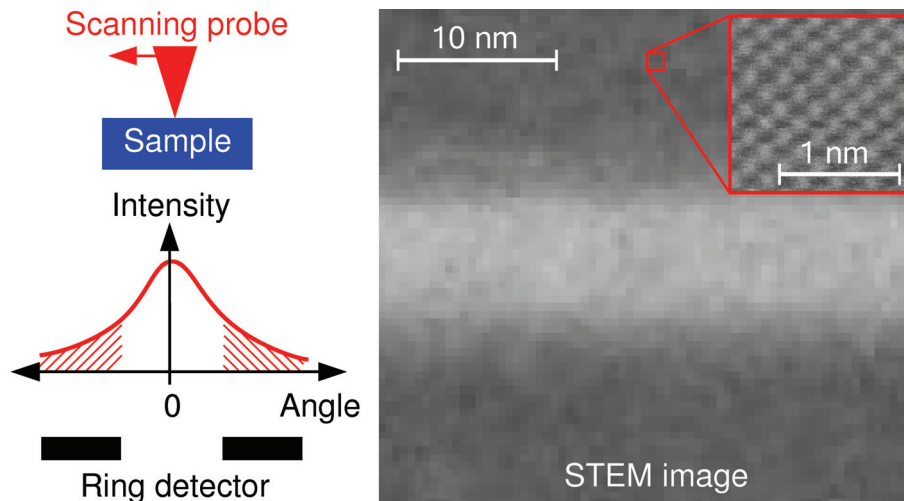


Figure 1.4: *Left*: Schematic to illustrate STEM image formation. *Right*: Experimental STEM image of the $\text{In}_{0.28}\text{Ga}_{0.72}\text{N}_{0.015}\text{As}_{0.985}$ quantum well taken at a Titan 80/300 facility at 300 kV.

integration time makes atomic resolution very difficult. It must furthermore be noted that atomic resolution cannot be achieved with the present (condenser) setting since it produces a very large spot of approximately 7 nm in diameter on the specimen.

Scanning transmission electron microscopy (STEM)

In STEM, the primary beam is focused onto the specimen as sharp as possible. This is achieved by the use of very small condenser apertures, which on the one hand reduce the beam current drastically in comparison to EDX and EELS measurements, but on the other hand this allows for atomically resolved imaging with a resolution of 0.12 nm at the Titan 80/300 facility. In STEM, no post-specimen lenses are involved in the imaging process. Instead, a ring detector situated in the diffraction plane collects all electrons that are scattered into an angular range of, e.g., 33-200 mrad at a certain position of the primary beam as illustrated by the shaded red region on the left of Fig. 1.4. A STEM image of the $\text{In}_{0.28}\text{Ga}_{0.72}\text{N}_{0.015}\text{As}_{0.985}$ quantum well dealt with above, as depicted on the right of Fig. 1.4, is finally obtained by mapping this signal versus the probe position. It is seen here that two

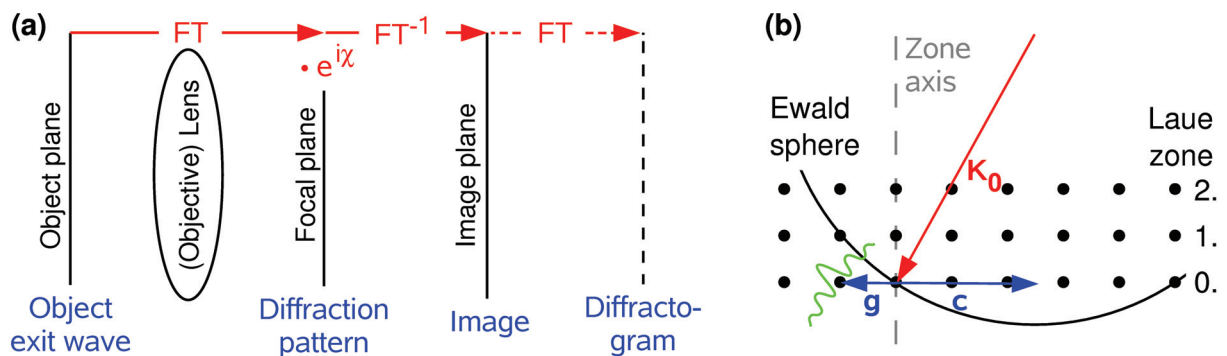


Figure 1.5: (a) Schematic of signal transfer by lenses considering selected planes. The dashed part rather corresponds to digital image analysis than being part of electron optics. (b) Explanation of electron scattering via Ewald construction. Reciprocal lattice points are depicted as black circles, the green curve represents a rod due to finite specimen thickness.

sources of information, namely contrast and lattice strain, are principally accessible in one STEM image which is promising for accurate high-resolution dual compositional mapping. Challenges of this method mainly consist in the correct simulation of contrast. Whereas low-angle scattering is dominated by the Bragg signal, diffuse scattering stemming from thermal and static atomic displacements makes the major contribution to the STEM detector. In practice, this involves computationally demanding simulations, not only because disorder must explicitly be taken into account, but also because convergence with respect to different displacement configurations is required. However, compositional analysis of ternary materials using quantitative STEM is based on comparing thickness- and concentration-dependent simulations of the STEM intensity with its experimental counterpart [26, 27, 28]. In particular, the thickness throughout an area of interest is interpolated from thicknesses at regions with known composition, such as GaAs buffer layers, so as to interpret the STEM signal in the quantum well region solely by means of stoichiometry. As to measurement of lattice strain, the flyback of the STEM probe results in a parallel offset among individual scan lines. Compensating for this effect is subject to active research [29, 30].

During the present thesis, the author intended to contribute to an understanding of STEM contrast concerning several aspects. First, section 3.3.4 is dedicated to the measurement of Debye-Waller factors for GaAs which are essential for the correct simulation of the thermal diffuse signal. Second, the thickness- and temperature dependence of the STEM signal has been measured and compared with both simulations and thicknesses obtained by different methods in order to verify STEM simulations for pure GaAs. Third, valence force field relaxation [31, 32] was implemented into the STEMsim [33] software, allowing for inclusion of SAD in STEM simulations. However, work on these topics is closely related to conventional TEM, on which the focus of this thesis lies. Hence STEM investigations are rather included as side notes than constituting an own chapter, which would be beyond the scope of this thesis. Taking together all aspects concerning STEM, the author sees no reason why it should not become as reliable for compositional mapping in InGaNAs as the conventional TEM method developed here when all findings are put together.

Conventional TEM

The basic principle of conventional TEM is complementary to the above methods as it relies on image formation by means of electromagnetic lenses as sketched in Fig. 1.5 (a). As a starting point, we choose the exit wave as present at the exit face of a TEM specimen. The subsequent objective lens has two important planes, where the Fraunhofer diffraction pattern (focal plane) and the image (image plane) can be observed, respectively. Mathematically, the object exit wave function and the wave function in the focal plane are connected via Fourier transform. A nonzero phase χ containing lens aberrations and defocus usually modifies the wave function in the focal plane, before an inverse Fourier transform yields the wave function in the image plane. In a TEM, subsequent electromagnetic lenses can be operated in two settings, that either image the focal plane (diffraction mode) or the image plane (imaging mode) of the objective lens on a recording facility. Mathematically, the wave function is multiplied with its complex conjugate here, which gives the image or diffraction pattern intensity. For the purpose of digital image analysis, the diffractogram is of great importance, which is the Fourier transform of the image intensity.

A compact understanding of electron diffraction at crystals is possible by means of the Ewald construction sketched in Fig. 1.5 (b). The black reciprocal lattice points can in this case be divided in three Laue zones of zero, first and second order. All reciprocal lattice vectors lying in one of the zones, such as \mathbf{g} shown in blue, correspond to lattice planes in real space which intersect in a line called zone axis depicted in grey. Incidence of the primary beam \mathbf{K}_0 shown in red is usually characterised by giving the zone axis indices and the reciprocal coordinates of the Laue circle centre \mathbf{c} depicted in blue, the Laue circle being the intersection of the Ewald sphere with one of the Laue zones. For large tilts from zone axis, the Laue circles practically degenerate to lines which is called systematic row condition. In the diffraction pattern, Bragg reflections show up that correspond to reciprocal lattice points close to the Ewald sphere, such as \mathbf{g} in Fig. 1.5 (b). In systematic row scattering geometry, only few reflections are involved, which is not only useful to enhance the intensity of weak reflections, but can also be exploited to reduce the thickness dependence of Bragg beam intensities arising from multiple scattering. Since the reciprocal lattice relies on the assumption of an infinite crystal, whereas TEM specimen are thinned down to a few tens of nanometres in thickness, each reciprocal lattice point extends to a sinc-shaped rod as exemplarily shown in green for point \mathbf{g} in Fig. 1.5 (b). As the period of the sinc-function is given by the specimen thickness, varying the direction of \mathbf{K}_0 produces rocking curves called thickness fringes, which are frequently used to measure specimen thickness. In convergent beam electron diffraction (CBED), where conical incidence is present by focusing the primary beam onto the specimen, diffraction discs appear in which thickness fringes or higher order Laue zone (HOLZ) lines appear as an inner disc structure. The latter can be understood from Fig. 1.5 (b), where one reflection in the first order Laue zone is in Bragg condition. Thus, scattering from the primary disc into the HOLZ reflection is enhanced for this specific direction of \mathbf{K}_0 , leading to an excess line in the HOLZ disc and a deficiency line in the primary disc. The HOLZ line positions are in part extremely sensitive to the radius of the Ewald sphere and to the position of the reciprocal lattice points. They are therefore frequently used to measure the TEM acceleration voltage and lattice parameters.

With aberrations χ sufficiently small and more than one diffracted beam passing the objective aperture situated in the focal plane of the objective lens, atomically resolved TEM imaging is possible as shown in Figs. 1.6 (a,b). Again, the $\text{In}_{0.28}\text{Ga}_{0.72}\text{N}_{0.015}\text{As}_{0.985}$ quantum well was analysed there by two different techniques called composition evaluation by lattice fringe analysis (CELFA [34]) and strain state analysis. In CELFA, the HRTEM fringe image depicted on the left of Fig. 1.6 (a) is formed by the primary and the diffracted 200 beam via an objective aperture. The strong contrast between the quantum well region and pure GaAs relies on a characteristic of zinc-blende alloys where the 200 structure factor strongly depends on composition. Practically, all frequencies except those close to the 200 reflection in the diffractogram are set to zero, which gives the map of the 200 fringe amplitude on the right of Fig. 1.6 (a). Then, this amplitude is normalised to a background obtained from regions with known composition and compared with its simulated counterpart. Consequently, accuracy of CELFA measurements is strongly dependent on the reliability of scattering factors used in the simulation, which is a nontrivial problem because low-order structure factors, such as 200, are sensitive to bonding and, eventually, SAD. Another feature of InGaNAs is that the 200 structure factor exhibits a null at certain compositions, which has two important consequences. First, the 200 fringe amplitude passes minima near $\text{In}_{0.28}\text{Ga}_{0.72}\text{N}_{0.015}\text{As}_{0.985}/\text{GaAs}$ interfaces as can clearly be seen on the right of Fig. 1.6 (a). Second, as the 200 structure factor suffers a phase jump

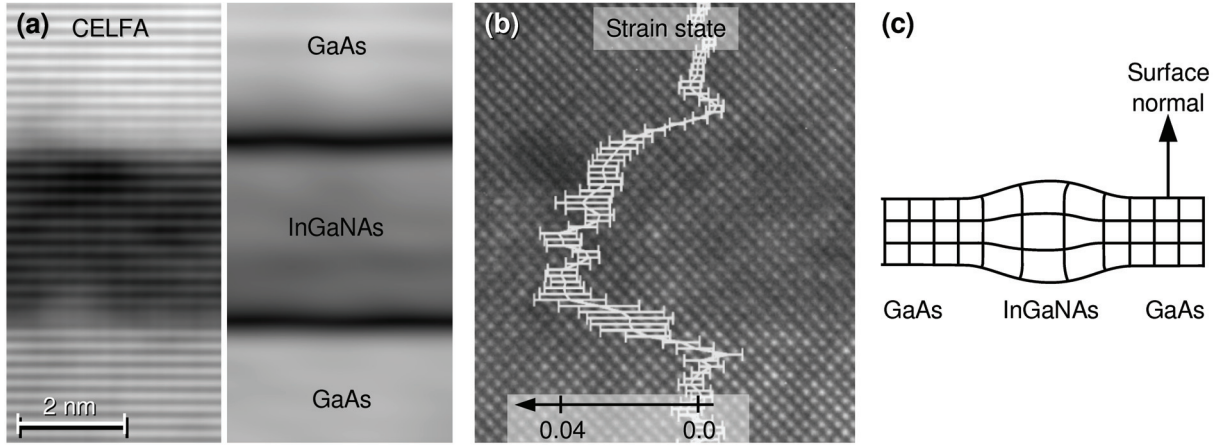


Figure 1.6: (a) CELFA image of the $\text{In}_{0.28}\text{Ga}_{0.72}\text{N}_{0.015}\text{As}_{0.985}$ layer taken at a Titan 80/300 facility at 300 kV with the 000 and 200 beams passing the objective aperture. Laue circle centre was $\mathbf{c} = (1.5\ 200)$ near zone axis [001]. The right part shows the amplitude of the fringe oscillation on the left. (b) HRTEM image of the same quantum well in zone axis [001] with superimposed strain in growth direction, measured using the DALI software. (c) Schematic to explain strain relaxation in surface normal direction for thin crystals with a compressively strained InGaNaNAs layer.

of π at the null, the lattice fringe pattern shifts by approximately half a period there, as is observed on the left of Fig. 1.6 (a). This makes strain state analysis from the same image impossible for indium contents above $x \approx 0.15$.

The principle of strain state analysis is thus exemplified using a HRTEM image in zone axis [001] taken without objective aperture as depicted in Fig. 1.6 (b). Superimposed we see the lattice strain measured from spacings of the (400) lattice planes using the DALI [35] software. It becomes evident that strain vanishes in the GaAs buffer layers, but takes values up to 0.04 inside the $\text{In}_{0.28}\text{Ga}_{0.72}\text{N}_{0.015}\text{As}_{0.985}$ layer. In strain state evaluations, this value is converted to chemical composition by application of elasticity theory and proper boundary conditions, which account for different stresses distorting native cubic InGaNaNAs unit cells tetragonally. Unfortunately, this makes strain state analysis thickness dependent, because compressively strained layers may relax in surface normal direction in thin specimen as sketched in Fig. 1.6 (c), resulting in a reduction of strain in growth direction. This is taken into account via a relaxation parameter r , being one for infinitely thick, and zero for infinitely thin specimen.

In summary, conventional TEM provides access to both chemically sensitive contrast and lattice strain measurement, but not yet at the same time. While approaching the end of this thesis, the reader will be presented a three-beam near-zone axis technique as an extension of the two-beam systematic row CELFA approach, allowing for measurement of chemically sensitive contrast and strain from one HRTEM image.

Structure of this thesis

This work is split into four main chapters. To avoid sourcing out established theoretical knowledge to a single chapter, theory is presented when explicitly needed, and results are presented where they fit best with respect to content. In this way, each of the chapters contains direct results of this work which have at least been submitted for publication

as regular articles. By presenting new aspects in all chapters, the author hopes to keep reading exciting throughout the whole thesis. Nevertheless each chapter is designed to be readable independently of the others, and hence contains individual introduction, discussion and summary sections.

Chapter 2 is dedicated to introduce the reader to contemporary simulation of object exit waves using ab-initio scattering factors for crystals with thermal and static disorder. In chapter 3, a method is presented that allows for computationally efficient refinement of the specimen thickness, the Laue circle centre, Debye parameters and structure factors from diffraction patterns acquired under almost parallel illumination. In particular, ab-initio results for the 200 structure factors of GaAs and InAs, as well as Debye-Waller factors for GaAs are refined, whereas the GaAs result is additionally verified by CBED. Chapter 4 presents a full ab-initio reliability study of crystal structural parameters, that is, atom positions and structure factors, under the influence of bonding and SAD. This was done to verify the combination of an atomistic treatment of bonding with (empirical) valence force field strain relaxation. Furthermore, a two-beam method for quaternary composition quantification in an InGaNaNs solar cell is also presented. Finally, chapter 5 extends InGaNaNs composition quantification to the whole composition range by introducing a three-beam imaging method that circumvents nonlinear imaging artefacts. As an example application, this technique is used to examine thermal annealing effects on chemical composition maps in an $\text{In}_{0.28}\text{Ga}_{0.72}\text{N}_{0.025}\text{As}_{0.975}$ layer. Please see the commented publications list on pages 155 ff for details on each chapter's published counterpart.

In order to interpret results of this thesis as a whole, a comprehensive discussion is provided in chapter 6 that composes the conclusions of the individual chapters to a consistent picture, whose role in the science of microscopy of semiconductor nanostructures is worked out finally.

Chapter 2

Electron scattering theory

2.1 Introduction

Fundamental to all observations in TEM is an interaction of the electron beam with the specimen. Studying one of the first theoretical considerations given by Bethe [36] in 1928 already reveals that the term *interaction* unifies three complex subitems, to which this chapter is dedicated: First, a realistic scattering potential must be set up, second interaction of relativistic electrons with this potential is to be described and third, propagation of the electron wave to the specimen exit face must be performed. Since Bethe's work, each of these three topics has been subject to extensive investigations, having lead to a vast number of important results for the TEM community. However, it goes without saying that one chapter of this thesis cannot raise the claim to derive or even summarise all aspects of importance for contemporary work in the field of TEM. Moreover, the author likes to not only review conventional quantitative TEM aspects, but also to present some first results of recent own work, making the choice which items to include even more difficult.

The actual content of this chapter can be understood by asking on which fundamentals the following ones are built: Section 2.2 picks just a single atom out of a crystal and not only introduces definitions like atomic scattering amplitudes (ASA) and Fourier transforms used throughout this work, but also gives the connection between scattering properties for X-rays and electrons. This is important for both presenting electron diffraction results (chapter 3) and making use of density functional theory (DFT) outputs in electron diffraction (chapter 4).

The model of an ideal crystal will be examined in detail in section 2.3 because it provides an efficient way for diffraction pattern and image simulation as will be utilised in each of the chapters 3, 4, 5 and in the DFT calculations. As the latter were used to derive atomic forces or electron scattering factors which entered nearly all simulations of reference data for composition quantification, DFT basics and their implementation in the WIEN2K code is paid some attention. Exploiting this knowledge, chemical bonding is explicitly considered by means of potential and charge density difference maps for GaAs. The section on bonding closes with the explanation of the modified ASA (MASA) approach according to Rosenauer et al. [9] which allows for atomistic treatment of this topic. Modified, composition-dependent ASA, calculated during this work for InGaNaNs, are presented and the treatment of compositional dependence is explained.

Sections 2.4 and 2.5 are dedicated to understand dynamical scattering of electrons. In particular, purpose and basics of Bloch wave and multislice simulations are explained,

respectively. However, focus is on Bloch waves because refinement routines for chapter 3 and simulations of TEM images for chapters 4 and 5 were developed in the framework of the Bloch wave approach, which is the fundament of the Bloch4TEM [37] program.

Section 2.6 temporarily leaves the ideal crystal approximation and explores thermal and static disorder, which give rise to, e.g., diffuse scattering that must be considered in quantitative analysis of Bragg intensities (chapters 3 and 5). Concerning static disorder due to atomic size effects, the principle of valence force field (VFF) calculations to derive static atomic displacements (SAD) is briefly reviewed. In the end of section 2.6, the author harks back to the ideal crystal model by explaining the treatment of thermal diffuse scattering (TDS) in terms of absorption on the one hand, and by proposing a way to analogously handle SAD diffuse scattering on the other. To this end, Bragg intensities obtained by Bloch wave simulations are compared with full multislice results. Chapter 2 closes with a discussion and important conclusions.

Survey of literature

For reasons mentioned above, this chapter in part presents standard knowledge for TEM and solid state physics sometimes in a compact manner, so that background information may be desirable. During decades, comprehensive textbooks appeared which not only elegantly summarise original work but also apply well known aspects to special situations. This introduces some difficulties in referencing, meaning that some issues either refer to a long list of literature or one more or less arbitrary reference. The following abstract is intended to put most of the references in this chapter in correct order with regards to content.

In the book of de Graef [38], most of the contemporary multislice and Bloch wave approaches is summarised. Development of the multislice method starts at Ref. [39] and was re-derived from the Schrödinger equation in Ref. [40], whereas the real space multislice method goes back to Ref. [41]. Modifications of this method have then been reported in Ref. [42] and its robustness against external parameters has been examined in Ref. [43] with details on propagation in [44]. Bloch wave treatment for Laue and Bragg scattering geometry goes back to Ref. [36] and is comprehensively summarised for TEM applications in Ref. [45]. Convergence studies can be found in Ref. [46], whereas role and application of the Bloch wave approach for refinements using experimental data is covered by the book of Spence [47] and Refs. [48, 49, 50, 51]. Detailed treatment of absorption due to TDS and SAD in Bloch wave simulations is composed in the book of Wang [52], whereas TDS absorptive potentials rely on the work in Refs. [53], [54] and [55]. Formally equivalent work for TDS of X-rays had been published previously in the first edition of James' book [56, ed. 1948]. A review of TDS and the introduction of TDS emission potentials in order to bring back TDS electrons to ideal crystal multislice simulations is found in Ref. [57]. Diffuse scattering at SAD relies on Ref. [58] and is elaborately included in the book of Cowley [59]. Empirical potentials for the derivation of SAD are often either of Stillinger-Weber or Keating type, according to Ref. [60] and Refs. [31, 61], respectively. Contemporary DFT calculations are pioneered by Refs. [62, 63], and the book of Springborg [64] dealt as a source for DFT basics. Concerning the WIEN2K implementation, the manuals by Cottenier and Blaha [65, 66] and original publications [67, 68, 69] may be used for understanding the governing parameters. Parameterised atomic scattering data can be found in Ref. [9] in case of MASA for InGaAs and various studies on size effects in combination with MASA are contained in Refs. [70, 71, 7]. Modified ASA for a variety

of strained ternary compounds will be available forthcoming in parameterised form in Ref. [72]. Absorptive potentials and/or ASA have been calculated and parameterised in isolated atom approximation by many groups, of which Refs. [73, 74, 75, 76, 77, 78] are frequently used. Temperature-dependent, parameterised Debye-Waller factors were calculated from neutron scattering experiments in Ref. [79] and re-parameterised in Ref. [80] for a variety of zinc-blende crystals. Most recent Debye-Waller factors rely on DFT calculations as published in Refs. [81, 82].

2.2 Scattering potential of single atoms

At first, we regard a single atom separated from a specimen. This abstraction makes sense because an atomic scattering potential valid for this atom may be derived which serves as a patch that can be put at all positions of this atom in a real specimen. It is additionally assumed that the scattering potential is a property of the atom only, that is, exchange effects between valence electrons of the atom and the beam electron are negligible which is true for incident energies above 1 kV [83]. Only elastic scattering is considered in the following.

From numerical methods, such as Hartree-Fock [84] or DFT calculations [63], either the electrostatic Coulomb potential $v(\mathbf{r})$ or the electron density $\varrho_e(\mathbf{r})$ or both are obtained for an atom of interest. Adding nuclear contributions $\varrho_Z(\mathbf{r})$ and inserting in Maxwell's equations yields $\nabla \cdot \mathbf{E} = \frac{e}{\varepsilon_0} \varrho(\mathbf{r})$ with electric field \mathbf{E} , elementary charge e , electric constant ε_0 , and total charge density $e\varrho(\mathbf{r}) = e\varrho_Z(\mathbf{r}) - e\varrho_e(\mathbf{r})$. Inserting $\mathbf{E} = -\nabla v(\mathbf{r})$ results in Poisson's equation

$$\nabla^2 v(\mathbf{r}) = -\frac{\varrho}{\varepsilon_0} = \frac{e}{\varepsilon_0} [\varrho_e(\mathbf{r}) - \varrho_Z(\mathbf{r})] \quad (2.1)$$

which establishes the fundamental connection between potential $v(\mathbf{r})$ and electron density $\varrho_e(\mathbf{r})$.

In the majority of cases it is advantageous to treat scattering in reciprocal space. For this purpose we define the Fourier transforms $f(\mathbf{q})$ and $f^X(\mathbf{q})$

$$f(\mathbf{q}) = \mathcal{F}[v](\mathbf{q}) = \int_{-\infty}^{\infty} v(\mathbf{r}) e^{-2\pi i \mathbf{q} \mathbf{r}} d^3 r \quad (2.2a)$$

$$f^X(\mathbf{q}) = \mathcal{F}[\varrho_e](\mathbf{q}) = \int_{-\infty}^{\infty} \varrho_e(\mathbf{r}) e^{-2\pi i \mathbf{q} \mathbf{r}} d^3 r \quad . \quad (2.2b)$$

By inverse Fourier transform of Eqs. (2.2) and by assuming the nucleus with positive charge Ze to be point-shaped at the origin, $\varrho_Z(\mathbf{r}) = Z\delta(\mathbf{r})$, Eq. (2.1) takes the form

$$\nabla^2 \int_{-\infty}^{\infty} f(\mathbf{q}) e^{2\pi i \mathbf{q} \mathbf{r}} d^3 q = \frac{e}{\varepsilon_0} \left[\int_{-\infty}^{\infty} f^X(\mathbf{q}) e^{2\pi i \mathbf{q} \mathbf{r}} d^3 q - \int_{-\infty}^{\infty} Z e^{2\pi i \mathbf{q} \mathbf{r}} d^3 q \right] \quad .$$

Permutation of integration and differentiation and dropping the integrals yields the Mott-Bethe relation

$$-4\pi^2 \mathbf{q}^2 f(\mathbf{q}) = \frac{e}{\varepsilon_0} [f^X(\mathbf{q}) - Z] \Leftrightarrow f(\mathbf{q}) = \frac{e}{4\pi^2 \mathbf{q}^2 \varepsilon_0} [Z - f^X(\mathbf{q})] \quad , \quad (2.3)$$

which is frequently used to translate $f(\mathbf{q})$ to $f^X(\mathbf{q})$ and vice versa.

It is important to note that, besides the mathematical definition in Eq. (2.2a), $f(\mathbf{q})$ can also be derived from the Schrödinger equation when elastic electron scattering at a single atom is considered. In this case, plane wave incidence with wave vector \mathbf{k} is assumed and superposed to a scattered wave with wave vector \mathbf{k}' and an amplitude which depends on momentum transfer $\mathbf{q} = \mathbf{k}' - \mathbf{k}$. Expanding the wave function to a Born series and neglecting all but the first term leads to Eq. (2.2a) for the angular dependence of the amplitude of the scattered wave. Therefore, $f(\mathbf{q})$ is equal to the ASA in first order Born approximation which ignores multiple scattering. Because of this formal equivalence of the ASA with the Fourier transforms in Eq. (2.2), $f(\mathbf{q})$ and $f^X(\mathbf{q})$ are referred to as *atomic scattering amplitudes* for electrons and X-rays, respectively. Consequently, this does not necessarily imply that multiple scattering is neglected since ASA often simply denote potential or electron density in reciprocal space in this work. On the other hand, the term ASA may refer to higher order Born approximations mainly in literature on X-ray diffraction, so that care must be taken because then it is not equal to the Fourier transforms in Eq. (2.2) anymore.

Electron ASA (2.2a) adopt the convention of the International Tables for Crystallography C [85, p.735-743] and are given in Vm^3 , ASA for X-rays are dimensionless according to volume B [86, p.10-24]. A related important quantity is the *scattering length* $\frac{2\pi m_e e}{h_P^2} f(\mathbf{q})$ with electron mass m_e and Planck's constant h_P . It is based on the traditional definition according to the Born approximation.

Another property generally assigned to an individual atom is the thermal displacement \mathbf{u} which takes finite values even at 0 K due to zero-point motion. It must thus be taken into account in any realistic simulation. The atomic potential then becomes time dependent, $v(\mathbf{r}, t) = v[\mathbf{r} + \mathbf{u}(t)]$, where it is assumed that the shape of $v(\mathbf{r})$ is not changed but shifted to a time dependent position $\mathbf{r} + \mathbf{u}(t)$. In the framework of Debye-Waller damping [57], the atom is considered to be at rest at the equilibrium position $\mathbf{u} = 0$ but causing a time-averaged potential $\tilde{v}(\mathbf{r}) := \langle v(\mathbf{r}, t) \rangle_t$. Hence, in Dirac notation, Eq. (2.2a) takes the form $\tilde{f}(\mathbf{q}) := \langle f(\mathbf{q}, t) \rangle_t = \langle \mathbf{k}' | \tilde{v}(\mathbf{r}) | \mathbf{k} \rangle$. Expanding $\tilde{v}(\mathbf{r})$ in a Taylor series around $\mathbf{u} = 0$ yields

$$\begin{aligned} \tilde{f}_x(\mathbf{q}) &= \left\langle \mathbf{k}' \left| v(\mathbf{r}) + \frac{\langle u_x^2 \rangle_t}{2} \cdot \frac{d^2 v(\mathbf{r})}{d x^2} + \frac{\langle u_x^4 \rangle_t}{24} \cdot \frac{d^4 v(\mathbf{r})}{d x^4} + \dots \right| \mathbf{k} \right\rangle \\ &= \langle \mathbf{k}' | v(\mathbf{r}) | \mathbf{k} \rangle + \frac{\langle u_x^2 \rangle_t}{2} \left\langle \mathbf{k}' \left| \frac{d^2 v(\mathbf{r})}{d x^2} \right| \mathbf{k} \right\rangle + \frac{\langle u_x^4 \rangle_t}{24} \left\langle \mathbf{k}' \left| \frac{d^4 v(\mathbf{r})}{d x^4} \right| \mathbf{k} \right\rangle + \dots \end{aligned} \quad (2.4)$$

where only vibrations along x -direction are examined without loss of generality. Note that odd powers of \mathbf{u} vanish when averaging over time. Recognising that Eq. (2.4) is essentially a sum of Fourier transforms, for which [59]

$$\left\langle \mathbf{k}' \left| \frac{d^n v(\mathbf{r})}{d x^n} \right| \mathbf{k} \right\rangle = [2\pi i (\mathbf{k}' - \mathbf{k})]^n \langle \mathbf{k}' | v(\mathbf{r}) | \mathbf{k} \rangle = (2\pi i \mathbf{q})^n f(\mathbf{q}) \quad (n = 0, 2, 3, \dots) \quad ,$$

Eq. (2.4) can be written as

$$\begin{aligned} \tilde{f}_x(\mathbf{q}) &= f(\mathbf{q}) \left[1 + \frac{1}{2} (2\pi i \mathbf{q})^2 \langle u_x^2 \rangle_t + \frac{1}{24} (2\pi i \mathbf{q})^4 \langle u_x^4 \rangle_t + \dots \right] \\ &\approx f(\mathbf{q}) \left[1 + \frac{1}{2} (2\pi i \mathbf{q})^2 \langle u_x^2 \rangle_t \right] \\ &\approx f(\mathbf{q}) e^{-2\pi^2 \mathbf{q}^2 \langle u_x^2 \rangle_t} \quad , \end{aligned} \quad (2.5)$$

where the first approximation corresponds to harmonic potentials and the second is due to Taylor expansion of the exponential function. The fundamental result of Eq. (2.5) is that thermal vibration results in Gaussian damping of ASA, called *Debye-Waller factor* $D(q)$, being determined by the mean squared displacement $\langle u_x^2 \rangle_t$. Since atomic vibrations may in general be anisotropic, $D(q)$ is commonly expressed as

$$D(q) = e^{-\frac{1}{4}\mathbf{q}\mathcal{B}\mathbf{q}} \quad (2.6)$$

with the second-rank tensor \mathcal{B} . Especially, using Bravais coordinates, \mathcal{B} is diagonal with $\mathcal{B}_{\alpha\alpha} = 8\pi^2\langle u_\alpha^2 \rangle_t$, $\alpha = x, y, z$. For cubic structures, vibrations are isotropic so that $D(q) = e^{-\frac{1}{4}Bq^2}$ with the scalar *Debye parameter* [73] $B = 8/3\pi^2\langle \mathbf{u}^2 \rangle_t = 8\pi^2\langle u_\alpha^2 \rangle_t$.

2.3 Scattering potential of ideal crystals

Knowing that the model of an ideal crystal with infinite extension and perfect translational symmetry is a too crude abstraction originating from Bravais' analysis in 1850 [87], which has rather been motivated by mineralogists' observations of crystal habitus than by scattering experiments, this model has at least three important applications in scattering theory today. First, it is highly efficient in case only Bragg intensities are of interest, because they can indeed be simulated correctly by assuming an ideal crystal. However, structure factors are to be modified according to disorder occurring in real crystals which section 2.6 deals with. Second, an ideal crystal is mostly used as a starting point for the derivation of properties of real crystals, such as thermal or static atomic displacements. Third, some quantities, especially chemical bonding, are robust against, e.g., thermal disorder which essentially affects scattering at high angles according to Eq. (2.6). Hence bonding effects may be studied on the basis of an ideal crystal which is one main topic of this section.

2.3.1 The structure factor

The strict periodicity in ideal crystals entitles us to write the electrostatic Coulomb potential for one Bravais unit cell as a sum over atomic potentials in it, and to copy it to all Bravais lattice points \mathbf{t} :

$$V^\kappa(\mathbf{r}) = V_{cell}^\kappa(\mathbf{r}) \otimes \mathcal{J}^\kappa(\mathbf{r}) \quad (2.7)$$

with $V_{cell}^\kappa(\mathbf{r}) = \sum_j \tilde{v}_{Z,j}^\kappa(\mathbf{r} - \mathbf{r}_j)$ and $\mathcal{J}^\kappa(\mathbf{r}) = \sum_{\mathbf{t}^\kappa} \delta(\mathbf{r} - \mathbf{t}^\kappa)$.

Here, V_{cell}^κ is the potential in one unit cell, j counts the atoms at positions \mathbf{r}_j in this cell, \otimes denotes convolution and κ indexes the crystal, e.g., GaAs or InAs. Strictly speaking, it is not obvious that V_{cell}^κ may be built by individual atomic potentials because it implies that the crystal potential, and with it the electron density, can be separated accordingly. However, this assumption leads to the structure factor as conventionally defined and must be verified when chemical bonding is taken into account, as will be explained later. In principle, indexing atoms by j is already unique because \tilde{v}_j^κ corresponds to a specific site j occupied by a certain element. Nevertheless it is useful to indicate also (and sometimes only) the atomic species on this site by atomic number Z since $\tilde{v}_{Z,j}^\kappa$ changes if different atoms are placed at site j . This notation is chosen as it allows to assign effects of a

redistribution of electrons due to chemical bonding to single atoms, as will be explained in section 2.3.5.

In the strict sense, thermal motion as implicitly present in $\tilde{v}_{Z,j}^\kappa$ should be neglected when dealing with an ideal crystal. However, the following derivation formally leads to the same results and, more important, to definitions commonly used. According to Eq. (2.6), $\mathcal{B} = 0$ yields the potential for atoms at rest. Fourier transform of Eq. (2.7) and using the convolution theorem yields $V^\kappa(\mathbf{q}) = \frac{1}{\Omega} \mathcal{F}[V_{cell}^\kappa](\mathbf{q}) \cdot \mathcal{F}[T^\kappa](\mathbf{q})$ with unit cell volume Ω . Evaluation of the first Fourier transform leads to

$$\begin{aligned} \mathcal{F}[V_{cell}^\kappa](\mathbf{q}) &= \sum_j \int \tilde{v}_{Z,j}^\kappa(\mathbf{r} - \mathbf{r}_j) e^{-2\pi i \mathbf{q} \mathbf{r}} d^3 r \\ &= \sum_j \int \tilde{v}_{Z,j}^\kappa(\mathbf{r}') e^{-2\pi i \mathbf{q} \mathbf{r}'} d^3 r' \cdot e^{-2\pi i \mathbf{q} \mathbf{r}_j} \\ &= \sum_j \tilde{f}_{Z,j}^\kappa(\mathbf{q}) e^{-2\pi i \mathbf{q} \mathbf{r}_j} \quad , \end{aligned} \quad (2.8)$$

where Eq. (2.2a) was used in the last line. Noting that the Fourier transform of \mathcal{J} is equal to the reciprocal lattice [59, p.42], we have

$$V^\kappa(\mathbf{q}) = \frac{1}{\Omega} \sum_j \tilde{f}_{Z,j}^\kappa(\mathbf{q}) e^{-2\pi i \mathbf{q} \mathbf{r}_j} \cdot \sum_{\mathbf{g}} \delta(\mathbf{q} - \mathbf{g}) \quad , \quad (2.9)$$

which gives in real space

$$V^\kappa(\mathbf{r}) = \sum_{\mathbf{g}} \left(\frac{1}{\Omega} \sum_j \tilde{f}_{Z,j}^\kappa(\mathbf{g}) D_{Z,j}^\kappa(\mathbf{g}) e^{-2\pi i \mathbf{g} \mathbf{r}_j} \right) e^{2\pi i \mathbf{g} \mathbf{r}} =: \sum_{\mathbf{g}} V_{\mathbf{g}}'^\kappa e^{2\pi i \mathbf{g} \mathbf{r}} \quad (2.10)$$

with complex Fourier coefficients $V_{\mathbf{g}}'^\kappa$ of the electrostatic Coulomb potential in braces. It is emphasised that ASA and Debye-Waller factors not only depend on crystal type κ , but also on site j . We thus conclude:

1. The same element may have different ASA and Debye-Waller factors in different crystals.
2. The same element at different sites in one crystal may have different ASA (due to bonding) and different Debye-Waller factors, too.

As a final step, we drop the assumption that $V^\kappa(\mathbf{r})$ is real and add an imaginary potential $W^\kappa(\mathbf{r})$, $V^\kappa(\mathbf{r}) \rightarrow V^\kappa(\mathbf{r}) + iW^\kappa(\mathbf{r})$, which enables us to account for absorption in simulations as will become important later. In complete analogy to the above derivation we define

$$V_{\mathbf{g}}^\kappa := V_{\mathbf{g}}'^\kappa + iW_{\mathbf{g}}^\kappa = \text{Re} \left(V_{\mathbf{g}}'^\kappa \right) + i \text{Im} \left(V_{\mathbf{g}}'^\kappa \right) + i \text{Re} \left(W_{\mathbf{g}}^\kappa \right) - \text{Im} \left(W_{\mathbf{g}}^\kappa \right) \quad , \quad (2.11)$$

and call $V_{\mathbf{g}}^\kappa$ the \mathbf{g} -Fourier component of the crystal potential. Throughout literature (including this work), $V_{\mathbf{g}}^\kappa$ appears in different units, depending on the subject investigated. The quantity $V_{\mathbf{g}}^\kappa$ itself is in units of V according to Eq. (2.2a). By multiplication with a proportionality factor $2m_e e h_P^{-2}$, it is given in units of m^{-2} and denoted by $U_{\mathbf{g}}^\kappa$. Furthermore, the length $F_{\mathbf{g}}^\kappa := 2\pi m_e e \Omega h_P^{-2} V_{\mathbf{g}}^\kappa$ is called the structure factor for electron

scattering. Note that none of these quantities contains experiment-specific parameters, such as the acceleration voltage of a TEM, so that the definitions are suitable for straight comparison of experimental or theoretical results among different groups.

Similar to ASA defined in Eq. (2.2), structure factors for electron scattering are often converted to X-ray structure factors $X_{\mathbf{g}}^{\kappa}$. This not only makes comparison between results of these two communities possible, but also allows for conversion of electrostatic potential to electron density. Inserting Eq. (2.2b) in Eq. (2.10) yields

$$X_{\mathbf{g}}^{\kappa} := \sum_j f_{Z,j}^{X,\kappa}(\mathbf{g}) e^{-2\pi i \mathbf{g} \mathbf{r}_j} = \sum_j Z_j D_{Z,j}^{\kappa}(\mathbf{g}) e^{-2\pi i \mathbf{g} \mathbf{r}_j} - \frac{2\pi \mathbf{g}^2 \varepsilon_0 \hbar^2}{m_e e^2} F_{\mathbf{g}}^{\kappa} \quad , \quad (2.12)$$

where the conventional definition [86, p.10-24] of $X_{\mathbf{g}}^{\kappa}$ was repeated on the left.

2.3.2 Isolated atom approximation

As ASA depend on crystal κ and site j , they are a very complicated and case sensitive quantity because the origin of both indices lies in local bonding. This in turn is mainly influenced by valence electrons of atoms or, equivalently, outer orbitals of electrons. It was already mentioned in section 2.2 that $f(\mathbf{q})$ is proportional to the probability amplitude for a scattering event at a single atom with momentum transfer \mathbf{q} in first order Born approximation. An electron scattered at outer orbitals suffers small changes in momentum only because most of the atomic potential is screened by inner orbitals, meaning that bonding modifies $f(\mathbf{q})$ solely for small values of \mathbf{q} . From the mathematical point of view this can also be understood since low spatial frequencies are needed to build up the outer part of the atomic potential. From this follows that one expects that neglect of the dependence on κ and j in derivation of $f_Z(\mathbf{q})$, called isolated atom approximation, gives reasonable results for medium and large momentum transfers, whereas care is to be taken for small \mathbf{q} .

This approach has a lot of practical advantages: First, ASA depend only on atomic number Z , so that they can be tabulated in very close form by listing $f_Z(\mathbf{q})$ for all elements. Second, $\varrho_e(\mathbf{r})$ and $v(\mathbf{r})$ obey spherical symmetry. According to Eq. (2.2), ASA then become real quantities which only depend on the modulus of \mathbf{q} , so that $f_Z(|\mathbf{q}|)$ can efficiently be fitted by, e.g., superposition of four Gaussians [78]. Third, this provides ASA for continuous $|\mathbf{q}|$ which is often needed to build up the potential of disordered crystals for multislice simulations.

We will not go into details of relativistic Hartree-Fock calculations which are typically used in most tabulated data sets because this work uses ASA as published in literature, mainly by Doyle and Turner [78], Bird and King [76] and Weickenmeier and Kohl [75]. However, it is worth mentioning that the Hartree-Fock approach constructs a many-electron wave function from the Slater determinant and solves the Hartree-Fock equations by adjusting the single-particle wave functions until self-consistency is reached. In single atom approximation, the single-particle Hamiltonian contains the kinetic energy, attraction of one nucleus as an external field, repulsive Coulomb and exchange interactions among electrons. Once self-consistency is obtained, $\varrho_e(\mathbf{r})$ is calculated from the ground state wave function, yielding ASA according to Eqs. (2.2).

2.3.3 Density functional theory

Once the wave function of a many-particle system is known it serves on the one hand to derive all other properties, but on the other hand it is a very complex object with no direct physical meaning. The approach to regard the electron density $\rho_e(\mathbf{r})$ as the central property of a system, and to derive observables from knowledge of $\rho_e(\mathbf{r})$ only, goes back to Thomas and Fermi [88, 89] who assumed that electrons form a gas with slowly varying $\rho_e(\mathbf{r})$. It gained fundamental importance for computational solid state physics with two theorems of Hohenberg and Kohn [62]: First, any ground-state property, such as the wave function and the ground-state energy E^0 , can uniquely be derived from the ground-state electron density $\rho_e^0(\mathbf{r})$ via a functional. Second, provided that the functional $E[\rho_e]$ which relates $\rho_e(\mathbf{r})$ and E is known, $E[\rho_e \neq \rho_e^0] \geq E[\rho_e^0]$. Thus ρ_e^0 can be derived via variational principle by variation $\delta E[\rho_e] = 0$. This extremely improves computational efficiency in comparison to Hartree-Fock calculations because the number of coordinate parameters reduces from $3N$ to 3 in DFT if spin is not taken into account and an N -electron system is considered. In this way the complexity of the system under investigation may be increased from single atoms (Hartree-Fock) to molecules and solids (DFT).

From $\delta E[\rho_e] = 0$ and $\int \rho_e(\mathbf{r}) d^3r = N$ one obtains

$$\frac{\delta}{\delta \rho_e} \left\{ E[\rho_e] - \mu \left[\int \rho_e(\mathbf{r}) d^3r - N \right] \right\} = 0 \quad , \quad (2.13)$$

and it becomes obvious that the functional $E[\rho_e]$ must be known which is not the case. It contains, however, contributions from kinetic energy T , external potential V_{ext} , repulsive Coulomb interaction among electrons V_C , as well as exchange and correlation effects E_{xc} , all being functionals of $\rho_e(\mathbf{r})$. Variation of Eq. (2.13) and neglect of nonlinear terms in $\delta \rho_e$ which occur for electron-electron interactions leads to [64, p.196f]

$$\frac{\delta T[\rho_e]}{\delta \rho_e} + V_{ext}(\mathbf{r}) + V_C(\mathbf{r}) + \frac{\delta E_{xc}[\rho_e]}{\delta \rho_e} = \mu \quad . \quad (2.14)$$

This equation drastically simplifies in the approach of Kohn and Sham [63], where a fictitious system is regarded with non-interacting electrons moving in an effective potential V_{eff} . This is constructed in such a way that it has the same ground-state electron density as the real system. In analogy to Eq. (2.14), variation leads to

$$\frac{\delta T'[\rho_e]}{\delta \rho_e} + V_{eff} = \mu \quad , \quad (2.15)$$

and comparison of Eqs. (2.14) and (2.15) identifies the effective potential

$$V_{eff}(\mathbf{r}) = \frac{\delta T[\rho_e]}{\delta \rho_e} - \frac{\delta T'[\rho_e]}{\delta \rho_e} + V_{ext}(\mathbf{r}) + V_C(\mathbf{r}) + \frac{\delta E_{xc}[\rho_e]}{\delta \rho_e} \quad , \quad (2.16)$$

where T and T' distinguish between the kinetic energies in both systems because non-interacting particles may behave differently.

Since electrons in the model system do not interact, the full Hamiltonian $\hat{\mathbf{H}}$ is the sum of single particle Hamiltonians $\hat{\mathbf{h}}_k$, $\hat{\mathbf{H}} = \sum_k \hat{\mathbf{h}}_k$. As $\hat{\mathbf{h}}_k$ acts on a single particle only, the state of the whole system is constructed from single-particle states $|\varphi_k\rangle$ via Slater determinant as in the Hartree-Fock formalism. This leads to N differential equations

$$\hat{\mathbf{h}}_k |\varphi_k\rangle = \varepsilon_k |\varphi_k\rangle \quad \Leftrightarrow \quad \left[\frac{-\hbar^2}{2m_e} \nabla^2 + V_{eff}(\mathbf{r}) \right] |\varphi_k\rangle = \varepsilon_i |\varphi_k\rangle \quad (2.17)$$

Table 2.1: Parameters used for the VFF and DFT-LDA calculations. DFT Lattice parameters have been calculated by Schowalter et al. [81]. Elastic constants are taken from a review by Vurgaftman et al. [11].

Property	InN	InAs	GaN	GaAs
a_{EXP} [nm]	0.5004	0.6058	0.4519	0.5653
a_{DFT} [nm]	0.4945	0.6038	0.4460	0.5612
C_{11} [GPa]	223	83	293	122
C_{12} [GPa]	115	45	159	57

called the Kohn-Sham equations. They are practically solved iteratively until self-consistency is obtained. The advantage in comparison to Hartree-Fock calculations is that V_{eff} depends on the position of the electron under consideration only and thus becomes a local potential. Moreover, Eq. (2.17) contains not only density functionals but also explicitly single-particle wave functions in a Schrödinger-type equation, so that kinetic energies in the model system are treated correctly, opposite to the density-based Thomas-Fermi approach.

It must be stressed again that the model system was constructed in such a way that, per definition, $\rho_e^0(\mathbf{r})$ must be in common with the real system. Especially ε_k and $|\varphi_k\rangle$ are parameters without direct physical interpretation, such as single-particle energy or orbital, because they are solutions to a fictitious potential. It is furthermore assumed that such a potential exists, which is not necessarily true in all, but fortunately in most cases with practical relevance [64, p.198]. However, the fact that the direct result of DFT calculations is the electron density $\rho_e^0(\mathbf{r})$ for ensembles of atoms makes it an ideal approach for the derivation of scattering potentials of solids according to Eqs. (2.2b), (2.3) and (2.10).

From Eq. (2.16) it can be seen that still the unknown functional $E_{xc}[\rho_e]$ enters the Kohn-Sham equations. In this respect, one way is to return to the Thomas-Fermi approach for the exchange and correlation part because $E_{xc}[\rho_e]$ is known for a homogeneous electron gas. Because $\rho_e(\mathbf{r})$ varies spatially in practice, E_{xc} at position \mathbf{r} is calculated from an electron gas with constant density $\rho_e^h = \rho_e(\mathbf{r})$. Because E_{xc} then depends only on electron density at one position, this approach is called *local density approximation* (LDA). Another way is to include also gradients of $\rho_e(\mathbf{r})$ for which various parameterisations exist and which is referred to as *generalised gradient approximation* (GGA).

Due to the fact that DFT calculations require no external physical parameters it is often referred to as an *ab-initio* method, though it was just pointed out that some approximations enter via LDA or GGA. Besides numerical consistency which we will attend later, DFT results must therefore be checked with respect to the approximation used, and, if available, with experimental results.

This circumstance will now be exemplified by means of the lattice parameter for GaAs. A series of DFT calculations for different lattice parameters was performed using the WIEN2K code [1]. Total energies found in the last cycle are plotted as a function of the lattice parameter in Fig. 2.1 for LDA results (black) and GGA results (grey). The range of experimental results for temperatures between 77 and 752 K found by Leszczynski et al. [90] is also marked. In the strict sense, DFT results ought to be compared with experiments at 0 K, but Fig. 2.1 clearly shows that the discrepancy between the energy minima for LDA and GGA is much larger than variation with temperature over about 700 K. Figure 2.1 also implies that neither LDA nor GGA lead to the correct lattice parameter, the former leading to an under-, the latter to an overestimation. Hence LDA strengthens, whereas GGA weakens interatomic bonds with respect to the true bond strength. This may be important for the derivation of crystal properties such as elastic

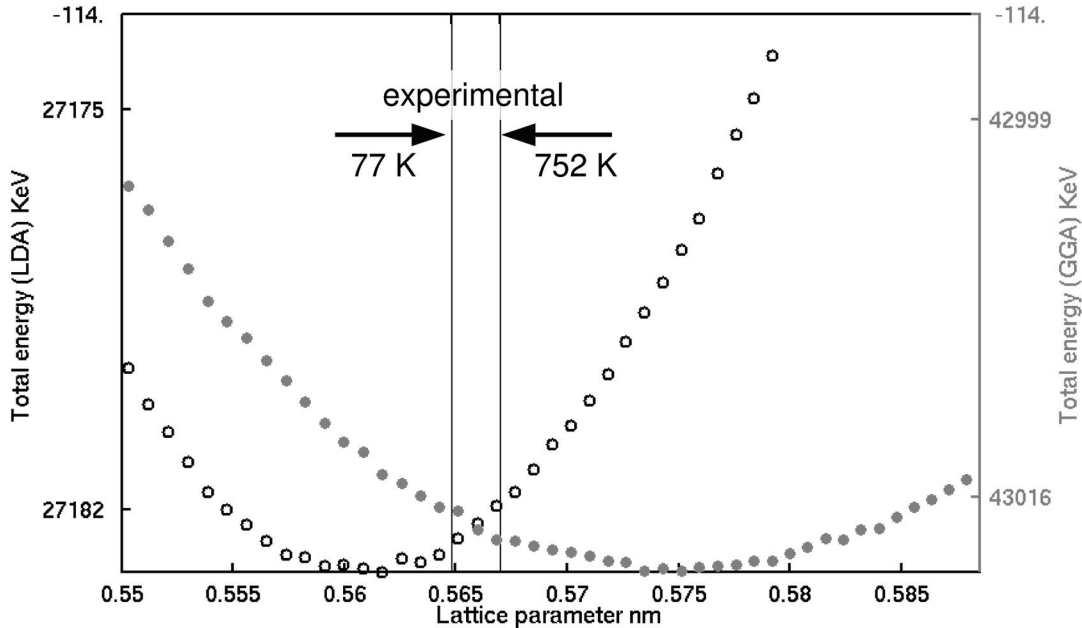


Figure 2.1: Concerning equilibrium lattice parameters for GaAs in experiment (vertical lines), DFT-LDA (black) and DFT-GGA (grey). Experimental values are taken from Leszczynski et al. [90] for the temperature range given there. DFT calculations have been performed using WIEN2K [1] with 1000 k-points and an RK_{max} -parameter of 7. Self-consistent cycles were iterated until energy convergence of 0.0001 Ry was reached. The equilibrium lattice parameter for LDA (GGA) is then given by the minimum of the blue (red) curve.

constants, phonon density of states, or the electrostatic Coulomb potential. However, it can be assumed that the true result lies somewhere between the results of LDA and GGA, so that finding the equilibrium lattice parameter for both approximations is a pre-stage for reasonable DFT calculations. Usually, DFT calculations are performed using both LDA and GGA. Further lattice parameters of binary crystals which are important for this work are listed in table 2.1.

Electron density is the main outcome of DFT and immediately yields X-ray structure factors according to Eq. (2.12). They can be converted to structure factors for electron scattering, enabling us to introduce bonding effects in TEM image and diffraction pattern simulation. However, a variety of crystal properties may be derived using DFT, of which in particular atomic forces are of direct interest in this work, so that the basic idea is briefly explained.

The force acting on atom j in a system with total energy E is given by

$$\begin{aligned}
 \mathbf{F}_j &= -\nabla_j E \\
 &= -\nabla \langle \psi | \hat{\mathbf{H}} | \psi \rangle \\
 &= -\langle \psi | \nabla \hat{\mathbf{H}} | \psi \rangle - \langle \nabla \psi | \hat{\mathbf{H}} | \psi \rangle - \langle \psi | \hat{\mathbf{H}} | \nabla \psi \rangle \quad .
 \end{aligned} \tag{2.18}$$

Here the energy was expressed as the expectation value of the full Hamiltonian $\hat{\mathbf{H}}$. The first term in Eq. (2.18) is called the *Hellmann-Feynman force*, the following terms are known as the *Pulay force*. Assuming that $|\psi\rangle$ is the exact solution of the Schrödinger equation $\hat{\mathbf{H}}|\psi\rangle = E|\psi\rangle$, we find $E\nabla\langle\psi|\psi\rangle = 0$ for the Pulay force. Then, the total force equals the Hellmann-Feynman force and for component α ($\alpha = x, y, z$) of the force on

atom j , located at \mathbf{R}_j , Eq. (2.18) yields

$$F_{j,\alpha} = -\frac{dE}{dR_{j,\alpha}} = -\left\langle \psi \left| \frac{d\hat{\mathbf{H}}}{dR_{j,\alpha}} \right| \psi \right\rangle . \quad (2.19)$$

The second identity holds for differentiation with respect to any parameter of the system as long as $|\psi\rangle$ solves the Schrödinger equation exactly, which is the statement of the Hellmann-Feynman theorem. However, expressing a true eigenstate of $\hat{\mathbf{H}}$ by an incomplete (finite) basis violates Parseval's equation and leads to residual Pulay forces. Note that the Pulay force vanishes also if $|\psi\rangle$ is expressed in a basis which does not depend on nuclear coordinates, e.g., plane waves. In practice, Pulay corrections must usually be taken into account because wave functions in DFT are constructed from wave functions of fictitious single particles via Slater determinant. This not necessarily yields the exact solution of the Schrödinger equation for the true system.

Knowledge of forces acting on each atom is the starting point for the derivation of several quantities. First, the forces themselves express whether the structure takes its energetic equilibrium with respect to atomic positions. Second, if forces exceed a given tolerance, DFT can be used to iteratively optimise the structure by shifting the atoms appropriately along the force vectors. Third, Hellmann-Feynman forces are the basis for direct methods as developed by Parlinski et al. [91] to calculate phonon dispersion relations. In this case, a crystal supercell is considered with all atoms at equilibrium positions except for one atom, which is slightly displaced. This causes Hellmann-Feynman forces on all other atoms which are calculated by DFT. Since forces and force-constant matrices are related according to Hooke's law, force-constant matrices can be derived from these forces. Finally, Fourier transform of the force constants yields the dynamical matrix whose eigenvalues correspond to phonon frequencies ω . In this way, phonon dispersions are obtained at high symmetry points in the Brillouin zone. As to TEM applications, Schowalter et al. proceed with the calculation of the phonon density of states $g(\omega)$ [81], from which the Debye parameter B at temperature T can be derived using [80]

$$B = \frac{4\pi^2\hbar}{m} \int_0^\infty \frac{g(\omega)}{\omega} \coth\left(\frac{\hbar\omega}{2k_B T}\right) d\omega \quad (2.20)$$

with Boltzmann's constant k_B .

2.3.4 The WIEN2K code

To profit from the versatile applications of DFT one important step is an efficient and accurate implementation of the DFT principle. One popular realisation is the WIEN2K program package that has been used frequently in this work, which is why fundamentals are reviewed briefly here. The arguments follow Schwarz et al. [69]. Detailed description of theoretical background, program code and -flow, file names, and information about accessible properties can be found in the manuals of Cottenier [65] and Blaha et al. [66].

The periodicity of an ideal crystal suggests using plane wave expansions of the single-electron wave functions $\varphi_k(\mathbf{r})$ in Eq. (2.17) according to the Bloch theorem. However, this basis set becomes inefficient where $\varphi_k(\mathbf{r})$ varies rapidly, which is the case near nuclei. Therefore, the crystal is decomposed into spheres centred around nuclei at \mathbf{r}_j (also known

as muffin-tins), and interstitial areas. In the latter, plane wave expansion is used, meaning a linear combination of plane waves,

$$\phi_{\mathbf{g}}(\mathbf{r}) = \frac{1}{\sqrt{\Omega}} e^{2\pi i(\mathbf{k}+\mathbf{g})\mathbf{r}} \quad , \quad (2.21)$$

with reciprocal lattice vector \mathbf{g} , unit cell volume Ω and wave vector \mathbf{k} . These plane waves are augmented inside the spheres, which is therefore called *augmented plane wave* (APW) approach. As the Schrödinger equation splits into a radial and an angular part there, $\phi_{\mathbf{g}}(\mathbf{r})$ is constructed by a linear combination of products of a radial function $u_l^j(r', \varepsilon)$ and spherical harmonics $Y_{lm}(\theta'_1, \theta'_2)$ with $\mathbf{r}' = \mathbf{r} - \mathbf{r}_j$ given in polar coordinates $(r', \theta'_1, \theta'_2)$. In the APW approach, the function u explicitly depends on energy ε , meaning that a different basis set ought to be used for each eigenvalue ε_k in Eq. (2.17), resulting in a computationally demanding task. In WIEN2K, four basis sets based on the APW approach are available inside the muffin-tins.

1. Linearised augmented plane waves (LAPW). In the LAPW ansatz, a linear dependence of $u_l^j(r', \varepsilon)$ on energy is assumed. In practice, only one radial function $u_l^j(r', \varepsilon_L)$ is calculated at the linearisation energy ε_L which is close to typical eigenvalues ε_k of the system. Additionally, its energy derivative, denoted by $\dot{u}_l^j(r', \varepsilon_L)$, is computed. Inside the spheres, $\phi_{\mathbf{g}}(\mathbf{r})$ takes the form

$$\phi_{\mathbf{g}}(\mathbf{r}) = \sum_{l,m} [a_{lm}^{j,\mathbf{g}} u_l^j(r', \varepsilon_L) + b_{lm}^{j,\mathbf{g}} \dot{u}_l^j(r', \varepsilon_L)] Y_{lm}(\theta'_1, \theta'_2) \quad , \quad (2.22)$$

where the energy dependence is expressed by means of a linear combination with weights $a_{lm}^{j,\mathbf{g}}$ and $b_{lm}^{j,\mathbf{g}}$. In the LAPW scheme, functions of the form in Eq. (2.22) are matched in value and slope with those according to Eq. (2.21) at the muffin-tin boundary. The term LAPW basis therefore refers to the combination of both for atomic spheres and interstitial areas, respectively. In the following approaches, the given wave function is zero outside muffin-tins.

2. Linearised augmented plane waves with local orbitals (LAPW+LO). The LAPW basis is efficient for the core states, being confined to the muffin tin spheres, and the valence states, being partly delocalised in the interstitial area. However, some electronic states called semi-core states are neither confined to muffin-tins nor to the interstitial region, so that additional local orbitals (LO) are introduced for certain quantum numbers l and m :

$$\phi_{LO}(\mathbf{r}) = \left[a_{lm}^{j,LO} u_l^j(r', \varepsilon_L^{(1)}) + b_{lm}^{j,LO} \dot{u}_l^j(r', \varepsilon_L^{(1)}) + c_{lm}^{j,LO} u_l^j(r', \varepsilon_L^{(2)}) \right] Y_{lm}(\theta'_1, \theta'_2) \quad . \quad (2.23)$$

This is very similar to one summand in Eq. (2.22), except that a second radial function $u_l^j(r', \varepsilon_L^{(2)})$ valid for the semi-core state energy $\varepsilon_L^{(2)}$ is added. The function ϕ_{LO} approaches zero value and slope at the interface to the interstitial region and is thus not joined with the plane waves.

3. Augmented plane waves with local orbitals (APW+lo). For LAPW, one requirement is to determine the coefficients a and b in Eq. (2.22) in such a way that $\phi_{\mathbf{g}}$

and its gradient matches the interstitial plane waves, making a and b dependent on \mathbf{g} . The APW+lo basis

$$\phi_{lo}(\mathbf{r}) = [a_{lm}^j u_l^j(r', \varepsilon_L) + b_{lm}^j \dot{u}_l^j(r', \varepsilon_L)] Y_{lm}(\theta'_1, \theta'_2) \quad (2.24)$$

is very similar but a and b do not depend on reciprocal lattice vectors making it a more flexible basis. To distinguish from LAPW+LO, local orbitals are abbreviated by lower case letters. Equation (2.24) introduces an additional lo with a radial function computed for a fixed energy ε_L to be given. The function ϕ_{lo} in the APW+lo scheme is matched to zero value (not necessarily slope) at the sphere boundary.

4. Augmented plane waves with additional local orbitals (APW+lo+LO).

For APW+lo, the same problem arises as for LAPW when dealing with semi-core states. Analogously, a second radial function $u_l^j(r', \varepsilon_L^{(2)})$ is calculated at a different energy $\varepsilon_L^{(2)}$ to be given, so that the APW+lo+LO basis reads:

$$\phi_{lo/LO}(\mathbf{r}) = [a_{lm}^j u_l^j(r', \varepsilon_L^{(1)}) + b_{lm}^j \dot{u}_l^j(r', \varepsilon_L^{(1)}) + c_{lm}^j u_l^j(r', \varepsilon_L^{(2)})] Y_{lm}(\theta'_1, \theta'_2) \quad (2.25)$$

Example basis set configuration for GaAs. In practice, all four basis sets may be used in one DFT calculation and typical settings for GaAs are as follows. Spherical harmonics are built up to $l_{max} = 10$. The global setting for the basis set for gallium and arsenic is LAPW with a linearisation energy of -0.3 Ry for both atoms. In case of gallium, four exceptions are made where a different basis is used. For the d-electrons, an APW+lo+LO basis is used at energies of $\varepsilon_L^{(1)} = -0.7850$ Ry (APW+lo) and $\varepsilon_L^{(2)} = -0.3$ Ry (additional LO) according to Eq. (2.25). Gallium s- and p-states are expanded in the APW+lo basis at energies of $\varepsilon_L = -0.3$ Ry as defined in Eq. (2.24). For arsenic, five exceptions are made. The d-electrons are expressed by APW+lo+LO at energies of $\varepsilon_L^{(1)} = -2.27$ Ry (for APW+lo) and $\varepsilon_L^{(2)} = -0.3$ Ry (for the additional LO). The same is done for the s-electrons at energies of $\varepsilon_L^{(1)} = -0.83$ Ry and $\varepsilon_L^{(2)} = -0.3$ Ry, respectively. A fifth orbital of APW+lo type is used for the p-states at $\varepsilon_L = -0.3$ Ry.

Finally, two central parameters governing accuracy of WIEN2K calculations will be explained.

The RK_{max} parameter. The reliability of expanding a function in terms of plane waves is governed by the cutoff in reciprocal space defined by a maximum spatial frequency K_{max} . The stronger the wave function varies in space, the higher K_{max} must be chosen. However, it was mentioned above that variations increase towards nuclei, whereas at distances smaller than the muffin-tin radius R_{MT} spherical harmonics times radial functions are used as basis sets. Thus, if R_{MT} is small, the interstitial area comes close to nuclei and hence K_{max} must be large because core charge density must be expressed by means of plane waves. In contrast, K_{max} can be reduced for large muffin-tins, but also here care must be taken because spherical harmonics are inadequate to represent wave functions at large distances from the nuclei. In summary, neither K_{max} nor R_{MT} alone are proper quantities to express computational accuracy, but the product $R_{MT} \cdot K_{max}$, called the RK_{max} parameter, yields a valuable rule of thumb. Practically, the DFT results are converged with respect to RK_{max} , typically leading to values between 5 and 10.

Number of k-points. Reciprocal lattice vectors correspond to wave vectors for plane waves which agree with the unit cell of a crystal. Copying this cell subsequently according to Eq. (2.7) in order to built up a macroscopic crystal virtually fills the first Brillouin zone continuously with allowed \mathbf{k} -vectors. In practice, wave functions are constructed using a discrete mesh of points in the first Brillouin zone, or, more precisely, in the irreducible wedge of it, being given by symmetry considerations. The number of k-points, that is, the sampling in reciprocal space, must be defined by the user in such a way that the DFT result of interest is robust against it. Of course the density of this mesh depends on the size of the supercell, which means that it may be sparse for large supercells (with a few tens of k-points) and tight for small ones (with a few thousands of k-points.).

2.3.5 Chemical bonding

In section 2.3.3, dependence of total energy in a GaAs unit cell on the lattice parameter was studied by DFT and it was found that a minimum exists according to Fig. 2.1. Physically, this represents the fact that a favourable interatomic distance of the Ga–As bond exists which corresponds to a certain electron density $\rho_e(\mathbf{r})$. Qualitatively, essential characteristics of chemical bonding, such as polarity, preferential nearest neighbour configurations and preferred electronic configurations, have been described already by Lewis in 1916 in an article titled *The atom and the molecule* [92]. This reminds us that the periodic table, being valid for isolated atoms, is usually an extreme abstraction from real matter and that properties of a molecule or crystal can in principle not just be expressed by a linear combination of properties associated with isolated atoms. Nevertheless the isolated atom approximation for, e.g., calculation of crystal potentials according to Eq. (2.7), has in many cases proven to be in good agreement with experiment. Thus we can not only expect that bonding mostly causes marginal changes of crystal potentials, but it can also be assumed that isolated atom potentials or charge densities are a good starting point to derive exact crystal potentials, as implied by Lewis’ title. Indeed, DFT calculations with the WIEN2K code first generate an initial electron density from isolated atoms and then refine it until self-consistency is obtained. For these reasons, DFT results for densities or potentials are often not mapped absolutely but in terms of the difference to isolated atoms, as will be examined for the GaAs case now.

The Bravais cell for zinc-blende GaAs is shown in Fig. 2.2 with gallium atoms at $[0\ 0\ 0]$, $[0\ 0.5\ 0.5]$, $[0.5\ 0\ 0.5]$ and $[0.5\ 0.5\ 0]$. The arsenic sublattice results from shifting these positions by $[0.25\ 0.25\ 0.25]$. For the gallium atom at origin, a muffin-tin sphere with $R_{\text{MT}} = 0.12\text{ nm}$, which was used for both gallium and arsenic in DFT calculations with WIEN2K, is exemplarily drawn. It indicates that tins of adjacent atoms are nearly in contact. With $RK_{\text{max}} = 8$ and 5000 k-points self-consistency was obtained in LDA after seven cycles. A direct result of the subroutine LAPW3 are X-ray structure factors $X_{\mathbf{g}}^{\text{GaAs}}$ which can straightly be converted to electron structure factors $F_{\mathbf{g}}^{\text{GaAs}}$ or, analogously, crystal potential Fourier components $V_{\mathbf{g}}^{\text{GaAs}}$ by applying Eq. (2.12). As to isolated atoms, ASA for electron scattering according to Weickenmeier and Kohl [75] were utilised to calculate both $V_{\mathbf{g}}^{\text{GaAs}}$ and $X_{\mathbf{g}}^{\text{GaAs}}$. By Fourier summation of type (2.10), electron density $\rho_e^{\text{GaAs}}(\mathbf{r})$ and electrostatic Coulomb potential $V_e^{\text{GaAs}}(\mathbf{r})$ were derived. To present results in a compact manner, both quantities are evaluated on selected lattice planes which are indicated in Fig. 2.2, too. Besides unit cell facets (100), (010) and (001), orthogonal planes (1 $\bar{1}$ 0) and ($\bar{1}\bar{1}$ 2) are of special interest because they contain one Ga–As bond between gallium at $[0\ 0\ 0]$ and arsenic at $[0.25\ 0.25\ 0.25]$.

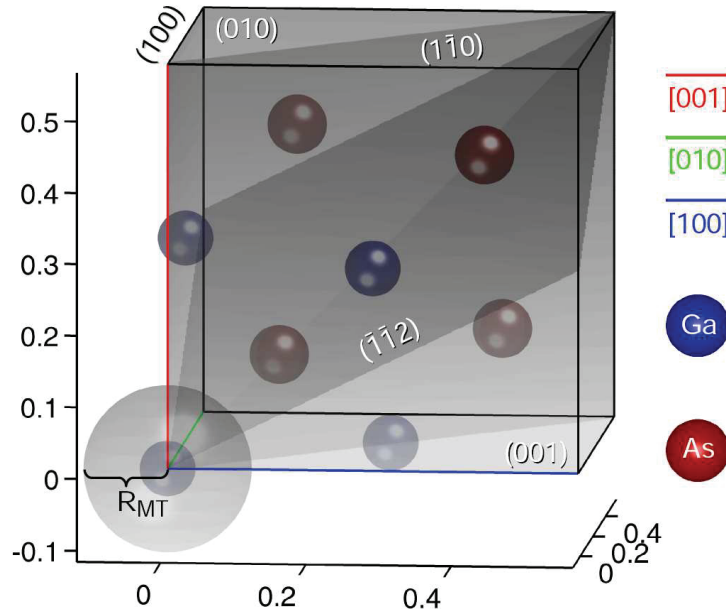


Figure 2.2: Bravais cell of zinc-blende GaAs illustrating positions of Ga atoms (blue) and As atoms (red). Additionally, selected lattice planes are shown on which electron density $\rho_e(\mathbf{r})$ and potential $V(\mathbf{r})$ were evaluated as depicted in Fig. 2.3. A sphere representing the muffin-tin area used in WIEN2K calculations is exemplarily drawn around one Ga atom. Scaling of the axes is in nm.

The left hand side of Fig. 2.3 shows resulting electron densities $\rho_{e,DFT}(\mathbf{r})$ obtained from DFT and $\rho_{e,ISO}(\mathbf{r})$ for isolated atoms in parts (a) and (b), respectively. Both maps exhibit that $\rho_e(\mathbf{r})$ is strongly peaked at atomic positions, taking values of about 4000 electrons per cubic Angstrom there. On this scale no difference between DFT and isolated atom densities can be constituted, which expresses the fact that only valence density changes slightly. In order to investigate electron redistributions due to bonding in more detail, Fig. 2.3 (c) depicts the electron density difference $\rho_{e,ISO}(\mathbf{r}) - \rho_{e,DFT}(\mathbf{r})$ calculated from figure parts (a) and (b). Here we get positive values where DFT yields smaller densities and negative ones for electron accumulation in DFT with respect to isolated atom densities. In some respects the difference map is against intuition because heuristic models explain bonding by electron transfer from one atom towards another. This results in covalent bonds where electrons accumulate along the bond, or it leads to ionic bonds where electrons are transferred more or less completely. However, planes $(1\bar{1}0)$ and $(\bar{1}\bar{1}2)$ in Fig. 2.3 (c) exhibit both electron deficiency and excess regions in the direct vicinity of atoms, this effect being pronounced around arsenic sites. Moreover, towards nuclei green regions emerge. This is expected since inner orbitals are not significantly affected by bonding. Therefore, since $\rho_{e,ISO}(\mathbf{r}) - \rho_{e,DFT}(\mathbf{r})$ exhibits only long-range variations with respect to atomic dimensions, we can draw the important conclusion that $\rho_{e,ISO}(\mathbf{r})$ and $\rho_{e,DFT}(\mathbf{r})$ differ only in their low-order Fourier coefficients $X_{\mathbf{g}}^{GaAs}$. Additionally, electron density differences are three orders of magnitude smaller than densities themselves, so that low order structure factors $X_{\mathbf{g}}^{GaAs}$ are modified only slightly as to their absolute values.

For the potentials $V_{DFT}(\mathbf{r})$, $V_{ISO}(\mathbf{r})$ and potential differences $V_{ISO}(\mathbf{r}) - V_{DFT}(\mathbf{r})$ in parts (d-f) on the right hand side of Fig. 2.3 completely analogous arguments hold. As expected from the density maps on the left, figure parts (d) and (e) in principle show

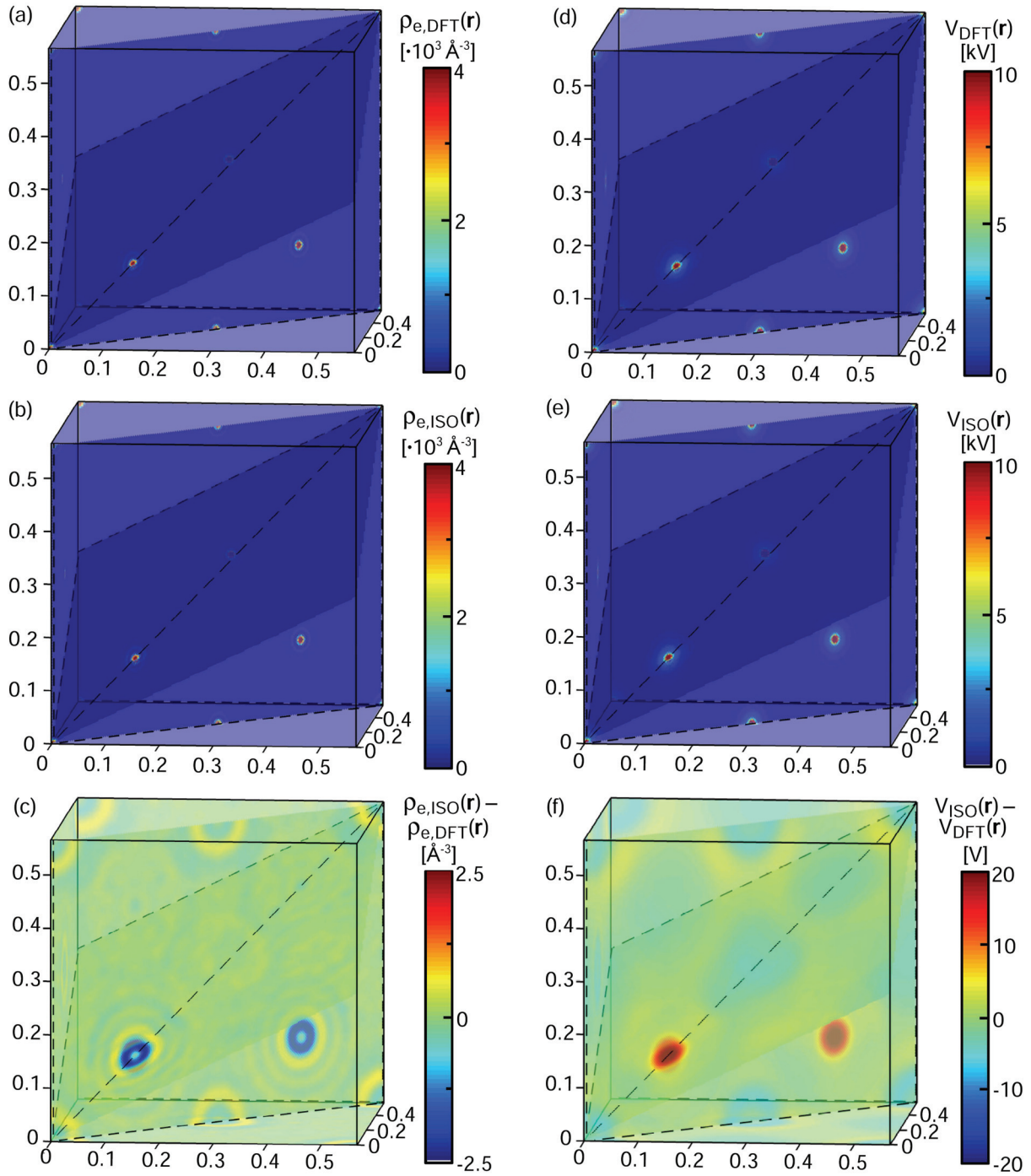


Figure 2.3: Comparison of DFT (indexed as *DFT*) and isolated atom (indexed as *ISO*) results for electron densities $\rho_e(\mathbf{r})$ (a-c) and crystal Coulomb potentials $V(\mathbf{r})$ (d-f) in a GaAs unit cell on selected cross-sections as indicated in Fig. 2.2. Axes are scaled in nm. In particular, the following quantities are mapped colour-coded: (a) electron density from DFT, (b) electron density for isolated atoms [75], (c) difference of (a) and (b), (d) crystal Coulomb potential from DFT, (e) crystal Coulomb potential for isolated atoms and (f) difference of (d) and (e). All maps were built up using Fourier components corresponding to spatial frequencies up to 70 nm^{-1} , whereas consistency with a cutoff of 100 nm^{-1} has been verified. Note that Debye-Waller damping is neither included in DFT nor in isolated atom data presented here.

potential-free space with strong gradients near nuclei where $V^{GaAs}(\mathbf{r}) \approx 10 \text{ kV}$. However, potential differences of up to 20 V between isolated atoms and DFT according to Fig. 2.3 (f) are relatively small and vary smoothly. Thus low-order Fourier components of the crystal potential $V_{\mathbf{g}}^{GaAs}$ are influenced most by bonding.

Modified atomic scattering amplitudes

Density functional theory results are valid for the ground state and especially correspond to atoms at rest. As described in section 2.2, Debye-Waller damping is an efficient way to account for finite temperature. However, Debye parameters are atom- or even site-specific, whereas DFT produces overall electron densities and crystal potentials valid for a unit- or supercell. Recently, Rosenauer et al. introduced the approach of *modified atomic scattering amplitudes* (MASA, [9]) that allows for the reassignment of X-ray structure factors obtained by DFT to ASA of individual atoms. Such a parameterisation is also desirable from another point of view: DFT is incapable to be applied to large supercells containing several hundreds to thousands of atoms, but this would be necessary to deal with dilute alloys. Nevertheless it can be expected that bonding effects remain a local quantity, meaning that, e.g., $\rho_e(\mathbf{r})$ around an atomic site is in principle determined by the type of and the distance to its nearest neighbours. In this case it is sufficient to perform a DFT calculation for a small cell only, to derive appropriate MASA from this calculation, and to use these MASA for all atoms (in an arbitrary large cell), which show the same or a similar coordination as in the small cell used in DFT. The check of validity of the MASA approximation is left to chapters 3 and 4. Here, important aspects concerning MASA are reviewed following Ref. [9].

In WIEN2K, the subroutine LAPW3 yields X-ray structure factors which are split into contributions of the muffin-tin spheres around each inequivalent atom ν and the interstitial area. Because electron density depends on bond lengths, the total X-ray scattering factor

$$X_{\mathbf{g}}^{\kappa}(\mathbf{a}) = A \cdot \left[X_{\mathbf{g}}^{Out,\kappa}(\mathbf{a}) + \sum_{\nu} X_{\mathbf{g},\nu}^{\kappa}(\mathbf{a}) \right] \quad (2.26)$$

depends on $\mathbf{a} := (a_1, a_2, a_3)$, a_{1-3} being the lattice parameters of the unit cell. As in Eq. (2.7), κ indexes the crystal, interstitial contributions are indexed by the superscript *Out*. The constant A is introduced because unit cell size in DFT may be different from that of the Bravais cell. For example, zinc-blende GaAs contains eight atoms in the Bravais cell, but due to symmetries, DFT can be performed using a small unit with two atoms only, resulting in $A = 4$. Consequently, LAPW3 yields only those structure factors which are not connected by symmetry. The full set of structure factors with correct phases is then obtained by applying transformation rules according to Brown [93].

As our aim is an assignment of DFT results to individual atoms, $X_{\mathbf{g}}^{Out,\kappa}(\mathbf{a})$ is distributed equally to the N inequivalent atoms. Finally, thermal movement is accounted for by multiplication of $X_{\mathbf{g},\nu}^{\kappa}(\mathbf{a})$ with appropriate Debye-Waller factors $D_{\nu}^{\kappa}(\mathbf{g})$. For $X_{\mathbf{g}}^{Out,\kappa}(\mathbf{a})$, a mean Debye-Waller factor $\frac{1}{N_{\nu}} \sum_{\nu} D_{\nu}^{\kappa}(\mathbf{g})$ is used, so that Eq. (2.26) can be transformed to

$$X_{\mathbf{g}}^{\kappa}(\mathbf{a}) = A \cdot \sum_{\nu=1}^N \left[\frac{D_{\nu}^{\kappa}(\mathbf{g})}{N} X_{\mathbf{g}}^{Out,\kappa}(\mathbf{a}) + D_{\nu}^{\kappa}(\mathbf{g}) X_{\mathbf{g},\nu}^{\kappa}(\mathbf{a}) \right] \quad (2.27)$$

Here, N appears in the denominator due to distributing contributions of interstitial areas to atomic sites.

On the other hand, the sum in Eq. (2.12) can also be decomposed in a sum over atom types ν and a sum over N_ν atomic positions \mathbf{r}_{j_ν} corresponding to the same type. This leads to

$$X_{\mathbf{g}}^\kappa(\mathbf{a}) = \left(\sum_{\nu=1}^N \sum_{j_\nu=1}^{N_\nu} Z_\nu D_\nu^\kappa(\mathbf{g}) e^{-2\pi i \mathbf{g} \mathbf{r}_{j_\nu}} \right) - \frac{2\pi \mathbf{g}^2 \varepsilon_0 h_P^2}{m_e e^2} F_{\mathbf{g}}^\kappa(\mathbf{a}) \quad (2.28)$$

$$=: \sum_{\nu=1}^N \left(\sum_{j_\nu=1}^{N_\nu} Z_\nu D_\nu^\kappa(\mathbf{g}) e^{-2\pi i \mathbf{g} \mathbf{r}_{j_\nu}} - \frac{2\pi \mathbf{g}^2 \varepsilon_0 h_P^2}{m_e e^2} F_{\mathbf{g},\nu}^\kappa(\mathbf{a}) \right) \quad , \quad (2.29)$$

where $F_{\mathbf{g},\nu}^\kappa$ is the contribution of atoms with type ν to the electron structure factor $F_{\mathbf{g}}^\kappa(\mathbf{a})$. In comparison to Eq. (2.12), the dependence on lattice parameters was added and Debye-Waller factors are determined by one index ν only because they refer to all equivalent atoms which must have identical vibrational modes by definition. Equating Eqs. (2.27) and (2.29) yields for the contribution of atoms of type ν to the electron structure factor

$$F_{\mathbf{g},\nu}^\kappa(\mathbf{a}) = \frac{m_e e^2}{2\pi \mathbf{g}^2 \varepsilon_0 h_P^2} \left[\sum_{j_\nu=1}^{N_\nu} Z_\nu D_\nu^\kappa(\mathbf{g}) e^{-2\pi i \mathbf{g} \mathbf{r}_{j_\nu}} - A \cdot D_\nu^\kappa(\mathbf{g}) \left(\frac{X_{\mathbf{g}}^{Out,\kappa}(\mathbf{a})}{N} + X_{\mathbf{g},\nu}^\kappa(\mathbf{a}) \right) \right] \quad . \quad (2.30)$$

In order to include the last summands in the sum over j_ν we multiply and divide them by $\sum e^{-2\pi i \mathbf{g} \mathbf{r}_{j_\nu}}$ and obtain

$$F_{\mathbf{g},\nu}^\kappa(\mathbf{a}) = \sum_{j_\nu=1}^{N_\nu} D_\nu^\kappa(\mathbf{g}) \underbrace{\left\{ \frac{m_e e^2}{2\pi \mathbf{g}^2 \varepsilon_0 h_P^2} \left[Z_\nu - A \left(\sum_{j_\nu=1}^{N_\nu} e^{-2\pi i \mathbf{g} \mathbf{r}_{j_\nu}} \right)^{-1} \left(\frac{X_{\mathbf{g}}^{Out,\kappa}(\mathbf{a})}{N} + X_{\mathbf{g},\nu}^\kappa(\mathbf{a}) \right) \right] \right\}}_{\text{MASA}} e^{-2\pi i \mathbf{g} \mathbf{r}_{j_\nu}} \quad . \quad (2.31)$$

Except for the units, Eq. (2.31) is formally equivalent to the definition of crystal potential Fourier components in Eq. (2.10), if the expression in curly braces is regarded as the ASA of atom ν with atomic number Z_ν for momentum transfer \mathbf{g} in crystal κ with lattice parameters \mathbf{a} . Note that \mathbf{g} also depends on \mathbf{a} which was omitted for reasons of brevity. Because bonding is accounted for by modification of ASA, the quantity in curly braces in Eq. (2.31) is called *modified atomic scattering amplitude* (MASA). Opposite to its original definition in Ref. [9], no relativistic correction was included here to avoid making MASA dependent on experiment. Furthermore, they were adapted to the definition of the Fourier transform in Eq. (2.2a) and thus they contain a minus sign in the exponential function. MASA as defined in Eq. (2.31) and Ref. [9] are in units of m , but they can easily be converted to volts by multiplication with $h_P^2 (2\pi m_e e \Omega)^{-1}$ and to m^{-2} by multiplication with $(\pi \Omega)^{-1}$.

To illustrate the nature of MASA, Fig. 2.4 offers a comparison of moduli and phases regarding DFT and isolated atom ASA according to Weickenmeier and Kohl [75] for GaAs and InAs. For the DFT calculations, WIEN2K was used in LDA approximation with 5000 k-points and $RK_{max} = 8$. Reflections shown correspond to the strongest ones visible for electron beam incidence along $[1\bar{1}0]$. In this setting, bonding effects can be studied well because in principle all low-order reflections appear. Common to figure parts (a-d) are the following general features: First, isolated atom ASA (solid lines) are defined continuously for arbitrary momentum transfer, whereas MASA (circles) correspond to

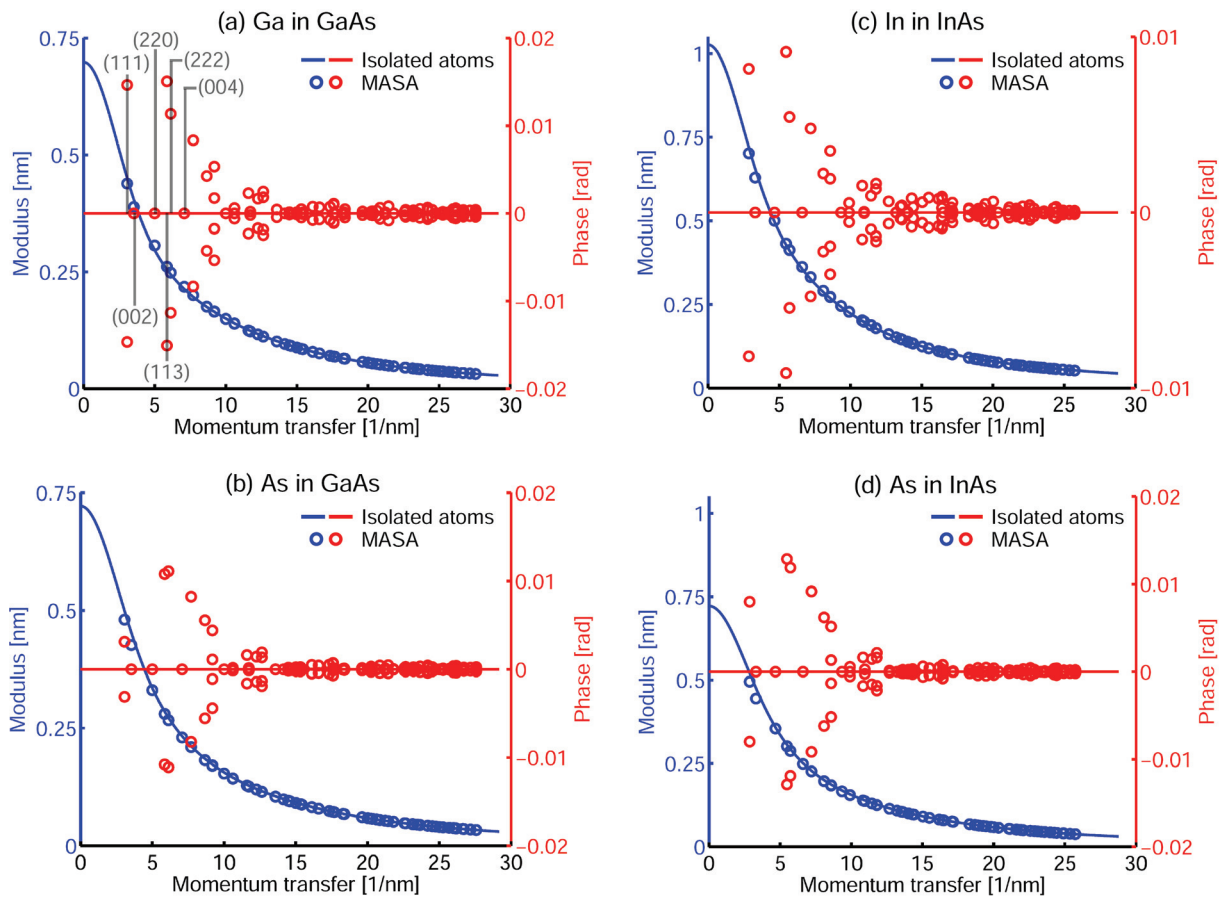


Figure 2.4: Comparison of MASA (circles) and ASA in isolated atom approximation (solid lines) according to Weickenmeier and Kohl [75] for pure GaAs (a,b) and pure InAs (c,d). Since, in general, ASA are complex, blue data depicts the amplitude and red data depicts the phase. Exemplarily, figure part (a) contains the assignment to selected reflections, which is transferable to parts (b-d).

discrete spatial frequencies determined by the reciprocal lattice. Second, the phase of isolated atom ASA vanishes due to the assumption of spherically symmetric atoms. In contrast, MASA are partly complex. Third, MASA approach isolated atom data for large momentum transfer regarding both moduli and phases. However, deviations for low transfers are indeed small, as expected from remarks to Fig. 2.3. Fourth, MASA do not only depend on momentum transfer modulus but also explicitly on direction. For example, Fig. 2.4 (a) contains the assignment of several spatial frequencies to selected reflections. Of course, reflections (111) , $(\bar{1}\bar{1}\bar{1})$, $(11\bar{1})$ and $(\bar{1}\bar{1}1)$ have the same length but split into two families with opposite phases. The same is true for (113) and many other reflections. For this reason, there is no easy way at present to parameterise MASA efficiently, as it has been done for isolated atoms by several groups [75, 76, 78]. Instead, Rosenauer et al. [9] focused on compositional dependence of the (002) MASA only, motivated by its central role in compositional analysis. Nevertheless Eq. (2.31) holds for any momentum transfer \mathbf{g} and provides a way to retain the atomistic approach also if bonding is involved. For a simulation of an electron diffraction pattern in zone axis $[1\bar{1}0]$ for example, any graph in Fig. 2.4 shows that a variety of MASA ought to be used instead of isolated atom scattering data.

Finally, it is emphasised that MASA explicitly depend on crystal κ . Whereas differences between gallium in GaAs and indium in InAs as shown in Figs. 2.4 (a) and (c) are expected, MASA moduli for arsenic differ by about 3% for $\mathbf{g} = (111)$ and by about 4% for $\mathbf{g} = (002)$ in Figs. 2.4 (b) and (d).

Compositional dependence

It was stated above that MASA depend on three main parameters, that is, first atomic number Z , second bond partners and third lattice parameters. In an alloy, the latter are a function of composition and boundary conditions for strain relaxation. In principle all possible bond types will occur which can be constructed by combining any atom type on one sublattice with any atom type on the other sublattice. As a first approximation we can assume that, despite each of these bond types prefers an individual bond length, atomic positions equal those in an ideal crystal with lattice parameters of the strained unit cell. This implies calculation of MASA for all binary compounds given by the possible types of bonds, however, using lattice parameters for the strained cell. For example, if MASA for a quaternary $\text{In}_x\text{Ga}_{1-x}\text{N}_y\text{As}_{1-y}$ alloy are to be simulated in dependence on x and y , the first step is to determine the corresponding set of concentration-dependent lattice parameters. Possible bond types in $\text{In}_x\text{Ga}_{1-x}\text{N}_y\text{As}_{1-y}$ lead to binary compounds InAs, GaAs, InN and GaN. Then, a variety of MASA calculations is performed for all four crystals and for all sets of lattice parameters. For instance, a series of DFT calculations for GaAs is carried out in which the lattice parameters vary, despite pure GaAs takes different ones. In this way, concentration-dependent MASA for gallium and arsenic, valid for all bonds Ga–As in the $\text{In}_x\text{Ga}_{1-x}\text{N}_y\text{As}_{1-y}$ alloy, are derived. The easiest way to finally derive structure factors for $\text{In}_x\text{Ga}_{1-x}\text{N}_y\text{As}_{1-y}$ is to assume a virtual crystal, where each MASA is simply weighted according to occupancies x and y . It is worth noting that, e.g., the MASA for gallium depends on both x and y ,

$$f_{Ga}^{\text{InGaNAs}}(\mathbf{g}) = (1-x) \cdot f_{Ga}^{\text{GaAs}}(\mathbf{g}) = (1-x) \cdot [(1-y) \cdot f_{Ga}^{\text{GaAs}}(\mathbf{g}) + y \cdot f_{Ga}^{\text{GaN}}(\mathbf{g})] \quad , \quad (2.32)$$

because y determines the relative occurrence of Ga–N and Ga–As bonds and $(1-x)$ measures the frequency of gallium.

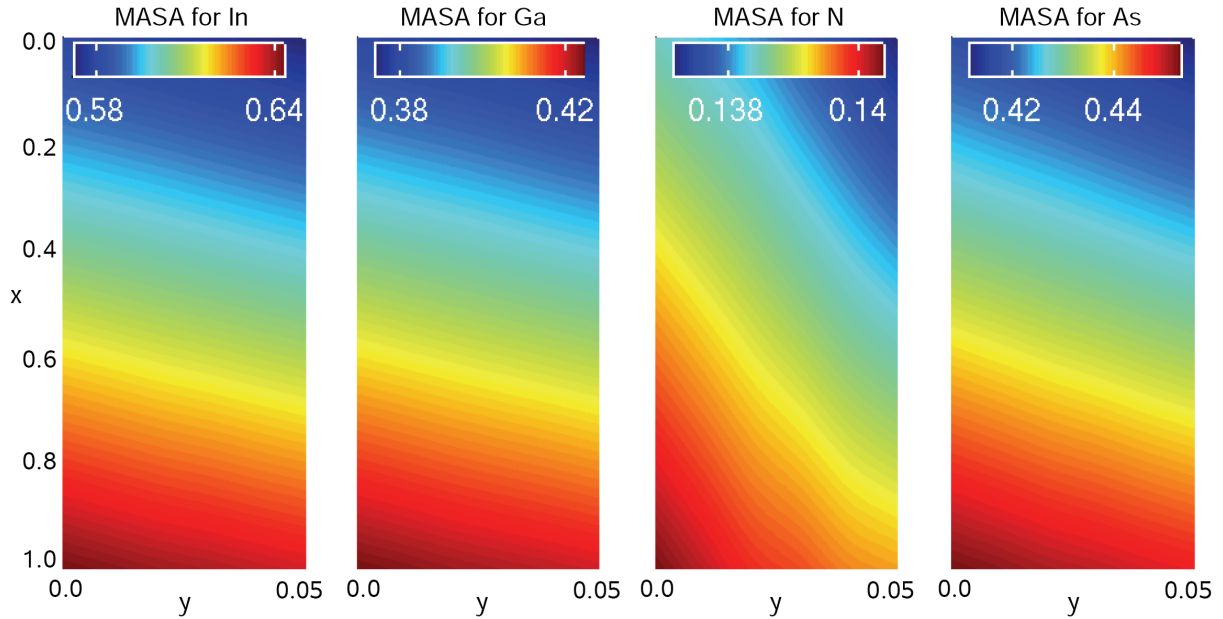


Figure 2.5: Compositional dependence of MASA in $\text{In}_x\text{Ga}_{1-x}\text{N}_y\text{As}_{1-y}$ for $x \in [0 \dots 1]$ and $y \in [0 \dots 0.05]$ as a colour-coded map in units of nm for the 002 reflection. Compositional dependence was realised in DFT by adjusting the lattice parameter of the Bravais cell of all possible binary III-V compounds to that of a strained InGaNs layer. Here, MASA for intermediate strain relaxation along electron beam direction (relaxation parameter $r = 0.5$) is shown.

We finally study the dependence of (002) MASA on composition using Fig. 2.5. Each MASA for an atom at one sublattice has already been averaged according to composition of the other sublattice. In this way, presentation of, e.g., two gallium MASA for gallium in GaAs and gallium in GaN, according to the summands in square brackets in Eq. (2.32), is circumvented by showing the resulting sum. However, weighting of each MASA with respect to occupancy of the element itself has been omitted in Fig. 2.5 to be able to see variations which solely stem from changes in lattice parameters and bond partners. Thus, MASA in virtual crystal approximation could directly be derived from Fig. 2.5 by multiplication of indium MASA with x , gallium MASA with $(1-x)$, and so on. Obviously MASA can differ by about 10% for the concentration range given here. For example, taking an indium atom in a dilute InGaAs alloy with $y = 0$ and small concentration x , this atom will be embedded in a crystal with lattice parameters close to those of GaAs and it would have a MASA of about 0.59 nm. Now, by increasing x up to 1.0 and keeping $y = 0$, the lattice parameter (and thus the bond length) increases, so that the indium MASA reaches a maximum of about 0.64 nm after growing nearly linearly. Analogous arguments hold to explain the dependence on y . However, the nitrogen MASA in the third graph of Fig. 2.5 demonstrates that linear dependence on x and y may not be assumed in general because isolines exhibit partly strong bowing, especially for large indium content.

2.4 Bloch wave approach

In the following sections of this chapter, substantial effort will be spent on separation of Bragg and diffuse scattering. Bloch wave simulations exploit properties of ideal crystals, namely perfect translational symmetry. They are thus highly efficient to obtain

amplitudes and phases of Bragg scattered beams as a function of specimen thickness and -orientation, chemical composition or crystal potential Fourier components. The Bloch wave approach has first been applied to electron scattering in 1928 by Bethe [36] and as a traditional method, it is explained in most books on electron microscopy. This section deals with this issue in a very compact manner to lay the basis for an understanding of the computational kernel of the Bloch4TEM program developed in the course of this work. For special applications of this program, that is, refinement of structure- and Debye-Waller factors by comparing experimental with simulated Bragg intensities, and for studies of bonding and SAD as to TEM image contrast, the reader is referred to chapters 3, 4 and 5.

It was shown by Ferwerda et al. [94] that, under conventional TEM conditions, scattering of relativistic electrons may be described spin-independently. It is hence governed by the Klein-Gordon equation

$$\left[\Delta + 4\pi^2 \left(\mathbf{K}_0^2 + \frac{2eEV^\kappa(\mathbf{r}) + e^2V^\kappa(\mathbf{r})^2}{h_P^2c^2} \right) \right] \Psi(\mathbf{r}) = 0 \quad \text{with} \quad \mathbf{K}_0^2 = \frac{e^2\Phi^2 + 2e\Phi m_e c^2}{h_P^2c^2} . \quad (2.33)$$

Here, \mathbf{K}_0 is the wave vector of the incident electrons, its length being determined by the accelerating voltage Φ . Additionally, total electron energy $E = m_e c^2 + e\Phi$ and potential $V^\kappa(\mathbf{r})$ of crystal κ enter Eq. (2.33), besides elementary charge e , electron mass m_e , vacuum light velocity c and Planck's constant h_P . According to Bloch's theorem, the wave function in the crystal, $\Psi(\mathbf{r})$, may be written as a product of a function $C(\mathbf{r})$ with the periodicity of the lattice and a plane wave with wave vector \mathbf{k} ,

$$\Psi(\mathbf{r}) = C(\mathbf{r}) e^{2\pi i \mathbf{k} \mathbf{r}} = \sum_{\mathbf{g}} C_{\mathbf{g}} e^{2\pi i (\mathbf{k} + \mathbf{g}) \mathbf{r}} , \quad (2.34)$$

where $C(\mathbf{r})$ was expanded in a Fourier series in the second step.

In order to solve Eq. (2.33), we neglect the quadratic term in V^κ because for relativistic electrons $2eE \gg e^2V^\kappa(\mathbf{r})^2$ is safely justified. We further account for the acceleration of beam electrons by the mean inner potential $V_0'^\kappa$ when entering the crystal and define $\mathbf{k}_0^2 = \mathbf{K}_0^2 + 2eE(h_Pc)^{-2}V_0'^\kappa$, where \mathbf{k}_0 is the wave vector of incident electrons in the crystal. Note that $V_0'^\kappa$ corresponds solely to the real part of $V^\kappa(\mathbf{r})$ as expressed by Eq. (2.11). Equation (2.33) then writes

$$[\Delta + 4\pi^2 \mathbf{k}_0^2] \Psi(\mathbf{r}) = -4\pi^2 U^E(\mathbf{r}) \Psi(\mathbf{r}) \quad \text{with} \quad U^E(\mathbf{r}) = \frac{2Ee}{h_P^2c^2} [V^\kappa(\mathbf{r}) - V_0'^\kappa] . \quad (2.35)$$

The introduction of U^E is convenient since it contains most of the physical constants, so that subsequent equations take a clear form. The superscript E indicates that the beam electrons experience a potential which is adapted to their energy. Inserting Eqs. (2.10) and (2.34) into Eq. (2.35) results in

$$\sum_{\mathbf{g}} e^{2\pi i (\mathbf{k} + \mathbf{g}) \mathbf{r}} \left\{ C_{\mathbf{g}} [\mathbf{k}_0^2 - (\mathbf{k} + \mathbf{g})^2] + \sum_{\mathbf{h}} U_{\mathbf{g}-\mathbf{h}}^E C_{\mathbf{h}} \right\} = 0 . \quad (2.36)$$

This equation is only fulfilled for each position \mathbf{r} if the term in curly braces vanishes,

$$C_{\mathbf{g}} [\mathbf{k}_0^2 - (\mathbf{k} + \mathbf{g})^2] + \sum_{\mathbf{h}} U_{\mathbf{g}-\mathbf{h}}^E C_{\mathbf{h}} = 0 , \quad (2.37)$$

so that we obtain as many equations as the number of beams included in the calculation. As the right term in Eq. (2.37) indicates, these equations are coupled, which can be

interpreted physically be means of interaction of beam \mathbf{g} with *all other* beams. Writing Eq. (2.37) in matrix form gives

$$\underline{\underline{U}}^E \cdot \underline{C} = 0 \quad \text{with} \quad U_{\mathbf{g}\mathbf{h}}^E = U_{\mathbf{g}-\mathbf{h}}^E + \delta_{\mathbf{g}\mathbf{h}} [\mathbf{k}_0^2 - (\mathbf{k} + \mathbf{g})^2] \quad , \quad (2.38)$$

where coefficients $C_{\mathbf{g}}$ are assembled in vector \underline{C} . Let us assume that N beams are included in the calculation. Then, matrix $\underline{\underline{U}}^E$ has the dimension $N \times N$, so that N coupled equations are obtained. Because Eq. (2.38) is quadratic in the wave vectors \mathbf{k} to be determined, $2N$ solutions of type (2.34) exist with individual wave vectors $\mathbf{k}^{(j)}$ and periodic functions $C^{(j)}(\mathbf{r})$. Since, at this stage, the number of unknowns exceeds the number of governing equations anyway, let us add $2N$ more unknowns to build the general solution $\Psi(\mathbf{r})$ by linear combination of individual Bloch waves, weighted with excitation coefficients $a^{(j)}$ to be determined:

$$\Psi(\mathbf{r}) = \sum_j a^{(j)} \psi^{(j)}(\mathbf{r}) = \sum_j a^{(j)} \sum_{\mathbf{g}} C_{\mathbf{g}}^{(j)} e^{2\pi i(\mathbf{k}^{(j)} + \mathbf{g})\mathbf{r}} \quad . \quad (2.39)$$

For relativistic electrons, we must now ask which of the $2N$ excitation coefficients contribute significantly. To this end, we split the wave vectors $\mathbf{k}^{(j)}$ inside the crystal into one normal component, being parallel or antiparallel to the specimen surface normal \mathbf{n} , and one tangential component, which is perpendicular to it. It can be shown [45] via continuity conditions for the Bloch waves at the specimen surface that only the normal component can change when entering the crystal. Now let \mathbf{n} point more or less antiparallel to \mathbf{k}_0 . Then, we can express the Bloch wave vectors inside the crystal by $\mathbf{k}^{(j)} = \mathbf{k}_0 - \gamma^{(j)}\mathbf{n}$. Diagonal terms in Eq. (2.38) take the form

$$\begin{aligned} U_{\mathbf{g}\mathbf{g}}^E &= U_0^E + 2\gamma^{(j)}\mathbf{n}(\mathbf{k}_0 + \mathbf{g}) - 2\mathbf{k}_0\mathbf{g} - \gamma^{(j)2} - \mathbf{g}^2 \\ &\approx U_0^E + 2\gamma^{(j)}\mathbf{n}\mathbf{k}_0 - (2\mathbf{k}_0 + \mathbf{g})\mathbf{g} \quad . \end{aligned} \quad (2.40)$$

The approximation made in the second step can already be found in Bethe's work [36] when Eq. (2.38) is solved for Laue diffraction, i.e. transmitted electrons. Using Ewald's representation of scattering geometry as sketched in Fig. 1.5 (b), this can be understood immediately: Since TEM specimen are thin, each reciprocal lattice point is replaced by a rod along the surface normal. Allowed scattering angles are defined by the intersections of these rods with the Ewald sphere, of which two exist for each rod. By Ewald construction, one finds that these correspond to two scattered waves, one travelling back to the entrance surface and one propagating through the crystal. By increasing the radius of the Ewald sphere, that is, increasing accelerating voltage, the excitation error of the backscattered wave becomes so large that backscattering becomes negligible. This can already be understood from kinematical treatment by applying a crystal shape function to the crystal potential, yielding hyperbolic damping of scattering probability with increasing distance to the Ewald sphere. If so, the anpassungen $\gamma^{(j)}$ are small and quadratic contributions can be neglected, which leads to the high energy approximation expressed by Eq. (2.40).

Inserting Eq. (2.40) into Eq. (2.38) finally gives the eigenvalue problem

$$\underline{\underline{A}}^E \cdot \underline{C}^{(j)} = -2\gamma^{(j)}\mathbf{n}\mathbf{k}_0 \cdot \underline{C}^{(j)} \quad \text{with} \quad A_{\mathbf{g}\mathbf{h}}^E = U_{\mathbf{g}-\mathbf{h}}^E - \delta_{\mathbf{g}\mathbf{h}}(2\mathbf{k}_0 + \mathbf{g})\mathbf{g} \quad , \quad (2.41)$$

that can easily be solved on contemporary computers. In contrast to Eq. (2.38), the characteristic equation of Eq. (2.41) is a polynomial of order N because N solutions for backward scattering were ignored.

In a last step, we determine the still unknown excitation amplitudes $a^{(j)}$ of the Bloch waves found by diagonalisation of Eq. (2.41) by considering boundary conditions at the specimen surface. In this respect, plane wave illumination is assumed in the following, which is sufficient for most applications because even for conical incidence, the result may be expressed as a superposition of plane wave results. Nevertheless, there is no general restriction to parallel illumination as shown by Allen et al. and Findlay et al. [95, 96] who considered the propagation of focused coherent probes in the framework of the Bloch wave approach. In terms of the anpassungen $\gamma^{(j)}$, Eq. (2.39) reads in Darwin representation (see, e.g., Ref. [38])

$$\Psi(\mathbf{r}) = \sum_{\mathbf{g}} \Psi_{\mathbf{g}}(z) e^{2\pi i(\mathbf{k}_0 + \mathbf{g})\mathbf{r}} \quad \text{with} \quad \Psi_{\mathbf{g}}(z) = \sum_j a^{(j)} C_{\mathbf{g}}^{(j)} e^{2\pi i\gamma^{(j)}z} \quad , \quad (2.42)$$

where z is the specimen thickness measured along \mathbf{n} and $\Psi_{\mathbf{g}}(z)$ denotes the (z -dependent) amplitude of Bragg beam \mathbf{g} . To present results in a close form, we again make use of matrix notation and assemble all eigenvectors $\underline{C}^{(j)}$ in Eq. (2.41) columnwise in matrix \underline{C} , all Fourier coefficients $\Psi_{\mathbf{g}}(z)$ and excitation amplitudes $a^{(j)}$ in column vectors $\underline{\Psi}(z)$ and \underline{a} , respectively. Consequently, all $\Psi_{\mathbf{g}}(z)$ in Eq. (2.42) are determined by $\underline{\Psi}(z) = \underline{C} \underline{\varepsilon}(z) \underline{a}$ with a diagonal matrix $\underline{\varepsilon}(z)$ whose entries are given by $\varepsilon_{jj}(z) = e^{2\pi i\gamma^{(j)}z}$. As we restrict on plane wave illumination, we have $\Psi_{\mathbf{g} \neq 0}(0) = 0$ at the entrance surface of the crystal. Since $\varepsilon_{jj}(0) = 1$, we get $\underline{\Psi}(0) = \underline{C} \underline{a}$, or, by inversion, $\underline{a} = \underline{C}^{-1} \underline{\Psi}(0)$. When this is inserted in the expression for $\underline{\Psi}(z)$, we end up at

$$\underline{\Psi}(z) = \underline{S} \underline{\Psi}(0) \quad \text{with} \quad \underline{S} = \underline{C} \underline{\varepsilon}(z) \underline{C}^{-1} \quad , \quad (2.43)$$

where the *scattering matrix* \underline{S} was defined. Because $\underline{\Psi}(0)$ contains only one nonzero entry, Eq. (2.43) is equivalent to picking only that one column of \underline{S} which corresponds to the position of the primary beam in $\underline{\Psi}(z)$.

It should be noticed that the matrix \underline{A}^E may possess no symmetry in the general case of a non-centrosymmetric crystal and absorption, which leads to complex eigenvalues $\gamma^{(j)}$ that attenuate the Bragg beam amplitudes with increasing specimen thickness. Furthermore, $\underline{\Psi}(z)$ is also complex and hence assigns modulus and phase to each Bragg scattered beam. This complex nature becomes important whenever interference between different Bragg beams occur, that is, in TEM imaging and large-angle convergent beam electron diffraction (CBED). For parallel beam electron diffraction (PBED), diffraction intensities are just given by elementwise multiplication of $\underline{\Psi}(z)$ with its complex conjugate.

Accuracy of Bloch wave simulations is mainly determined by the reliability of the potentials which build up the matrix \underline{A}^E in Eq. (2.41). However, precision is primarily dependent on the number of beams included, so that stability of simulations with respect to inclusion of further beams must be checked. In this respect, problems may arise in numerical accuracy and convergence of the diagonalisation of \underline{A}^E if scattering geometry is such that \underline{A}^E is large and contains both very weak and strong beams simultaneously. For less than 1000 beams, this is usually not observed, but the number of beams rapidly increases if higher order Laue zones are included. In this case, beams are divided in two sets S and S' , the former containing strong beams, the latter containing weak ones. The decision whether a beam is strong or weak depends on its structure factor and on its proximity to the Ewald sphere (excitation error). Criteria can be found in, e.g., Ref. [46]. However, matrix \underline{A}^E explicitly contains only beams of S , but its entries are modified

through the beams of S' according to [46]

$$A_{\mathbf{g}\mathbf{g}}^{E'} = A_{\mathbf{g}\mathbf{g}}^E - \lambda \sum_{\mathbf{h}'} \frac{U_{\mathbf{g}-\mathbf{h}'}^E U_{\mathbf{h}'-\mathbf{g}}^E}{2s_{\mathbf{h}'}} \quad \text{and} \quad A_{\mathbf{g}\mathbf{h}}^{E'} = A_{\mathbf{g}\mathbf{h}}^E - \lambda \sum_{\mathbf{h}'} \frac{U_{\mathbf{g}-\mathbf{h}-\mathbf{h}'}^E U_{\mathbf{h}'}^E}{2s_{\mathbf{h}'}} \quad (\mathbf{g} \neq \mathbf{h}) \quad , \quad (2.44)$$

known as *Bethe potentials*. In Eq. (2.44), $s_{\mathbf{h}'}$ is the excitation error of beam \mathbf{h}' and λ stands for the electron wavelength inside the crystal. The summations in Eq. (2.44) can become quite extensive as, for every entry of \underline{A}^E , summation over typically a few hundreds of beams must be carried out, together with calculation of respective potentials. Nevertheless the eigenvalue problem is significantly reduced, so that Bethe perturbation is worth the effort in many cases, especially if iterative solution of Eq. (2.41) is necessary in refinements or CBED simulations. In practice, beams are selected as follows: Given a spatial cutoff frequency g_{max} , all beams inside the corresponding sphere are selected. Then, spherical shells are defined by maximum excitation errors s_{max} and s'_{max} , the former defining beams of S and the latter those of S' . Finally, certain Laue zones may be selected.

2.5 Multislice approach

For several TEM applications, such as high-angle annular dark field scanning TEM, diffuse scattered electrons must explicitly be taken into account. Moreover, reliability checks of approaches which exploit perfect translational crystal symmetry in subsequent sections are based on comparison with multislice results, so that a brief summary of this approach seems expedient.

Again we start with Eq. (2.35), but use the ansatz of a modulated plane wave $\Psi(\mathbf{r}) = A(\mathbf{r}) e^{2\pi i \mathbf{k}_0 \mathbf{r}}$ and leave $U^E(\mathbf{r})$ unconstrained. Assuming incidence to be along $-z$, this leads to

$$\frac{\partial^2 A(\mathbf{r})}{\partial z^2} + \Delta_{xy} A(\mathbf{r}) - 4\pi i k_0 \frac{\partial A(\mathbf{r})}{\partial z} + 4\pi^2 U(\mathbf{r}) A(\mathbf{r}) = 0 \quad , \quad (2.45)$$

where Δ_{xy} contains the second-order derivatives in lateral (x - and y -) directions. In high energy approximation, the second-order derivative along z may be neglected for usual dynamical calculations [42], so that Eq. (2.45) writes

$$\frac{\partial A(\mathbf{r})}{\partial z} = [\overline{\Delta} + \overline{U}] A(\mathbf{r}) \quad \text{with} \quad \overline{\Delta} := \frac{\Delta_{xy}}{4\pi i k_0} \quad \text{and} \quad \overline{U} := \frac{\pi}{i k_0} U(\mathbf{r}) \quad . \quad (2.46)$$

As implied by its name, the basic idea of the multislice algorithm is to solve Eq. (2.46) by considering a fictitious crystal in which potential-free space of thickness ϵ and infinitesimal thin slices that contain the full potential of the slice alternate. That is, Eq. (2.46) is solved formally by

$$A(x, y, n\epsilon) = \mathcal{B}_n \mathcal{B}_{n-1} \dots \mathcal{B}_1 A(x, y, 0) \quad \text{with} \quad \mathcal{B}_j(x, y) := e^{\epsilon(\overline{\Delta} + \overline{U}_j)} \quad . \quad (2.47)$$

Care must be taken in the evaluation of \mathcal{B}_j because $\overline{\Delta}$ and \overline{U} are operators. According to the Zassenhaus theorem applied to second order in ϵ , and expanding the result in a Taylor series up to ϵ^2 , \mathcal{B}_j takes the form

$$\mathcal{B}_j \approx e^{\frac{1}{2}\epsilon\overline{\Delta}} e^{\epsilon\overline{U}_j} e^{\frac{1}{2}\epsilon\overline{\Delta}} \quad . \quad (2.48)$$

The interaction with one slice can therefore be interpreted as follows: First, only $\overline{\Delta}$ acts on the wave function and propagates it through potential-free space to the slice centre at

$\epsilon/2$. Then, only \overline{U} acts and modifies the wave function according to the potential of the slice, whereas no propagation takes place. Finally, solely $\overline{\Delta}$ acts again and the wave is propagated further to the slice exit plane.

We now look at the propagator operator in more detail. In free space \overline{U} vanishes, and propagation is equal to a convolution operation, that is [38]

$$A(x, y, z + \epsilon) = e^{\epsilon \overline{\Delta}} A(x, y, z) = \mathcal{F}^{-1} \left[e^{-\pi i \frac{\epsilon}{k_0} (q_x^2 + q_y^2)} \right] \otimes A(x, y, z) = \mathcal{P}_\epsilon \otimes A(x, y, z) \quad , \quad (2.49)$$

where \mathcal{P}_ϵ is known as the *Fresnel propagator*, yielding the modification of a wave after travelling a distance ϵ . In Eq. (2.49), q_x and q_y are coordinates in a Fourier plane perpendicular to z . Up to now, propagation is only possible in z -direction, which was chosen to be parallel to \mathbf{k}_0 . Therefore, inclined illumination of a specimen ought to be realised by explicitly rotating the full crystal. However, for small tilts, two approximations exist [59] which simplify calculations. First, each slice may be shifted slightly along the tangential component of \mathbf{k}_0 . Second, the Fresnel propagator can be modified and adopts the following form in Fourier space, if ϑ_x and ϑ_y denote the tilt angles in x - and y -direction:

$$\mathcal{F} \left[\mathcal{P}'_\epsilon \right] = e^{-\pi i \frac{\epsilon}{k_0} (q_x^2 + q_y^2)} e^{2\pi i \epsilon (q_x \tan \vartheta_x + q_y \tan \vartheta_y)} \quad . \quad (2.50)$$

Expressing \mathcal{P}'_ϵ in Fourier space is convenient since the convolution in Eq. (2.49) is accomplished in reciprocal space by multiplication of the Fourier transforms of \mathcal{P}'_ϵ and $A(x, y, z)$ with each other. The result is then transformed back to real space.

Finally the interaction with the crystal potential \overline{U} must be regarded. Owing to the multislice idea, $\overline{\Delta}$ is zero and \overline{U}_j in Eq. (2.48) must contain the full potential of slice j , which is equivalent to

$$A(x, y, z + \epsilon) = A(x, y, z) e^{\int_z^{z+\epsilon} \overline{U}(x, y, z') dz'} = A(x, y, z) e^{\frac{\pi}{ik_0} U_P} \quad . \quad (2.51)$$

The quantity U_P is the projection (along z) of the potential (as seen by the electrons), caused by all atoms in the slice. It is proportional to the *projected potential* $V_P = h_P^2 c^2 (2Ee)^{-1} U_P$, given in units of Volts and containing no relativistic correction. Often, constants are collected in the definition of the *interaction constant* $\sigma = 2\pi Ee (h_P^2 c^2 k_0)^{-1}$. It is obvious that Eq. (2.51) modifies only the phase of the wave function if we neglect absorption for a moment. For this reason, the effect of the exponential factor in Eq. (2.51) is known as the *phase grating*.

Since Fresnel propagation (2.49) is usually carried out in Fourier space, whereas the phase grating (2.51) is an operation in real space, alternating application according to Eqs. (2.48) and (2.47) involves permanent back and forth Fourier transformation. Even the use of fast Fourier transforms makes this aspect the limiting factor as to the efficiency of a simulation. Especially inclusion of TDS electrons requires large spatial cutoff frequencies since the TDS background obeys only weak damping in reciprocal space as may be seen from Fig. 2.6.

2.6 Scattering potential of real crystals

To understand electron scattering quantitatively, disorder in real specimens must be taken into account. In this section, disorder stemming from thermal motion of atoms and from

static atomic displacements is considered in more detail. The former is inevitably present in any crystal even at vanishing temperature due to zero point atomic motion. The latter is especially important in the presence of point defects causing local strain fields. These may be caused by missing or interstitial atoms and atoms of different size. Here, the focus is on size effects.

Techniques for image- or diffraction pattern simulation fall in two main categories. On the one hand, a real crystal is indeed built up by disturbing atom positions of an ideal crystal according to thermal and/or static displacement statistics. Especially simulation of static disorder requires taking into account large supercells, through which the incident electron wave is propagated via multislice methods. This approach may evolve into computationally intensive simulations since averaging over several atomic ensembles is usually necessary. However, the advantage of this approach is that it is not restricted to Bragg reflections and can thus be used to calculate, e.g., the diffuse background in electron diffraction patterns. On the other hand, the model of an ideal crystal may be retained, but scattering potentials are to be modified in such a way that Bragg scattered electrons are simulated correctly. Diffuse scattered electrons are regarded as losses and thus treated in terms of absorption, which can be accounted for by adding appropriate imaginary parts to the crystal potential [53], as already mentioned in conjunction with Eq. (2.11). Besides studying the influence of thermal diffuse scattering (TDS) on Bragg intensities, this section deals with the derivation of static atomic displacements (SAD). Finally, an efficient way to account for SAD diffuse losses by means of TDS absorptive potentials is introduced.

2.6.1 Thermal diffuse scattering

In the strict sense, thermal movement of atoms ought to be described time-dependently. However, electrons accelerated by 300 kV in a TEM travel with more than 75% of the velocity of light in vacuum. To pass a 100 nm thick specimen, an electron needs less than 0.5 fs. On the other hand, typical phonon frequencies range below 10 THz, which is equivalent to vibrational periods which are three orders of magnitudes above this value. It follows from this that beam electrons in a TEM rather see a snapshot of a crystal at a certain instant than time-averaged potentials, as it is assumed in the framework of Debye-Waller damping explained in section 2.2. Corresponding to the ergodic hypothesis, instead of introducing any time dependence in the scattering problem, TDS patterns are calculated by averaging over several simulations for a "frozen" crystal. Simulations are performed under the same conditions, except for the displacement configuration. As to the neglect of energy losses during electron-phonon scattering, it was shown recently [97, 98] that this concept is equivalent to a full quantum mechanical treatment of inelastic phonon scattering. In nomenclature, we shall distinguish between *frozen lattice* [54] and *frozen phonon* [52], the former assuming independent atomic vibrations according to the Einstein model, the latter accounting for correlated displacement of atoms. In this work, we restrict on frozen lattice simulations, of which one for GaAs is shown at the head of Fig. 2.6.

On the left the squareroot of the amplitude of the wavefunction in the diffraction plane is shown in order to highlight the contribution of Bragg reflections. On the right, intensity was scaled logarithmically to display TDS background. Concerning the Bragg reflections it becomes obvious that their intensity is decreasing strongly with increasing momentum transfer. This is not only because the distance of corresponding reciprocal lattice points to the Ewald sphere gets larger, but also because Debye-Waller damping according to

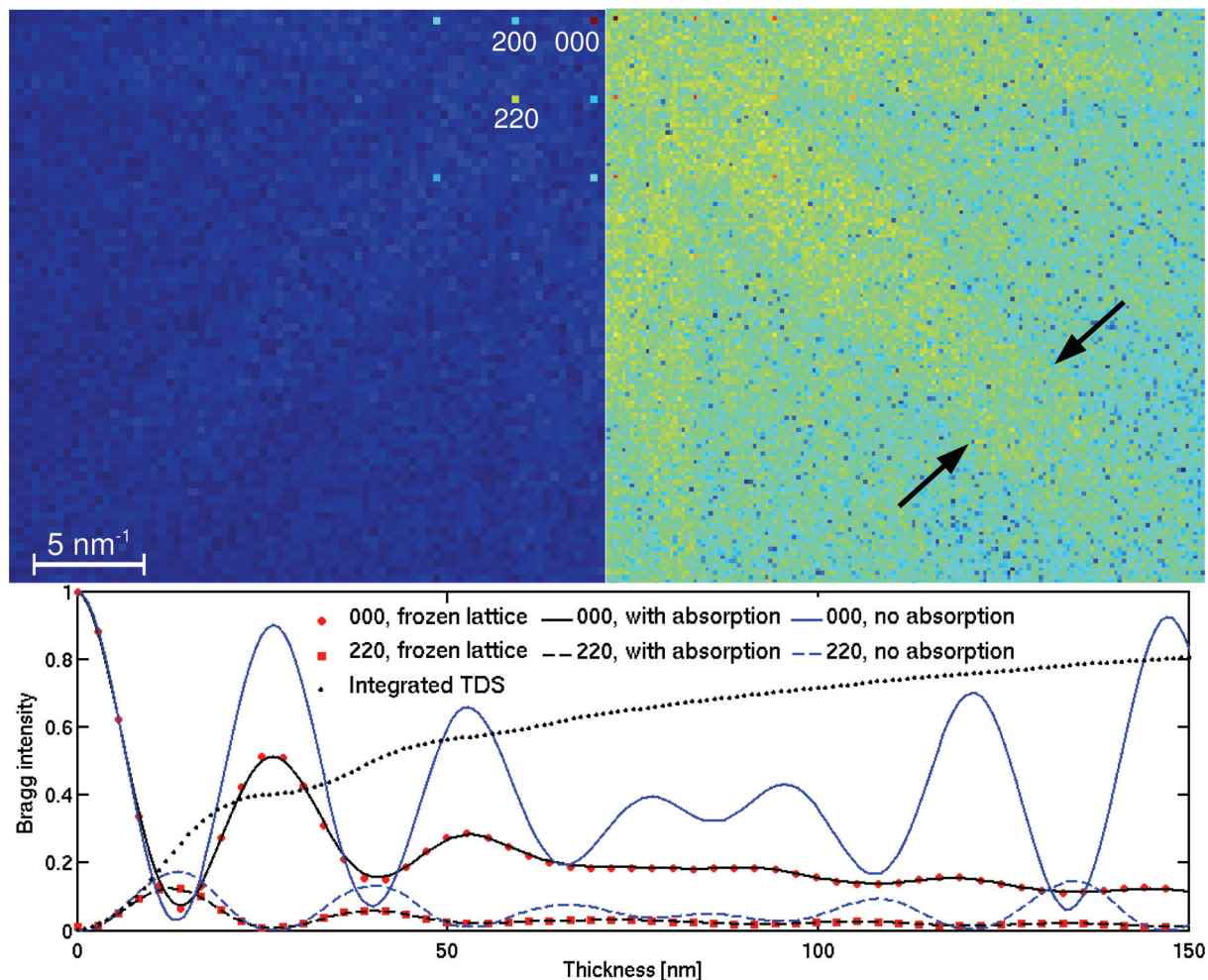


Figure 2.6: *Top*: Frozen lattice multislice simulation of a GaAs diffraction pattern in zone axis [001] for a specimen thickness of 50 nm. Intensity was scaled differently to pronounce Bragg reflections (left) and TDS background (right). The arrows mark a Kikuchi band. *Bottom*: Pendellösung plots for various beams (distinguished by line style) and various models (different colour). Blue and black graphs correspond to Bloch wave simulations with and without considering TDS absorptive form factors, respectively. Red data was obtained from frozen lattice multislice simulations. The dotted black line represents the total amount of TDS electrons.

the Gaussian in Eq. (2.6) is occurring here. For Bragg beams this is exact because they can be considered to be the contribution of the perfect lattice to the diffraction pattern. Indeed, averaging a thermally vibrating lattice over time results in a lattice with perfect translational symmetry but blurred atomic potentials. To investigate the dependence of Bragg intensities on thickness, a series of diffraction patterns in frozen lattice approximation with different thicknesses was simulated. The intensity of pixels corresponding to beams 000 and 220 is plotted in red as a function of thickness (pendellösung plot) in the lower part of Fig. 2.6. Both graphs exhibit periodic behaviour, being a fingerprint of multiple scattering. Furthermore, damping with increasing thickness is observed which is due to TDS scattered electrons lacking in Bragg beams, as becomes obvious from the upper right part of Fig. 2.6. Regarding conventional lattice imaging techniques, significant Bragg signal is required, so that high-resolution TEM is usually limited to some tens of nanometres. Nevertheless TDS electrons may be Bragg-scattered again, leading to a set of Kikuchi bands of which one is marked by black arrows in Fig. 2.6. They are extremely helpful to find a certain crystallographic orientation since they cross in the centres of circles defined by intersection of the Ewald sphere with reciprocal lattice planes that are nearly perpendicular to the incident beam (Laue circles).

Thermal diffuse scattered electrons must explicitly be taken into account for simulations of absolute contrast in high-resolution TEM [97] because they add to the image background. Furthermore, TDS is important in high-angle annular dark field scanning TEM (HAADF-STEM) image simulations because TDS intensity dominates over Bragg intensity at large scattering angles at room temperature. However, for diffraction work on Bragg scattering, which chapter 3 deals with, and high-resolution TEM, where solely intensity oscillation (not absolute contrast) is of interest, an approach is desirable which on the one hand yields correct Bragg intensities in the presence of TDS, but on the other hand circumvents calculation of the exact distribution of TDS electrons in reciprocal space. To show that it is not sufficient to include Debye-Waller factors for this purpose, blue curves in Fig. 2.6 show Bloch-wave (see section 2.4) pendellösung plots of beams 000 and 220 using ASA from Doyle and Turner which have been damped by Debye-Waller factors according to Eq. (2.6). Oscillations in these graphs exhibit that dynamical interaction among Bragg scattered beams is treated correctly, but the damping envelope with thickness is missing. In other words, the sum over all beam intensities is one for arbitrary thickness, being in conflict with the observation of diffuse TDS background in diffraction patterns. We conclude that inclusion of the Debye-Waller factor alone is not sufficient. Applied to ASA, it only affects the relative intensity of Bragg scattered beams.

Considering the Bloch wave approach, this can easily be explained: It follows from Eq. (2.11) that $V_{\mathbf{g}}^{\kappa} = V_{-\mathbf{g}}^{\kappa*}$ if $W_{\mathbf{g}}^{\kappa} = 0$. Then, the matrix $\underline{\underline{A}}^E$ in Eq. (2.41) is hermitian and thus owns real eigenvalues. Furthermore, thickness characteristics are governed by matrix $\underline{\underline{\varepsilon}}$ in Eq. (2.43) which contains eigenvalues of $\underline{\underline{A}}^E$ in the exponent. Similar to Lambert-Beer's law in optics, complex eigenvalues in $\underline{\underline{\varepsilon}}$ cause exponential damping. Therefore, choosing an appropriate absorptive potential $W_{\mathbf{g}}^{\kappa} \neq 0$ in Eq. (2.11) destroys any symmetry of $\underline{\underline{A}}^E$ and leads to complex eigenvalues, yielding the correct thickness dependence of Bragg beams.

Since Hall and Hirsch [54] gave first expressions in 1965 for absorptive potentials for TDS in the framework of a two-beam Bloch wave theory, a variety of publications on this topic has accumulated, dealing with parameterised potential calculations [76, 77, 99, 73, 74, 75, 100]. Since absorptive potentials have not explicitly been calculated in this work but were implemented as published in Refs. [75, 77], a detailed derivation is judged to be

beyond the scope of this chapter. Instead, the general approach is briefly sketched and the reader is referred to Ref. [54] for basic ideas, Ref.[101, chap. 7] for detailed derivation, or Ref. [57] for a review. The central result is the definition of an *absorptive form factor*

$$f'_Z(\mathbf{q}) = f'_Z(q) = \lambda \int f_Z(\mathbf{s}) f_Z(\mathbf{s} - \mathbf{q}) e^{-\frac{1}{4}B\mathbf{q}^2} \left(1 - e^{-\frac{1}{2}B(\mathbf{s}\mathbf{q} - \mathbf{q}^2)}\right) d^2s \quad (2.52)$$

for electrons with wavelength λ . In this equation, integration is over the Ewald sphere and B denotes the Debye parameter defined in context with Eq. (2.6). Note that $f'_Z(q)$ is a function of atomic number Z and momentum transfer modulus q only. It contains no dependence on crystal κ or site j which is equivalent to an isolated atom approximation. In this respect, we have seen in section 2.3.5 that MASA differ only slightly from ASA for isolated atoms and marginal influence on the integral in Eq. (2.52) can hence be expected, which however is an assumption to be verified in a separate study. Equation (2.52) principally is derived by

1. Expressing the full diffraction pattern in the two-beam [54], many-beam [101] Bloch wave, or kinematical [57] limit. For the latter, the intensity is given by [57]

$$I(\mathbf{s}, \mathbf{U}) = |C|^2 \sum_{\mathbf{g}} \sum_{\mathbf{h}} \psi_{\mathbf{g}} \psi_{\mathbf{h}}^* \left[\sum_j e^{2\pi i(\mathbf{g}-\mathbf{h})(\mathbf{r}_j + \mathbf{u}_j)} f^j(\mathbf{s} - \mathbf{g}) f^{j*}(\mathbf{s} - \mathbf{h}) + \sum_{j,k;j \neq k} e^{-2\pi i(\mathbf{s}-\mathbf{g})(\mathbf{r}_j + \mathbf{u}_j) + 2\pi i(\mathbf{s}-\mathbf{h})(\mathbf{r}_k - \mathbf{u}_k)} f^j(\mathbf{s} - \mathbf{g}) f^{k*}(\mathbf{s} - \mathbf{h}) \right] \quad (2.53)$$

where \mathbf{s} is a vector in reciprocal space, \mathbf{g} and \mathbf{h} are reciprocal lattice vectors, C is a constant and \mathbf{r}_j refers to atom positions in an ideal crystal. $\psi_{\mathbf{g}}$ describes one Fourier coefficient for the wave function of the incident electron wave. By \mathbf{U} , one certain displacement configuration is described with individual atomic displacements \mathbf{u}_j .

2. Averaging intensity (called incoherent summation) in Eq. (2.53) over time as for thermal displacements we have $\mathbf{U} = \mathbf{U}(t)$ (assuming uncorrelated displacements \mathbf{u}_j),
3. Calculating Bragg intensities in the framework of Debye-Waller damping, and
4. Subtracting the result from the incoherent summation.
5. Integration over all possible scattering vectors equals the total amount of TDS electrons, which can be split into contributions of individual atoms, as expressed by Z in Eq. (2.52).

Finally, crystal potential Fourier components as defined in Eq. (2.11) are obtained by the replacement $f_{Z,j}^{\kappa}(\mathbf{q}) \longrightarrow f_{Z,j}^{\kappa}(\mathbf{q}) + i f'_Z(q) \cdot \hbar_P^2 (2\pi m_e e \Omega)^{-1}$ in Eq. (2.10). It must be emphasised that $f_{Z,j}^{\kappa}(\mathbf{q})$ may be complex (as is the case for certain MASA), which is not due to absorption because the real-space potential built this way stays real.

This section closes with some remarks on the black graphs in Fig. 2.6 which were simulated under the same conditions as the blue ones but using absorptive form factors from Ref. [75] corresponding to the same Debye parameters as in the frozen lattice simulation. Perfect agreement with the latter (red) shows that it is possible to decouple calculation of Bragg intensities from TDS background. This is an important point because it is neither necessary to average over different displacement ensembles, nor must the assumption of

ideal translational symmetry be dropped, which allows application of, e.g., Bloch wave simulations for quantitative simulations if only Bragg intensities are of interest. To show that no intensity is "hidden" in beams not shown in Fig. 2.6, the dotted black curve expresses the TDS intensity sum, obtained by subtracting the sum of all 980 Bragg intensities from the intensity of the incident beam. Already for a specimen thickness of 50 nm, more than 50% of the incident electrons are scattered to the TDS background.

2.6.2 Calculation of static atomic displacements

It was pointed out in section 2.3.3 in connection with Fig. 2.1 that (strain) energy is a function of the lattice parameters. This function has a minimum for a certain lattice parameter, to which corresponds an equilibrium bond length that is characteristic for the bond partners and the crystal structure. So far, lattice parameters for mere binary zinc-blende compounds can be given and, except for thermal displacements, atoms reside at positions of the perfect lattice. We now consider alloys without external stress to investigate the effect of replacing native atoms on a certain sublattice by foreign but isovalent atoms. On the one hand, it was already observed by Vegard in 1921 [102] that the alloy lattice parameter is principally given by the lattice parameter of the pure materials involved, weighted according to the actual stoichiometry of the alloy. On the other hand, random placement of impurity atoms can be regarded as a localised effect since each impurity is a source of a stress field that more or less rapidly decays with distance. Heuristically, it is obvious that atoms in the vicinity of impurities will accommodate to this stress and take an equilibrium position permanently displaced from the position in the perfect lattice.

The fact that these static atomic displacements (SAD) include both macroscopic (because random alloys must be represented by large supercells) and microscopic (because bonding is involved) aspects makes them difficult to treat. In general, SAD are derived by shifting atomic positions in an ideal crystal iteratively along respective force vectors until the strain energy minimum is reached. Principally this can be done with highest accuracy using DFT and Eq. (2.19), where for each displacement configuration a new electron density (and hence a new potential) is derived self-consistently, but this is only possible for unrealistically small cells. For large cells with up to $\approx 10^6$ atoms, *valence force field* (VFF) methods are applied which rely on empirical potentials derived from elastic constants. In the following, a brief summary of Keating's approach [31] as implemented by Rubel et al. [32] will be given. For comparison with DFT, the reader is referred to chapter 4.

The total strain energy E_{total} is split into contributions of the individual atoms, $E_{\text{total}} = \sum_j E_j$, where j runs over all atoms in a supercell. In generalisation for zinc-blende mixed crystals [103], E_j is the sum of bond-stretching terms

$$E_j^\alpha(\mathbf{r}_j) = \frac{1}{4} \sum_{k=1}^4 \frac{3}{4R_{jk}^2} \alpha_{jk} (\mathbf{r}_{jk}^2 - \mathbf{R}_{jk}^2)^2 \quad (2.54a)$$

and bond-bending terms

$$E_j^\beta(\mathbf{r}_j) = \frac{1}{4} \sum_{k,l=1; k \neq l}^4 \sum_{k \neq l}^4 \frac{3}{4R_{jk}R_{jl}} \beta_{kjl} (\mathbf{r}_{jk}\mathbf{r}_{jl} - \mathbf{R}_{jk}\mathbf{R}_{jl})^2 \quad . \quad (2.54b)$$

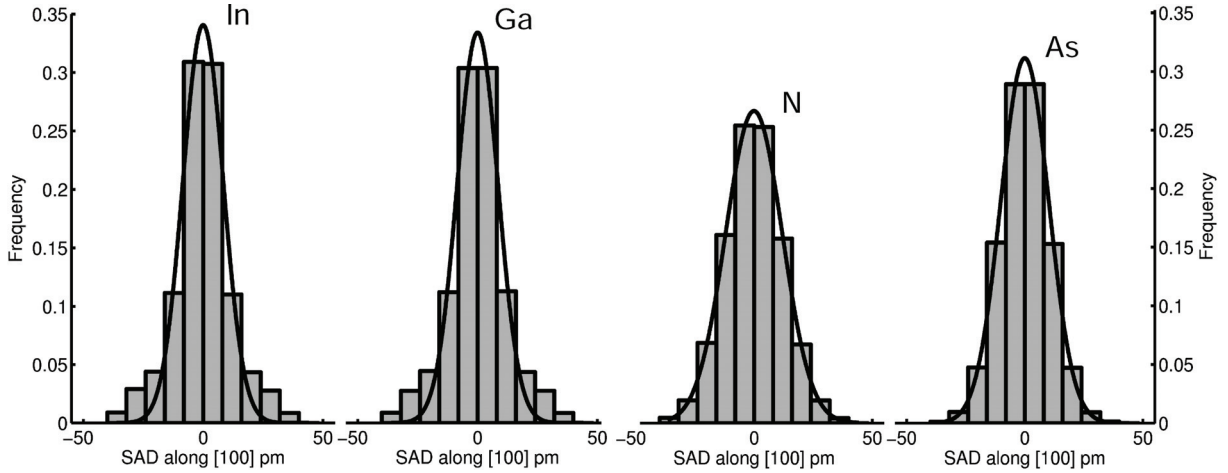


Figure 2.7: Histogram of SAD (bars) and Gaussian least-squares fit (black curves) in x -direction for an $\text{In}_{0.25}\text{Ga}_{0.75}\text{N}_{0.05}\text{As}_{0.95}$ supercell. The dimension of the cell was 10×10 Bravais cells laterally and 100 nm in z -direction. Displacements have been obtained by VFF strain relaxation.

In Eqs. (2.54), \mathbf{r}_j denotes the position of atom j and $\mathbf{r}_{jk} = \mathbf{r}_j - \mathbf{r}_k$ connects atoms j and k , whereas k and l index the four nearest neighbours of atom j . Analogous definitions hold for equilibrium positions \mathbf{R}_j . The parameter α_{jk} is called the bond-stretching force constant for a binary crystal with equilibrium lattice parameter a^{jk} , defined by atoms j and k . It is related to the stiffness coefficients via $4\alpha_{jk} = a^{jk}(C_{11}^{jk} + 3C_{12}^{jk})$. The term for bond-bending involves two nearest neighbours because it expresses energy contributions stemming from changes of the angle θ_{kjl} between two adjacent bonds, becoming obvious from $\mathbf{R}_{jk}\mathbf{R}_{jl} = R_{jk}R_{jl}\cos(\theta_{kjl})$. The bond-bending force constant β_{kjl} is calculated from symmetric bonds only, $4\beta_{kjk} = a^{jk}(C_{11}^{jk} - C_{12}^{jk})$. If atoms k and l are of different type, the mean of $\beta_{kjk} + \beta_{ljl}$ is taken. A summary of material constants used in this work is given in table 2.1.

As for MASA, we choose an InGaNAs alloy to demonstrate the impact of SAD derived by VFF. In Fig. 2.7, histograms of SAD in x -direction are shown for all four elements. A 100 nm thick GaAs supercell with lateral extension of 10×10 Bravais cells was generated. 25% of gallium and 5% of arsenic have been replaced randomly by indium and nitrogen, respectively. Lattice parameters according to Vegard's rule [102], generalised for quaternary compounds in Eq. (4.1), were used for $x = 0.25$ and $y = 0.05$ for an unstrained cell. It becomes obvious from Fig. 2.7 that SAD occur for all four elements with a maximum of about 45 pm in each case. However, the widths of the distributions differ significantly, being largest for nitrogen. Furthermore, it was checked by least-squares fitting if SAD may be represented by a Gaussian, as depicted by the black solid lines in Fig. 2.7. For non-metal atoms nitrogen and arsenic, this is indeed the case whereas indium and gallium statistics exhibit differences for large SAD. These may correspond to metal atoms in the direct vicinity of nitrogen atoms which cause the strongest local strain field due to their more than 40% smaller atomic radii compared to arsenic. It must be stressed that SAD of a few tens of nanometres exceed mean squared thermal displacements roughly by a factor of five at room temperature. Another important result of Fig. 2.7 as to the extension of strain fields caused by point defects can be derived by the following consideration. If atomic size effects influenced only nearest neighbours significantly, a number of about 3500 nitrogen atoms in the supercell could cause about four times as many metal atom

displacements, that is 14000. Regarding SAD statistics for indium and gallium in Fig. 2.7, the two central bins may be associated with negligible displacement, so that about 40%, or, equivalently, 28000 metal atoms experience SAD of 10 pm or more. Therefore, point defects can cause strain fields extending considerably beyond nearest neighbours.

2.6.3 Huang scattering

Static disorder is the origin of diffuse scattered electrons that on the one hand add to the thermal diffuse background and on the other hand lack in Bragg scattered beams. The first who published a quantitative analysis of both phenomena was K. Huang in 1947 [58], who considered the scattering of X-rays at a dilute crystal alloy with varying lattice parameters due to spherically symmetric point centres of distortion. Analytical treatment principally involves the same steps as the calculation of TDS intensity in section 2.6.1, but can branch to many different results, depending on the analytical shape assumed for the strain field. As we have seen in section 2.6.2, present computing power is sufficient to derive strain fields for cells containing about 10^6 atoms using VFF, so that we can drop the restriction that strain must obey an analytical expression.

Initially, we do not care about the explicit distribution of Huang scattered electrons and look only at their total amount. An intermediate result is again Eq. (2.53) because no assumptions as to the displacement field \mathbf{U} entered its derivation [57]. Instead of regarding one unit cell at different instants to realise time averaging, we now consider different unit cells in a large crystal supercell and evaluate all SAD in statistical manner. This picture is based on the assumption that, for a sufficiently large number of unit cells, any possible configuration of atoms and nearest neighbours will be present. It is equivalent to the introduction of an average perfect lattice in which long-range order is conserved [9]. In this approach, rather SAD statistics, as exemplarily shown in Fig. 2.7, than the strain field itself governs the calculation. It has been shown by Cochran and Kartha [104] that randomly distributed point defects lead to Gaussian distribution of SAD under the assumption that each individual displacement can be written as a superposition of displacements caused by each individual defect. This is not necessarily the case, as can be seen in SAD statistics for gallium and indium in Fig. 2.7, but Eq. (2.53) may then be evaluated straight forward: A result for absorptive form factors where thermal displacements obey Gaussian statistics was given in Eq. (2.52). Thus, a formally equivalent absorptive form factor for Huang scattering losses can be derived [104, 52], where the widths of the Gaussians in Fig. 2.7 replace the mean squared thermal displacements which determine Debye parameters B defined in connection with Eq. (2.6). Moreover, existing parameterised absorptive form factors intended for thermal diffuse losses can be used to derive absorptive form factors for Huang scattering at impurities.

Figure 2.8 deals with another important characteristic as to the comparison of Huang scattered and TDS electrons. Two frozen lattice multislice simulations [33] of diffraction patterns have been carried out for a $\text{GaN}_{0.06}\text{As}_{0.94}$ supercell. First, thermal displacements were set to zero and SAD have been calculated from VFF. Part of the resulting diffraction pattern is shown at the bottom of Fig. 2.8. In contrast to Fig. 2.6, it can be observed that diffuse scattered electrons prefer the vicinity of Bragg peaks. The upper part of Fig. 2.8 represents a black rocking curve between the two arrows below. Second, SAD were set to zero but thermal displacements have been generated according to room temperature [81], yielding the red rocking curve in Fig. 2.8. From both curves, three main differences can immediately be deduced. First, Bragg peaks are much sharper in case of TDS and back-

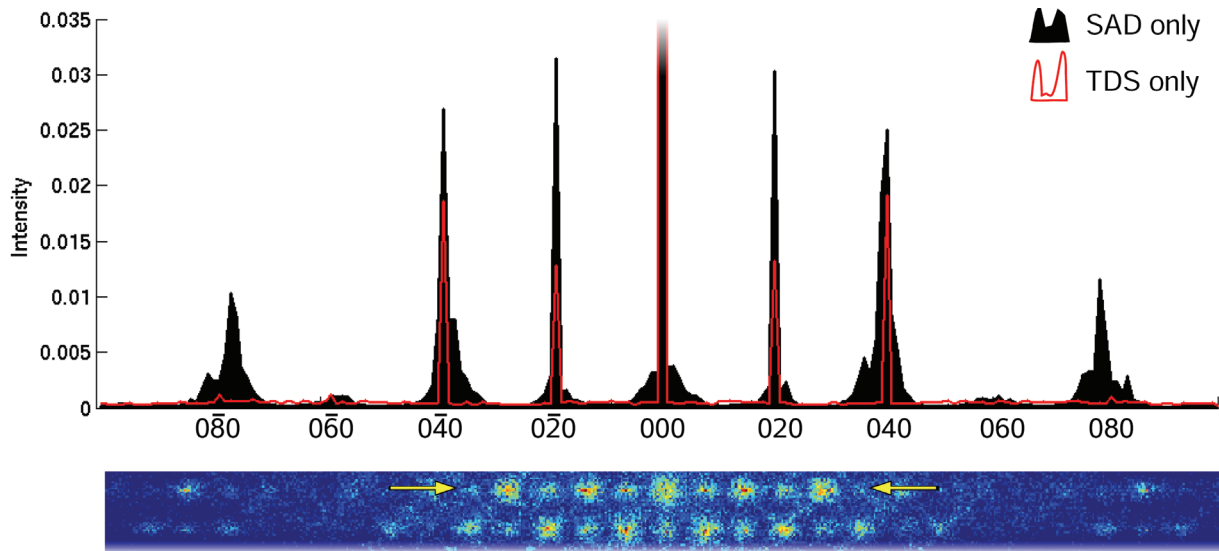


Figure 2.8: Comparison of TDS and Huang scattered electrons for a 50 nm thick $\text{Ga}_{0.94}\text{N}_{0.06}\text{As}$ supercell with a lateral extension of 10×10 Bravais cells. Frozen lattice multislice simulations have been performed using the STEMsim software [33] assuming solely thermal disorder (red curve) according to Debye parameters of 300 K [81], or solely SAD obtained by VFF (black curve). The inset at bottom depicts a part of the diffraction pattern corresponding to SAD. Arrows indicate the path for the rocking curve at top.

ground intensity is distributed smoothly in between them as the red curve shows. Second, both types of disorder suffer different damping with increasing momentum transfer, resulting in significant intensities for high-index reflections in case of SAD scattering only, where reflections in the first Laue zone are visible as becomes obvious from the bottom of Fig. 2.8. Note that mean SAD and mean thermal displacements are of comparable magnitudes. Thus, SAD do not obey a simple Debye-Waller damping scheme. Third, Huang

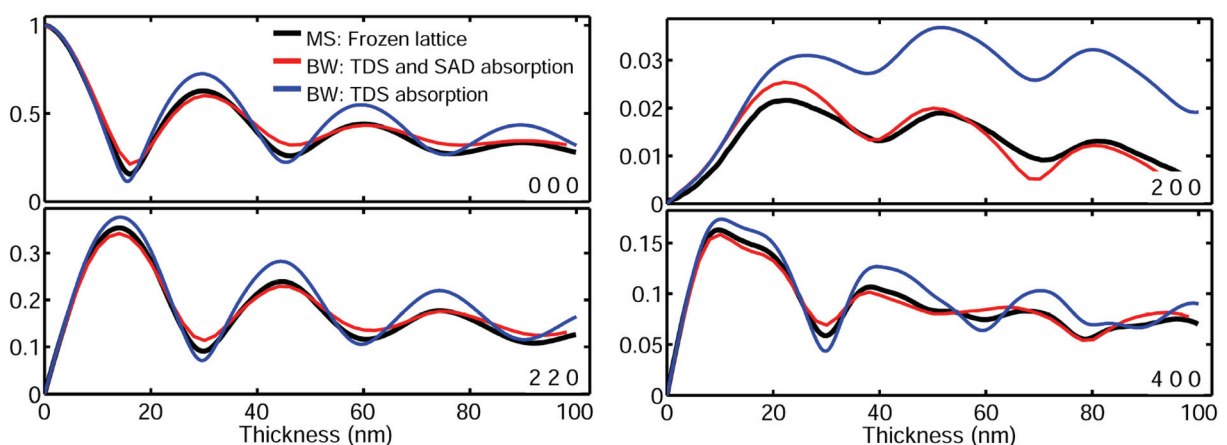


Figure 2.9: Pendellösung plots in zone axis [001] for an $\text{In}_{0.25}\text{Ga}_{0.75}\text{N}_{0.05}\text{As}_{0.95}$ alloy obtained by different models for selected reflections. Black curves originate from frozen lattice multislice simulations, whereas blue and red graphs correspond to Bloch wave simulations. For the blue curve, absorptive form factors rely on TDS only, whereas red data relies on a sum of TDS and SAD absorptive form factors. Please see text for details.

scattering can cause asymmetric (diffuse) Bragg peaks, as most dominantly present for $\langle 040 \rangle$ and $\langle 080 \rangle$, where for the latter also peak positions differ between the SAD and the TDS case. This issue was studied analytically for a doped monatomic primitive lattice by, e.g., Cowley [59]. He gives three contributions to the distribution of Huang scattered electrons, of which all three are symmetric about the reciprocal space origin. However, one term then falls monotonically with momentum transfer, another is symmetric about each Bragg peak and a third term is anti-symmetric about each Bragg peak, the latter being responsible for the asymmetric 040 reflections in Fig. 2.8. Whether peaks bend towards the centre or the opposite way depends on the relative ASA and sizes of impurity and host atoms [59].

2.6.4 Absorptive form factors for Huang scattering

In section 2.6.1 it was demonstrated how Bragg intensities can be calculated accurately in the presence of thermal disorder employing absorptive form factors that add to the imaginary part of ASA. For static disorder, an analogous procedure would be desirable. This section therefore deals with comparison of frozen lattice multislice simulations and Bloch wave results under the influence of both types of disorder simultaneously, exemplified for scattering at an $\text{In}_{0.25}\text{Ga}_{0.75}\text{N}_{0.05}\text{As}_{0.95}$ crystal.

For this purpose, 30 supercells of 100 nm thickness with lateral extension of 10 Bravais cells were generated, each obeying the same stoichiometry but different distributions of indium and nitrogen. For each of these supercells, VFF relaxation as outlined in section 2.6.2 was performed and thickness-dependent diffraction patterns were simulated for 10 thermal displacement configurations in each of the supercells. For the simulations, the STEMsim [33] software was used exploiting the frozen lattice multislice option. Debye parameters were chosen according to Ref. [81] for 300 K. Figure 2.9 shows corresponding pendellösung plots of selected beam amplitudes as black graphs.

Moreover, Bloch wave simulations were performed using structure factors from a VFF-relaxed $50 \times 50 \times 50$ $\text{In}_{0.25}\text{Ga}_{0.75}\text{N}_{0.05}\text{As}_{0.95}$ supercell. In the strict sense, such a cell generates $50^2 \cdot N$ beams to be included in the simulation if N beams are to be taken into account for conventional Bravais cells. This is equivalent to accounting for diffuse scattered electrons in between the Bragg peaks according to Fig. 2.8. Instead, the summation over j in Eq. (2.10) runs over all 10^6 atoms, but only those \mathbf{g} compatible with a conventional Bravais cell are evaluated and used in the diagonalisation of $\underline{\underline{A}}^E$ in Eq. (2.41), since our aim is to regard Huang scattered electrons as losses and treat them by absorptive form factors.

However, Fig. 2.9 depicts two types of Bloch wave results: The blue graph was obtained by using absorptive form factors [75] that solely rely on TDS, that is mean thermal atomic displacements according to Ref. [81] for 300 K. For the red one, further absorptive form factors [75] were added, having been derived from the mean SAD of each atomic species according to statistical evaluations analogous to Fig. 2.7. As expected, the red curves suffer stronger damping with thickness and agree well with the multislice results in this respect. In contrast, the blue graphs exhibit comparably large differences, especially for the weak 200 beam, where an error of 100% is observed for intermediate specimen thickness. Nevertheless no exact agreement between red and black data is observed, especially at multiples of the respective extinction distances.

2.7 Discussion

2.7.1 General remarks

Recalling that the problem of electron scattering at crystals is threefold as stated at the beginning of this chapter, it became obvious that the main attention was drawn to setting up potentials. In contrast, interaction of electrons with these potentials and their propagation through the specimen could be presented in a far closer form in the sections on Bloch wave and multislice theory. This represents the fact that rather knowledge of potentials than algorithms themselves limit the accuracy of specimen exit wave simulations.

Most effort has been spent on treating ideal crystals which may be astonishing because multislice simulations on contemporary computers can definitely handle potential landscapes which include both bonding and SAD. Unfortunately, length scales of the DFT approach used in this work and VFF are complementary, so that incorporating both phenomena exactly is currently not possible for realistic crystal dimensions. In this respect, the reader might have noticed that, whenever comparison between Bloch wave and frozen lattice multislice pendellösung plots has been performed (Figs. 2.6 and 2.9), atomic scattering factors were based on isolated atom data [75]. For both static and thermal disorder the explanation why bonding may only be accounted for in the Debye-Waller damping scheme is straight forward: According to Eq. (2.8), the Coulomb potential can be built up by summing ASA in reciprocal space and by multiplying each ASA with an appropriate phase factor that represents the position of atom j in the cell. On the other hand, we see from Figs. 2.8 and 2.6 that the phase grating must be sampled at all spatial frequencies and not only at those compatible with the reciprocal lattice, in order to be able to describe scattering to areas in between the Bragg peaks. This is in conflict with the definition of MASA in Eq. (2.31), being defined only for spatial frequencies allowed in the cell used for the DFT calculations. Hence, MASA can only be used in combination with the ideal crystal model yet.

One way out of this conflict could be the use of approximate DFT calculations, such as DFT tight-binding approaches [105], in order to save computational resources and to allow for larger supercells. Another possibility is to generate large supercells with thermal and static disorder, and to cut out three-dimensional patches of smaller cells which are capable for full DFT calculations. Recently, implementation of DFT results in multislice simulations has been reported [106, 107, 108], but it seems that no application to statistical disorder has yet been made. To this end, the supercell potential can be derived by merging all patches together under appropriate boundary conditions for the continuity of the electron density and its derivative. However, imaging and diffraction techniques used in this work are based on the accurate simulation of Bragg beams only, so that the MASA approach is sufficient here. Nevertheless one can argue whether MASA, derived for ideal crystals, are still valid if atom positions are subject to SAD. As to structure factors for the InGaNAs system, this atomistic treatment of bonding has been found to be in best agreement with full DFT by Müller et al. [7], as will be explained further in chapter 4.

Nothing was said so far concerning experimental verification of DFT or VFF results. The reader is referred to chapter 3 or Refs. [5, 109, 6, 110] for the former, and to chapter 4 or Refs. [7, 111, 112] for the latter.

2.7.2 Significance of MASA

From Fig. 2.4 it appears subtle to stress the importance of bonding since MASA differ only marginally from isolated atom ASA. However, to examine the effect of bonding on diffracted beam intensities, rather structure factors than individual MASA are important. Let us therefore consider kinematical scattering only to gain a quick insight to the impact of bonding: Diffraction patterns of specimen orientations near zone axis [001] contain only reflections where h, k, l are all even. Then, MASA are real and we do not need to take care about the imaginary part of MASA or their dependence on direction. For example, we find

$$V_{400}^{GaAs} = 4 [f_{Ga}^{GaAs}(7.08/\text{nm}) + f_{As}^{GaAs}(7.08/\text{nm})] \approx 4.73 \text{ V}$$

for the 400 structure factor in GaAs using MASA, whereas isolated atom ASA [75] give a value of 4.75 V. As kinematical scattering is considered here, expected intensities I_{400} are proportional to the structure factors squared, resulting in a ratio of 1.01 for $I_{400}^{MASA}/I_{400}^{ISO}$, that is, only 1% deviation. In striking contrast, we find a value of 0.6 for $I_{200}^{MASA}/I_{200}^{ISO}$, that is, 40% difference. This is because

$$V_{200}^{GaAs} = 4 [f_{Ga}^{GaAs}(3.5/\text{nm}) - f_{As}^{GaAs}(3.5/\text{nm})] \approx -0.4 \text{ V} \quad (2.55)$$

in case of MASA. Here, the structure factor itself is very small because it depends on the difference of ASA for gallium and arsenic, respectively. Hence, a small difference between MASA and isolated atom ASA can mean a large relative error for Bragg intensities.

In fact, the 200 reflection is of fundamental importance in composition quantification in zinc blende semiconductor nanostructures because its intensity depends strongly on composition according to Eq. (2.32). It is therefore essential to account for bonding when evaluating 200 dark field or fringe contrast, since relative errors for compositions in an InGaNAs quantum well may rise to a few tens of percent, as will become obvious in chapter 4.

2.7.3 Significance of SAD

Using VFF, it was shown in section 2.6.2 that the magnitude of SAD can become comparable to that of thermal displacements. By frozen lattice simulations, it was found that SAD leave characteristic fingerprints in the Bragg peak profile and increase the intensity of the diffuse background in diffraction patterns, which is in accordance with analytical calculations in Ref. [59]. That SAD and TDS have different physical origins is not only expressed by the occurrence of diffuse peaks in diffraction patterns in case of SAD, but can also be seen from the fact that SAD do not simply obey a Debye-Waller damping scheme, which differs from expressions derived in Refs. [52, 59]. This means that it is not sufficient to know the mean SAD of one atomic species and to derive an appropriate damping factor. Instead, large supercells of typically 10^6 atoms (containing SAD) are used to calculate structure factors, on which two remarks are important. First, Rosenauer et al. [9] demonstrated that it is possible to express the overall influence of SAD by correction factors applied to (M)ASA. In this way, a compact representation of the impact of SAD can be given, however, for each individual reflection. Second, it was shown by Glas [8] that SAD can significantly affect structure factor phases, an aspect which is systematically studied for InGaNAs alloys in Ref. [7] and in chapter 4.

Just as for TDS, a direct consequence of Huang scattering is a weakening of Bragg intensities which is not accounted for in absorptive potentials for conventional Bloch

wave simulations. In contrast to the derivation of TDS absorptive form factors which exploit the fact that the distribution of displacements is exactly Gaussian, absorptive form factors for Huang scattering can only approximately be given by assuming Gaussian SAD statistics. However, the model introduced in section 2.6.4, which adds absorptive form factors (e.g., according to Ref. [75]) for Huang scattering to ASA, produces the correct damping of pendellösung amplitudes with respect to configuration-averaged full multislice simulations. It is nevertheless understandable that no exact congruence is reached between Bloch wave and frozen lattice simulations: Opposite to TDS, displacements are not exactly represented by Gaussian statistics which may be the reason for this, but it should be noticed that the exact [001] zone axis case considered here involves a comparably large number of beams, resulting in strong dynamical effects among them.

It must be stressed that the physical nature of thermal and static disorder is very different. Electron scattering at SAD remains an elastic process which especially is time-independent and where each incident electron sees the same crystal, being opposite to TDS. In both cases, we shall derive simulated results from ensemble averages. However, for the TDS case this is justified because we can assume that the crystal indeed occupies each vibrational state during illumination in the range of seconds. In the SAD case, the strain field is persistent in practice and averaging over many unit cells and/or configurations originates from the lack of knowledge as to the distinct form of the displacements. It could be interesting to explore this issue by electron holography. Theoretical [97] as well as experimental [113] work indicates that side bands in electron holograms are perfectly energy filtered, whereas the centre band suffers contrast decrease. Static disorder is neither source for inelastic scattering nor time-/configuration dependent, so that recording, e.g., a GaNAs/GaAs quantum well with preferably high nitrogen content, together with parts of the GaAs substrate could leave SAD-specific contrast in the side band.

2.8 Summary and conclusions

The present chapter provided fundamentals for contemporary simulation of elastic scattering of high energy electrons for application in TEM. It has been shown that electron redistributions due to chemical bonding can be obtained by density functional theory (DFT), whose basic principle for the calculation of electron density and interatomic forces has been explained. Composition-dependent modified atomic scattering amplitudes (MASA) for quaternary zinc-blende $\text{In}_x\text{Ga}_{1-x}\text{N}_y\text{As}_{1-y}$ have been calculated by DFT and differences to isolated atom data have been worked out. The MASA concept, as introduced for ternary $\text{In}_x\text{Ga}_{1-x}\text{As}$ by Rosenauer et al. [9], has been reviewed. It is designed to describe bonding in the framework of an atomistic approach. Consideration of phases and amplitudes of atomic scattering amplitudes for several reflections has shown that largest impact of bonding is on low-order reflections. Furthermore, a review of strain energy minimisation using valence force field methods according to Keating [31] was given. Thermal disorder and atom size effects in $\text{In}_x\text{Ga}_{1-x}\text{N}_y\text{As}_{1-y}$ have exemplarily been investigated by both multislice and Bloch wave methods, which have been reviewed briefly. In this respect, comparison of pendellösung plots has motivated the definition of absorptive form factors which add to thermal ones and account for Huang scattering losses to the background of diffraction patterns. Inclusion of both bonding and static atomic displacements (SAD) in the simulation of high-resolution TEM images is realised by calculating structure factors from atom positions in strain-relaxed supercells in combination with MASA, where structure factors are only evaluated at spatial frequencies compatible with the Bravais

cell.

In conclusion, both SAD and bonding are to be accounted for when low-order reflections are involved, so as to simulate respective Bragg intensities or conventional high-resolution TEM images. It is, however, sufficient to solely account for SAD if high-angle scattering is to be analysed, as it is the case in high-angle annular dark field scanning TEM.

Chapter 3

Measurement of structure factors and Debye parameters by electron diffraction

3.1 Introduction

Evaluations using modern measurement techniques in the field of transmission electron microscopy (TEM) involve simulations as an essential part. Besides the propagation of the electron wave through the optical system of a TEM, any method must cope with the realistic treatment of electron-specimen interactions. Additionally, comparison between experiment and simulation requires knowledge of actual imaging conditions, such as thickness, crystallographic orientation and temperature of the specimen. However, these outer parameters may either be measured or relegated to marginal importance by choosing optimised imaging conditions.

For the simulation of Bragg intensities, both Bloch wave and multislice methods lead to identical results. In methodological respect, these approaches treat high-energy electron scattering dynamics exactly. Physically plausible results will nevertheless only emerge in case correct scattering potentials enter the simulation. Presently most of the simulations rely on atomic scattering amplitudes (ASA) that are usually obtained from numerical calculations for isolated atoms as published in, e.g., Refs. [75, 78]. In the Debye-Waller damping limit, ASA are furthermore altered by the Debye-Waller factors with Debye parameters from, e.g., Gao and Peng [80].

During the past decades, density functional theory (DFT) has offered impressive insight to solid state properties from a theoretical point of view and yields ab-initio data for crystal potentials [9] and Debye parameters [81]. One should, however, bear in mind that the experimental verification should keep pace with new theoretical data as focused on in chapter 2. This chapter therefore deals with the *measurement* of low-order structure factors and Debye parameters by electron diffraction.

TEM methods for the measurement of these quantities traditionally involve the refinement of convergent beam electron diffraction (CBED) patterns [114, 51, 6]. However, quantitative CBED requires not only advanced experimental facilities such as energy filters, but also time-consuming simulations for the refinement procedures, especially for crystals with large unit cells. For the refinement of crystal structures, these circumstances have motivated the development of the parallel beam electron diffraction (PBED) technique and the program package ELSTRU by Jansen et al. [115]. In the PBED case,

recorded Bragg intensities can be calculated by only one simulation per refinement cycle, so that a modern PC is usually sufficient. Furthermore, Jansen et al. have shown that, under certain circumstances, energy filtering is not necessary for PBED structure refinement [116].

In this chapter, a method to measure structure factors and Debye parameters from PBED patterns is presented. Bloch wave refinement routines have been developed in which specimen thickness, specimen tilt, structure factors and Debye parameters can automatically be optimised simultaneously using an arbitrary number of diffraction patterns to obtain best agreement between experimentally recorded and simulated Bragg intensities.

The PBED method is first applied to the low-order 200 structure factors of GaAs and InAs in order to study bonding effects as predicted by DFT in section 2.3.5 and by the modified ASA (MASA) concept published by Rosenauer et al [9]. Second, reflections of higher-order Laue zones (HOLZ) are used to refine Debye parameters for GaAs at liquid nitrogen temperature, which are then compared with DFT values from Schowalter et al. [81].

To allow for a consolidated discussion of the PBED method, CBED measurements of the 200 structure factor and Debye parameters for GaAs are also presented. Gallium arsenide was chosen as one target material not only because DFT predicts large impact of bonding as was shown in section 2.7.2 and by Rosenauer et al. [9], but also because comparison with experimental results of several groups is possible [117, 6, 110, 118]. The material InAs was chosen for two reasons: First, to verify that the accuracy of PBED measurements of the 200 structure factor is sufficient to detect also relatively small bonding effects. Second, verification of the MASA concept for both GaAs and InAs has important consequences on composition evaluation by lattice fringe analysis (CELFA [34]) applied to $\text{In}_x\text{Ga}_{1-x}\text{As}$.

This chapter is organised as follows. First, experimental details on diffraction pattern acquisition are documented in section 3.2. This is followed by two larger sections on PBED and CBED. Besides results themselves, the former contains a detailed description and test of the PBED method, and it provides rules to recognise physically plausible refinements. The latter profits from extensive literature on CBED, so that only a brief methodical summary is given. In addition to refinement results, accurate measurements of the TEM acceleration voltage are presented. Finally, section 3.5 contains a comparison of the PBED and the CBED method and a discussion of the results, before important conclusions will be drawn in section 3.6.

Outline of electron diffraction techniques

It was the purpose of chapter 2 to describe Bragg scattering at real crystals in the framework of the ideal crystal approach by introducing various corrections to structure factors. On the one hand this makes structure factors quite a complicated quantity. On the other hand, the fact that structure factors depend on a lot of physical quantities provides a way to access atom positions, accelerating voltage, lattice parameters, Debye parameters, static atomic displacements (SAD) and atomic potentials in diffraction experiments. Additionally, sections 2.4 and 2.5 revealed dependence of diffraction intensities on specimen thickness and -orientation. It is obvious that an experiment which aims at the measurement of one of these effects must be designed carefully, so as to eliminate the influence of all other parameters. The reader should therefore not be surprised that the

pure binary compounds GaAs and InAs are studied here, whereas InGaNAs alloys are of interest in following chapters on composition quantification. For both bulk GaAs and bulk InAs atom positions and lattice parameters are known and SAD are absent, so that acceleration voltage, specimen thickness and -orientation, bonding and Debye parameters govern diffracted intensities. Reliable values for the acceleration voltage can either be taken from the nominal values of modern TEM or measured independently (both is done in the present work). The specimen orientation can easily be measured from the intersection of Kikuchi bands (see Fig. 2.6), HOLZ line symmetry or from the Laue circle centre. Innermost reflections are most sensitive to bonding (see Fig. 2.4), whereas outermost (HOLZ) reflections are most sensitive to temperature (see Eq. (2.6)). Strong reflections in between may be used to reliably guess an initial thickness of the specimen. The term "initial" expresses that the final result of the measurements is obtained via numerical refinement. This is necessary because principally all parameters indeed have more or less strong influence on the whole diffraction pattern, by, e.g, dynamical diffraction.

As to the Mott-Bethe relation (2.3, 2.12), X-ray and electron structure factors are not independent, and both communities are concerned with their measurement. However, one advantage of electron over X-ray diffraction is that electron structure factors of low order are significantly more sensitive to bonding than their X-ray equivalent [47, 119]. For GaAs, the relative difference between the 200 X-ray structure factor from DFT [9] and the structure factor for isolated atoms [75] is about 9%, whereas it is 27% for 200 electron structure factors. For InAs, bonding makes a difference of only 0.3% in the X-ray case, but 2.3% in case of electron structure factors, which stresses the importance of electron diffraction for the investigation of bonding. Another practical advantage of electron diffraction is the use of electron optics in TEM to form nanometre-sized probes. In this way, the probability that crystal defects, bend contours or thickness gradients contribute to the diffraction pattern can be reduced drastically.

Because (to the best knowledge of the author) PBED is here used for the measurement of structure factors for the first time, a brief presentation of the family of structure factor measurement techniques by TEM appears appropriate. However, a variety of reviews also exists [47, 120, 121].

The first technique to be mentioned goes back to the 1960s (e.g. Uyeda [123]) and, if applicable, is said to be the most accurate one for structure factor measurement. It exploits Eq. (2.44) for a two-beam diffraction geometry with beam \mathbf{g} strongly excited, and one weak beam $\mathbf{g}/2$ treated via Bethe potentials. For proper electron wavelength λ or, equivalently, a critical acceleration voltage, $A_{\mathbf{g}\mathbf{0}}^{E'} = 0$ results which states a relation between $U_{\mathbf{g}}$ and $U_{\mathbf{g}/2}$. At this voltage, the diffracted intensity of beam \mathbf{g} vanishes (3-beam case) or at least passes a minimum (many beam case), independently of specimen thickness. Unfortunately, this effect occurs only if $U_{\mathbf{g}} < U_{\mathbf{g}/2}$ which is not satisfied in our case, where U_{400} is nearly an order of magnitude larger than U_{200} . Note that a beam with a large structure factor may appear weak when the excitation error is large. An example for Copper is shown in Fig. 3.1 (a).

A second method utilises dynamical scattering effects on the intersection of HOLZ lines in a CBED disc. At the crossing, incidence is such that three beams are in Bragg condition simultaneously. Depending on the structure factors, strong multiple scattering is present at this point, meaning that the probability for an electron to be re-scattered from the HOLZ reflection to one of the two other reflections is very large (which is known as the Renninger effect in X-ray scattering). Thus, HOLZ line intensity is strongly reduced at the intersection point, where the two HOLZ lines modify to hyperbolae with a gap in

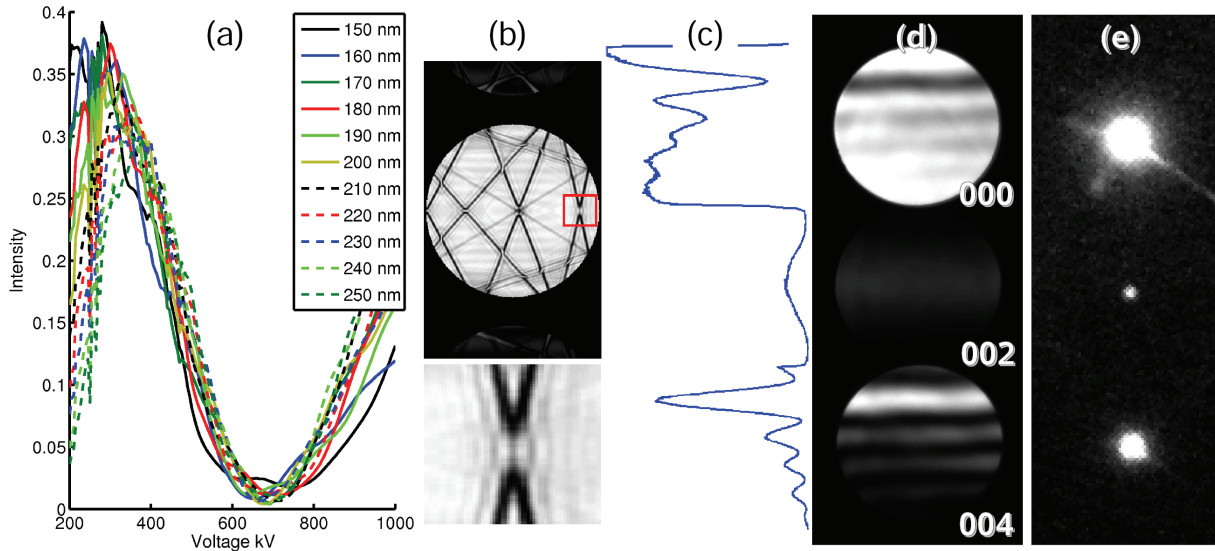


Figure 3.1: Graphical outline of electron diffraction methods for structure factor refinement. (a) Bloch4TEM [37] simulation of the critical voltage for the 400 intensity in Copper as observed by Lally et al. [122]. The minimum position is robust against specimen thickness, as differently coloured graphs show. (b) Bloch4TEM [37] simulation of HOLZ line splitting in GaAs. Instead of taking straight course, HOLZ lines split to hyperbolae with a gap. (c,d) Experimental GaAs CBED pattern, part (d) serving as experimental data for Tsuda's method [51], whereas part of it is used by Zuo and Spence [6], as rocking curves in (c) show. (e) Same as in (d), but acquired under parallel illumination. Integrated peak intensity from this pattern builds the data for PBED refinements.

between which is used to determine structure factors. This simple method is, however, less accurate because of many-beam dynamical effects which additionally influence the gap [47]. The simulation in Fig. 3.1 (b) illustrates the principle of HOLZ line splitting.

The CBED evaluations in this chapter have their origin in a third approach, whose importance raised enormously with computational efficiency. Starting in 1967, Goodman and Lehmpfuhl [124] studied CBED patterns quantitatively via comparison of rocking curves with multislice simulations. This was not only done to test the (at that time) new multislice algorithm, but also to measure the 200 structure factor of MgO which is sensitive to ionisation of atoms. Since then, CBED techniques branched into several sub-disciplines, namely systematic row and two-dimensional analysis as shown in Figs. 3.1 (c) and (d), respectively. Famous representatives of the former approach are, e.g., Zuo and Spence who developed Fortran code for the simulation of CBED patterns [47] and for automated structure refinement using the simplex method [125]. Having initially been applied to GaAs [6], this method has found a vast amount of applications, the measurement of bonding in wurtzite GaN [126] being the most recent one. Fitting a single rocking curve in a CBED pattern is on the one hand well justified, because intensity distribution in a systematic row is often only one-dimensional. On the other hand, most of the experimental data is ignored in this case, motivating the approach of Tsuda and Tanaka [51] where full two-dimensional CBED discs are subject to the refinement. In this way, refinement of a single CBED pattern can be used to determine many parameters simultaneously, as the most recent application to atom positions, atomic displacement parameters, low-order structure factors, space group and lattice parameters of the low-temperature phase of FeCr_2O_4 has demonstrated [127]. Convergent beam electron diffraction work in this

chapter is based on this approach, and Tsuda's program package MBFIT (Many-beam dynamical calculations and least-squares fitting) has been used.

It is worth mentioning that PBED, depicted in Fig. 3.1 (e), exploits the full intensity of a diffracted beam as is the case for Tsuda's method. This is promising with respect to counting statistics, especially if weak reflections are subject to investigations, as in the present study. Typical data for each of the five methods sketched here is composed and explained in Fig. 3.1.

3.2 Experimental

The specimen used for both the PBED and the CBED work was cut from a standard GaAs wafer in such a way that the surface normal of the specimen and one of the $\langle 010 \rangle$ directions include an angle of 31° . For the PBED measurement of Debye parameters, GaAs was prepared in $\langle 010 \rangle$ zone axis. After mechanically grinding the specimen by the tripod method, an Ar^+ ion polishing facility (Gatan precision ion polishing system, Model 691) was used for final etching with an ion energy of 3.6 keV and incident angles between 3° and 5° . All diffraction patterns have been recorded at a Titan 80/300 facility operated at 300 kV.

3.2.1 PBED pattern acquisition

Condenser and diffraction lens settings to approach nearly parallel illumination conditions are described in section 3.3.1, in addition to optimum probe diameter considerations. For the acquisition of PBED patterns in this work, a focused ion beam facility (FEI Nova 200 NanoLab) was used to prepare a suitably small C2 aperture with a diameter of $8 \mu\text{m}$ from a thin platinum foil.

Structure factor measurement. Eleven PBED patterns of GaAs and 13 PBED patterns of InAs have been recorded on Imaging plates (Ditabis) with exposure times in the range of 5-10 s, without energy filtering. Six zero loss energy filtered GaAs PBED patterns have also been recorded with a post-column Gatan Imaging Filter (GIF Tridiem 863) on a $2\text{K} \times 2\text{K}$ CCD camera. A slit width of 10 eV and exposure times between 1 s and 5 s have been used. Amongst all exposures, thickness and orientation were varied slightly by different beam shift and specimen tilt settings near zone axis $[053]$ (GaAs) and $[\overline{053}]$ (InAs). Since both GaAs and InAs are polar crystals, neither preparation nor spot diffraction patterns alone can assure that the intended zone axis is definitely present, since PBED patterns along incidence directions with permuted and/or inverted particular indices may look nearly identical. For this reason, CBED patterns have additionally been recorded at a thicker specimen region with one of the 200 reflections in Bragg condition. Polarity can then be measured by evaluating the HOLZ line pattern and -contrast. This can either be done via a method described by Taftø and Spence [128] by considering the coupling between the weak 200 reflection (in Bragg condition) and weak odd-index reflections, or by qualitative comparison with simulated CBED patterns, as was done in this work in section 3.4.2.

Debye parameter measurement. Seven GaAs diffraction patterns which were oriented as close as possible in zone axis $\langle 010 \rangle$ have been recorded on Imaging plates (Ditabis)

with exposure times 0.5 s and 1 s. A Gatan double tilt cold stage holder (Model 636) filled with liquid nitrogen (77 K) was used to cool the specimen to a temperature of 99 K, as measured by the cold stage controller. No energy filtering was used.

3.2.2 CBED pattern acquisition

All CBED patterns have been recorded with incidence directions near the zone axis [053] and the $\bar{2}00$ reflection strongly excited. A C2 aperture with a diameter of 100 μm was used and the probe was focused into the specimen in the *Probe-microprobe* setting of the condenser lens system. Eight zero loss energy filtered CBED patterns have been recorded using a GIF Tridiem 863 on a 2K \times 2K CCD camera. One of these patterns was taken at a thicker region in order to achieve significant deficiency HOLZ line contrast for the measurement of the high voltage as described in section 3.4.2. A slit width of 10 eV and an exposure time of 0.25 s were used. The camera length was selected such that the 000, $\bar{2}00$ and $\bar{4}00$ discs fill the CCD chip. These three discs are sufficient because they contain all information needed: the fringes in $\bar{4}00$ are highly sensitive to the specimen thickness, the intensity of $\bar{2}00$ is significantly influenced by the 200 structure factor, the HOLZ line pattern inside the discs can be used to measure orientation and polarity of the crystal. One additional CBED pattern has been recorded with a smaller camera length, in order to measure Debye parameters from the intensity of HOLZ reflections.

3.3 Parallel beam electron diffraction

3.3.1 Description of the method

Central features of the PBED method are

1. Acquisition of diffraction patterns from nanometre-sized areas using a parallel beam,
2. Extraction of integrated Bragg intensities and the subtraction of background,
3. Estimation of reliable initial thicknesses for the refinement, and
4. Bloch wave simulation of PBED patterns, as well as a least-squares refinement of desired properties.

These steps are sketched in Fig. 3.2. Detailed analysis of the reliability of both the background subtraction using the program GREED and initial thickness guesses will be given below.

The necessity of nanodiffraction can be understood from the fact that thickness and orientation vary locally at real specimens. In this respect, we profit from experiences collected with the program multislice least-squares (MSLS [115]) where it was found that probe diameters around 10-15 nm are well suited for quantitative refinements. As too small probes will lead to artefacts in the shape of Bragg peaks, a lower limit for the probe diameter is derived in this section. Furthermore, the influence of errors induced by a slight beam convergence and background subtraction is examined quantitatively and rules for the identification of physically plausible initial guesses are deduced. Fundamental to all simulations and refinements is the Bloch4TEM software, which is initially briefly described.

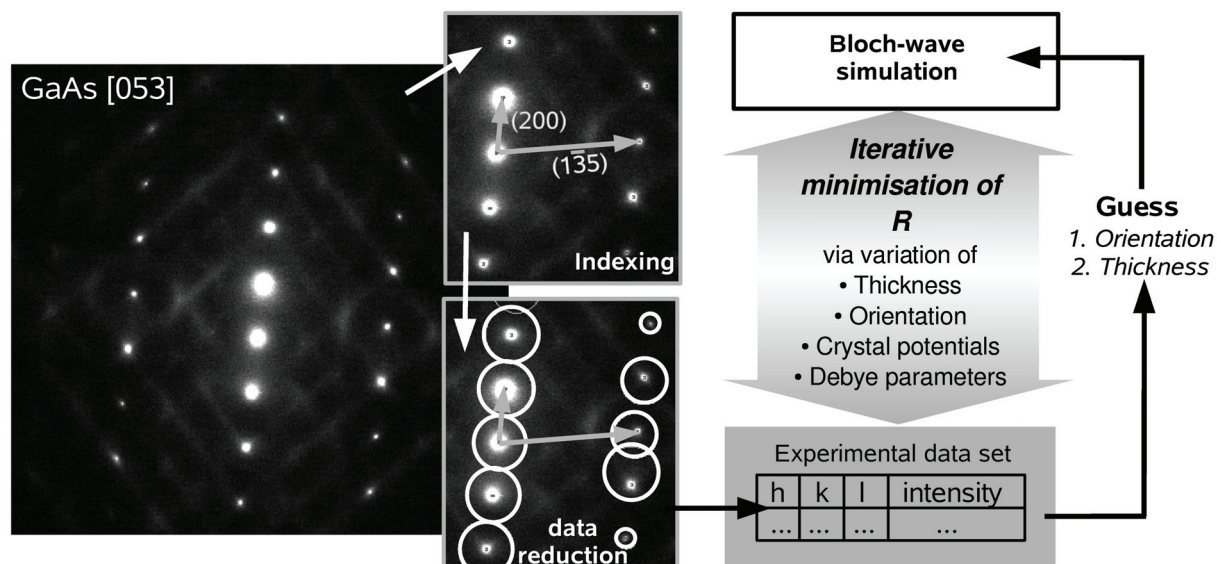


Figure 3.2: Schematic showing the principle of the PBED method. The left part visualises the data reduction using the program GREED, whereas the right part depicts the interplay of experiment and simulation (refinement procedure).

The Bloch wave refinement routine Bloch4TEM

The program Bloch4TEM [37, 5] was developed in which the Bloch wave theory described in section 2.4 was implemented in MATLAB routines. The program can use ASA and/or absorptive form factors from Weickenmeier and Kohl [75] or Bird and King [76]. Furthermore, ASA according to Doyle and Turner [78] and MASA calculated from DFT due to the concept of Rosenauer et al. [9] as described in section 2.3.5 may be used.

As to electron diffraction work, the program can simulate PBED as well as CBED patterns. Additionally, Kikuchi/HOLZ hyperbolae are implemented in kinematical approximation, which is useful for quick analysis of Kikuchi patterns concerning polarity, zone axis identification and dependence of HOLZ line intersections on accelerating voltage. Where possible, the program code is adapted to parallel computation on multiple processors using the MatlabMPI implementation of Kepner and Ahalt [129]. This especially increases computational efficiency of CBED simulations and PBED refinements. The latter profits from parallelisation in case structural parameters are refined using several experimental data sets simultaneously.

Bragg intensities are read from one ascii-file for each data set which contains the integrated, background-corrected intensity for all significant reflections. The program is able to refine specimen thickness and -orientation, as well as moduli of arbitrary structure factors and the three individual components of the Debye tensor \mathcal{B} along the crystallographic basis vectors. (That is, coordinate system is to be chosen such that \mathcal{B} is diagonal.) Arbitrary constraints can be defined, so as to refine either symmetry related structure factors or components of \mathcal{B} to the same value. Another important quantity is the scaling factor s , which is used to scale simulated intensities with respect to the number of counts recorded in experiment. It is thus equal to the ratio of all summed significant experimental and the corresponding summed simulated intensities and can be adjusted automatically after each refinement cycle.

Congruence between experimental and simulated intensities I^e and I^s is quantified by

the R-value [115]

$$R = \frac{\sum_k \sum_i^{N_k} (I_i^e - s_k I_i^s)^2}{\sum_k \sum_i^{N_k} (I_i^e)^2} \quad , \quad (3.1)$$

where the sum over k runs over all data sets involved in the refinement. The sum over i includes all significant reflections of data set k which are sensitive to the quantity to be refined. Note that scaling factors s_k may be different for each set, as are thickness and orientation. The R-factor can either be minimised using the simplex or the Levenberg-Marquardt algorithm, depending on which MATLAB toolboxes are available. Please be aware of the similarity to the MSLS principle [115] which uses the same definition of R as in Eq. (3.1), except that reflection weights are additionally introduced. Depending on experimental conditions, results obtained from MSLS refinements, such as Debye parameters or the specimen thickness, may be used as input for a post refinement of structure factors using Bloch4TEM, provided that the MSLS results are robust against the expected change of structure factors in question.

It is important to keep in mind that structure factors $F_{\mathbf{g}}^E$, crystal Coulomb potentials $V_{\mathbf{g}}^E$ in Volts, or crystal potentials $U_{\mathbf{g}}^E$ in nm^{-2} enter Bloch wave simulations relativistically corrected, as indicated by superscript E . These quantities are connected by

$$U_{\mathbf{g}}^E = \frac{2em_e}{h_P^2} \cdot V_{\mathbf{g}}^E = \frac{1}{\pi\Omega} \cdot F_{\mathbf{g}}^E \quad , \quad (3.2)$$

and results will be expressed in all three terms because of their common use in the community. Equation (3.2) contains Planck's constant h_P , the charge e and the mass m_e of an electron, and the unit cell volume Ω . Potentials will be given also without relativistic correction to make them independent of the acceleration voltage (and thus experiment), whereas the thermal atomic displacement parameters are inherent quantities of the measurements and will be given in terms of Debye parameters B defined in connection with Eq. (2.6).

In the following, $U_{\mathbf{g}}$ is referred to as the crystal potential. Furthermore, we will use the term *200 potential* substitutionally for all ± 200 , ± 020 and ± 002 potentials, since they are all equal and treated as constraint during the refinements. Results of structure factor measurements will also be converted to X-ray structure factors $X_{\mathbf{g}}^k$ according to Eq. (2.28).

For the decision which beams should be included in the calculation, Bloch4TEM proceeds as described at the end of section 2.4. In PBED work here, all results are converged with respect to the number of beams included exactly, that is, no use of Bethe corrections is made. In this way, it is assured that kinematically forbidden reflections may also be excited by multiple scattering. Moreover, contributions of HOLZ may be excluded or incorporated by calculating the projection of each vector \mathbf{g} on the zone axis. Note that the matrix $\underline{\underline{A}}^E$ or $\underline{\underline{A}}^{E'}$ shows no symmetries in the present case of non centro-symmetric crystals with absorption. Throughout this chapter, the term *absorption* refers to losses of electrons in the Bragg scattered beams to the diffuse background in the diffraction pattern caused by thermal diffuse scattering (TDS) processes [76, 75], as analysed in section 2.6.1.

According to Eq. (2.43), diffracted beam amplitudes, phases and intensities are computed from the scattering matrix $\underline{\underline{S}}$ and thickness refinement is performed by iteratively optimising matrix $\underline{\underline{\varepsilon}}(z)$. Refinement of specimen orientation optimises \mathbf{k}_0 on the main diagonal of $\underline{\underline{A}}^E$ or $\underline{\underline{A}}^{E'}$, as defined in Eq. (2.41). One structure factor occurs frequently in

$\underline{\underline{A}}^E$ or $\underline{\underline{A}}^{E'}$ due to multiple scattering, and respective entries are changed during optimisation. In contrast, Debye parameter refinement means a re-calculation of the full matrix before substitution of crystal potentials to be refined.

Crystal potential Fourier components generally take the form of Eq. (2.11). However, we consider only sphalerite-type systems in this chapter and restrict refinements to crystal potentials corresponding to reciprocal lattice vectors having all even components. In this case, Eq. (2.11) simplifies to

$$V_{\mathbf{g}} = \text{Re}(V'_{\mathbf{g}}) + i\text{Re}(W_{\mathbf{g}}) = \text{Re}(V_{\mathbf{g}}) + i\text{Im}(V_{\mathbf{g}}) \quad , \quad (3.3)$$

and $U_{\mathbf{g}}$ accordingly, where relativistic correction was omitted. Thus the real part of $U_{\mathbf{g}}$ corresponds solely to $V'(\mathbf{r})$ and the imaginary part corresponds solely to $W(\mathbf{r})$, which separates electrostatic and absorptive contributions, respectively. To investigate chemical bonding effects, we therefore have to refine only the real part whereas we take the imaginary part from Ref. [75].

Practical considerations

Principally, the alignment of the condenser system to approach parallel illumination is straight forward: First, the diffraction lens should be focused on the objective aperture, which assures that the focal plane of the objective lens is imaged on screen. Second, Bragg spots should be focused by changing the condenser lens excitation by means of the C2 lens, because observation of sharp Bragg spots in the focal plane means parallel illumination. If the objective aperture is not exactly in the focal plane of the objective lens, a slight beam convergence will not be noticed because it is compensated by an overfocus of the diffraction lens. Therefore, a small beam convergence of 0.5 mrad was applied in the simulation of test patterns. Additionally, realisation of parallel illumination becomes more complicated if probes with diameters below 10 – 15 nm are required. On the one hand, smaller probes reduce the errors arising from locally varying specimen orientation and thickness gradients. On the other hand, plane wave incidence contradicts nanodiffraction experiments by definition. Note that selected area electron diffraction (SAED) can be critical due to lens errors occurring in the intermediate image. For this reason, the PBED pattern should rather be formed by small probes than by SAED.

To estimate the effect of the Bessel-like broadening of the Bragg spots with decreasing probe diameter, standard Bloch wave simulations of the object exit wave for GaAs crystals in [010] orientation have been performed. The effect of a finite probe diameter has been approximated by setting the exit wave function to zero outside a circular region as shown in Fig. 3.3(a), where a probe diameter of 3.5 nm was used. This treatment relies on the fact that we consider only thin specimens with thicknesses of a few tens of nanometres. Then, broadening of the beam inside the crystal may be negligible, so that the exit wave function will be nonzero only in a region comparably large as the probe size.

The corresponding diffraction pattern is shown in Fig. 3.3(b) in logarithmic scale. Obviously, Bragg intensities spread significantly around their Bragg position, which can lead to problems if Bragg spots and TDS background are to be separated. For GaAs crystals at 300 kV it was found that the extension of Bragg peaks is negligible for spot diameters above 5 nm.

From this we conclude that probe diameters between 5 nm and 15 nm are well suited for quantitative PBED, whereas the upper limit depends on the homogeneity of specimen thickness and -orientation in the illuminated region. This might be checked from case

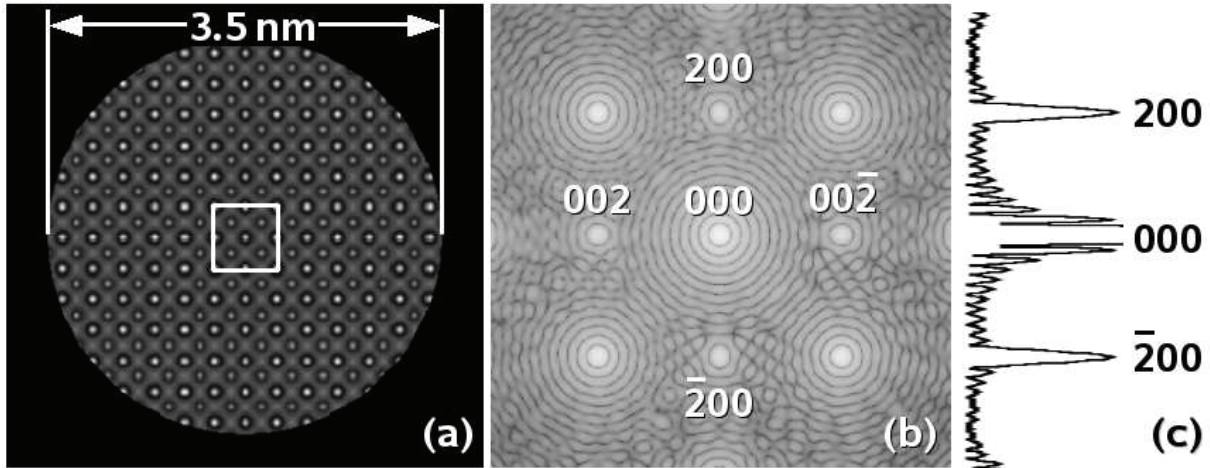


Figure 3.3: Simulations of the object exit wave amplitude (a) for a thickness of 20 nm and the corresponding diffraction pattern (b,c) in logarithmic scale in order to estimate a lower limit for the probe diameter. The white square marks a GaAs unit cell in [010] projection. In this case, a too low diameter of 3.5 nm was chosen because the Bragg peaks overlap significantly in a Bessel-like manner.

to case by looking at bending- and thickness contours in imaging mode. To come to the required probe diameter range, C2 apertures from 3 μm thick platinum foils using a focused ion beam facility were cut. In a FEI Titan 80/300, parallel probes being 12 ± 1.5 nm in diameter were achieved with a C2 aperture diameter of 8 μm . Further probe size measurements were carried out at a Philips CM 200 with a C2 aperture diameter of 5 μm , leading to a probe size of 7 ± 1.5 nm. This approaches the lower limit estimated above.

Estimation of systematic errors

The PBED method profits from the assumption of plane wave incidence where illumination of the specimen can be described by only one primary wave vector \mathbf{k}_0 . In this subsection, errors arising from the assumption of plane wave incidence are worked out by simulating realistic diffraction patterns and feeding them into the PBED data reduction and refinement procedure. A realistic probe in a TEM aligned for parallel illumination contains the effect of the spherical aberration of the condenser lens system, the cutoff of high spatial frequencies due to the micron-sized C2 apertures and a slight misalignment of the diffraction lens focus which leads to a slightly convergent beam, as described in the last subsection. This probe must then be propagated through the specimen by a multislice algorithm to take into account displacements of atoms due to their thermal movement. The frozen lattice [54] approximation as described in section 2.6.1 was applied here where these displacements are uncorrelated among atoms. This yields the TDS background in between the Bragg reflections, together with features like Kikuchi bands. Scattering factors were taken from Ref. [75], and the STEMsim software [33] was used for simulation.

Conditions for the frozen lattice simulation were similar to those of the actual measurements in section 3.3.2. For a FEI Titan 80/300 operated at 300 kV, a probe was simulated with a C_s value of 2 mm for the condenser lens system and a beam convergence of 0.5 mrad was applied, leading to a probe with a full width at half maximum of 10 nm. Three diffraction patterns for GaAs in zone axis [053] have been simulated

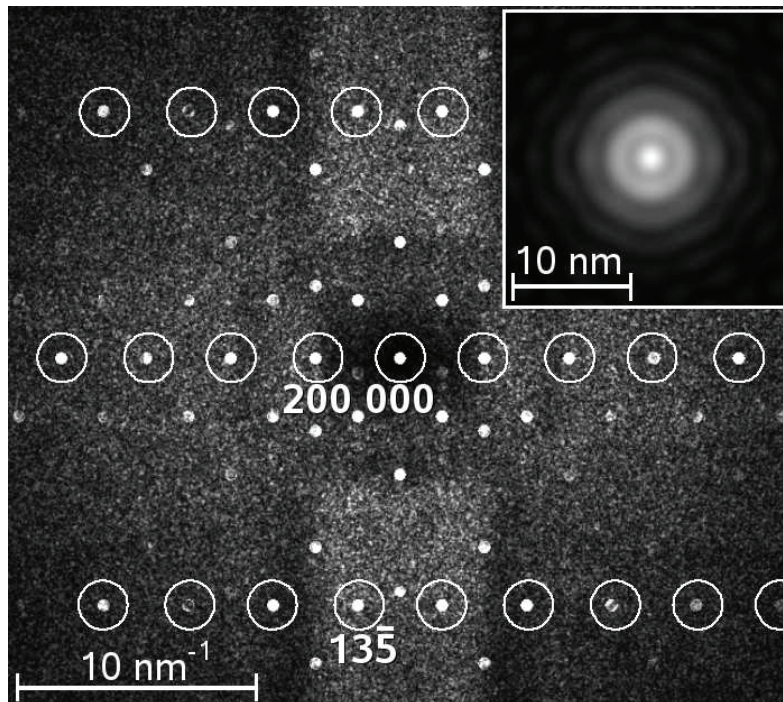


Figure 3.4: Frozen lattice simulation of a diffraction pattern (part) in $[053]$ zone axis. The inset shows the probe that was propagated through the sample. Encircled reflections belong to the zero order Laue zone (ZOLZ) and were used for data reduction with GREED. The scaling of intensities was adjusted such that the TDS background is visible. Usually HOLZ reflections are considerably weaker than the encircled ones.

with thicknesses of 13.19 nm, 23.08 nm and 32.96 nm, respectively. Debye parameters of $B_{\text{Ga}} = 0.7 \text{ \AA}^2$ and $B_{\text{As}} = 0.6 \text{ \AA}^2$ were chosen which correspond to a temperature of 300 K [81]. The lateral extension of the supercell was $40 \times 40 \text{ nm}^2$.

A part of the 32.96 nm simulation is shown in Fig. 3.4 with emphasis on the TDS background. Reflections belonging to the ZOLZ are encircled and form the experimental data set for the minimisation of R in Eq. (3.1). The respective Bragg intensities were extracted using the program GREED (Graphical extraction/reduction of electron diffraction data), which is part of the ELSTRU software package as MSLS [115]. Main steps of the GREED routine are identification and indexing of Bragg peaks, followed by the data reduction which subtracts the local background. The background level is found by increasing the radius of a circle around each peak until changes of intensity on the circle fall below a threshold value. In this way, Bragg scattered intensity less TDS background is obtained, which can directly be compared with Bloch wave simulations using TDS absorptive form factors as has been shown in section 2.6.1. The primary beam has been excluded from this procedure because its intensity is usually not available in experiment due to a saturation of the recording medium. An inset in Fig. 3.4 depicts the probe that was propagated through the sample to illustrate that the illumination is not homogeneous throughout the specimen surface. Besides the encircled ZOLZ peaks, HOLZ reflections are present in Fig. 3.4, so that HOLZ are included in all Bloch wave simulations.

The R -value was computed as a function of the specimen thickness (thickness scan) for each data set to find initial thickness guesses for the refinements. The curves $R(t)$ are shown in Fig. 3.5. In this case, already the correct zone axis orientation and also the scattering data from Ref. [75] were used in the Bloch4TEM simulation. From Eq. (3.1) we

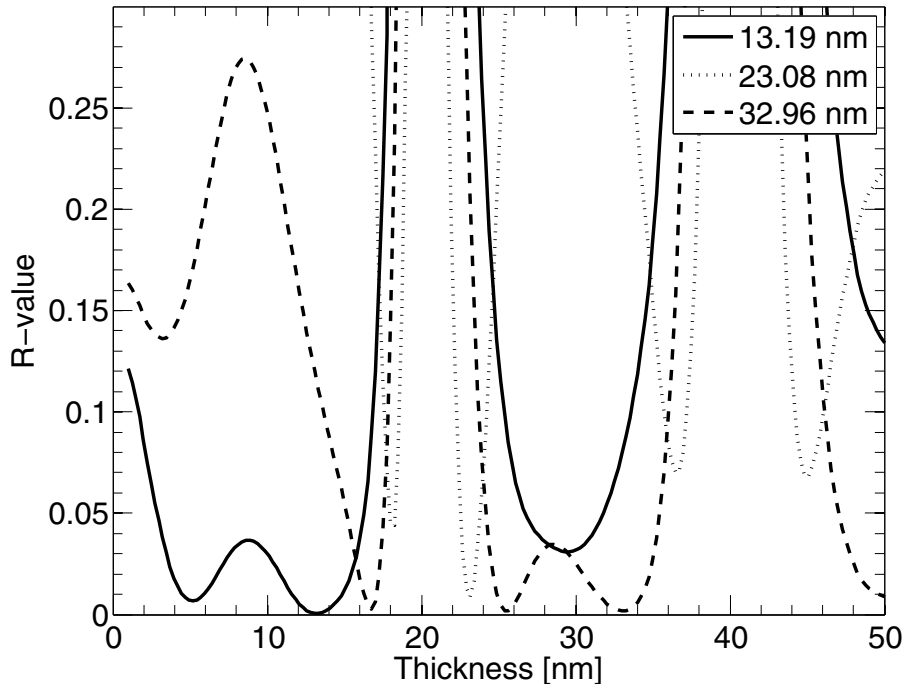


Figure 3.5: Thickness scans for the three simulated data sets. Possible initial thicknesses for the refinements correspond to minima positions of the $R(t)$ curves. The legend shows the true thicknesses used in the frozen lattice simulations.

therefore expect the R -value to drop to zero for the thicknesses used in the frozen lattice simulations if the background subtraction in GREED was exact. For each of the three thickness scans, we see that this is indeed approximately the case, even if there are several comparably deep minima for the 32.96 nm simulation, a point that will be addressed later.

With an initial thickness derived from the thickness scan, the refinement of the thickness, the centre of Laue circle (COLC) and the real part of the 200 potential was started. Initial values for the COLC and the crystal potential $\text{Re}(U_{200}^E)$ were equal to the true ones used in the frozen lattice simulation. This was done to study how accurately the quantities of interest in real measurements are represented at the minimum of the R -value. Starting thicknesses, refined quantities and the minimised R -values are listed in table 3.1. From the R -values we see that systematic errors, arising from background subtraction and from the assumption of plane wave incidence, raise the R -value less than 1 % in all three cases. To judge the quality of the refinements, one has to keep in mind that the optimisation takes

Table 3.1: Refinement results for the three simulated data sets. Column titles refer to the true thicknesses used in the frozen lattice simulation. Refinements started with thicknesses t_0 . Thickness, COLC and the 200 crystal potential were simultaneously refined for each data set separately. The last line lists the optimised R -value.

		13.19 nm	23.08 nm	32.96 nm
t_0	[nm]	13.07	23.16	33.01
t	[nm]	13.07	23.24	33.09
COLC		(0 0 0)	(0 0 0)	(0 0 0)
$\text{Re}(U_{200}^E)$	[nm ⁻²]	-0.576	-0.572	-0.556
R		0.1 %	0.8 %	0.20 %

place in a multidimensional parameter space, where several constellations of parameters may lead to the same R-value. In our case this space is five-dimensional if we include the scaling factor in the refinement, so that resulting thicknesses, COLC and potentials can differ from their true values. The refined thicknesses in table 3.1 differ 0.16 nm from their intended value in the worst case. The COLC never deviated more than $1 \cdot 10^{-5}$ reciprocal basis vectors from the true position which was (0 0 0). Finally, the largest inaccuracy of the crystal potential $\text{Re}(U_{200}^E)$ refinement occurs for the 13.19 nm simulation, where the result is 0.03 nm^{-2} below the potential used in the frozen lattice simulation of the diffraction patterns, which was -0.546 nm^{-2} . In view of the verification of the MASA model mentioned in the introduction, this accuracy is sufficient since we expect $\text{Re}(U_{200}^E)$ to be -0.426 nm^{-2} .

Ambiguity of refinement results

In practice, the situation is different from the case considered above because the refinement aims at determining low order structure factors whose values may be needed already for the thickness scan. Excluding the respective reflections from the thickness scan has proven to give the best results in this case. However, interaction of all scattered beams will still lead to inaccurate starting values for the thickness. For example, the deepness of the minima in Fig. 3.5 can depend on the magnitude of low order structure factors, so that the global minimum does not need to be the true one. To simulate this case, the thickness scans from Fig. 3.5 have been repeated with $\text{Re}(U_{200}) = -0.666 \text{ nm}^{-2}$ with the 200 intensities excluded from the computation of the R-value and the scaling factor. Thus we simulate the situation where the experimental data set corresponds to a crystal potential U_{200} that is 0.12 nm^{-2} larger than the potential used for the thickness scan. The resulting $R(t)$ curves are depicted in Fig. 3.6.

It can clearly be seen that several minima of comparable deepness occur because the information of the 200 beams is missing. But it also becomes obvious that there is a minimum close to the true position in all cases. In experiments, any of these minima may be the true one if the thickness is not measured separately by different methods. In the following, we will therefore discuss the plausibility of each of these possible initial thickness guesses and give rules to identify the physically reliable one.

It is in the nature of refinement procedures that the system is already well understood, so that only some parameters will be modified slightly. In our case, these parameters are the low order crystal potentials which are modified due to chemical bonding. However, scattering factors from Kohl and Weickenmeier [75] are assumed to be valid for higher momentum transfers. Therefore, the plausibility of refinement results or initial guesses can be checked by verifying that known quantities are reproduced. As an example, we will consider the possible initial guesses for the specimen thickness of the 32.96 nm simulation. From Fig. 3.6, seven possible starting thicknesses t_0 were derived from the R-value minima positions. For each of these thicknesses, the R-value was computed as a function of $\text{Re}(U_{400}^E)$ in a range $\text{Re}(U_{400}^E) \in [3 \dots 6] \text{ nm}^{-2}$. In these $R(U)$ curves, the R-value was computed from the 400 intensities only and plotted in Fig. 3.7 on logarithmic scale. The true real part of U_{400}^E used in the frozen lattice simulations is marked by the black triangle.

If the correct thickness and 200 potential entered the simulation of the $R(U)$ curves in Fig. 3.7, we would see a minimum at the position of the black triangle. But as the simulation of the $R(U)$ curves was performed with deviating 200 potential and thicknesses, the simulation must alter the 400 potential in order to reproduce the 400 intensities of the data set. In our case, $|\text{Re}(U_{400}^E)| \approx 8 \cdot |\text{Re}(U_{200}^E)|$ reveals that the 200 potential has

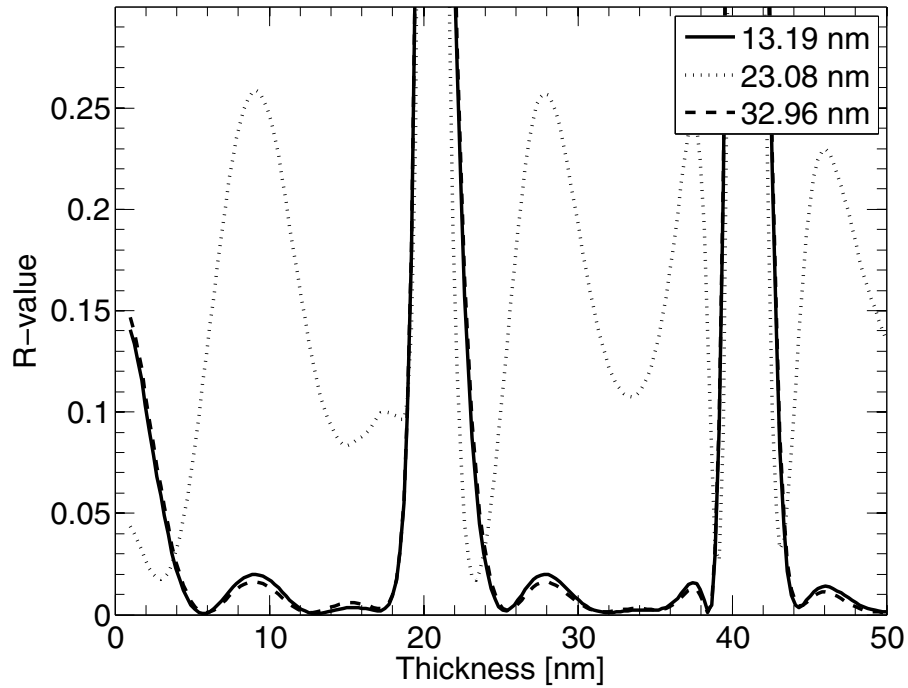


Figure 3.6: Thickness scans for the three simulated data sets analogous to Fig. 3.5, except that the 200 potential was set differently. Furthermore, the ± 200 reflections were excluded from the computation of the scaling and the R-value. The legend shows the true thicknesses used in the frozen lattice simulations.

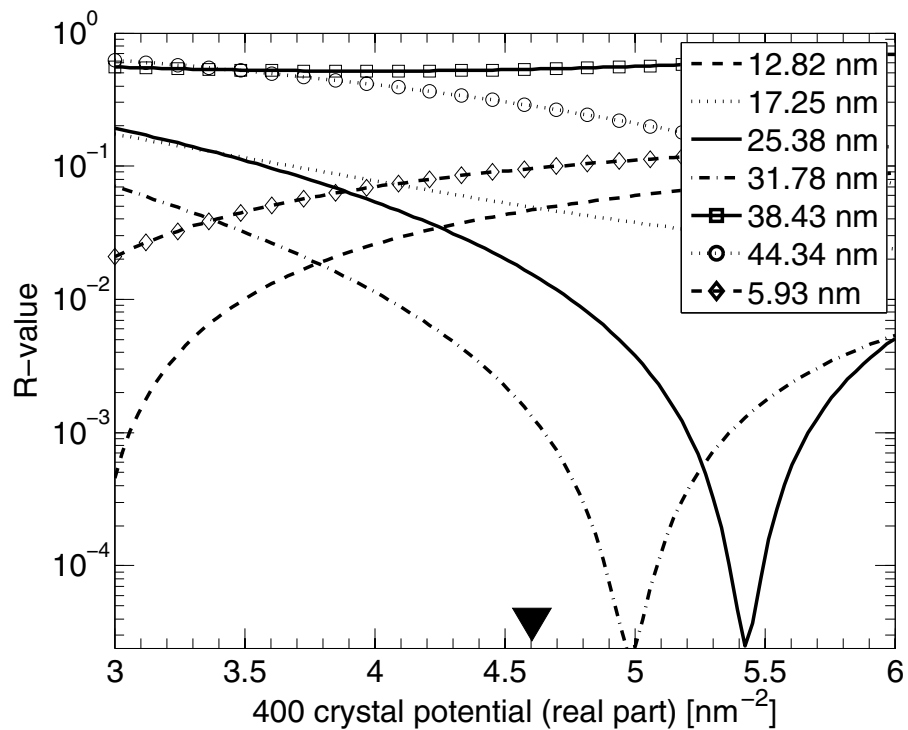


Figure 3.7: Dependence of the R-value on the 400 crystal potential (real part) for the 32.96 nm thick frozen lattice simulation. Different curves correspond to different thicknesses t_0 (see legend) taken from the minima positions in Fig. 3.6. Because the R-values cover a wide range, the R-axis is scaled logarithmically. The black triangle marks the 400 potential computed from [75].

little influence on the 400 intensities. This means that the R-value minimum in Fig. 3.7 must be close to the triangle if the correct – or nearly correct – thickness is used in the simulation. Obviously this is the case for $t_0 = 31.78$ nm (dash-dotted line) and eventually also for $t_0 = 25.38$ nm (solid line). Using these two values as an initial guess for the thickness, the 200 potential (starting from $\text{Re}(U_{200}^E) = -0.666$ nm⁻²), the orientation and the thickness were refined simultaneously. Finally, the 400 and 800 potentials were also included in the refinement to check whether they are refined to their true values. The results are shown in table 3.2.

Since both R-values in table 3.2 are comparably low, further criteria are needed to identify the correct result. The refinement starting with a thickness of 31.78 nm yields 400 and 800 crystal potentials which deviate less than 1.8 % from the intended ones. Opposite to this, the refinement with $t_0 = 25.38$ nm results in a 20 % too large value for $\text{Re}(U_{400})$ and a 22 % too low real part for U_{800} . Thus, the thickness and the real part of the 200 potential that result from the refinement starting with $t_0 = 31.78$ nm seem most probable. Indeed, both quantities are in best agreement with the values used in the frozen lattice simulation within the errors derived above.

Few was said as to the refinement of the orientation. This is because the results were always appreciably accurate when the initial guess for the COLC did not deviate more than 0.5 reciprocal basis vectors from the true one. This accuracy can easily be achieved by evaluating the intersections of Kikuchi bands.

We close our studies of ambiguous refinement results with a comment concerning the astonishing similarity between the thickness scans of the 13.19 nm and the 32.96 nm simulations in Fig. 3.6. Both thicknesses fall into a region where the 400 reflections have intensity maxima and strongly dominate the diffraction pattern and thus the denominator of Eq. (3.1). In principle, this behaviour originates from the pendellösung-type dependence of diffracted intensities on thickness according to Fig. 2.6, meaning that similar diffraction patterns are repeating periodically with thickness. Note that TDS indeed increases with thickness, which may hardly be noticed in thickness scans or refinements when balanced by a simultaneous raise of the scaling factor. However, here the R-value can in both cases only rise significantly at those thicknesses where 400 is weak (which is the case near 20 nm and 40 nm), because only then the differences in the nominator of Eq. (3.1) can become comparably large as the denominator. Critically examining the refinement results for unknown properties by checking the outcome for known properties is thus an essential part of the PBED method. For the 13.19 nm simulation, the 200, 400 and 800 potentials are refined to their true values only for a starting thickness around 13 nm.

t_0 [nm]	t [nm]	$\text{Re}(U_{200}^E)$ [nm ⁻²]	$\text{Re}(U_{400}^E)$ [nm ⁻²]	$\text{Re}(U_{800}^E)$ [nm ⁻²]	R
31.78	32.92	-0.567	4.683	1.606	0.16 %
25.38	24.77	-0.608	5.550	1.289	0.15 %
true:	32.96	-0.546	4.604	1.586	–

Table 3.2: Refinement results for the 32.96 nm simulation in dependence of the initial guess for the starting thickness t_0 . Results for the COLC refinement are not shown because the orientation was stable within fluctuations of $1 \cdot 10^{-5}$ reciprocal basis vectors. The last line lists the true values which were used in the frozen lattice simulation.

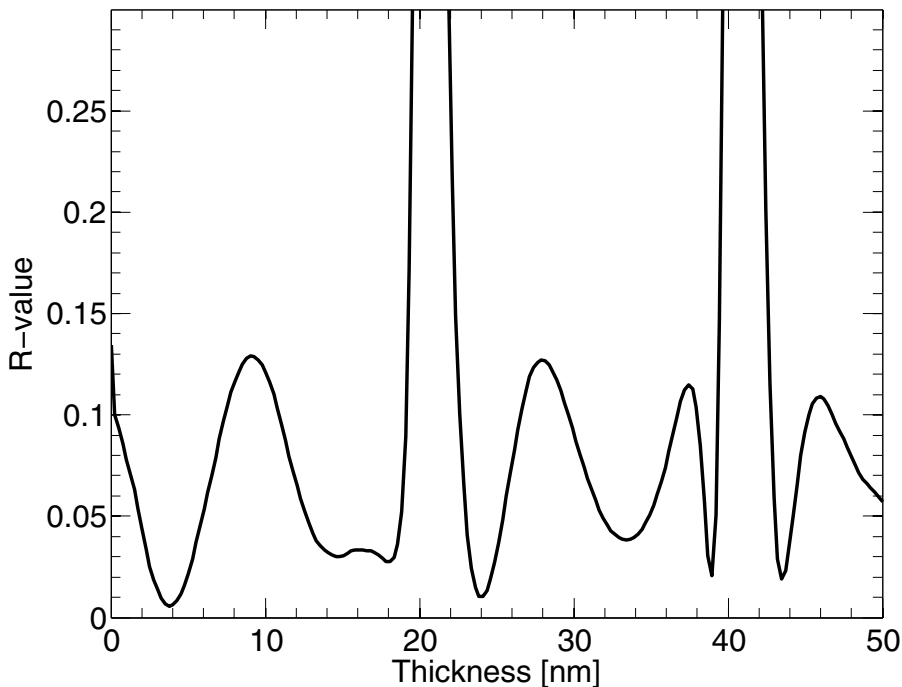


Figure 3.8: Thickness scan for an experimental data set. Possible initial thicknesses for the refinements correspond to minima of the $R(t)$ curve.

3.3.2 Measurement of the 200 potential for GaAs

Prior to PBED analysis of experimental diffraction patterns, polarity was measured from positions of HOLZ reflections and HOLZ line contrast as explained in section 3.4.2. As both CBED and PBED work was done using the same sample, the resulting zone axis, being $[053]$, is the correct setting for PBED simulations, too.

Estimation of initial thicknesses for the refinement

For each experimental data set, an initial COLC was estimated by evaluating the intersections of Kikuchi bands. In order to find initial guesses for the thickness refinement, $R(t)$ curves were calculated for each set as done in section 3.3.1. To show that the evaluation of real PBED patterns is strictly analogous to that of the simulated ones, the procedure is exemplified using only one experimental pattern for reasons of brevity.

A typical thickness scan is shown in Fig. 3.8 for one data set (set N^o 1 in table 3.3) where no energy filter was used. Note that the 200 intensities have been excluded from the computation of the R-value and the scaling factor. The function $R(t)$ exhibits six local minima with R-values below 5%, whose positions mark possible starting thicknesses for the refinement. To identify the most plausible thickness, six $R(U_{400})$ curves are depicted in Fig. 3.9 which correspond to the thicknesses taken at the minima in Fig. 3.8. The curves for $t_0 = 14.57$ nm, $t_0 = 38.94$ nm, and $t_0 = 43.47$ nm have no minimum at all near the potential we expect from Ref. [75], which is indicated by the black triangle. Thicknesses $t_0 = 3.51$ nm and $t_0 = 33.42$ nm show minima around $R(U_{400}) = 3.5$ nm⁻², but the curve corresponding to $t_0 = 24.12$ nm is much more plausible, not only because its minimum R-value is nearly an order of magnitude lower, but also because the minimum position is closest to what we expect from the isolated atom approximation. In this way, initial thicknesses for six of the 11 unfiltered and for three of the six zero loss filtered data sets

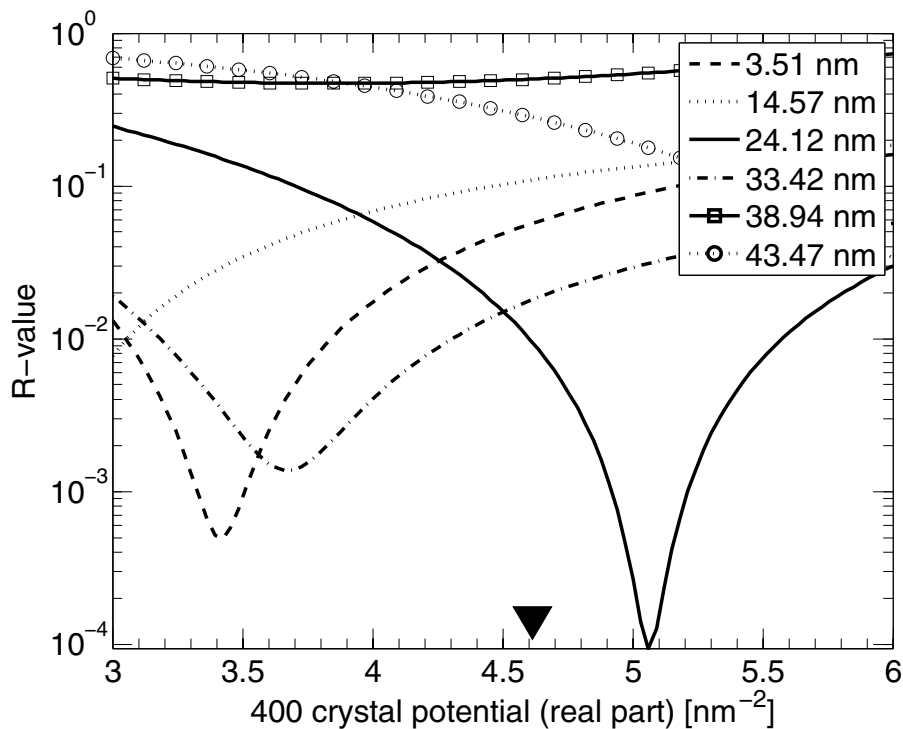


Figure 3.9: Dependence of the R-value on the 400 crystal potentials (real part) for an experimental PBED pattern. Different curves correspond to different thicknesses t_0 (see legend) taken from the minima positions in Fig. 3.8. Because the R-values cover a wide range, the R-axis is scaled logarithmically. The black triangle marks the 400 potential computed from [75].

have been found. For the remaining sets, the R-values either exceeded 30% at the minima of $R(U_{400})$ or no minimum did show up at all in a physically plausible range. Hence nine sets are left for refinement. Please note that no quantity has been refined until here.

Refinement results for the 200 potential

The final refinement results were obtained from mainly three subsequent steps. As specimen thickness and -orientation are considered to contain the major errors in the beginning, both quantities were refined simultaneously in a first run without using the 200 intensities. Second, solely the 200 potential was refined using thickness and COLC results from the first step. The refinement starting value $\text{Re}(U_{200}^E) = -0.546 \text{ nm}^{-2}$ was calculated according to Ref. [75]. Third, all three parameters thickness, COLC and $\text{Re}(U_{200}^E)$ were refined simultaneously using the results from the first two steps as input. The scaling factor was always included in the refinements and each data set was treated separately for the present. Typically, convergence was achieved after approximately 20 iterations in the last refinement step, which took roughly 5-10 minutes on a 2.66 GHz PC. Depending on the orientation, 780 – 800 beams from four Laue zones have been included in the calculation. Debye parameters of $B_{\text{Ga}} = 0.68 \text{ \AA}^2$ and $B_{\text{As}} = 0.59 \text{ \AA}^2$ were used (without being refined), which correspond to a temperature of 295 K according to [81]. The assumption that the specimen is at room temperature is based on the fact that the $8 \mu\text{m}$ C2 aperture drastically decreases beam current density. Refinement results are shown in table 3.3. Unrelativistic structure factors given in different units according to Eqs. (3.2) and (2.28) are listed in table 3.8. For conversion to X-ray structure factors see also Fig. 3.16.

Table 3.3: Refinement results of the PBED method for nine experimental data sets of GaAs. Initial and refined thicknesses correspond to columns t_0 and t , respectively. The last three columns list the refined COLC and the 200 potential (real part) with the minimised R-value, the lower part shows the statistical evaluation.

N ^o	t_0 [nm]	t [nm]	COLC	Re(U_{200}^E) [nm ⁻²]	R
unfiltered data sets					
1	24.12	24.07	(0.00 0.00 0.00)	-0.419	0.023
2	15.52	15.50	(0.96 0.00 0.00)	-0.413	0.040
3	25.17	25.01	(1.42 0.13 $\overline{0.22}$)	-0.435	0.048
4	23.45	22.59	(0.00 0.00 0.00)	-0.347	0.073
5	28.45	28.56	(0.41 $\overline{0.24}$ 0.39)	-0.395	0.027
6	25.02	24.84	($\overline{0.97}$ $\overline{0.15}$ 0.24)	-0.393	0.042
zero loss filtered data sets					
7	20.52	20.32	(0.21 0.00 0.00)	-0.421	0.024
8	18.72	18.44	(0.38 0.04 $\overline{0.06}$)	-0.418	0.041
9	22.93	22.93	($\overline{0.28}$ $\overline{0.16}$ 0.27)	-0.361	0.024
Average potential				$\langle \text{Re}(U_{200}^E) \rangle = -0.400 \text{ nm}^{-2}$ $\sigma = 0.029 \text{ nm}^{-2}$	
Standard deviation					

From initial and refined thicknesses in table 3.3, it can be seen that the preliminary thickness guesses t_0 are accurate to a nanometre for all data sets. Furthermore, the COLC reveal that all specimen orientations are close to zone axis [053] since the largest tilt of 2.51 mrad occurs for set N^o 3. A qualitative comparison of the refinement results for Re(U_{200}^E) in the fifth column in table 3.3 with the starting value of Re(U_{200}^E) = -0.546 nm⁻² already exhibits a deviation of more than 0.1 nm⁻² towards larger values for the 200 potential in any of the nine refinements.

As to the effect of zero loss filtering, neither the R-values nor the refined potentials of sets N^o 7-9 indicate that an energy filter is necessary, since they are in good agreement with the results of the unfiltered data sets.

Except for set N^o 4, the R-values are below 5%, indicating reliable results. Set N^o 4 is exceptional also concerning the 200 potential, which is largest here. Nevertheless, we see that Re(U_{200}^E) for set N^o 9 is nearly comparably large, however with a very small R-value of 2.4%. Since an R-value of 7% is still reasonable, set N^o 4 has also been included in the statistical evaluation, which is shown at the bottom of table 3.3. In comparison to the isolated atom approximation [75, 76], the average real part of the 200 potential changed by more than 20%, which is discussed in section 3.5.

We now turn towards the constraint refinement using all data sets simultaneously. This means that one R-value in Eq. (3.1) is calculated from all nine data sets, and that only one 200 potential results. Although zone axis [053] is very sparse, with few reflections corresponding to high momentum transfer, refinement of Debye parameters was also included using all ZOLZ reflections. However, the reader is referred to section 3.3.4 for more details on accurate Debye parameter refinement using HOLZ. Nevertheless it was found by Jansen et al. [115], by considering only ZOLZ reflections as well, that refinement of Debye parameters is possible in case several diffraction patterns with different thicknesses and/or orientations are used, which is fulfilled here. The actual refinement therefore included optimisation of the nine individual thicknesses, orientations and scal-

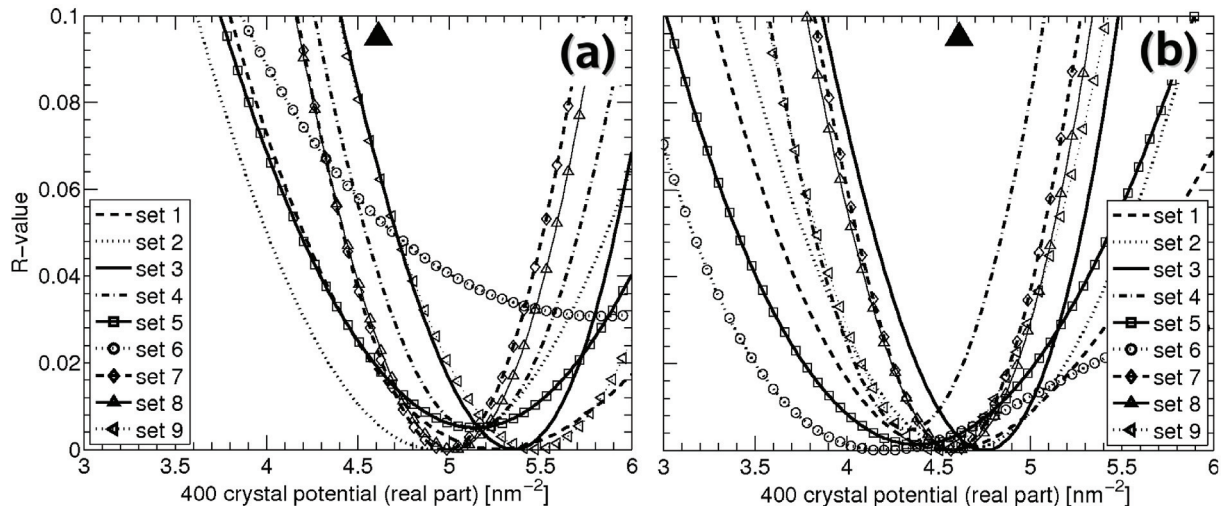


Figure 3.10: Dependence of the R-value on the 400 crystal potential (real part) for the experimental data sets (a) before and (b) after the refinement of the 200 potential. The curves can be assigned to the results in table 3.3 with the list in the legend. The black triangle marks the 400 potential computed from [75].

ing factors, as well as the two Debye parameters and the 200 potential. Starting values have been chosen from table 3.3. Finally, an R-value of 0.034 was achieved and Debye parameters of $B_{\text{Ga}} = 0.65 \text{ \AA}^2$ and $B_{\text{As}} = 0.56 \text{ \AA}^2$ were found. For the 200 potential, a value of $\text{Re}(U_{200}^E) = -0.398 \text{ nm}^{-2}$ was found which is practically identical with the mean result of the separate refinements in table 3.3. Refined thicknesses deviated less than 1 nm from those in table 3.3 and results for the orientations were identical with the ones given in table 3.3.

Behaviour of the 400 crystal potential

In contrast to the 200 potential, the 400 potential is not expected to be significantly modified by chemical bonding. Therefore, we used these potentials for plausibility arguments above to decide which specimen thickness should enter the refinement. The minimum of the solid curve in Fig. 3.9 is indeed closest to what one expects from the isolated atom approximation, but nevertheless there is no exact coincidence. To judge whether this deviation is in fact due to the wrong 200 potential used for the R-value calculation in Fig. 3.9, the behaviour of the curve $R(U_{400})$ before and after the refinement of the 200 potential is depicted in Fig. 3.10 for each set.

Figure 3.10 (a) depicts the results before the refinement of the 200 potential, i.e. only thicknesses and orientations had been optimised using isolated atom scattering data. Obviously, a 400 potential of $\text{Re}(U_{400}^E) \approx 5.2 \text{ nm}^{-2}$ is found for most data sets. This is about 0.6 nm^{-2} larger than the potential according to isolated atoms [75] (black triangle). In contrast to this, Fig. 3.10 (b) clearly reveals a much better agreement between the R-value minima of each set and the isolated atom approximation. However, even in Fig. 3.10 (b) the minima scatter significantly around their average position. In this case, this is not severe because the worst R-value is still only 2% (set N^o 4) for the isolated atom potential. Furthermore, it is exactly this set which showed the largest deviation of $\text{Re}(U_{200})$ during the refinements above. We will not go into further details of each curve in Fig. 3.10, but give average results for $\text{Re}(U_{400}^E)$ instead, which have been deduced

Table 3.4: Refinement results of the PBED method for eight experimental data sets of InAs. Initial and refined thicknesses correspond to columns t_0 and t , respectively. The last three columns list the refined COLC and the 200 potential (real part) with the minimised R-value, the lower part shows the statistical evaluation.

N ^o	t_0 [nm]	t [nm]	COLC	Re(U_{200}^E) [nm ⁻²]	R
1	32.99	32.98	(0.44 1.04 1.73)	1.619	0.058
2	66.26	66.11	(0.00 0.00 0.00)	1.600	0.077
3	63.03	62.60	(0.45 0.08 1.01)	1.610	0.004
4	19.3	19.24	(0.00 0.00 0.00)	1.599	0.010
5	16.59	16.52	(0.17 0.18 0.30)	1.606	0.031
6	16.30	16.40	(0.18 0.97 1.61)	1.648	0.074
7	19.07	19.06	(0.07 0.86 1.42)	1.612	0.033
8	98.01	98.03	(0.08 0.87 1.45)	1.657	0.002
Average potential				$\langle \text{Re}(U_{200}^E) \rangle = 1.619 \text{ nm}^{-2}$	
Standard deviation				$\sigma = 0.022 \text{ nm}^{-2}$	

from the positions of the minima. From data sets N^o 1-9 we obtain $\text{Re}(U_{400}^E) = 5.238 \pm 0.284 \text{ nm}^{-2}$ for Fig. 3.10 (a) and $\text{Re}(U_{400}^E) = 4.5042 \pm 0.167 \text{ nm}^{-2}$ for Fig. 3.10 (b). Thus the 400 potential for isolated atoms of 4.616 nm^{-2} only agrees with experiment if the refinement result for $\text{Re}(U_{200}^E)$ is used.

3.3.3 Measurement of the 200 potential for InAs

Although tests of the PBED method have been applied to GaAs in section 3.3, we can expect that the main conclusions as to derivation of plausible thicknesses are valid in general. This is especially the case for InAs which is very similar to GaAs except for lattice parameters and ASA. Thus, 200 crystal potential measurement proceeds in complete analogy to section 3.3.2, and only central results will be given.

At first, polarity was measured as described for the GaAs case in section 3.4.2. Here, orientations near zone axis $[0\bar{5}3]$ describe HOLZ lines adequately. After data reduction with the program GREED, plausible thicknesses and orientations have been found for eight data sets. Then, thickness, orientation and the 200 potential were refined for each set separately using fix Debye parameters of $B_{\text{In}} = 1 \text{ \AA}^2$ and $B_{\text{As}} = 0.86 \text{ \AA}^2$ corresponding to 295 K [81]. Results are listed in table 3.4. Please see table 3.8 for the unrelativistic values in different units according to Eqs. (3.2) and (2.28). X-ray structure factors are also shown in Fig. 3.16.

Obviously the behaviour is similar to the refinements for the 200 potential of GaAs in table 3.3, meaning that initial thicknesses are only slightly modified. Moreover, R-values and standard deviations are comparable. The average 200 potential found here is about 2% larger than the starting value of $\text{Re}(U_{200}^E) = 1.587 \text{ nm}^{-2}$ for isolated atoms [75].

As in section 3.3.2, simultaneous refinement of the 200 potential and Debye parameters, as well as thicknesses, orientations and scaling factors was performed. In this way, a 200 potential of $\text{Re}(U_{200}^E) = 1.614 \text{ nm}^{-2}$ and Debye parameters of $B_{\text{In}} = 0.87 \text{ \AA}^2$ and $B_{\text{As}} = 0.68 \text{ \AA}^2$ were found. Thus, Debye parameters are slightly lower than theoretical values. However, the 200 potential agrees well with table 3.4, so that exact measurement of InAs temperature factors is left to future experiments of the form described in section 3.3.4.

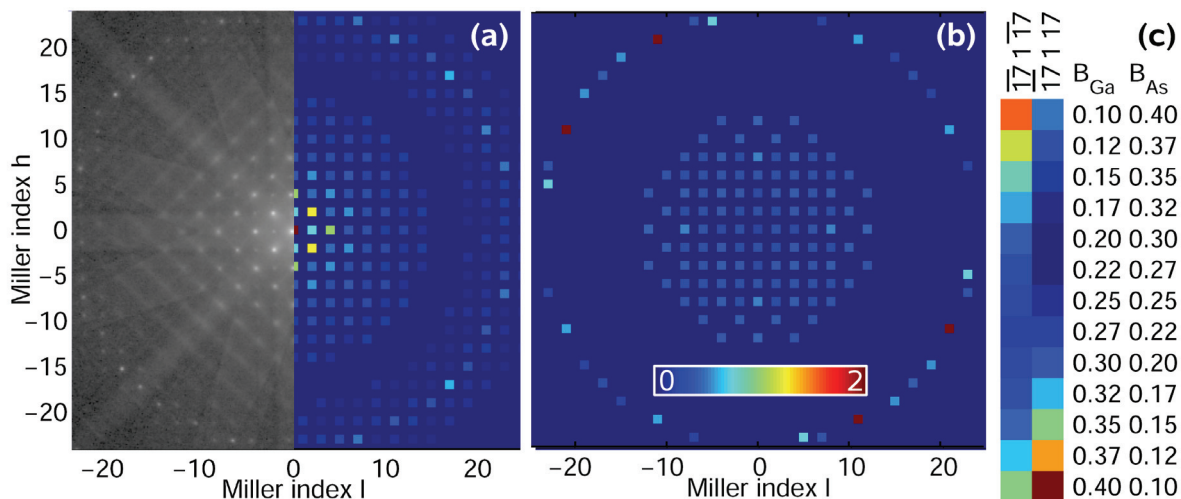


Figure 3.11: Analysis of the sensitivity of FOLZ reflections in $\langle 010 \rangle$ zone axis (GaAs) on different Debye parameter settings. Part (a) shows half an experimental PBED pattern with ≈ 59 nm thickness and the corresponding Bloch4TEM [37] simulation in the right half for $B_{\text{Ga}} = B_{\text{As}} = 0.25 \text{ \AA}^2$. Part (b) reflects the standard deviation of Bragg intensities normalised to the simulation in (a) obtained from 13 diffraction patterns, each having different Debye parameters for Ga and As with the constraint that the mean Debye parameter is 0.25 \AA^2 . In (c), intensity dependence on $B_{\text{Ga}}/B_{\text{As}}$ is shown for two reflections with linear colour scaling, increasing from blue to red.

3.3.4 Measurement of Debye parameters for GaAs

Before prematurely starting the refinement of Debye parameters, we should ask if we can expect it to be in analogy to a refinement of certain structure factors. Unfortunately the answer is no. Although this chapter is substantially dedicated to verify the MASA concept, that is, *atomic* scattering data, experimental validation of MASA takes an indirect path. Yet no ASA has been refined but crystal potentials as a whole. It becomes clear from Eq. (2.55) that an infinite number of combinations of $f_{\text{Ga}}^{\text{GaAs}}$ and $f_{\text{As}}^{\text{GaAs}}$ exists that lead to the same 200 potential. Moreover, there is no simple rule which connects MASA of several reflections (unlike the representation of isolated atom ASA by superposition of Gaussians [78, 75]), meaning that inclusion of more reflections will not help to solve the under-determined problem to measure $f_{\text{Ga}}^{\text{GaAs}}$ and $f_{\text{As}}^{\text{GaAs}}$ separately for the 200 spatial frequency. Hence individual refinement of Debye parameters B_{Ga} and B_{As} is not analogous to the refinement of certain crystal potentials because they describe atomic properties which do not appear as such in diffraction patterns at first sight.

Nevertheless the situation for Debye parameter refinement is different from the (fictitious) refinement of atomic ASA, because the former are identical for each reflection, whereas the latter differ among them. Mathematically, this is a direct consequence of the Debye-Waller damping scheme introduced in section 2.2, where it was found that, once the Debye parameter is known, the relation between all ASA is given and exactly Gaussian. However, the aim of individual Debye parameter refinement should be approached with care since it could be that several settings for Ga and As produce very similar diffraction patterns.

In the left half of Fig. 3.11 (a) an experimental PBED pattern recorded at 99 K is shown on logarithmic intensity scale. It can clearly be seen that first order Laue zone (FOLZ) reflections are significantly present due to specimen cooling. In sum, 300-400 significant FOLZ and ZOLZ reflections have been extracted for each of the experimental

Table 3.5: Refinement results of the PBED method for Debye parameter measurement using starting values from Schowalter et al. [81] and Gao and Peng [80].

Set N ^o	1	2	3	4	5	6	7
Separate refinement							
t [nm]	59.00	54.68	55.18	55.37	54.71	55.70	54.74
COLC h, l	0, 0	0.03, $\overline{0.03}$	0.03, $\overline{0.02}$	0.02, $\overline{0.01}$	$\overline{0.03}$, $\overline{0.04}$	0.14, $\overline{0.05}$	$\overline{0.01}$, $\overline{0.04}$
Simultaneous refinement							
Start [81]	$B_{\text{Ga}} = 0.269 \text{ \AA}^2$ and $B_{\text{As}} = 0.233 \text{ \AA}^2$						
Result	$B_{\text{Ga}} = 0.275 \text{ \AA}^2$ and $B_{\text{As}} = 0.242 \text{ \AA}^2$						
Start [80]	$B_{\text{Ga}} = 0.250 \text{ \AA}^2$ and $B_{\text{As}} = 0.264 \text{ \AA}^2$						
Result	$B_{\text{Ga}} = 0.270 \text{ \AA}^2$ and $B_{\text{As}} = 0.239 \text{ \AA}^2$						

PBED patterns. The following analysis proceeds in three main steps.

First, each PBED pattern is regarded separately in order to find initial thicknesses and orientations as described in section 3.3.1. Since incidence was near zone axis $\langle 010 \rangle$, 202 and 400 potential scans were used to unambiguously determine initial thicknesses. Orientations and thicknesses have then been refined using about 15 low-order ZOLZ reflections.

Next, Debye parameters were considered in more detail, and choosing correct starting values for the refinement is the first problem. As mentioned in section 3.3.1, the refinement idea is based on the assumption that parameters in question are in principal already well known. However, for the present temperature of 99 K, we find $B_{\text{Ga}} = 0.250 \text{ \AA}^2$, $B_{\text{As}} = 0.264 \text{ \AA}^2$ according to Gao and Peng [80], but $B_{\text{Ga}} = 0.279 \text{ \AA}^2$, $B_{\text{As}} = 0.241 \text{ \AA}^2$ from the average over local density and generalised gradient approximation from Schowalter et al. [81]. Thus, the ratio $B_{\text{Ga}}/B_{\text{As}}$ is opposite in both references, whereas the mean Debye parameters $\overline{B}_{\text{GaAs}} = 1/2(B_{\text{Ga}} + B_{\text{As}})$ are nearly identical. This behaviour has motivated a pre-refinement of the mean Debye parameter with the constraint $\overline{B}_{\text{GaAs}} = B_{\text{Ga}} = B_{\text{As}}$, starting at 0.258 \AA^2 . In this way it was checked that the magnitude of the Debye parameters from literature is correct before attempting a determination of the individual Debye parameters for Ga and As. It is in the nature of the R-value (3.1) that weak reflections contribute marginally. Therefore, FOLZ reflections have been weighted by a factor of 1000, as was reported also by Tsuda and Tanaka [51]. The refined value $\overline{B}_{\text{GaAs}} = 0.229 \text{ \AA}^2$ is close to the average started with.

As shown in Fig. 3.11 (a), many FOLZ reflections are present. In order to refine B_{Ga} and B_{As} individually, we now look for FOLZ reflections which are indeed sensitive to the ratio $B_{\text{Ga}}/B_{\text{As}}$ in a diffraction pattern for a specimen thickness equal to the experimental one in Fig. 3.11 (a), i.e. 59 nm. To this end, a series of diffraction patterns was simulated under identical conditions, except that $B_{\text{Ga}}/B_{\text{As}}$ was varied among different simulations. In particular, both Debye parameters were not chosen independently but in such a way that $\overline{B}_{\text{GaAs}} = 0.25 \text{ \AA}^2$. The distinct values are listed in figure part (c), together with resulting intensities of two selected FOLZ reflections. As can be seen there, the intensities $\overline{171\overline{17}}$ and $\overline{171}17$ not only depend on the ratio $B_{\text{Ga}}/B_{\text{As}}$, but also exhibit the opposite trend, meaning that intensity of the former is strongest for low B_{Ga} , whereas the latter is intense for large B_{Ga} . We therefore conclude that reflections exist which are promising for unique separate refinement of B_{Ga} and B_{As} . To get an overview, the standard deviation of the intensity of significant reflections with respect to Debye parameter variation as

shown in Fig. 3.11 (c) has been calculated. Figure 3.11 (b) depicts the result which was normalised to the respective beam intensities of the simulation with $B_{\text{Ga}} = B_{\text{As}} = 0.25 \text{ \AA}^2$. Obviously most reflections show only marginal dependence on the ratio $B_{\text{Ga}}/B_{\text{As}}$, especially low-order ZOLZ beams. This is important because it means that thicknesses found from the ZOLZ refinements are relatively robust against the ratio $B_{\text{Ga}}/B_{\text{As}}$. In contrast, several FOLZ reflections exhibit standard deviations of about 200%. In this way, 10-15 FOLZ reflections have been determined for each experimental PBED pattern which were used for the calculation of R . Both Debye parameters have then been refined independently using seven data sets, among which B_{Ga} on the one hand and B_{As} on the other hand have been constrained. The refinement was performed several times under identical conditions, except that starting values for B_{Ga} and B_{As} were set differently in order to check if the R-value minimum found is stable. In particular, Gao and Peng's [80] and DFT values from Schowalter et al. [81] have been used for 99 K.

Refinement results are summarised in table 3.5, together with literature data. For both settings of starting values similar results for the Debye parameters are obtained. It is worth noting that again, as in section 3.3.2, $B_{\text{Ga}} > B_{\text{As}}$ is found, even when starting with the opposite trend according to [80]. From multiple refinements starting at Debye parameters in the range given in table 3.5 an error of 0.003 \AA^2 was estimated from the standard deviations of refinement results for both atomic species.

3.4 Convergent beam electron diffraction

3.4.1 Methodical summary

Tsuda and Tanaka have presented a method to refine crystal structural parameters, such as atom positions, Debye parameters and low order structure factors from two dimensional, zero loss filtered CBED patterns in Ref. [51]. The method will be outlined briefly here, for details see Refs. [51, 114]. Their method contains computer programs for the preprocessing of raw experimental data, as well as for the nonlinear least-squares fitting by many-beam Bloch wave simulations (program MBFIT). During preprocessing, distortions of the CBED discs and deviations from the intended disc positions due to aberrations of the optical system are corrected for by estimating and refining elliptical distortion coefficients, as well as disc shifts. A subtraction of the diffuse background along a given direction (usually parallel to a Kikuchi band or to thickness fringes) is performed by linear interpolation between background intensities just outside the disc. What is actually refined is a circular portion of the disc, typically having a diameter of 70-90% of the experimental disc in order to eliminate Fresnel fringes stemming from diffraction at the edge of the C2 aperture.

The program MBFIT minimises the factor S defined by

$$S = \sum_m w_m (I_m^e - s \cdot I_m^s)^2 \quad , \quad (3.4)$$

where the superscript indicates experimental and simulated intensities, respectively. The scaling factor s is defined as in Eq. (3.1). Weights w_m are derived from the error due to electron counting statistics and the error induced by background subtraction. Depending on the quantities to be refined, the weights of reflections which are most sensitive to the respective parameter changes may be emphasised manually. Two further quantities, the

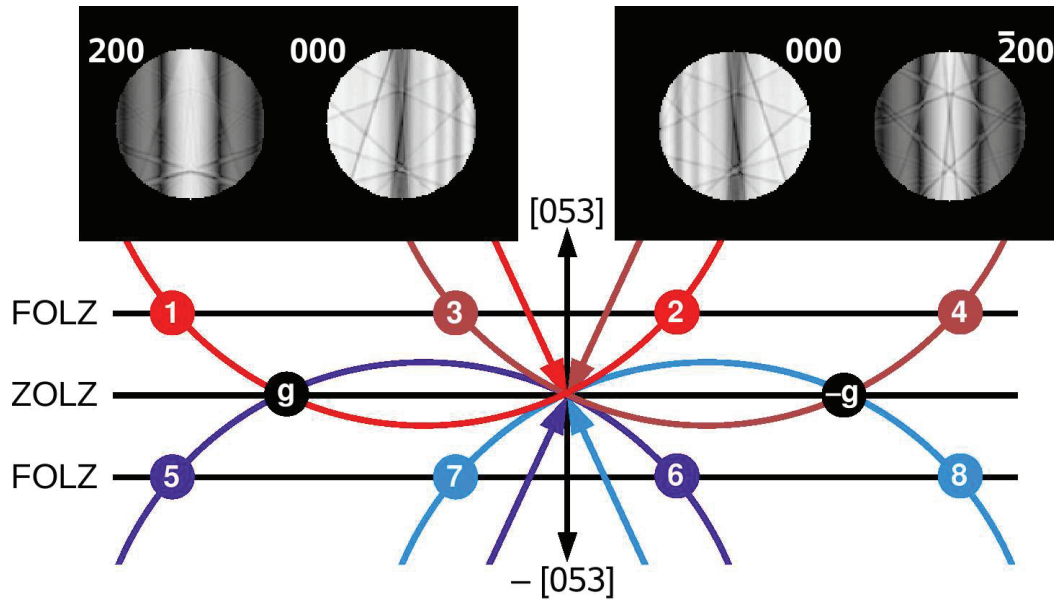


Figure 3.12: *Top*: Bloch4TEM [37] CBED simulation showing different HOLZ line contrast in CBED discs. Zone axis $[053]$ was assumed, with (200) (left) and $(\bar{2}00)$ (right) in Bragg condition. *Bottom*: Ewald construction sketching different excitation conditions when the tangential and/or perpendicular component of \mathbf{k}_0 is inverted, distinguished by colour.

reliability factor R_w and the goodness of fit (GOF), defined by

$$R_w = \sqrt{\frac{S}{\sum_m w_m (I_m^e)^2}} \quad \text{and} \quad GOF = \sqrt{\frac{S}{N - M}} \quad , \quad (3.5)$$

are calculated to measure the quality of the refinement. In Eq. (3.5), N and M denote the number of data points and the number of refined parameters, respectively. The procedure to select and calculate potentials which are to be included in the calculation is similar to that described in section 2.4, except that the program feature to account for further potentials via the generalised-Bethe-potential method [130] is used in this work in order to save computation time in each refinement cycle. Scattering factors for isolated atoms are used according to Bird and King [76].

3.4.2 Refinement preconditions

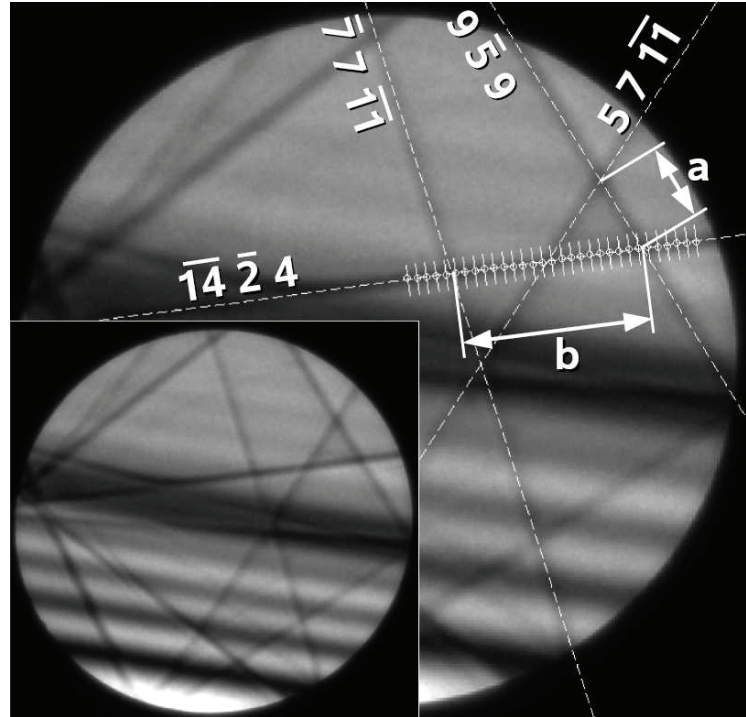
All CBED patterns have been preprocessed as described in section 3.4.1 and Ref. [51]. See section 3.2.2 for experimental details.

Polarity of GaAs

Both GaAs and InAs are crystals without inversion centre, which can lead to violation of Friedel's law, that is, different intensity of conjugate reflections. Opposite to wurtzite-GaN [131], this can even happen if these reflections correspond to identical structure factors, as it is the case for ± 200 here. However, HOLZ line symmetry and -contrast is used in the following to find the correct polarity.

If only the angle between one of the $\langle 100 \rangle$ directions and the surface normal is known by preparation as described in section 3.2.2, a lot of possibilities exist. In particular, the

Figure 3.13: Calibration of the acceleration voltage for an experimental CBED pattern. The ratio a/b can be determined from the indicated HOLZ lines in the primary disc, which are fitted linearly. Linear equations are found by fitting intensity minimum positions (white circles) obtained from perpendicular line scans (solid white lines) as shown for the $\bar{1}4\bar{2}4$ line. Dashed lines correspond to the fit results.



zone axis may be along $\pm[053]$, $\pm[035]$, $\pm[305]$, $\pm[503]$, $\pm[350]$ or $\pm[530]$. In the present CBED work, one of the 200 reflections was always set near Bragg condition. Given one of these zone axis directions, it must therefore additionally be checked whether 200 or $\bar{2}00$ is strongly excited. Of course some combinations tilt/zone axis yield the same CBED pattern, which can be studied via knowledge of diffraction groups. Here, relevant possibilities have been simulated and were compared with experimental CBED patterns.

Polarity effects are illustrated in Fig. 3.12 for zone axis $\pm[053]$. At the top, two Bloch4TEM [37] simulations are shown, one assuming 200, another $\bar{2}00$ to be in Bragg condition for $[053]$ zone axis. Whereas ZOLZ effects are seen to be comparable owing to identical crystal potentials, HOLZ line contrast is significantly different. At the bottom of Fig. 3.12, Ewald constructions are used to visualise this behaviour: In case of incidence as shown in light red, $g = (200)$ is at Bragg condition and reflections 1 and 2 in the first order Laue zone (FOLZ) are excited. By inverting the tangential component of \mathbf{k}_0 , $g = (\bar{2}00)$ and FOLZ reflections 3 and 4 are strongly excited. Since crystal potentials of 1 and 2 on the one hand, and those of 3 and 4 on the other hand, may be different, different HOLZ line contrast is produced by the light and dark red geometry. Moreover, one must check the blue cases 5 – 8, which result from zone axis inversion and may again produce different contrast.

In summary, agreement of HOLZ line contrast and -symmetry between experimental GaAs CBED patterns and simulations was found for zone axis $[053]$ and $g = (\bar{2}00)$ at Bragg condition.

Acceleration voltage of the TEM

The acceleration voltage must be measured separately because positions of HOLZ lines may depend significantly on it. Therefore, GaAs CBED patterns in $[053]$ zone axis were simulated with $\bar{2}00$ in Bragg condition using 16 different voltages between 295 kV and 305 kV. The ratio a/b from the intersection of HOLZ lines in the primary disc was determined as shown in Fig. 3.13.

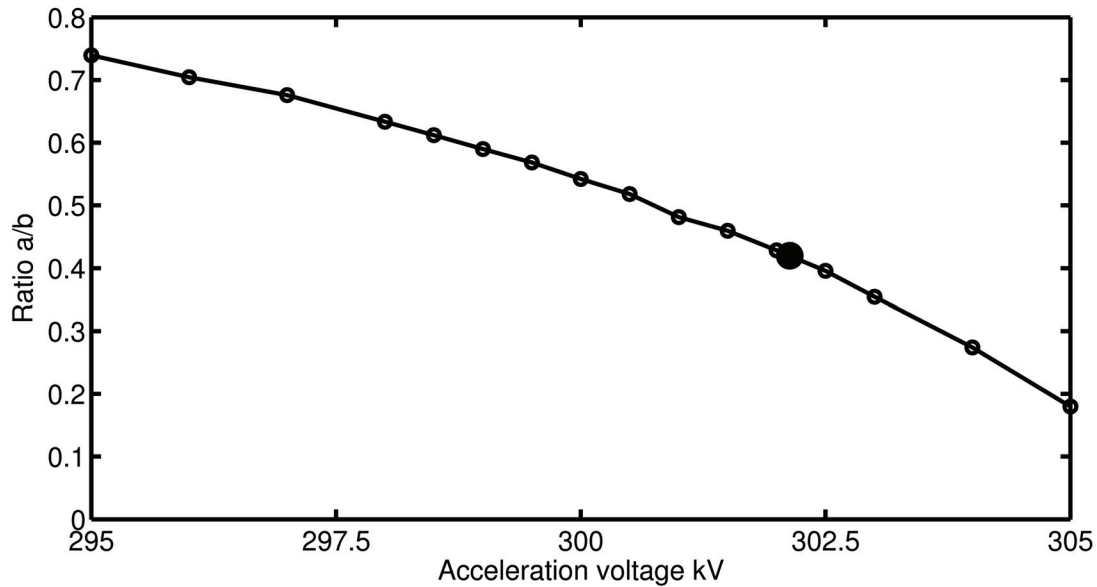


Figure 3.14: Reference curve for the ratio a/b determined by the acceleration voltage. In addition to calibration data (black line, simulated), the ratio found experimentally is shown as a thick black point.

First, straight lines have been marked by eye along respective HOLZ lines. Second, a number of perpendicular intensity line scans has been calculated, so that the minimum of each line scan yields one position on the HOLZ line. Third, these minimum positions were fitted to obtain four linear equations, from which the ratio a/b was calculated. The actual accelerating voltage was finally obtained by comparing the experimental ratio a/b with the calibration curve shown in Fig. 3.14. This procedure leads to a voltage of 302.1 kV, which has in the following been used in all refinements. As HOLZ line positions may also depend on lattice parameters, and hence on temperature, reliability of this result has been checked by simulating a CBED pattern for 302.1 kV using lattice parameters corresponding to a temperature of 350 K. The ratio a/b obtained from this pattern still matched the one found above.

experiment	calculation	difference	reflection
			$\overline{14}\overline{2}4$
			$\overline{15}1\overline{1}$
			$131\overline{1}$

Table 3.6: Results for the fitting of HOLZ reflections to determine the Debye parameters. Specimen thickness and scaling factor had been determined from ZOLZ reflections which are not shown. The GOF of the refinement is 5.00.

Debye parameters of GaAs

Due to the comparably large C2 aperture and due to focussing of the probe, high beam current densities are present in the investigated specimen area, leading to an unknown increase of temperature and hence of Debye parameters. Reflections from HOLZ of a CBED pattern recorded with a smaller camera length were used to refine B_{Ga} and B_{As} . Afterwards, these Debye parameters were kept fixed throughout structure factor refinements. During the refinement of Debye parameters, isolated atom scattering data according to Ref. [76] were used. The signal of HOLZ reflections is relatively low because care had to be taken that the primary beam would not damage the CCD chip. However, three significant HOLZ reflections could be extracted from the raw data and were used to refine Debye parameters, starting from the values for room temperature given in section 3.3.2. Before, thickness and scaling factor had been determined from the 400 discs.

Observed and calculated discs, as well as the differences for the refinement result of $B_{\text{Ga}} = 0.76 \text{ \AA}^2$ and $B_{\text{As}} = 0.62 \text{ \AA}^2$ are depicted in table 3.6. It can be seen that the refinement is more accurate along the centre of the respective HOLZ line, whereas the calculation does not contain the blurring of the lines. This may be due to the fact that calculated intensities have not been convoluted with the modulation transfer function of the CCD, which is analysed in Ref. [51]. In addition, one should check via frozen lattice simulations whether TDS alters HOLZ line contrast. Since determining Debye parameters is not our main goal of CBED work here, we neglect the slight changes introduced by these effects here. However, comparison with Debye parameters found by PBED in section 3.3.2 ($B_{\text{Ga}} = 0.65 \text{ \AA}^2$ and $B_{\text{As}} = 0.56 \text{ \AA}^2$) implies specimen heating in CBED due to sharp focusing of the incident beam.

Initial thicknesses

For each data set, most plausible thicknesses and scaling factors have been determined from the GOF plotted versus specimen thickness (analogous to the $R(t)$ curves in section 3.3.2). Before, the orientations had been found from the deficiency HOLZ lines inside the ZOLZ discs. A typical example for one data set (set N^o 1 in table 3.7) is depicted in Fig. 3.15. Notice that the two-dimensional intensity distribution inside the discs is used to calculate the GOF also for the thickness scan.

Obviously a thickness $t_0 = 145 \text{ nm}$ is a good starting point for the refinement because this minimum drops to a value $GOF = 6.285$, which is by far the lowest in the plotted thickness range. The fact that the thickness scan leads to an unambiguous result in the CBED case has its origin in the thickness fringes of the $\bar{4}00$ disc, which is shown as an inset in Fig. 3.15. According to Fig. 1.5 (b), these fringes are a result of the systematic row like character of zone axis $[053]$ and finite crystal size, the latter leading to sinc-shaped reciprocal lattice rods along the specimen surface normal and hence intensity oscillations as a function of incidence. See table 3.7 for starting thicknesses t_0 of the other data sets.

3.4.3 Measurement of the 200 potential for GaAs

The intensity distribution of the $\bar{4}00$ disc has initially been used to refine thicknesses and scaling factors, starting from the results of the thickness scan (section 3.4.2). Then, the $\bar{2}00$ disc was also included in the refinement of the thickness, together with the scaling factor and $\text{Re}(U_{200}^E)$, the latter starting at -0.534 nm^{-2} , which corresponds to isolated atom data from Ref. [76]. Using the resulting thickness and the resulting scaling factor

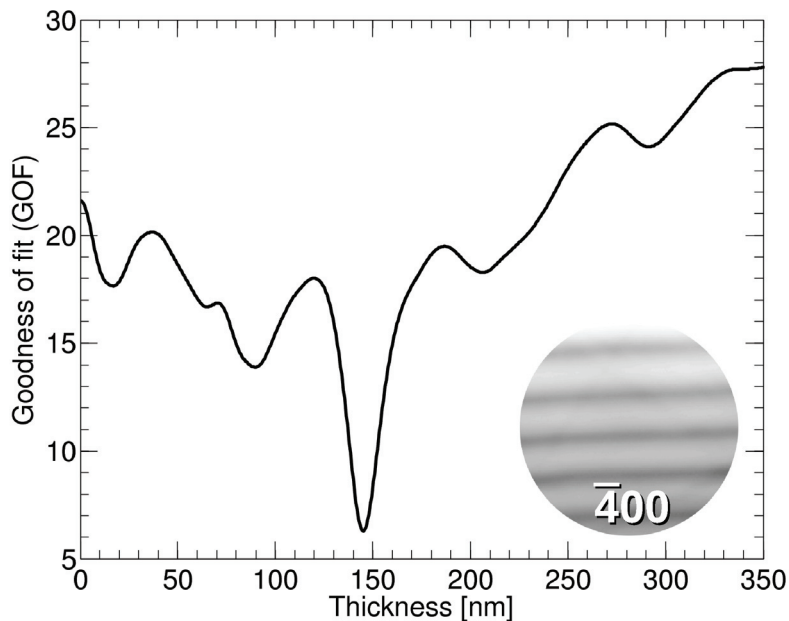


Figure 3.15: CBED thickness scan for data set N° 1. Possible initial thicknesses for the refinement correspond to minima of the GOF. The inset shows the $\bar{4}00$ disc, which contains thickness fringes having a period that is characteristic for the specimen thickness.

of this refinement, the real part of the 200 potential has finally been refined by means of the $\bar{2}00$ intensity. Each data set was treated separately. Table 3.7 summarises the final refinement results. Columns 2-7 depict observed and calculated intensities, together with the respective difference for each data set. From these difference plots, it can be seen that calculation and experiment are in very good agreement after the refinement. In any case, the 200 potential has been refined to about 0.1 nm^{-2} larger values, compared to isolated atom data. The HOLZ line patterns show that orientation varies among different data sets, and so does the thickness t .

Although the initial thickness guesses t_0 have been stated to be unique according to Fig. 3.15, refined thicknesses deviate considerably from the starting values (more than 10 nm for set N° 2). This may be due to the fact that crystal potentials for isolated atoms had been used during the thickness scans. However, most R_w values do not exceed 7%, indicating reliable results. The worst R_w of 9.8% and GOF of 2.486 result for set N° 4, which was nevertheless included in the statistical evaluation shown at the bottom of table 3.7, because neither the visualisation of the difference between calculation and experiment, nor the resulting potential give reason to doubt this result, if we compare with the rest of the table. Comparing the average 200 potential from table 3.7 with isolated atom scattering data [75, 76], we realise that the real part changed by approximately 20%. This is similar to the PBED result and will be discussed in section 3.5. Together with PBED results, table 3.8 summarises unrelativistic results converted to several units according to Eqs. (3.2) and (2.28). For graphical comparison to PBED, see also Fig. 3.16.

Table 3.7: Results of the refinement of the thicknesses and the 200 potential of GaAs for the seven CBED data sets. Experimental and calculated intensity distributions inside the $\bar{4}00$ and $\bar{2}00$ discs are shown together with the respective difference. Starting thicknesses t_0 and refined thickness values t are given for each set, followed by the refined relativistic 200 potential (302.1 kV), which contains the Debye parameters $B_{\text{Ga}} = 0.76 \text{ \AA}^2$ and $B_{\text{As}} = 0.62 \text{ \AA}^2$. See Eq. (3.5) for the definition of GOF and R_w . The lower part shows the statistical evaluation.

N ^o	$\bar{4}00$		$\bar{2}00$		t_0 [nm]	t [nm]	$\text{Re}(U_{200}^E)$ [nm ⁻²]	GOF	R_w
	experiment	calculation	experiment	calculation					
1					145.0	143.66	-0.426	1.673	0.046
2					98.0	84.33	-0.483	1.430	0.050
3					121.5	117.22	-0.453	2.068	0.067
4					136.0	149.04	-0.418	2.486	0.098
5					145.0	139.68	-0.448	2.348	0.069
6					156.5	144.30	-0.396	1.771	0.050
7					115.5	107.21	-0.423	2.124	0.061
Average potential					$\langle \text{Re}(U_{200}^E) \rangle = -0.435 \text{ nm}^{-2}$				
Standard deviation					$\sigma = 0.028 \text{ nm}^{-2}$				

3.5 Discussion

3.5.1 Validity of the PBED test results

The report on testing the PBED method has been restricted to GaAs in zone axis [053] to approach conditions of the actual measurements. However, errors induced by, e.g., TDS background subtraction or by the assumption of plane wave incidence can be thought to be extensively independent of material and zone axis. This is also reflected by the application of the PBED method to InAs which yields reasonable results as well.

The resulting R-values in tables 3.1 and 3.2 appear to be extremely low, since experimental R-values are a few percent in magnitude (tables 3.3 and 3.4). This just expresses that slightly convergent aberration-manipulated probes, together with the background subtraction are not responsible for the increase of the minimal R-value in practice. Instead, amorphous layers on the specimen surfaces, variations of thickness and orientation throughout the illuminated area, and Poissonian noise may govern discrepancies between experimental and simulated data sets. Concerning amorphous layers, the background subtraction will be accurate only if no significant rings form in reciprocal space, as pointed out in Ref. [115]. Analogous to this reference, the effect of a thickness gradient in the illuminated area was tested exemplarily for set N^o 1 in table 3.3, i.e. the experimental data set was compared with the average over five simulated diffraction patterns in the range between 23 nm and 25 nm. The refinement results $t = 23.9$ nm and $\text{Re}(U_{200}) = 0.412 \text{ nm}^{-2}$ show that nearly the average thickness is obtained and that influence on the refinement of the potential is very low.

Except for the magnitude of the R-values, evaluation of test patterns in section 3.3.1 and experimental data sets in section 3.3.2 was analogous. This is an important point because we derived rules for the identification of plausible results, e.g., of the thickness scan, using the test data sets and applied the same rules to the experimental situation. Furthermore, errors of the refinement of the 200 potential are of the same magnitude, indicating that test conditions had been chosen appropriately. Even though the R-values for the experimental data sets are an order of magnitude larger than those for the test patterns, the error of the refinement of the 200 potential remains comparable with that obtained by testing the PBED method.

3.5.2 Methodological aspects

Results obtained in this work by both the PBED and the CBED method are summarised without relativistic correction in table 3.8, which contains also theoretical values expected for isolated atoms and from the MASA concept. Related properties, such as the Coulomb potential in V, the structure factor in nm and the X-ray structure factor, are also given as calculated from Eqs. (3.2) and (2.28). For the InAs case, two results are given which correspond to Debye parameters from literature [81] and those found by simultaneous refinement as described at the end of section 3.3.3. Even though electron structure factors are nearly identical, different Debye parameters lead to deviating X-ray structure factors. However, exact measurement of Debye parameters for InAs should in principle be performed including HOLZ reflections (as done for GaAs in section 3.3.4) and is left as a future task. At first, our focus is on the measured 200 potentials for GaAs to compare PBED and CBED methodologically.

Strictly speaking, the mean PBED and CBED results for $\text{Re}(U_{200})$ may not be compared directly because of the different Debye parameters used. Nevertheless, the influence

of the Debye parameters on the 200 potential is very low because the impact of Gaussian damping decreases with decreasing momentum transfer, and because the difference between temperatures in both experiments is approximately only 30 K [81]. Hence both the PBED and the CBED method lead to 200 potentials which agree well with each other within the margin of error, which is given in brackets for $\text{Re}(U_{200})$ in table 3.8. However, knowledge of Debye parameters is still important to measure the correct specimen thickness, because both quantities may be correlated as to the minimisation of R in the PBED case [115]. Furthermore, the R -values of a few percent in tables 3.3 and 3.7 agree well with the R -values in earlier publications of PBED refinements [115, 116] using MSLS, and CBED results obtained with the MBFIT program [51]. The latter reference also contains maximum GOF around 2, as in the present work.

The fact that both methods, PBED and CBED, show a different average 200 potential was also investigated with respect to the different scattering data sets [75, 76] used. The PBED refinements based on Weickenmeier and Kohl [75], as well as Bird and King [76] yield identical averages and standard deviations.

Regarding the precision of both methods, table 3.8 exhibits nearly the same standard deviations for PBED and CBED. This is surprising since the outcome of the refinement of one CBED data set is in fact already the average over thousands of diffraction patterns, each corresponding to one pixel (and therefore one orientation) in the CBED disc. Practically, errors for a single refinement derived from standard error propagation rules alone, as described in Ref. [47], for example, are usually unphysically low due to the large number of data points. For this reason, statistical evaluation of several independent measurements was preferred in this work, resulting in more realistic standard deviations.

The simultaneous Bloch4TEM PBED refinement of thickness, orientation and 200 crystal potential of one data set took a few minutes on a single 2.66 GHz CPU, whereas only one refinement cycle for the refinement of the 200 potential alone would have occupied one CPU for nearly 10 hours using the CBED method with the same number of beams. CBED therefore requires computer clusters if two-dimensional diffraction patterns are to be simulated.

Care must be taken when comparing precisions and calculation times only. table 3.7 shows that the refinement results of the CBED method can be judged by visual control of the difference plots. In principle, this is also possible for the Bragg intensities of the PBED patterns, but of course the explanatory power is much less in this case, because reflections show no inner structure, such as HOLZ lines or thickness fringes, which represent physical properties such as specimen orientation or -thickness. It is connected with this aspect that thickness scans look much more unique in the CBED case due to the fringes in the $\bar{4}00$ disc, an information which is missing in PBED patterns. Here, only the dynamical interaction of all scattered beams can be used for the thickness estimate. This is in principle no limitation because in most cases, the correct starting thickness can be found by checking the behaviour of other quantities which are known with adequate accuracy. In this work, crystal potentials of intermediate order, such as 400, were used for this purpose. It should be noticed that the thicknesses obtained from the PBED patterns are much smaller than those measured from the CBED patterns, owing to the fact that refinement results for the thickness and for the orientation have been tested by comparison with the output of MSLS. The latter only applies to thicknesses below 15-40 nm [115]. Furthermore, the results of the thickness scans for the PBED patterns are much closer to the final refinement result, since t_0 and t deviate less than 1 nm, whereas the difference can exceed 10 nm using the CBED method.

An important point is also the overlap between CBED discs of different Laue zones. As shown in Fig. 3.4, HOLZ reflections are very close to some of the ZOLZ reflections. Since the TDS background is estimated from the direct vicinity of the discs, background subtraction may fail in case more or less intense HOLZ reflections are in contact or overlap with a ZOLZ disc. In contrast, PBED peaks are usually well-separated.

For the zero loss filtered diffraction patterns analysed in this work, it was assumed that energy filtering contributes to the scaling factor only, which is common to all reflections. However, the PBED results show that energy filtering does not alter the refinement results, whereas it is essential for achieving high precision in CBED work [51].

It is worth mentioning that the accurately measured acceleration voltage of the TEM was used for the CBED refinements, but not for the PBED method, where the nominal value as indicated at the TEM was taken. To estimate the error induced by this approximation, refinements from section 3.3.2 have been repeated with the voltage measured by CBED in section 3.4.2, assuming a deviation of 2.1 kV from 300 kV to be a typical error of the voltage indicated at the TEM. The resulting 200 potential deviated less than 0.003 nm^{-2} from the results in table 3.3 (which correspond to a voltage of 300 kV). Hence statistical errors are larger than the effect of a slightly modified acceleration voltage.

3.5.3 Discussion of the results for the 200 potentials

GaAs

Crystal potentials of GaAs have in the past been studied experimentally by several groups with different methods under various experimental conditions. Figure 3.16 (a) depicts all measured 200 potentials of the present work, converted to X-ray structure factors, in the lower part. The upper part contains all results from literature the author is aware of.

Zuo et al. found $|V_{200}|$ to be $0.43 \pm 0.008 \text{ V}$ from measurements at 90 K and 120 kV by fitting one-dimensional CBED intensity profiles [6] as described in section 3.1 and illustrated in Fig. 3.1 (c). Since temperatures of the present work are more than 200 K larger, a direct comparison of results is hardly possible, because the ratio $B_{\text{Ga}}/B_{\text{As}}$ changes significantly from low to high temperatures. This means that the contribution of Ga atoms (relative to that of the As atoms) to the structure factor increases [79, 80] ($B_{\text{Ga}} < B_{\text{As}}$) or decreases [81] ($B_{\text{Ga}} > B_{\text{As}}$) with increasing temperature. However, referring to the isolated atom approximation [75] and Debye parameters from Ref. [79] for 90 K, the result from Zuo et al. corresponds to a change by a factor of 0.83, which deviates a few percent from what we expect from table 3.8. As to the error margins given in Ref. [6], measurements here seem to be much less precise on the first view, since present standard deviations are larger by a factor of approximately 3.5. It is supposed that Zuo et al. find their errors from standard error propagation rules for a single refinement, being much smaller in practice than statistical errors of table 3.3, as mentioned in section 3.5.2. It should furthermore be noted that K. and J. Gjønnnes, together with Zuo and Spence, again published results on the 200 structure factor in GaAs obtained the same way and under the same conditions [117]. However, two slightly different X-ray structure factors result as depicted by the star and the diamond Fig. 3.16. Hence derivation of reliable errors from statistics among several independent measurements is crucial for any method dealt with here.

Stahn et al. measured structure factor amplitudes and Debye parameters by X-ray studies [110] and found $|X_{200}| = 6.34$ with an error of 1-2% at 297.65 K, as depicted as a black square in Fig. 3.16. For 287.15 K, they found $B_{\text{Ga}} = 0.666 \text{ \AA}^2$ and $B_{\text{As}} =$

Table 3.8: Collection of PBED and CBED results obtained in this work together with different theoretical data sets according to Weickenmeier and Kohl (WK [75]), Bird and King (BK [76]) and Rosenauer et al. (MASA [9]). Note that different Debye parameters are involved in PBED and CBED and that all values are non-relativistic. The standard deviations of the $\text{Re}(U_{200})$ refinements are given in brackets and correspond to tables 3.7 and 3.3. Related crystal properties like the structure factor F , the Coulomb potential V and the X-ray structure factor X_{200} are also listed.

Crystal	Method	$\text{Re}(U_{200})$ [nm ⁻²]	$\text{Re}(V_{200})$ [V]	$\text{Re}(F_{200})$ [nm]	X_{200}	
Debye parameters: $B_{\text{Ga}} = 0.68 \text{ \AA}^2$ and $B_{\text{As}} = 0.59 \text{ \AA}^2$						
GaAs	PBED	-0.252 (0.019)	-0.379	-0.143	-6.366	
	WK	-0.346	-0.520	-0.196	-5.630	
	BK	-0.331	-0.498	-0.188	-5.738	
	MASA	-0.268	-0.403	-0.152	-6.210	
	Debye parameters: $B_{\text{Ga}} = 0.76 \text{ \AA}^2$ and $B_{\text{As}} = 0.62 \text{ \AA}^2$					
	CBED	-0.273 (0.018)	-0.411	-0.155	-6.350	
	WK	-0.350	-0.526	-0.199	-5.784	
	BK	-0.335	-0.504	-0.190	-5.892	
MASA	-0.272	-0.409	-0.154	-6.364		
Debye parameters: $B_{\text{In}} = 1.00 \text{ \AA}^2$ and $B_{\text{As}} = 0.86 \text{ \AA}^2$						
InAs	PBED	1.020 (0.014)	1.534	0.712	53.687	
	WK	0.999	1.503	0.697	53.847	
	BK	0.949	1.427	0.662	54.252	
	MASA	1.021	1.535	0.712	53.682	
	Debye parameters: $B_{\text{In}} = 0.87 \text{ \AA}^2$ and $B_{\text{As}} = 0.68 \text{ \AA}^2$					
	PBED	1.017	1.530	0.710	53.754	
	WK	0.999	1.503	0.697	54.115	
	BK	0.948	1.427	0.662	54.516	
MASA	1.021	1.535	0.713	53.719		

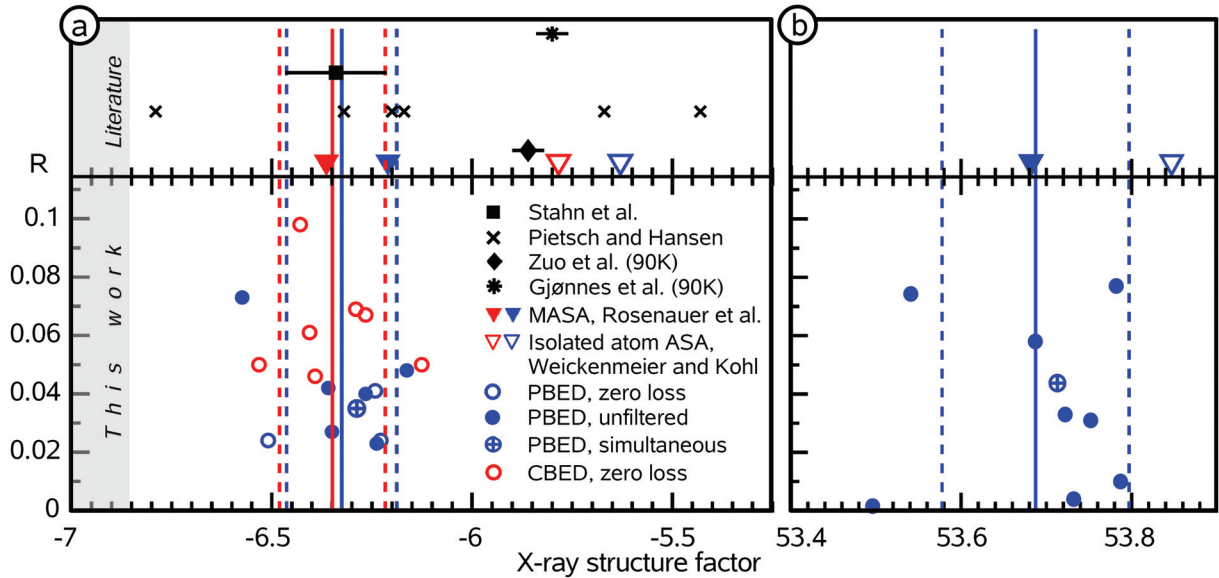


Figure 3.16: Compilation of all measurements (lower part) of the 200 potential for (a) GaAs and (b) InAs (converted to X-ray structure factors), together with literature values (upper part). Blue and red data in (a) correspond to PBED and CBED measurements, respectively. These differ in settings for the Debye parameters given in table 3.8. Triangles depict theoretical data according to Refs. [75] and [9] for isolated atom ASA and MASA, respectively. Experiments from literature stem from Stahn et al. [110], Pietsch and Hansen [118], Zuo et al. [6] and Gjønnes et al. [117].

0.566 \AA^2 , which agrees well with the data in Ref. [81]. The same is true for all Debye parameters found by PBED in the present work. Additionally, CBED measurements here confirm that $B_{\text{Ga}} > B_{\text{As}}$, unlike Refs. [79, 80]. Comparing X_{200} from Stahn et al. with experimental values given in table 3.8, all three measurements are in very good agreement. Differences do not exceed 0.026, which is less than $1/5$ of the error σ of the present measurements. Analogous arguments hold for the comparison with the review of Pietsch and Hansen [118], shown as crosses in Fig. 3.16. They give experimental results in the range $|X_{200}| \in [5.43 \dots 6.79]$ with a mean value of 6.10 and a standard deviation of 0.484.

We close this discussion with a comparison of the measured 200 crystal potential with that expected theoretically from the isolated atom approximation [75, 76] and from the MASA concept [9] since verification of the MASA concept had been one central goal. In this respect, it might be interesting for the reader to know that the necessity of the present measurements has also been doubted by some people, with the argument that so many accurate values exist in literature, which are sufficient to judge whether MASA or isolated atom ASA are more realistic. It is left to the reader to answer this question from the upper part of Fig. 3.16 (a) only, where MASA and isolated atom data are shown as filled and open triangles, respectively. However, as can be seen from $\text{Re}(U_{200})$ in table 3.8 and from the lower part of Fig. 3.16 (a), both CBED and PBED measurements agree only with the MASA concept within the margins of error (dashed lines in Fig. 3.16 (a)), with respect to the statistical mean (straight lines in Fig. 3.16 (a)). In contrast, isolated atom potentials deviate more than 20% and cannot be verified. Discussing the accuracy of both the PBED and the CBED method would imply that the true 200 potential is known. Granted that the DFT potentials are true, the CBED method would be more

accurate, since the result matches the DFT value nearly perfectly. However, one has to keep in mind that seven of the nine PBED results are very close to what is expected from the MASA model, and only measurements № 4 and 9 yield considerably larger potentials, which has significant impact on the statistical average. Furthermore, the 200 potential found by simultaneous refinement (encircled plus) tends to be closer to the MASA concept than the statistical mean.

Using the PBED method, it was also shown that the 400 potential according to the isolated atom approximation only agrees with experiment if we use the refined 200 potential for the simulation of diffraction patterns. This additionally confirms the MASA concept which matches with isolated atom scattering data asymptotically for high momentum transfers. For the 400 potential, a difference of 0.3% is expected, which is smaller than the experimental errors.

InAs

As already mentioned in the introduction of this chapter, bonding in InAs is expected to affect the 200 potential much less than in GaAs. In methodological respect, it is therefore of interest if accuracy and precision of the PBED method are sufficient to verify the difference between MASA and isolated atom scattering factors. Even though Debye parameters for InAs are relatively inaccurately known from experiment, PBED measurements in table 3.8 are significantly closer to the MASA value than to isolated atom structure factors. With regard to Fig. 3.16 (b), both the mean of the individual (straight line) and the simultaneous refinement (encircled plus) exhibit that isolated atom data must be rejected, as it lies outside the error margins. What is in perfect agreement with the measurement is the X-ray structure factor obtained from the MASA concept using Debye parameters from Schowalter et al. [81], around which all single refinements scatter. To the knowledge of the author, no other experiments on InAs structure factor measurement are available.

Relevance of charge density (difference) maps

When Zuo et al. first published results on GaAs [6], they presented also charge density difference maps as explained in section 2.3.5. Quickly a debate arose between them and Bernard and Zunger [132, 133] as to the convergence of the charge density with respect to a cutoff of Fourier coefficients in reciprocal space. The two positions are characterised as follows: On the one hand, the Fourier series over $X_{\mathbf{g}}$ converges after a few terms because high order X-ray structure factors are damped due to finite temperature (Zuo et al.). On the other hand, each electron sees a static crystal, for which convergence is obtained far beyond the cutoff applied by Zuo et al. (Bernard and Zunger).

The reader might have noticed in Fig. 2.3 that the cutoff was set to 70 nm^{-1} . Apart from the fact that this information will never be transferred by any optical system, it can never be observed since experiments access indeed the average over a large number of such static, but slightly distorted, electron densities. The dilemma therefore is that a density reconstructed from structure factor measurement is actually not present in crystals, whereas the density obtained from theory cannot be observed. Recalling that our goal was to check the reliability of the 200 potential obtained by DFT, we can leave this debate to academic interest. Here, knowledge of this single potential enables us to minimise errors of, e.g., the CELFA method. Both techniques, diffraction work here and CELFA, are well described within the Debye-Waller damping scheme, and a discussion (or charge density difference mapping) as described above is not advisable at this place.

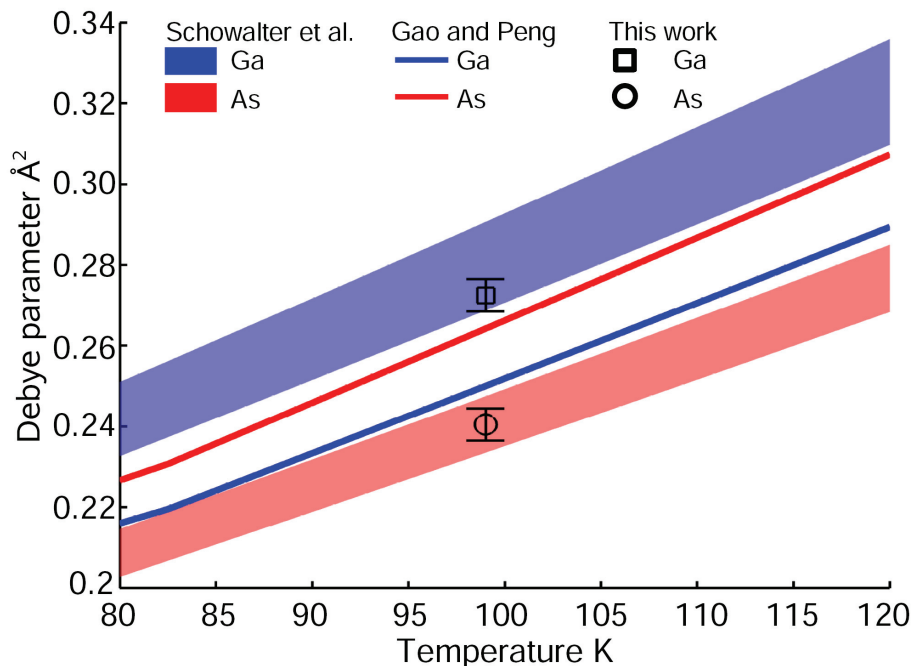


Figure 3.17: Comparison of measured GaAs Debye parameters with literature data from Schowalter et al. [81] and Gao and Peng [80]. For the former, corridors are plotted whose lower and upper limits are determined by LDA and GGA, respectively.

3.5.4 Discussion of Debye parameters for GaAs

At first sight, the importance of Debye parameters seems marginal, especially when dealing with low order structure factors. Nevertheless we have seen in section 3.5.3 that conversion to X-ray structure factors is significantly dependent on Debye parameters, especially on the ratio $B_{\text{Ga}}/B_{\text{As}}$. As experimental data near room temperature, present PBED refinements of B_{Ga} and B_{As} at 99 K exhibit $B_{\text{Ga}} > B_{\text{As}}$, in accordance with DFT data from Schowalter et al. [81]. Moreover, Fig. 3.17 shows that the present experiment also meets DFT quantitatively, as it lies well inside the corridors defined by local density and generalised gradient approximation (LDA, GGA). Error bars are suitably small to conclude that Debye parameters from Gao and Peng [80] for 99 K must be rejected.

However, it should be noticed that Debye parameters found by PBED for 300 K are slightly smaller than Schowalter’s DFT values. As stated in section 3.3.2, conditions are not supposed to be optimised for such a refinement. Instead of using ZOLZ reflections in zone axis [053], an experiment in zone axis $\langle 010 \rangle$ would be preferable due to the large number of high-order reflections in the FOLZ. Since Debye-Waller damping at 300 K is very strong, recording significant FOLZ intensity requires working at lower acceleration voltage, e.g., at 80 kV. For both PBED refinements of Debye parameters, it may also be that the assignment to the actual temperature is wrong. At 99 K, the value indicated at the cooling stage controller was trusted. The temperature of 300 K was manually assigned. If we do it the other way round and assign a temperature to the refinement result, we end up near 281 K which is still plausible. Nevertheless, independent measurement of temperature is important to be considered in future.

In methodical respect, the success of PBED refinement using HOLZ is encouraging for several reasons. In comparison to CBED, no inner structure of reflections is to be resolved, meaning that PBED patterns may be recorded at comparably small camera lengths.

Because CBED requires both energy filtering and high sampling of the CBED discs up to HOLZ, in-column energy filters in combination with imaging plates are preferable. However, many if not most of contemporary TEM are equipped with post-column filters and a CCD camera, which possesses a lower resolution and smaller dynamical range. In such a setup, several parts of a CBED pattern ought to be recorded separately and merged afterwards, which means considerably larger effort than recording a PBED pattern, for that energy filtering is not necessarily required.

It is worth noting that seven data sets had been used for the refinement in the present work, which could efficiently be refined through set-wise parallelisation. In the CBED case, thousands of Bloch wave simulations must be carried out for a single diffraction pattern, slowing down refinements even when parallel computing is utilised. Moreover, inclusion of HOLZ drastically raises the number of beams further, and with it the numerical effort.

Side note to quantitative STEM

We briefly consider the relevance of knowing accurate Debye parameters for quantitative high-angle annular dark field (HAADF) scanning TEM (STEM) evaluations. One prerequisite for, e.g., composition evaluation in semiconductor nanostructures is accurate knowledge of specimen thickness [28]. This is obtained by comparison of the HAADF signal in specimen regions with known composition with STEM simulations. Since the HAADF signal is essentially given by TDS, which in turn depends on the mean thermal atomic displacements or, equivalently, Debye parameters, accuracy of thickness measurement is determined by the accuracy of the knowledge of Debye parameters.

To see whether experimental and simulated HAADF intensities agree, a GaAs wedge has been cleaved along $\{110\}$ planes. Thus, projected along $\langle 100 \rangle$, specimen thickness increases linearly with distance from the edge. Off-zone 400 dark field imaging has been used to calibrate thickness via pendellösung-type (see, e.g., Fig. 2.6) thickness contours, whose period is constant and corresponds to 20 nm thickness change found by Bloch wave simulations [37]. Scanning TEM HAADF images have been taken at 300 K and 99 K. The basic idea is illustrated on the right of Fig. 3.18.

By averaging the HAADF intensity parallel to the wedge edge and normalising to incident beam intensity, experimental thickness dependence as shown by the black and red circles in Fig. 3.18 was obtained. On the other hand, frozen lattice multislice simulations have been performed with the STEMsim [33] software for 99 and 300 K with Debye parameters from Schowalter et al. [81]. In principle, agreement between experiment and simulation is found for both temperatures. However, at 99 K we see that experimental values tend to be slightly larger than simulated ones, especially for larger thicknesses. In this respect, we must keep in mind that not the error of the HAADF signal, but the error of the thickness is governing accuracy of composition evaluations using STEM. Towards thicknesses around 100 nm, differences between simulation and experiment correspond to 15 – 20 nm thickness error at 99 K. In contrast, the 300 K curves are in good agreement with maximum thickness errors of about 7 nm at 50 nm thickness.

In summary, simulation and experiment fit well at high temperature, whereas simulations at low temperature underestimate the HAADF signal. Let us assume that Debye parameters found by PBED refinements in section 3.3.4 are correct for 99 K. From this follows that Debye parameters and, equivalently, temperatures differ among simulated and recorded red curves in Fig. 3.18 which could be explained by specimen heating during STEM exposure. This argument is supported by Debye parameters found with CBED in section 3.4 which are larger than expected for room temperature, as discussed in sec-

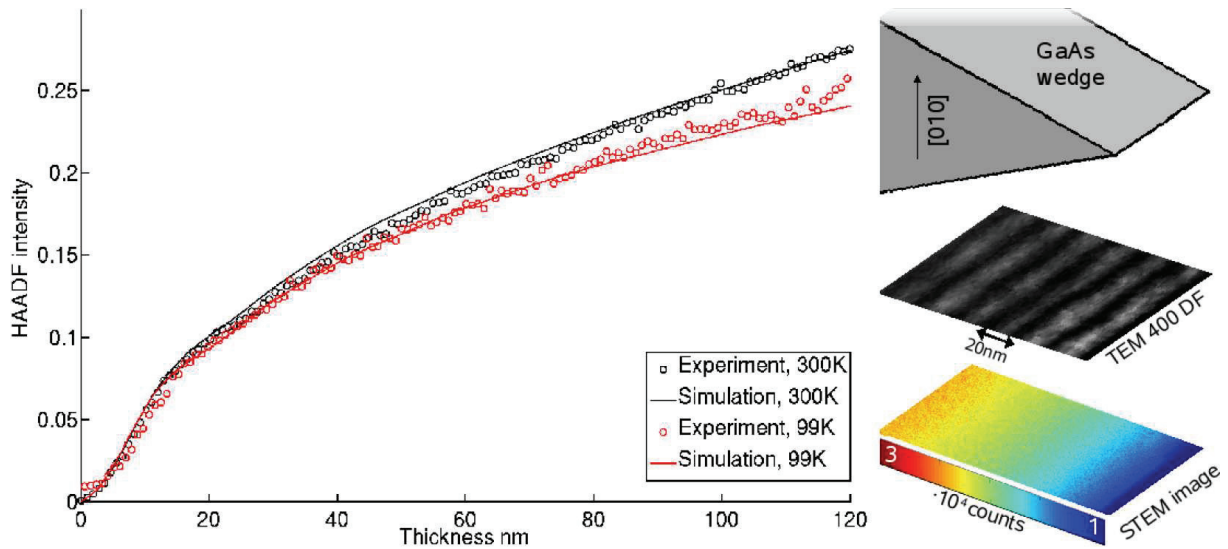


Figure 3.18: Comparison of measured (circles) and simulated [33] (solid lines) thickness dependence of the STEM-HAADF signal normalised to incident intensity for 300 K (black) and 99 K (red). Acceptance of the detector was 33 – 200 mrad. The right part depicts the acquisition of STEM images and 400 dark field contours, which have been used for thickness calibration of the GaAs wedge.

tion 3.5.2. Since STEM and CBED are essentially the same, specimen heating in STEM seems plausible. Nevertheless the effect should be much smaller for STEM, since not only local exposure time is smaller, but also beam current density decreases strongly, which might explain that heating is observed only at low temperature where the HAADF signal is very low. However, future experiments ought to check this by systematic sampling of a large temperature range, including temperatures significantly above 300 K.

3.6 Summary and conclusions

The diffraction of parallel electron nanoprobes can be used to measure specimen thickness, specimen orientation, crystal potential Fourier components and Debye parameters accurately with a modicum of experimental and computational effort. This makes the method suitable for deducing statistical averages from multiple independent measurements or for the measurement of structure factors for a variety of materials. A C2 aperture of a few microns in diameter in combination with a field emission gun is recommended to obtain nearly parallel probes and significant beam current densities at the same time. Still, the beam current is very low in the parallel beam electron diffraction (PBED), making specimen heating negligible unlike for the focused probes used in convergent beam electron diffraction (CBED). This means that Debye parameters for the temperature of the specimen holder may be taken from literature, so that their refinement is not necessary for low order structure factor measurement.

A considerable advantage of the CBED method is the possibility to check refinement results visually by comparing the internal structure of diffraction discs. However, the necessity of an accurate high voltage measurement increases the effort slightly, whereas zero loss energy filtering and the use of computer clusters for simulation of whole CBED discs are disadvantages from the financial point of view.

The concept of modified atomic scattering amplitudes (MASA) is verified for GaAs

by both PBED and CBED measurements in this work. Using PBED only, MASA have moreover been found to be valid for bulk InAs. This has important consequences for the composition evaluation by lattice fringe analysis (CELFA) method. As herewith both benchmarks (pure GaAs and pure InAs) of the chemically sensitive 200 potential in $\text{In}_x\text{Ga}_{1-x}\text{As}$ obtained from MASA have been validated, and because compositional dependence can be assumed to be linear, CELFA applied to $\text{In}_x\text{Ga}_{1-x}\text{As}$ will be in error in case reference data for isolated atoms is used. Since the CELFA method applies to many other sphalerite-type materials, the PBED method together with experimental conditions presented here is one efficient approach for future measurements of the respective chemically sensitive 200 potentials. In statistical manner, precision of PBED and CBED, obtained from independent refinements, are comparable.

Up to now, no inconsistency has been found between scattering data from density functional theory (DFT) and experiment. This also holds for Debye parameters, for which DFT values could be confirmed in this work by PBED. Whereas most of this thesis concentrates on conventional TEM and thus low-order structure factors, relevance of accurate Debye parameters has been demonstrated for quantitative scanning TEM. Best agreement was found at room temperature, but the impact of specimen heating during exposure seems to rise with decreasing temperature.

Chapter 4

Effects of bonding and static atomic displacements on composition quantification in $\text{In}_x\text{Ga}_{1-x}\text{N}_y\text{As}_{1-y}$

4.1 Introduction

The investigation of semiconductor nanostructures using TEM is an important feedback for the improvement and understanding of epitaxial and degradation processes of, e.g., optoelectronic devices, such as laser diodes and solar cells. These structures usually consist of (a sequence of) alternating nanometre-sized quantum well or quantum dot layers in host crystals, such as GaAs. InGaNAs has gained special interest during the last decade due to the possibility of lattice-matched growth of solar cells in the low-indium regime and strained high-indium infrared laser structures for telecommunication. For the present chapter, it is interesting to compare the progress in epitaxy, optical characterisation and theoretical modelling as described in chapter 1 with the progress in TEM for quaternary composition evaluation.

While a central question in the field of InGaNAs deals with short- and long-range order of indium and nitrogen, no TEM method has yet been developed at all to quantitatively measure both compositions locally. One method was presented by Grillo et al. [2] who used the superposition of a 200 dark field image recorded in a systematic row geometry, with an in-zone high resolution TEM (HRTEM) image to extract chemically sensitive contrast and strain. However, recording the same specimen area twice, under completely different imaging conditions is already extremely difficult, and superposition of both images cannot recover atomic resolution. Another approach was used by Litvinov et al. [3] who deduced nitrogen composition profiles via application of the composition evaluation by lattice fringe analysis (CELFA, [34]) method to both, an $\text{In}_x\text{Ga}_{1-x}\text{N}_y\text{As}_{1-y}$ and an $\text{In}_x\text{Ga}_{1-x}\text{As}$ quantum well grown under identical conditions except for the nitrogen incorporation. Being designed for ternary compounds only, nitrogen profiles could be obtained by assuming that indium is incorporated in the same manner in both wells, which must not necessarily be the case. Finally, the distribution of strain using 220 dark field imaging before and after thermal annealing has been shown to homogenise by Rubel et al. [22] and it has been interpreted in terms of a correlation of indium and nitrogen by the same authors.

Any approach in the field of TEM that aims at quantitative compositional analysis involves at least two main sub-disciplines. First, theoretical understanding of the mea-

surement is absolutely necessary because in principle all techniques derive their result from comparison with theoretical data. It was recently demonstrated theoretically by Rosenauer et al. [9] and experimentally by Müller et al. [5, 109] (see also chapter 3) that electron redistributions due to chemical bonding must be considered in binary GaAs and InAs. Yet it is evident that TEM analysis of quaternary InGaNAs with the long-term goal to investigate, e.g., the coordination of nitrogen, must include bonding. Moreover, it has been pointed out by Glas already in 1995 [112] that static atomic displacements (SAD) due to different radii of atoms on the same sublattice significantly alter TEM image contrast, too. As proposed about a decade later by the same author, the effect of SAD on structure factor moduli and phases of $\text{In}_x\text{Ga}_{1-x}\text{N}_y\text{As}_{1-y}$ ought to be studied systematically.

As outlined in chapter 2, both phenomena, bonding and SAD, are theoretically treated on complementary scales: SAD are derived from valence force field (VFF, [31, 32]) calculations and supercells with about 10^6 atoms, whereas bonding effects must be obtained from density functional theory (DFT), being limited to cells with about 10^2 atoms. However, the model of modified atomic scattering amplitudes (MASA, [9]), derived from DFT calculations for Bravais cells as reviewed in section 2.3.5, allows for an assignment of bonding in ideal crystals to atomic scattering amplitudes (ASA) of single atoms. This implies the following procedure for efficient structure factor modelling including both bonding and SAD, as suggested by Rosenauer et al. [9], who tested this approach theoretically for the 200 structure factor of InGaAs. However, SAD are significantly smaller there than in dilute nitrides. A large supercell is to be generated and relaxed by VFF. The structure factor of this cell is then calculated by indeed considering the displaced atoms, but conventional isolated atom ASA are replaced by (ideal crystal) MASA, assuming that SAD in the picometre range do not alter electron redistributions drastically. This ansatz is called *atomistic* approach in the following. Details on this procedure are also found in section 2.6.4. This proposed theoretical concept is verified for InGaNAs in the first part of this chapter. In particular, section 4.2 turns towards comparison of full DFT with VFF results by means of residual forces after strain relaxation. In order to densely sample the low-nitrogen-content range, large cells with 216 atoms are analysed. Atomistic and full DFT structure factors are compared as to moduli and phases.

Second, an experimental setup is to be designed that provides two sources of information for an unambiguous determination of both indium and nitrogen. Similar to Grillo et al. [2], strain and chemically sensitive contrast is evaluated here. Unlike them, we use two-beam CELFA imaging, which allows for simultaneous measurement of 200 lattice fringe strain and -contrast, and therefore atomic scale compositional mapping of both indium and nitrogen from one HRTEM image. Admittedly application of this method is limited to indium compositions below the null of the 200 structure factor, where fringe contrast passes a minimum and is shifted by π . However, the advantage of this approach is that we can profit from experiences collected with ternary alloys as to optimised imaging conditions and systematic errors. Thus no additional experimental complexity is introduced which entitles us to focus on the study of theoretical concepts mentioned above. For a treatment concentrated on the development of experimental techniques the reader is referred to chapter 5 or Ref. [134], where three-beam imaging is exploited to measure strain and contrast from 220 and 200 lattice fringes, being not coupled through nonlinear imaging. Here, an $\text{In}_{0.08}\text{Ga}_{0.92}\text{N}_{0.03}\text{As}_{0.97}$ solar cell structure is investigated experimentally using different models for the simulation of reference data in section 4.3, where strain state analysis and CELFA are also briefly reviewed.

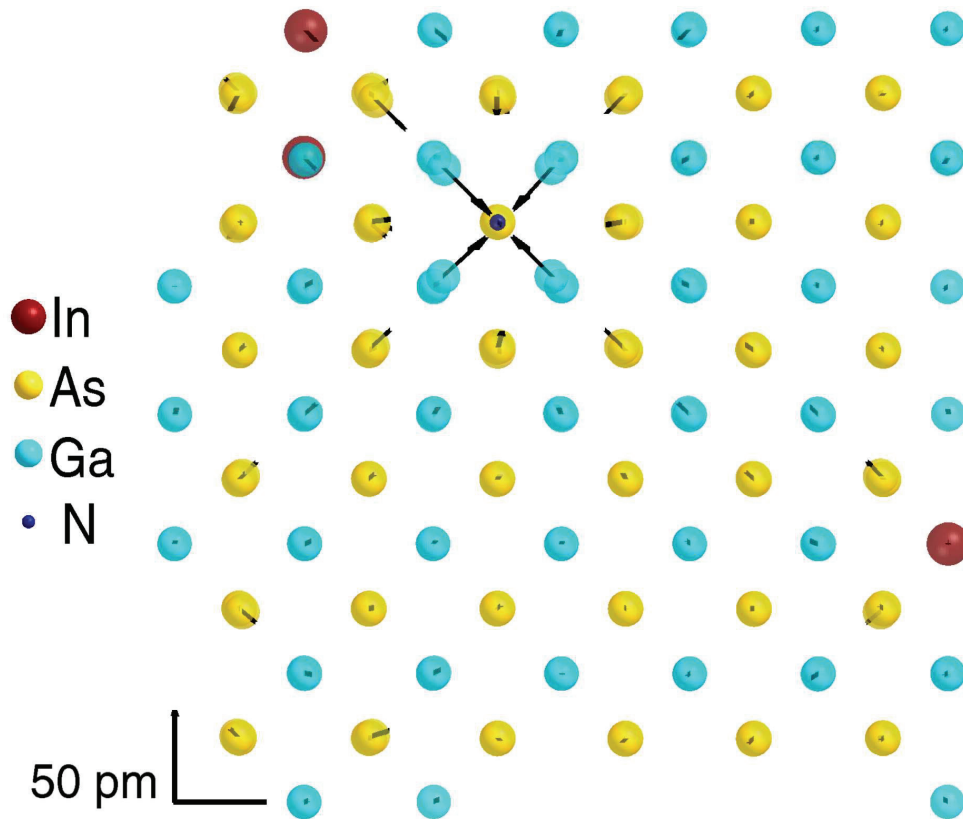


Figure 4.1: Static atomic displacements obtained from VFF for one of the 25 supercells containing 3 In atoms and 1 N atom. View is along $[100]$, displacements are enlarged by a factor of 4. See trihedral bottom left for absolute scaling of SAD.

This chapter closes with the discussion of experimental results in the framework of bonding effects and SAD in section 4.4. A summary of this chapter and important conclusions are found in section 4.5.

4.2 Valence force field and first-principles calculations

An accurate way to treat a quaternary structure including SAD is to place indium and nitrogen atoms at random positions of the respective sublattice in an ideal crystal and to use this structure as an initial guess for a relaxation based on forces derived from first principles, that is, DFT as described in section 2.3.3. However, as a systematic study of various supercells with different indium and nitrogen compositions is intended here, this approach is unreliable since, e.g., one solution of the Kohn-Sham equations (2.17) with respect to converged Hellmann-Feynman forces takes about five days on four 2.88 GHz CPU. In order to not only reduce computational effort drastically, but also to compare VFF calculations with ab-initio calculations as to residual forces, structure relaxation has been sourced out using empirical potentials. Then, only one DFT calculation was performed using the WIEN2K [66] code, yielding the desired Hellmann-Feynman forces acting on each atom.

4.2.1 Minimisation of strain energy

GaAs supercells have been chosen to be $3 \times 3 \times 3$ Bravais cells in size. Then, 0, 3, 6, 9 or 12 gallium atoms have been replaced randomly by indium and 0, 1, 2, 3 or 4 arsenic atoms by nitrogen. This corresponds to a 5×5 grid of concentrations between 0 and 0.111 for indium and between 0 and 0.037 for nitrogen, respectively. To derive a property $\alpha(x, y)$ for $\text{In}_x\text{Ga}_{1-x}\text{N}_y\text{As}_{1-y}$ from properties of binary crystals, linear interpolation according to Vegard's rule [102] for ternary compounds is taken as a basis. Thus, in generalisation for quaternary materials we find

$$\alpha(x, y) = xy \cdot \alpha_{\text{InN}} + x(1 - y) \cdot \alpha_{\text{InAs}} + y(1 - x) \cdot \alpha_{\text{GaN}} + (1 - x)(1 - y) \cdot \alpha_{\text{GaAs}} \quad , \quad (4.1)$$

e.g., for the lattice parameters.

Local strain induced by the indium and nitrogen dopant atoms was then minimised by VFF according to Keating's model [31] as implemented by Rubel et al. [32]. For a detailed description see also section 2.6.2. Elastic constants, lattice parameters and bond lengths $R_{jk} = a_{\text{EXP}}\sqrt{3}/4$ are listed in table 2.1.

Whereas the impact of SAD was regarded in statistical manner only in section 2.6.2, we now look at their characteristics concerning direction and strength at certain atoms in more detail. For this purpose, a VFF-relaxed cell with 3 indium atoms and 1 nitrogen atom is depicted in Fig. 4.1. Vectors represent SAD, enlarged by a factor of 4 to improve visibility. However, it can clearly be seen that SAD concentrate near impurity atoms and that they are several times larger in the environment of nitrogen than near indium, being about 40 pm in the former and about 15 pm in the latter case. Moreover, Fig. 4.1 exhibits that the sense of SAD is opposite in both environments, confirming the intuitive approach which explains SAD in terms of atom size effects. Finally, the strain field, especially that caused by nitrogen, reaches farther than a lattice parameter, making SAD a complex topic. This means that strain fields of several impurities are not independent but influence each other.

4.2.2 Density functional theory results

Each of the 25 structures has been strain-relaxed using VFF as exemplified in Fig. 4.1. Using the WIEN2K [66] software explained in section 2.3.4, DFT calculations have been performed using these cells as input. All calculations have been carried out in local density approximation (LDA) with a force convergence criterion of 0.01 mRy/bohr. The number of k-points was set to 14. The product of cutoff frequency and the minimum muffin-tin radius (RK_{max}) was 6.0. A self-consistent solution of the Kohn-Sham equations (2.17) was found after 20 – 30 cycles, depending on the respective supercell. Note that solely forces have been calculated self-consistently and that no DFT structure optimisation was performed. Consistency with calculations using 28 k-points and $\text{RK}_{\text{max}} = 7.0$ was checked. Equilibrium lattice parameters for the binary crystals have also been found by DFT [81] and are listed in table 2.1.

Residual forces

Since direct comparison of relaxed positions from DFT with those of VFF is unpracticable for these large cells, plausibility of VFF atomic positions is first regarded by means of residual global atomic forces as calculated in the last cycle of DFT. Resulting force vectors for each atom are depicted in Fig. 4.2 exemplarily for the supercell containing 12

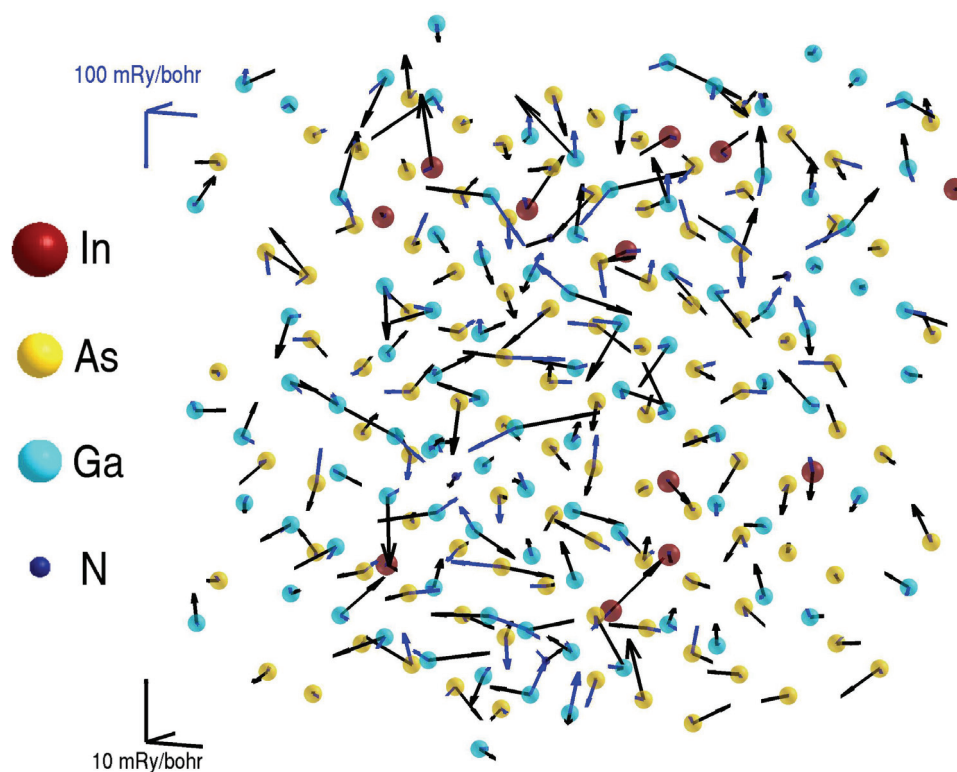


Figure 4.2: Residual forces resulting from DFT for a supercell containing 12 In and 4 N atoms before (blue) and after (black) VFF optimisation. The trihedrals top and bottom left refer to the scaling of the respective force vectors.

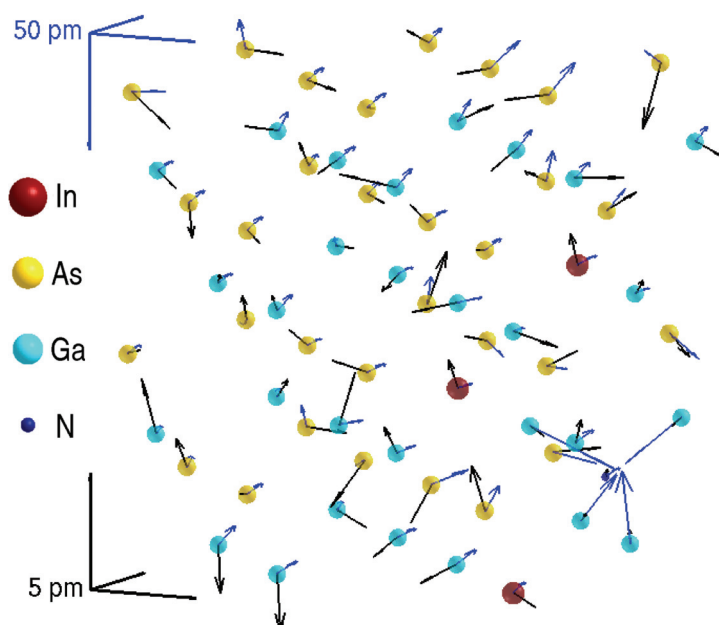


Figure 4.3: Comparison of SAD found by VFF and DFT. *Blue*: SAD vectors ($\times 5$) from VFF. *Black*: Difference vectors ($\times 50$) between relaxed positions from DFT and VFF, respectively. See the blue or black trihedron top and bottom left for an absolute scaling of the SAD and difference vectors, respectively.

indium and 4 nitrogen atoms. The discussion of this cell may be thought of as the most representative because it contains the most dopant atoms.

Blue and black vectors in Fig. 4.2 indicate forces acting on each atom before and after the VFF relaxation, respectively. As the trihedrals in Fig. 4.2 indicate, VFF relaxation reduces forces by approximately one order of magnitude, because blue vectors are frequently about 80mRy/bohr in length, whereas black ones correspond to 10mRy/bohr in the worst case. Moreover, it can be seen that strong forces occur in the vicinity of substitutional indium- and nitrogen atoms for the unrelaxed supercell, whereas the magnitudes and directions of force vectors in the relaxed cell are distributed more or less statistically. In the picture of the VFF method, we must therefore interpret forces of maximal 10mRy/bohr as a systematical error of this approach for a relaxed supercell.

As the magnitude of these forces is still larger than typical residual forces after structure optimisation using DFT only, the impact of this error on SAD is addressed in the following. This was done using a computationally less demanding 64-atom $2 \times 2 \times 2$ supercell with 3 indium atoms and 1 nitrogen atom. First, atom positions have been optimised by VFF, and second, this structure was further optimised using WIEN2K. In this way, difference vectors have been obtained which point from atom positions found by DFT to respective positions found by VFF. They are thus a direct measure of the error for SAD computed with the VFF approach. Figure 4.3 depicts these difference vectors in black for each atom, magnified by a factor of 50.

It can be seen that discrepancies between VFF and DFT are statistically distributed and not concentrated on specific sites of e.g. the dopant atoms. The blue vectors in Fig. 4.3 depict the SAD directly, magnified by a factor of 5. Here, the strong local lattice distortions induced by the nitrogen atom bottom right becomes obvious as in Fig. 4.1. As to the accuracy of the VFF method, we must conclude that differences to DFT results, being 2.58 pm in the maximum, are more than an order of magnitude lower than the SAD themselves, which take values up to 37.96 pm. Therefore, the error falls in the range of thermal vibrational amplitudes, which are typically a few picometers in magnitude. Thus, atom positions deduced from VFF are physically plausible, even with residual forces found in Fig. 4.2. In view of the goal to express the structure factor of a large, VFF-relaxed cell by means of an atomistic approach, the criterion that VFF yields reliable atomic positions is met. Hence, what remains questionable is whether MASA represent bonding sufficiently accurate for these cells, which is analysed now.

Structure factors

Using the linearised-augmented plane wave routine LAPW3 of the WIEN2K software, X-ray structure factors have been calculated according to Eq. (2.26) for all 25 supercells. Since DFT does not account for thermal motion, Debye-Waller factors are disregarded (i.e. set equal to 1) in the following. However, as we are only interested in a comparison of models at this stage, this makes sense even if real structure factors must include temperature factors. Note that this does not even correspond to the real situation at absolute zero due to the zero-point atomic motion. All X-ray structure factors have been converted to electron structure factors using the Mott-Bethe formula (2.12) [9, 47]. These DFT electron structure factors for the relaxed supercells can be used to analyse the reliability of atomistic models as to the effects of bonding and SAD by comparison with structure factors derived from Eq. (2.10).

In case of isolated atom ASA, structure factor calculation is no problem since ASA are uniquely defined when the atomic species is given. For MASA, the situation is different

since they depend on crystal type κ according to Eq. (2.31). Because we aim to include *local* bonding, application of the virtual crystal approximation to the composition of the full supercell, as described by Eq. (2.32), is assessed to be a too crude approximation. Instead, it is assumed that Eq. (2.32) holds for a smaller unit defined by the atom of interest and its four bond partners. In particular, the final MASA for an atom is found as follows: First, the atomic species of the atom of interest is determined. Second, the four nearest neighbours are searched for. For atoms at the edge of the cell, periodic boundary conditions are applied. Third, atomic species of these neighbours are determined. Fourth, four MASA are calculated from a lookup table according to the four binary crystal types defined by the atom of interest and its respective neighbour. It should be noticed that not the local lattice parameter is used at this step but that given by the whole cell in order to save computation time for cells with 10^6 atoms. Finally, the mean of the four MASA is taken and assigned to the atom of interest. As an example, let us consider an indium atom in an InGaNAs supercell with lattice parameters \mathbf{a} , where \mathbf{a} is a vector containing the three lattice parameters which may be different due to tetragonal distortion in quantum wells. Let this indium atom be bound to three arsenic atom and one nitrogen atom, then we find for its MASA

$$f_{In}^{\mathbf{a}}(\mathbf{g}) = \frac{1}{4} \left(3 \cdot f_{In}^{\mathbf{a},InAs}(\mathbf{g}) + f_{In}^{\mathbf{a},InN}(\mathbf{g}) \right) \quad . \quad (4.2)$$

We start with the analysis of the chemically sensitive 200 structure factor¹. The result obtained from DFT for the relaxed supercell is depicted in Fig. 4.4 in dependence on the indium- and nitrogen content.

Even for the small concentration ranges considered here, Fig. 4.4 exhibits strong but smooth variation of $\text{Re}(V_{200})$ with composition, as it is typical for chemically sensitive zinc blende systems. In the following, we assume that the data in Fig. 4.4 represent the most accurate scattering data for the 25 supercells considered, because it stems directly from DFT and no model assumptions concerning SAD and ASA entered the simulations. Therefore, we can use these structure factors as a reference to check the accuracy of atomistic models.

To this end, four maps have been calculated analogous to Fig. 4.4 using either MASA or isolated atom ASA with atom positions in the relaxed supercell, as well as either MASA or isolated atom ASA with atom positions in the unrelaxed supercell. Structure factors obtained this way were subtracted from those in Fig. 4.4. Instead of looking at differences as a function of composition, they will be analysed statistically to stress the behaviour of different models, and to present results in a compact manner. Histograms of these differences are depicted in Fig. 4.5. Consequently, we expect an absolute frequency of 25 at zero for an exact model, since the atomistic 200 structure factors equal those from full DFT for all compositions then.

From the view of atomistic models, Fig. 4.5 can be interpreted as follows. For the first two data sets (a) and (b), V_{200} was calculated from Eq. (2.10) with correct atom positions r_j in a relaxed supercell, that is SAD are accounted for by VFF. In case of data set (a), MASA were used to calculate structure factors, whereas ASA for isolated atoms entered the derivation of data set (b). Obviously, the neglect of bonding effects can lead to large deviations of 0.054-0.123 V. According to table 3.8, this means a relative error of up to 30%, if normalised to the 200 potential of GaAs. In contrast, the bars of set (a) are

¹For the $3 \times 3 \times 3$ supercells this corresponds to the 600 structure factor. However, we refer to the nomenclature for Bravais cells in this chapter.

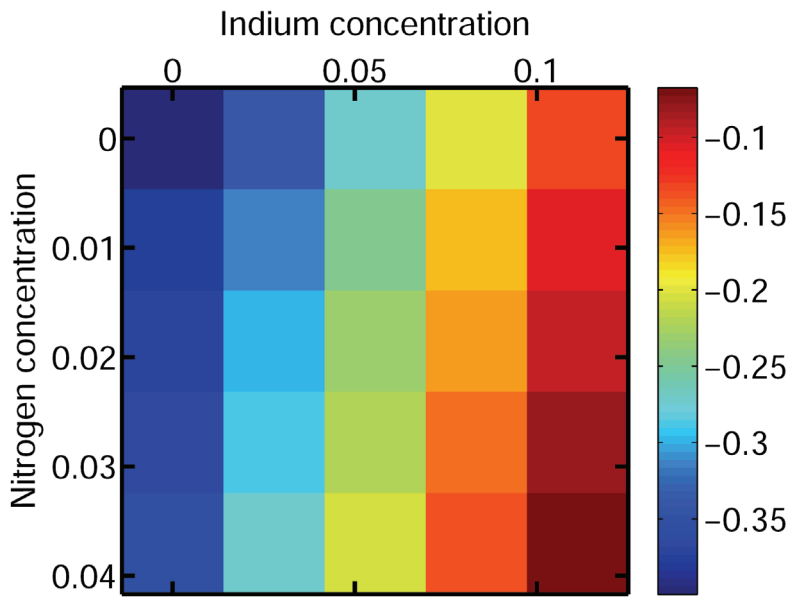


Figure 4.4: V_{200} (real part) in volts as a function of In- and N-content obtained from first principles for the relaxed $3 \times 3 \times 3$ InGaNAs supercells. Concentrations correspond to 0, 1, 2, 3, 4 N- and 0, 3, 6, 9, 12 In-atoms, respectively.

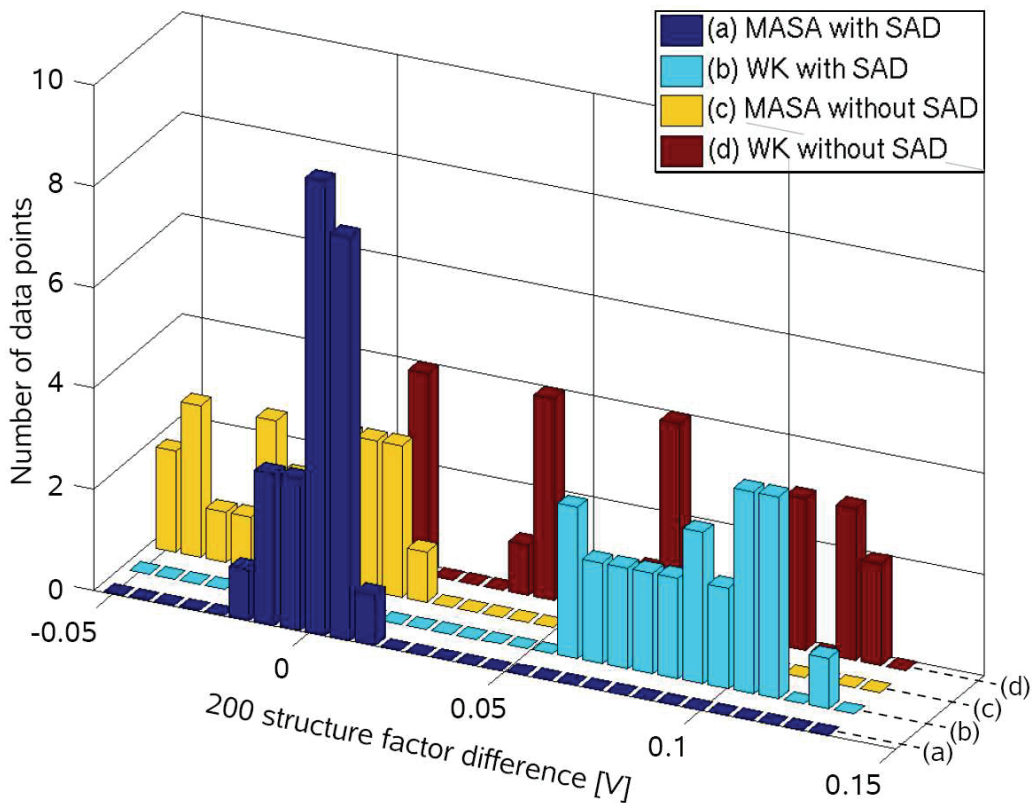
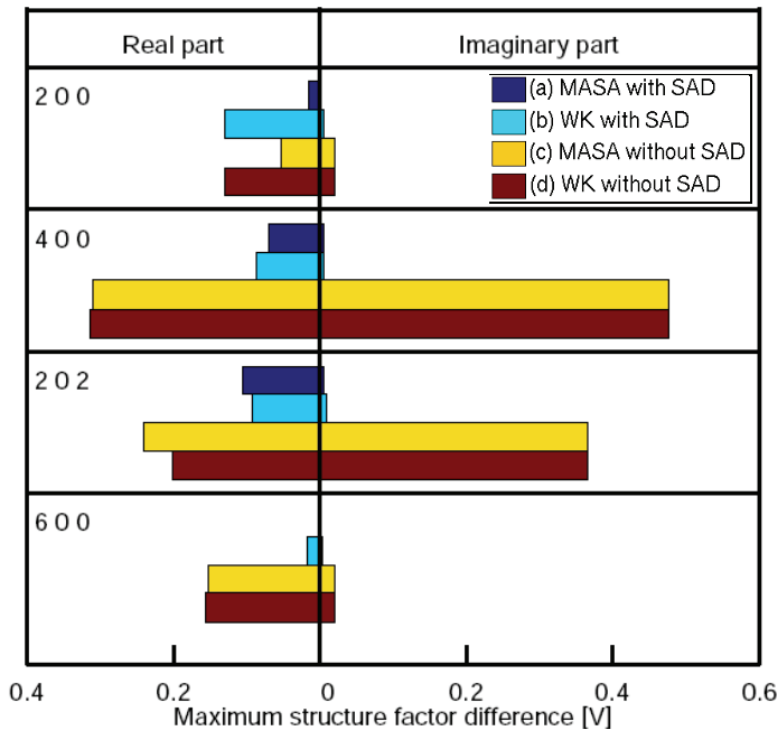


Figure 4.5: Histogram to show the reliability of different atomistic models (see legend) for the 200 structure factor. Differences between the 25 structure factors in Fig. 4.4 and those obtained from the respective model have been calculated and the absolute frequency is shown for 29 difference intervals. Data sets (a) and (c) contain bonding effects via MASA, (b) and (d) correspond to isolated atom scattering data due to Weickenmeier and Kohl (WK [75]). Furthermore, (a) and (b) contain SAD, (c) and (d) do not.

Figure 4.6: Comparison of structure factors obtained from several atomistic models (see legend) and those calculated by DFT in terms of the largest difference to full DFT (see Fig. 4.4 for $\text{Re}(V_{200})$). Real and imaginary parts are treated separately, and only moduli of differences are given. Data sets (a) and (c) contain bonding effects via MASA, (b) and (d) correspond to isolated atom ASA (WK [75]). Furthermore, (a) and (b) contain SAD, (c) and (d) do not.



concentrated relatively closely around zero, where an 0.015 V too large structure factor is found in the worst case. However, the MASA concept together with SAD yields the most accurate and the most precise 200 structure factor for the structures considered here. Data sets (c) and (d) both exhibit a much lower precision than the respective counterparts (a) and (b). In the case of MASA without SAD, (c), a tail towards negative differences develops, which means that the structure factors obtained this way are principally too large.

We eventually look at the reliability of structure factors obtained from atomistic models by considering also higher-order structure factors. These may not only be of importance, e.g., for the simulation of reference data for chemical compositional analysis or conventional TEM images in zone axis, but also to see if atomistic approaches are able to represent structure factor phases in presence of SAD correctly [8]. For the 400, 202 and the chemically sensitive 600 structure factors, analogous maps to Fig. 4.4 have been calculated, as in case of 200, using the approximations (a-d) described above. However, presentation of the results was further simplified via replacing the full histograms in Fig. 4.5 by considering solely the largest occurring difference to full DFT. To judge the behaviour of structure factor phases, real- and imaginary parts have been considered separately. In this way, an upper limit for the errors induced by atomistic treatment is derived. Results are plotted in Fig. 4.6, together with the results for V_{200} .

It can clearly be seen that the discrepancy between the MASA model (a,c) and isolated atom scattering factors (b,d) becomes negligible for higher-order structure factors. This expresses the fact that low-order structure factors are most sensitive to electron redistributions due to bonding, as was found before [5, 6] and in chapter 3. It is important to note that the 400 and 202 structure factors are more than an order of magnitude larger than V_{200} , which relativises the seemingly large error. For example, we find real parts of $V_{200} = -0.149 V$, $V_{400} = 4.667 V$, $V_{202} = 6.783 V$ and $V_{600} = -0.03 V$ for $x = 0.083$ and $y = 0.028$, which is very close to the composition of the sample analysed experimentally in section 4.3. However, the neglect of SAD can produce enormous errors as the bars cor-

responding to approaches (c) and (d) take large values of nearly half a volt. Depending on the structure factor, this corresponds to a relative error of 3-40%.

We conclude that SAD must be considered in $\text{In}_x\text{Ga}_{1-x}\text{N}_y\text{As}_{1-y}$ systems in order to get reliable structure factor amplitudes and phases. The use of MASA is important mainly for the 200 structure factor and approaches isolated atom scattering data for higher spacial frequencies. This is because electron redistributions due to chemical bonding primarily affect the outermost orbitals of an atom which corresponds to low spatial frequencies in the Fourier spectrum. However, not only the dynamical interaction among diffracted beams but also the correct intensity of the 200 reflection require bonding effects to be considered for a quantitative comparison between experiment and simulation.

4.3 Experimental composition quantification in InGaNAs

4.3.1 Methodical summary

We now turn towards the evaluation of strain and contrast in experimental two-beam lattice fringe images. The composition of ternary zinc blende alloys such as InGaAs has been extensively studied in the past either with respect to lattice strain or normalised 200 lattice fringe contrast [34]. Both quantities are usually measured from lattice fringes acquired by inserting an objective aperture around the beams $\mathbf{g}_1 = 000$ and $\mathbf{g}_2 = 200$ in the focal plane of the objective lens. That 200 fringe contrast is strongly dependent on composition can immediately be seen from Fig. 4.4. To motivate the analysis of strain, we must take a combined look at Vegard's rule in Eq. (4.1) and lattice constants of binary materials in table 2.1. From this follows that the lattice parameter of, e.g., an $\text{In}_x\text{Ga}_{1-x}\text{N}_y\text{As}_{1-y}$ alloy depends on compositions x and y and may thus be used to measure it. However, the situation is more complicated since Eq. (4.1) holds for situations without stress. In real crystals, internal stresses are indeed present because quantum layers are epitaxially grown pseudomorphically on a substrate. In bulk specimen, this constrains two of the lattice constants to be equal to those of the substrate. As a consequence of specimen thinning during TEM specimen preparation, stress along the surface normal may release partially or fully, depending on specimen thickness. In the following, the concept to describe the deformation of unit cells in the framework of elasticity theory is briefly reviewed.

Strain state analysis

A complete picture of elasticity theory can be achieved in three steps. First, we must find out how coordinates in a continuum may transform in general and how it is described mathematically. Second, a formalism to account for internal stress must be given and third, a relation between strain and stress is needed.

According to Joos [135], considering all possible coordinate changes less rotation and translation as a whole leads to the strain tensor $\underline{\underline{\epsilon}}$. The new coordinate after deformation is then given by $\mathbf{r}' = \mathbf{r} + \underline{\underline{\epsilon}}\mathbf{r}$, where \mathbf{r} is the coordinate of a point in the undeformed object. For example, we find for the change of the x -component $x' - x = \epsilon_{11}x + \epsilon_{12}y + \epsilon_{13}z$, implying that pure elongation/compression is expressed by diagonal terms of $\underline{\underline{\epsilon}}$, whereas off-diagonal entries lead to a change of the angle between two vectors. Given an elastic deformation and a representation of $\underline{\underline{\epsilon}}$ in a certain coordinate frame, this will lead to

internal forces and hence stress, which again is a tensor as $\underline{\underline{\epsilon}}$, denoted by $\underline{\underline{\sigma}}$. Off-diagonal elements represent shear stress, whereas in diagonalised form only principal stresses exist. Since both $\underline{\underline{\sigma}}$ and $\underline{\underline{\epsilon}}$ can be represented by two-dimensional arrays, they are second-rank tensors.

It is obvious that both quantities are not independent, because deformation induces stress and the other way round. In particular, stress and strain tensors are coupled by a generalisation of Hooke's law. Using Einstein's summing convention, we have

$$\sigma_{ij} = C_{ijkl} \epsilon_{kl} \quad , \quad (4.3)$$

where C_{ijkl} is the stiffness tensor with rank 4. However, due to symmetries many of the entries in each of the three tensors are not independent, so that Hooke's law (4.3) can be represented using two-dimensional matrices. In this Voigt notation [136], stress and strain take the form

$$\underline{\underline{\sigma}}^{6 \times 1} = \underline{\underline{C}}^{6 \times 6} \underline{\underline{\epsilon}}^{6 \times 1} \quad \text{and} \quad \underline{\underline{\epsilon}}^{6 \times 1} = (\underline{\underline{C}}^{6 \times 6})^{-1} \underline{\underline{\sigma}}^{6 \times 1} \quad , \quad (4.4)$$

where $\underline{\underline{\sigma}}^{6 \times 1}$ and $\underline{\underline{\epsilon}}^{6 \times 1}$ are vectors whose first three entries are given by the diagonal of $\underline{\underline{\sigma}}$ and $\underline{\underline{\epsilon}}$. The latter three components of, e.g., $\underline{\underline{\sigma}}^{6 \times 1}$, are given by σ_{23} , σ_{31} , σ_{12} and for $\underline{\underline{\epsilon}}^{6 \times 1}$ accordingly. In addition, the shape of $\underline{\underline{C}}^{6 \times 6}$ is determined by crystal symmetries [136]. For the cubic phase, $C_{11}^{6 \times 6}$, $C_{12}^{6 \times 6}$ and $C_{44}^{6 \times 6}$ determine $\underline{\underline{C}}^{6 \times 6}$ uniquely. The second expression in Eq. (4.4) is of major importance for strain state analysis, because it allows for computation of $\underline{\underline{\epsilon}}^{6 \times 1}$ when boundary conditions for $\underline{\underline{\sigma}}^{6 \times 1}$ and the compliance matrix $(\underline{\underline{C}}^{6 \times 6})^{-1}$ are given. In the following, solely Voigt's notation is used and the superscript is omitted. It is nevertheless important to keep in mind that tensors of ranks 2 and 4 are considered, especially if coordinate transformations are to be accomplished (that is, rotation of C_{ijkl}).

Specimens investigated in this chapter are grown along [100] and thinned for TEM investigations along [010]. As there is neither shear nor stress in growth direction, $\underline{\underline{\sigma}}$ has nonzero components only in the (100) plane. In particular, $\sigma_2 = \sigma_3$ for bulk InGaNAs due to cubic symmetry and $\sigma_2 = [0 \dots \sigma_3]$ for thinned specimens. However, σ_2 is not expressed absolutely but in terms of σ_3 via $\sigma_2 = r \cdot \sigma_3$ with a parameter $r = [0 \dots 1]$ measuring the relaxation along zone axis direction. Thus, we have $r = 0$ for infinitely thin specimen and $r = 1$ for infinitely thick ones. Solving for ϵ_1 in Eq. (4.4) using these boundary conditions results in

$$a_{[100]} = a(\sigma = 0) + \frac{C_{12} [a(\sigma = 0) - a_{sub}] (1 + r)}{C_{11} + C_{12} - rC_{12}} \quad (4.5)$$

for the lattice parameter $a_{[100]}$ (in growth direction) of the tetragonally distorted cell. Equation (4.5) also contains the lattice parameter of the substrate, a_{sub} , and that of a (fictitious) fully relaxed cell of the layer, which is denoted by $a(\sigma = 0)$. Its compositional dependence can be derived from Eq. (4.1). In this way, reference lattice parameters can be calculated concentration-dependent, serving as a lookup table for strain state analysis. As the local measurement of absolute lattice parameters in HRTEM is difficult, both measurement and simulation are usually normalised to a_{sub} , so that we can define the relative fringe distance in [100] direction

$$\varepsilon_{[100]} = \frac{d_{[100]}}{d_{sub,[100]}} = \frac{a_{[100]}}{a_{sub}} \quad (4.6)$$

to be the measured parameter from lattice fringe images. For the second identity, it was assumed that the (absolute) fringe distances $d_{[100]}$ and $d_{sub,[100]}$ are equal to the distance of

the corresponding lattice planes, meaning that they are not altered by imaging through aberrations and defocus. As an example, dashed contours in Fig. 4.8 exhibit strong dependence of this ratio on composition. Moreover, this graphic shows the impact of tetragonal distortion: Whereas the lattice mismatch between InAs and GaAs is only about 7%, InAs would take a 13% larger lattice constant in growth direction than GaAs for a relaxation of $r = 0.5$. The degree of thin foil relaxation in zone axis direction does usually not only depend on elastic constants and specimen thickness, but also on the thickness of the strained layer and the composition profile. In particular, the ratio of specimen- and layer thickness governs the magnitude of r [137]. Whereas finite element simulations ought to be performed to determine the degree of thin foil relaxation reliably, we restrict investigations on intermediate relaxation $r = 0.5$ in this work and give estimates for the maximum errors assuming $r = 0$ and $r = 1$ where strained layers are investigated (chapter 5). To nevertheless estimate the thickness ranges in which $r = 0$ and $r = 1$ become valid, the model of Treacy [138] can be used to obtain the average lattice parameter in zone axis direction. For a 6 nm thick GaAs/In_xGa_{1-x}As/GaAs layer, it was found that $r = 1$ is valid above approximately 70 nm, whereas $r = 0$ is significantly wrong above 5 nm. Note that the simple expression (4.5) is only valid for cubic material thinned along [010]. Formulae become significantly more complicated for other crystal systems and/or thinning along high-index zone axes.

Composition evaluation by lattice fringe analysis (CELFA)

For a two-beam imaging condition the image intensity at position \mathbf{r} reads

$$I(\mathbf{r}) = A_1^2 + A_2^2 + 2A_1A_2T_{12} \cos(2\pi\mathbf{g}_2\mathbf{r} - \phi_{12} - \varphi_{12}) \quad , \quad (4.7)$$

where $A_n \exp(i\varphi_n)$ is the amplitude of diffracted beam \mathbf{g}_n , $\varphi_{12} = \varphi_1 - \varphi_2$ is the phase difference between the two beams and $T_{12} \exp(i\phi_{12})$ denotes the transmission cross coefficient. Note that most quantities in Eq. (4.7) do not only depend on composition, but also on thickness and specimen tilt in general, an aspect which will be discussed later. The measured quantity is the normalised fringe amplitude a_N defined by

$$a_N(\mathbf{r}, t, x, y) = \frac{A_1(\mathbf{r}, t, x, y)A_2(\mathbf{r}, t, x, y)}{A_1(\mathbf{r}, t, 0, 0)A_2(\mathbf{r}, t, 0, 0)} \quad , \quad (4.8)$$

meaning that the contrast is not measured absolutely but normalised to GaAs.

The central part of Fig. 4.7 depicts an experimental 200 lattice fringe image acquired with a specimen tilt corresponding to a Laue circle centre of (1.5 0 20). The bright fringes top and bottom correspond to GaAs buffer layers enclosing an In_xGa_{1-x}N_yAs_{1-y} quantum well grown by metal organic vapour phase epitaxy, which exhibits a significantly lower contrast. By applying an aperture around the 200 reflection in the diffractogram and inverse Fourier transformation, the local distribution of the 200 fringe amplitude is obtained. In practice, regions with known composition, in this case the GaAs buffer layers, are used for a fifth-order polynomial fit of a surface serving as a reference where the measured signal is normalised to.

Application to an experimental image

A map of a_N derived this way is shown on the left in Fig. 4.7. It can clearly be seen that the normalised amplitude in the quantum well region takes only about 30% of the

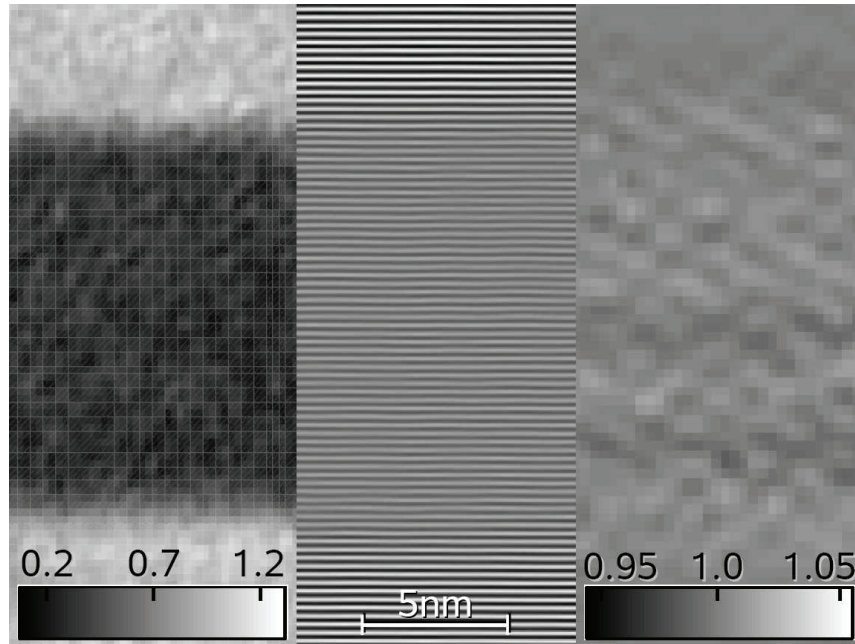


Figure 4.7: Evaluation of contrast and local relative fringe distance $\varepsilon_{[100]}$ in an experimental 200 lattice fringe image. The central part shows the recorded fringe image (part) which has been noise filtered for better visibility. The map on the left depicts the fringe amplitude normalised to GaAs as defined in Eq. (4.8). On the right, $\varepsilon_{[100]}$ is shown which was measured from local cosine fit in the fringe image.

amplitude in the GaAs substrate. In order to measure the local fringe distance depicted on the right in Fig. 4.7 with subpixel precision, first those pixels with highest intensity on each fringe have been determined, second these positions have been refined by local cosine fit according to Eq. (4.7), and third the local fringe distance has been normalised to the average value measured in the GaAs buffer. The map in Fig. 4.7 exhibits lattice-matched growth with slight fluctuations of less than 1%, which may arise from uncertainties in the measurement of the local fringe distances due to the low contrast in the quantum well area. By comparison of the local normalised amplitude and the local normalised fringe distances with corresponding reference data, atomic-scale concentration maps for indium and nitrogen can be derived.

4.3.2 Simulation of reference data

The composition-dependent strain in growth direction was derived from elasticity theory corresponding to Eq. (4.5) in combination with Eq. (4.1) using lattice parameters a_{EXP} and elastic constants C_{11} and C_{12} for the binary compounds given in table 2.1. It was assumed that an $\text{In}_x\text{Ga}_{1-x}\text{N}_y\text{As}_{1-y}$ quantum well is embedded dislocation free in GaAs and thinned along zone axis [010].

According to Eq. (4.7), composition-dependent Bloch wave amplitudes have been simulated using the Bloch4TEM software [37] as explained in section 2.4. Lattice parameters were calculated for tetragonally distorted cells and simulations have been performed assuming each of the four atomistic models dealt with in section 4.2. A Laue circle centre of (1.5 0 20) was used as for the experimental image in Fig. 4.7 and about 150 beams from two Laue zones have been included. Debye parameters were chosen according to Ref. [81] for 300 K. To include SAD, supercells with 10^6 atoms have been relaxed using

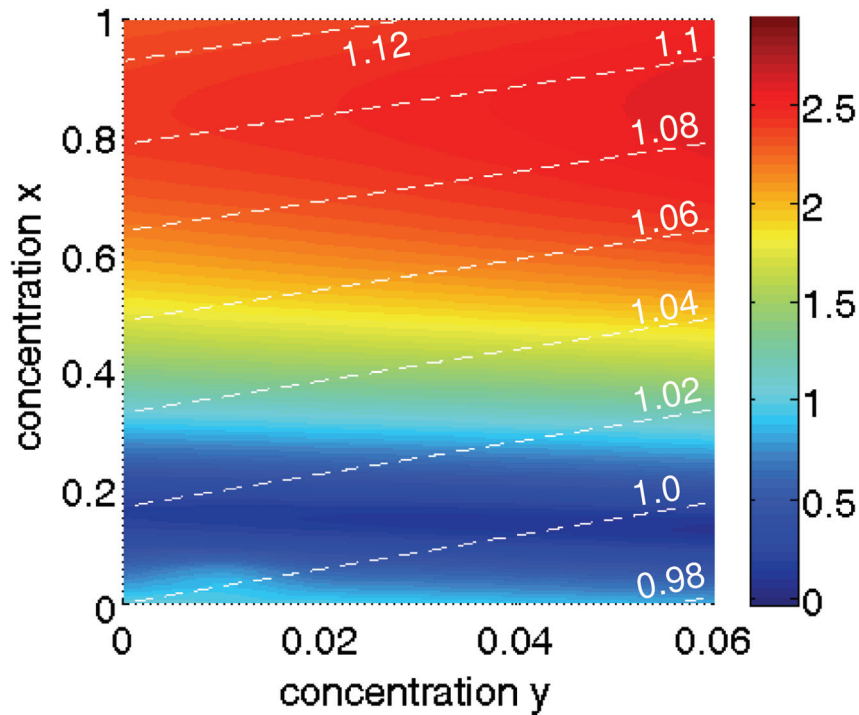


Figure 4.8: Reference data for $a_N(50 \text{ nm}, x, y)$ (colour-coded) and the relative fringe distance $\varepsilon_{[100]}$ (dashed white contour lines). In the case shown here, atomic scattering factors contained bonding and SAD via MASA and VFF relaxation, respectively. Simulations have been carried out for a thickness range of 0 – 100 nm, of which the 50 nm simulation is shown. Both data sets correspond to a relaxation of $r = 0.5$.

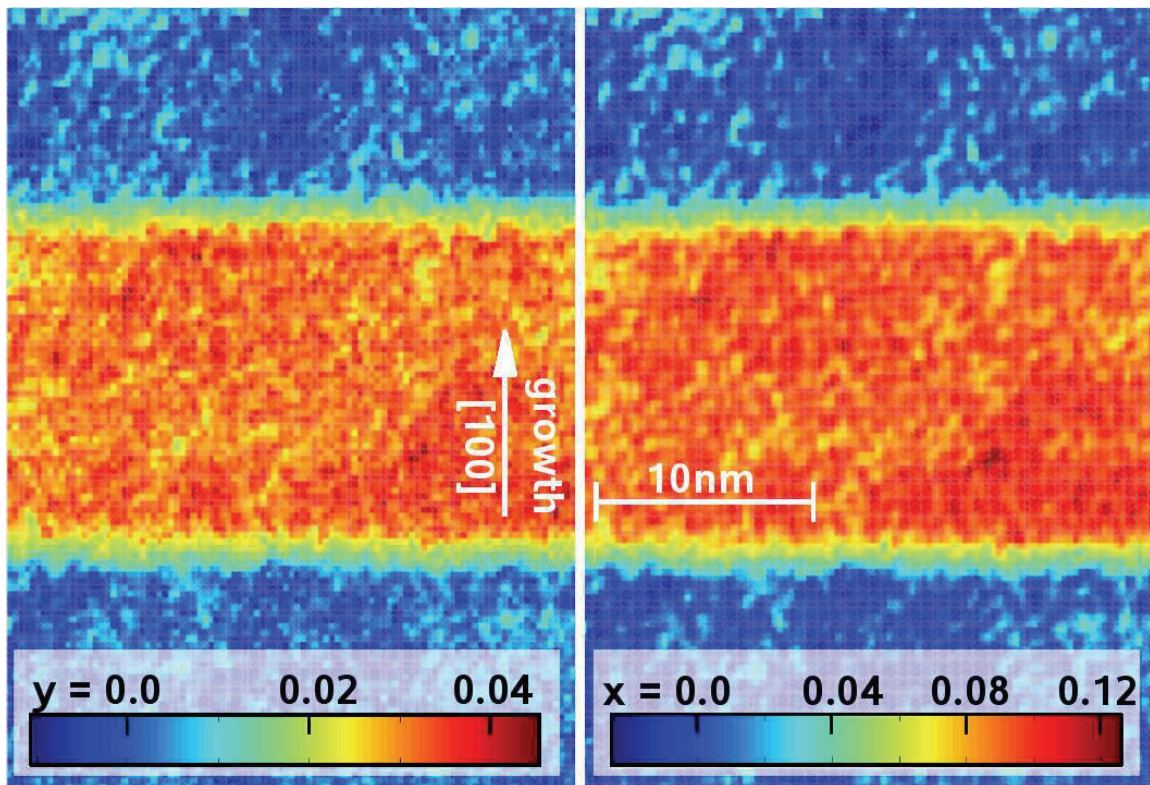


Figure 4.9: Local distributions of indium and nitrogen in a quantum well region derived from reference amplitudes which include MASA and SAD according to Fig. 4.8.

the VFF program [32] introduced in section 2.6.2 and structure factors were derived from the relaxed cells.

Together with isolines for the relative fringe distance, Fig. 4.8 depicts a map of $a_N(50 \text{ nm}, x, y)$ according to Eq. (4.8) for indium contents $x \in [0 \dots 1]$ and nitrogen contents $y \in [0 \dots 0.06]$. As amplitude and isolines for the relative fringe distance incline an angle of about 20 degrees, an amplitude-strain pair can in principle be assigned a concentration pair (x, y) . However, the null of the 200 structure factor defines a valley depicted in dark blue, so that two solutions exist below $x \approx 0.35$. Nevertheless it is in general no problem to distinguish between both because φ_{12} suffers a phase jump of π here which becomes obvious in the fringe image. Note that, although the 200 structure factor vanishes, the normalised amplitude still takes finite values of 10-15%. Figure 4.8 also exhibits that the indium content determines both local fringe distance and normalised amplitude, whereas the nitrogen content modifies the normalised amplitude only marginally and primarily affects the fringe distance.

4.3.3 Composition maps and profiles

The distribution of indium and nitrogen derived from reference data including bonding via MASA and SAD via VFF is shown in Fig. 4.9. Both concentration maps exhibit a 15 nm wide quantum well with nearly uniform composition inside the well and gradual change at its edges. As to the state of relaxation in beam direction, it should be mentioned that it has no influence on the result for this structure since it was grown lattice-matched to GaAs as depicted in Fig. 4.7.

The impact of bonding and SAD on composition evaluation is presented in the form of composition profiles shown in Figs. 4.10 and 4.11. Error bars represent the standard deviation for the lateral average in Fig. 4.9 and take values of 1% and 0.7% for indium and nitrogen, respectively. The black graphs have directly been derived from composition maps in Fig. 4.9, whereas composition maps for the other curves are not shown.

For both elements, we can divide the composition profiles into two pairs of curves of which one contains bonding (blue and black lines) and the other not (red and green lines). In both figures 4.10 and 4.11, the effect of MASA results in a decrease of the mean concentration, being 0.03 for x and 0.01 for y . In contrast, SAD affect the profiles by a shift to larger concentrations as the black graphs show. However, this shift is very small as it lies within the error bars, indicating that imaging conditions are rather robust against the effect of SAD. Furthermore, a slight correlation of the indium and nitrogen profiles can be observed which can be attributed to small fluctuations of the experimentally measured fringe amplitude according to Eq. (4.8). As Fig. 4.8 exhibits, this leads to little vertical shifts of the amplitude contours, either in- or decreasing both x and y . Since this correlation is well inside the error bars, it must rather be assigned to experimental errors than to a physical connection between the distributions of indium and nitrogen. The most interesting aspect is to figure out which of the models applied in Figs. 4.10 and 4.11 is the most reliable one. For this purpose, an InGaAs quantum well has been grown immediately after the quaternary well studied above to assure that growth conditions are comparable as far as possible. Hence, the same amount of indium should be observed. This well has been investigated by the same method, that is, evaluation of both local fringe distances and contrast, so as to check also whether nitrogen is found to be absent. Resulting composition profiles are composed in Fig. 4.12, where solid lines correspond to indium and dashed ones correspond to nitrogen. Concerning the latter, all four approaches

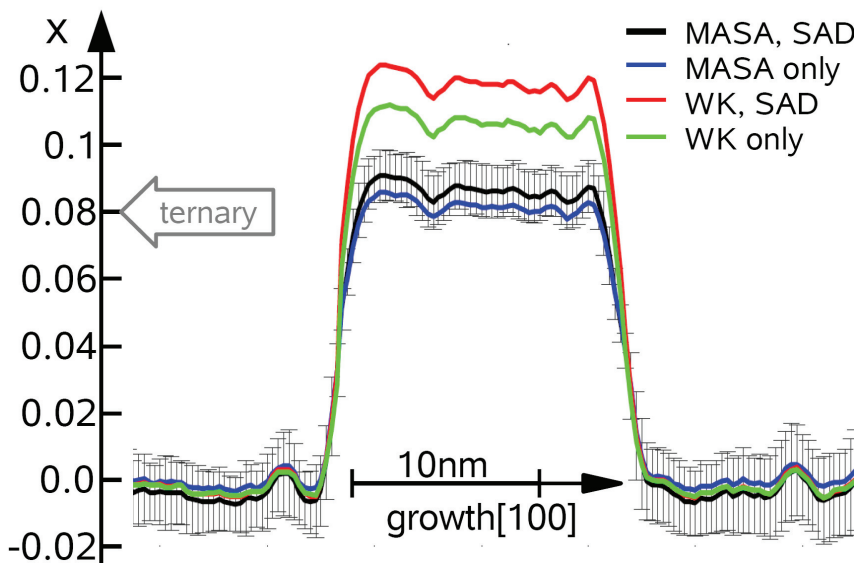


Figure 4.10: Indium composition profiles calculated from maps analogous to the right composition map in Fig. 4.9 by averaging horizontally. The four curves differ in the reference data sets used, which are explained in the legend. The result of Fig. 4.12 for the mean indium concentration in a ternary InGaAs well grown on the same sample during the same session is indicated by the grey arrow.

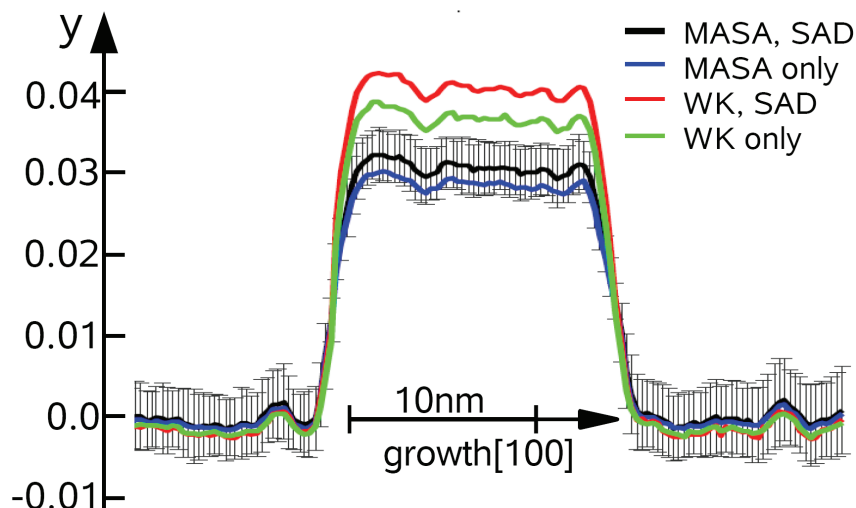


Figure 4.11: Nitrogen composition profiles calculated from maps analogous to the left composition map in Fig. 4.9 by averaging horizontally. The four curves differ in the reference data sets used, which are explained in the legend.

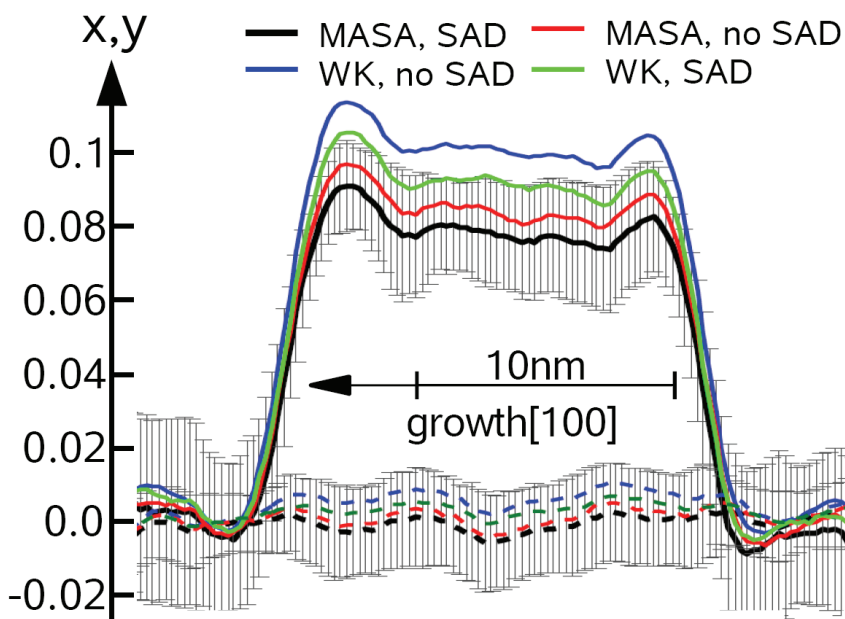


Figure 4.12: Profiles for In (upper curves) and N (lower curves) compositions for a ternary $\text{In}_x\text{Ga}_{1-x}\text{As}$ quantum well grown in the same session as the InGaNAs layer evaluated in Fig. 4.9. The *ternary* annotation in Fig. 4.10 was determined from the mean concentration corresponding to the black curve here.

confirm $y \approx 0$ within the error margins. Nevertheless the mean of the curves for isolated atoms (WK) lies slightly above zero, indicating that the MASA graphs are more plausible. It should be noticed that this is not a general biasing because $y \approx 0$ is found outside the well again. For indium, neglect of bonding leads to mean concentrations of 0.09 and 0.1 without and with SAD, respectively. In contrast, we find $x \approx 0.08$ for the MASA approach. It is now straight forward to compare with the indium profiles in Fig. 4.10: The correct model ought to result in the same (mean) content. Since isolated atom data lies above $x \approx 0.1$ and nearly reaches $x \approx 0.12$ in case of SAD, results significantly differ from Fig. 4.12. On the other hand, MASA results agree well when comparing Figs. 4.10 and 4.12, as indicated by the *ternary* arrow.

In summary, this behaviour could be expected from the theoretical considerations in section 4.2, as well as from the analysis of Rosenauer et al. [9], where it was found theoretically that SAD have a minor effect on the 200 structure factor of $\text{In}_x\text{Ga}_{1-x}\text{As}$ (compared to bonding).

4.4 Discussion

4.4.1 Modelling of scattering properties

Section 4.2 was intended to give a detailed theoretical analysis of SAD and bonding effects on structure factors. Besides this, it was shown that atom positions obtained from VFF agree with DFT results within an accuracy in the range of thermal disorder even for relatively complex structures containing 12 indium and 4 nitrogen atoms.

Relevance for structure factors

Concerning the modelling of structure factors via atomistic models, some further comments as to the analysis in section 4.2.2 follow. First, the MASA model describes bonding effects on low order structure factors best in terms of the difference to full DFT calculations. Of course it would in principle be possible to use accurate DFT structure factors obtained from relaxed supercells in general, but note that the distribution of foreign substitutional indium and nitrogen atoms is of statistical nature which can not (yet) be managed by DFT due to the strongly limited supercell size. Furthermore, the MASA approach allows for the inclusion of Debye-Waller factors as conventionally defined. Second, Fig. 4.6 shows that SAD can severely affect structure factor phases of the 202 and 600 structure factor, which are real when neglecting SAD. This has already been pointed out by Glas [8], and Fig. 4.6 exhibits that both isolated atom scattering amplitudes and MASA combined with SAD represent this effect with nearly the same accuracy. However, best agreement between full DFT calculations and atomistic approaches has already been reported in Refs. [9, 32] for ternary materials if muffin-tin results from DFT are combined with SAD calculated by VFF.

Furthermore, this study shows that the consideration of SAD may result in larger moduli of the 200 structure factors, whereas it tends to act as a damping factor for higher order structure factors. From Eq. (2.10) we see that the exponential terms may affect different atomic species differently, depending on the respective SAD. As the 200 structure factor is very small and essentially given by the difference between group III and group V ASA, this may result in a larger structure factor, explaining the fact that the consideration of SAD leads to higher concentrations in Figs. 4.10 and 4.11.

Until here, nothing was said as to absorptive potentials for Huang scattering introduced in section 2.6.4 in order to keep the presentation of results clear. In fact, none of the evaluations shown in Figs. 4.10, 4.11 and 4.12 accounts for diffuse losses in Bragg scattered beams induced by static disorder. Nevertheless respective evaluations have been performed with the result that SAD curves presented here are not significantly altered. At first view this contradicts pendellösung plots shown for the 200 beam in Fig. 2.9, where large impact of diffuse scattering is expected. However, we must keep in mind that indium content is three- and that of nitrogen is nearly two times larger than compositions here, causing strong static disorder in the structure investigated in section 2.6.4. In addition, the 200 reflection is excited much stronger here due to the systematic row condition, and relative importance of damping with thickness is thus less. Towards in-zone orientations, the influence of Huang scattering losses on Bragg beams becomes stronger, as will be shown in chapter 5.

Side note to quantitative STEM

On the one hand, it is interesting to know that MASA in combination with SAD built the most reliable atomistic approach to calculate structure factor moduli and phases. On the other hand, Glas' statement that any quantitative analysis ignoring SAD "would be seriously in error" cannot be verified as their influence on composition profiles is small for the sample investigated here. In drastic contrast, the present verification of SAD derived from VFF is fundamental for quantitative high-angle annular dark field (HAADF) scanning TEM (STEM), as was shown for ternary $\text{In}_x\text{Ga}_{1-x}\text{As}$ by Grillo et al. [27]. However, HAADF-STEM contrast is often also called *Z-contrast*, owing to the fact that electron ASA are sensitive to atomic number Z as implied by, e.g., Eq. (2.3). For $\text{In}_x\text{Ga}_{1-x}\text{As}$, this rule of thumb is not violated if SAD are neglected, since in either case $\text{In}_x\text{Ga}_{1-x}\text{As}$ layers exhibit bright contrast, compared to GaAs at equal thickness. For example, Fig. 4.13 shows an $\text{In}_{0.28}\text{Ga}_{0.72}\text{As}$ quantum well in the centre, whose bright appearance with respect to the GaAs buffer can intuitively be understood by the *Z-contrast* rule since the atomic number of indium is about 60% larger than that of gallium. Contrary to this, the $\text{GaN}_{0.015}\text{As}_{0.985}$ layers also appear brighter than GaAs buffer layers, although the atomic number of nitrogen is only 20% of the arsenic one. The massive dependence of HAADF contrast on thermal disorder has been discussed already in section 3.5.4. Consequently, Huang scattering [58] (see also section 2.6.3) caused by SAD is currently discussed to be responsible for the contrast anomaly in GaNAs.

This issue has been studied in more detail in Fig. 4.14, where the composition- and thickness-dependent HAADF-STEM signal was simulated using the STEMsim [33] software. All results are normalised to the signal expected for GaAs at equal thickness. For the dashed graphs, no SAD have been taken into account, whereas VFF relaxation was performed in case of the solid graphs. These two groups of curves exhibit opposite behaviour concerning three aspects. First, expected contrast is reversed for thicknesses beyond 50 nm, meaning that neglect of SAD leads to a deficiency of intensity on the HAADF detector in GaNAs regions (dashed graphs), whereas GaNAs appears brighter if SAD are accounted for (solid graphs). Second, compositional dependence is opposite, too. In case of SAD, HAADF intensity on the detector increases with nitrogen content, in contrast to the dashed curves. Third, compositional dependence is extremely weak if SAD are neglected, as even for $\text{GaN}_{0.08}\text{As}_{0.92}$ the HAADF signal is about 98% of the signal expected for GaAs. This is contrary to the SAD case, where 15% brighter contrast is found, depending on specimen thickness. From this the conclusion must be drawn that

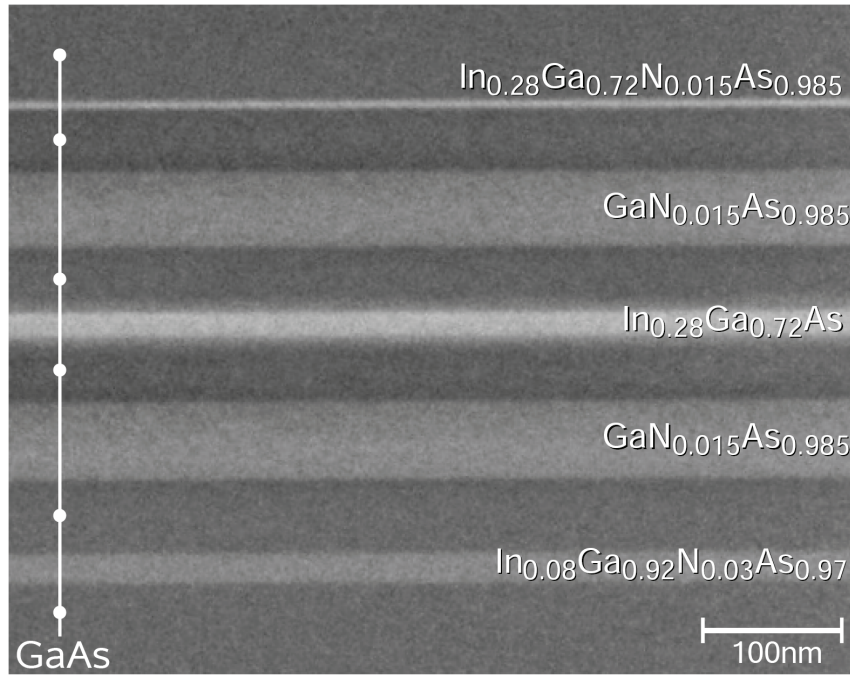


Figure 4.13: HAADF-STEM image of a stack of quantum wells of different type recorded on a Titan 80/300 at room temperature with detector acceptance angles between 33 and 200 mrad. Incidence was along [010]. Bright contrast in GaNAs layers must rather be assigned to SAD than to atomic number Z .

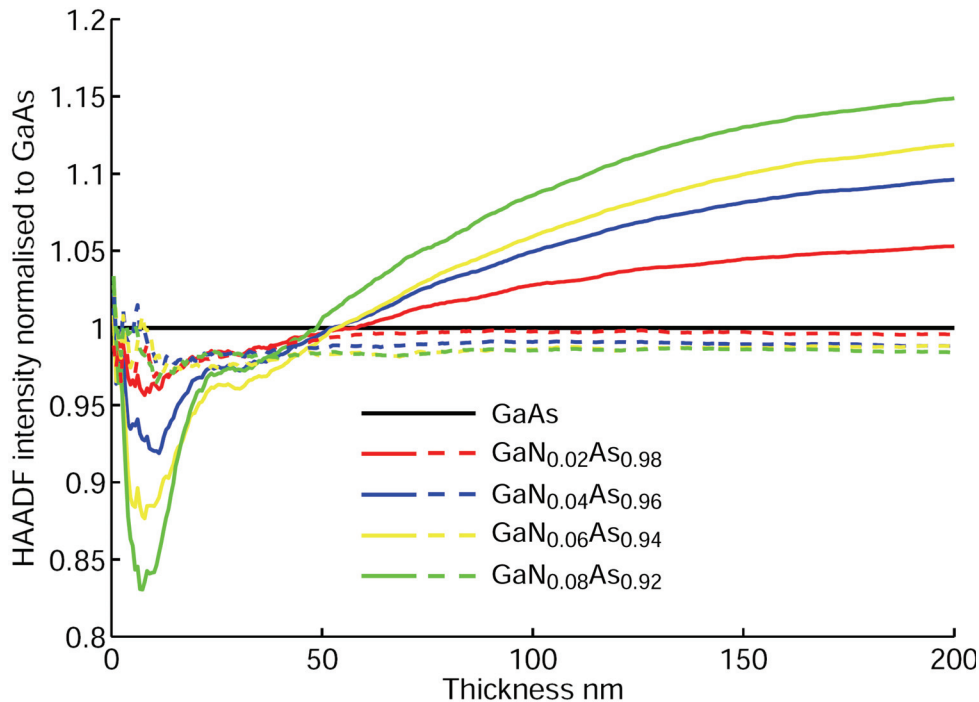


Figure 4.14: Frozen lattice simulation of HAADF-STEM contrast in GaNAs with incidence along [010] using the STEMsim [33] software. *Solid graphs*: SAD derived from VFF. *Dashed graphs*: SAD neglected. Detector acceptance was 33-200 mrad, inhomogeneous detector sensitivity was accounted for. Supercell size was 7×7 Bravais cells laterally, Debye parameters correspond to 300 K [81]. Results have been averaged over 10 thermal configurations and are normalised to GaAs.

the experimental HAADF-STEM image in Fig. 4.13 can qualitatively only be explained if SAD are taken into account. From bulk GaAs below and above the quantum wells in Fig. 4.13, a specimen thickness of about 80 nm has been measured using STEM as described in section 3.5.4. Since the specimen was prepared by focused ion beam milling, it can be assumed that thickness is nearly homogeneous also in the well regions, so that image contrast must be interpreted by means of simulated data beyond 50 nm in Fig. 4.14. However, a full quantitative comparison is beyond the scope of this work which is intended to focus on conventional TEM. For details, the reader is referred to Refs. [29, 30]. Nevertheless we herewith find the important result that, besides verification of SAD obtained by VFF, STEM-HAADF contrast in GaNAs is rather dominated by SAD of adjacent atoms than by nitrogen atoms themselves. Furthermore, reliable models to account for the influence of strain relaxation along zone axis direction on HAADF contrast are under development [139, 140], being essential for composition quantification at interfaces using STEM. An indication that this effect is responsible for a deficiency of intensity near the well edges is its absence in the lattice-matched lowermost InGaNAs layer in Fig. 4.13.

4.4.2 Methodical aspects

Since the two-beam method presented here requires only recording of a single 2-beam image the experimental effort is very low on the one hand but still allows for atomically resolved concentration maps on the other hand. This is very important for an accurate study of diffusion and segregation processes in dependence on, e.g., annealing conditions, on which extensive studies have already been published in Refs. [141, 4], for example. Although an additional free parameter is introduced (that is, a second composition), precisions for x and y found here are comparable with conventional applications of the CELFA method to ternary materials. In comparison to the method proposed by Grillo et al. [2], the method presented here overcomes the problem of correlating two images that contain chemically sensitive and strain information separately, and which were taken under very different specimen tilts in order to allow for a kinematic treatment of the 200 dark field amplitude. Nevertheless the present method requires significant presence of 200 fringes which is not given for all compositions as Fig. 4.8 shows. However, the dynamical simulation of (normalised) image contrast is essential since the 200 reflection vanishes for no concentration pair (x, y) , whereas the 200 structure factor does.

As two-beam imaging is based on the interference of scattered beams, systematical errors arising from unknown specimen thickness and composition gradients are briefly addressed in the following. The former may affect the normalised amplitude $a_N(\mathbf{r}, t, x, y)$ in Eq. (4.8) and the latter can distort the maps of the local distances according to φ_{12} in Eq. (4.7). In this respect it turned out that errors are dominated by the dependence on x , so that the analysis for a constant nitrogen content of 0.03 is presented, which is typical for the experiment dealt with here.

According to Eq. (4.8), the elimination of the thickness dependence of $a_N(\mathbf{r}, t, x, y)$ is desirable, if the specimen thickness is not measured separately. The black curve in Fig. 4.15 depicts the standard deviation $\sigma_t(x, 0.03, t)$ of all amplitudes a_N corresponding to the same composition but different thicknesses in the range $t \in [10 \dots 100 \text{ nm}]$. Up to $x \approx 0.5$, we indeed find that $\sigma_t < 0.05$. In the worst case, errors of $\Delta x = 0.01$ and $\Delta y = 0.003$ can result then, which was found by comparison with Fig. 4.8. However, for larger concentrations x , either the thickness should be measured or imaging conditions ought to be modified with respect to specimen tilt.

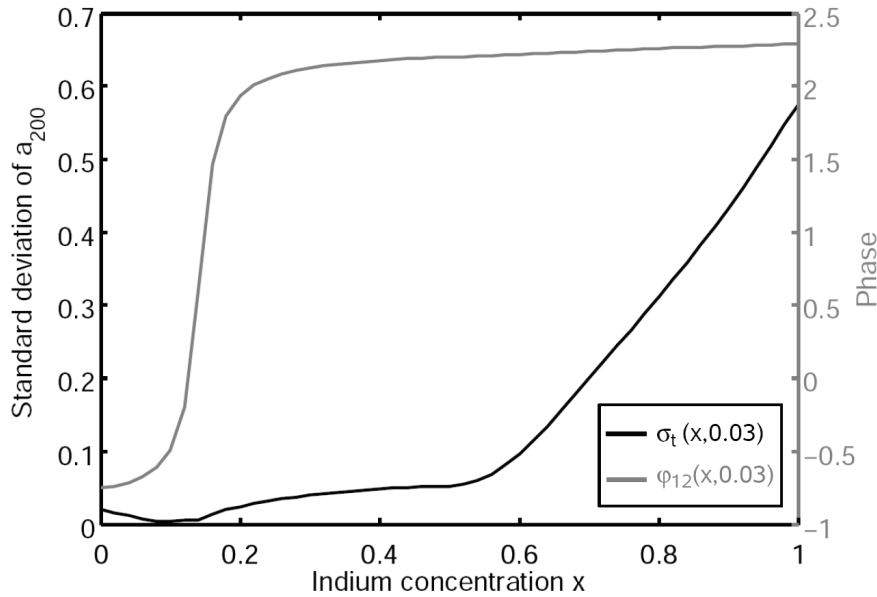


Figure 4.15: Graphs to estimate systematical errors due to inaccurately known specimen thickness (black) and chemical shifts by concentration gradients (grey). Calculations were performed using the MASA model and SAD. The black curve depicts the standard deviation σ_t of a_N according to Eq. (4.8) calculated from a thickness range $t \in [10 \dots 100 \text{ nm}]$. The phase φ_{12} occurring in Eq. (4.8) can cause invalid measurements of local fringe distances, if strongly depending on composition. As the grey curve exhibits, this is the case mainly near the phase jump region at $x \approx 0.15$. Only the result for $y = 0.03$ is shown because the behaviour of σ_t and φ_{12} is dominated by the dependence on x .

Since the positions of lattice fringes are not only determined by the lattice constant but also by the phase difference φ_{12} as expressed in Eq. (4.8), the grey graph was added to Fig. 4.15. It exhibits a widely flat behaviour except for the phase jump region near $x \approx 0.15$. The phase φ_{12} is constant for constant specimen thickness and constant chemical composition, so that it causes erroneous fringe positions mainly in the presence of concentration gradients. From this follows that we can safely trust the mean result of $\bar{x} \approx 0.08$ for the inner well region according to Fig. 4.9. From Figs. 4.10 and 4.11 we conclude that this is reached within about 10 monolayers, resulting in an average gradient of 0.008 per monolayer. Then, the grey curve in Fig. 4.15 exhibits a chemical phase shift of 0.025 near $x \approx 0.08$, resulting in an error $\Delta y = 0.01$ for the respective fringe and even less for Δx . It may be due to this effect that all composition profiles in Figs. 4.10, 4.11 and 4.12 show a slight enrichment of indium or nitrogen at the very edge of the well.

4.4.3 Composition profiles

As expected from the theoretical studies in section 4.2, Figs. 4.10, 4.11 and 4.12 exhibit partly large differences in the resulting compositions, depending on the model for the scattering data used. From the experimental point of view, comparison of the results for the quaternary structure with those for the equivalent ternary structure in Fig. 4.12 confirms an average indium content of $\bar{x} = 0.08$. Together with the fact that the well was grown lattice-matched, this means that the average nitrogen content is $\bar{y} = 0.03$. This is in best agreement with bandgap and X-ray diffraction measurements by Volz et al. [15]. For a sample grown under the same conditions a gap of 1 eV and a lattice-matched structure

was found, which can uniquely be assigned to $\text{In}_{0.08}\text{Ga}_{0.92}\text{N}_{0.03}\text{As}_{0.97}$. Thus the MASA curves in Figs. 4.10 and 4.11 are the most plausible ones.

Concerning the effect of SAD on composition evaluation, Figs. 4.10 and 4.11 show that both MASA with and without SAD agree with each other within the experimental errors. For the indium profile, the blue curve is closest to the expected concentration, whereas it is the black curve in case of nitrogen. We therefore conclude that SAD have very little effect on composition evaluation for the experimental conditions and concentrations dealt with here. A Laue circle centre of $(1.5\ 0\ 20)$ corresponds to a systematic row condition where only a few beams are involved. Thus, the change in structure factor moduli and phases for higher order structure factors addressed in section 4.2.2 has little influence on the 200 reflection due to a reduction of dynamical effects. However, large differences are observed for simulations in zone axis where the thickness dependence of beam amplitudes is altered significantly.

4.5 Summary and conclusions

The influence of both static atomic displacements (SAD) and bonding on structure factors has been investigated by means of comparing full density functional theory (DFT) calculations with atomistic models. First, it was found that SAD derived from valence force field (VFF) methods are accurate to a few picometres, which is lower than mean thermal displacements near room temperature. Second, modified atomic scattering amplitudes (MASA) derived from DFT are a valid representation of bonding effects even in complex structures where strong SAD due to nitrogen impurities are present. In particular, SAD may affect both modulus and phase of low- and high-order structure factors, whereas bonding alters only the 200 structure factor considerably. Thus both effects must be accounted for in dynamical many-beam simulations, for which combined use of MASA and VFF provides an efficient way to include both phenomena that usually need to be treated on complementary (length) scales. In contrast to the isolated atom approach, MASA depend on nearest neighbour configuration of each atom in a supercell. They therefore principally allow for the treatment of correlated distributions of indium and nitrogen, as is often discussed in the framework of annealing procedures.

An experimental TEM two-beam method was introduced which allows for two-dimensional elemental mapping of compositions in $\text{In}_x\text{Ga}_{1-x}\text{N}_y\text{As}_{1-y}$ alloys from a single 200 lattice fringe image. Fringe contrast and lattice strain can simultaneously be measured at atomic scale and are compared with simulated reference data. As to strain, a brief review of elasticity theory has been given. For dynamical simulations of diffracted beam amplitudes, Bloch-wave routines were developed that can handle scattering data from the four atomistic approaches (i.e. neglect of bonding, SAD or both) presented here. For a lattice-matched $\text{In}_{0.08}\text{Ga}_{0.92}\text{N}_{0.03}\text{As}_{0.97}$ solar cell structure, it was found that accounting for bonding improves accuracy of composition measurement by up to 25%, whereas SAD make a minor effect on composition profiles due to systematic-row imaging conditions used. No significant correlation or anticorrelation between indium and nitrogen profiles could be observed for this structure. Except for gradual in-/decrease of both compositions at the well interfaces, both composition profiles exhibit rectangular shape. Especially no nitrogen enrichment at the interfaces could be observed.

Since application to compositions below the null of the 200 structure factor poses some limitation to the two-beam method, it would be desirable to deduce strain information from fringes different than 200, e.g. from 202. However, the methodical concept and

the knowledge about models for scattering data gained in this chapter can directly be transferred to such experimentally more advanced techniques (see chapter 5).

To demonstrate the importance of SAD for TEM, high-angle annular dark field (HAADF) scanning TEM (STEM) images of InGaNAs and its ternary derivatives have been recorded. Unlike expected from a simple Z -contrast rule, bright contrast in $\text{GaN}_{0.015}\text{As}_{0.985}$ was observed and could successfully be assigned to Huang scattering at SAD by frozen lattice multislice simulations. This lays the basis for future compositional analysis of dilute nitrides using HAADF STEM.

Chapter 5

Atomic scale annealing effects on InGaNAs studied by TEM three-beam imaging

5.1 Introduction

One main driving force in microscopy of semiconductor nanostructures is an understanding of macroscopically observable phenomena from atomic scale characterisation. In particular, the correlation of thermal annealing effects on photoluminescence (PL) and structural properties of quaternary $\text{In}_x\text{Ga}_{1-x}\text{N}_y\text{As}_{1-y}$ layers remains an unsolved problem. In that respect, laser structures with $x \approx 0.3$ and $y \approx 0.02$ are of special interest because PL emission near wavelengths 1.3, or, preferably, 1.55 μm can principally be achieved [142], which meets the nearly dispersion-less transmission windows of optical fibres. In addition, electrons are strongly confined in InGaNAs quantum wells due to the deep conduction band states in this material system, allowing for high thermal stability [143].

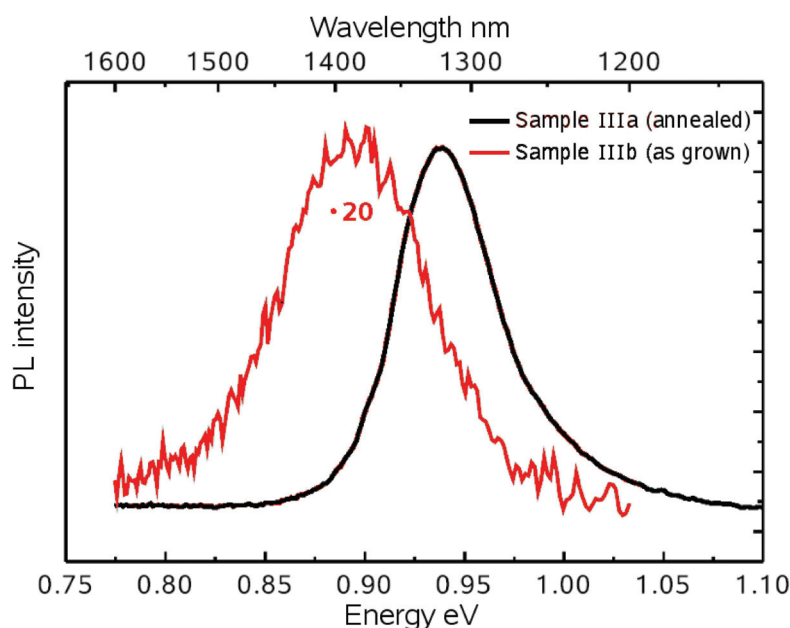


Figure 5.1: Room-temperature PL spectra for the laser structures investigated by TEM before (red, scaled by a factor of 20) and after 15 min of thermal annealing under N_2 stabilisation (black). Spectra have been recorded by the group of M. Hetterich, Karlsruhe Institute of Technology.

Let us anticipate the optical characterisation of an $\text{In}_{0.28}\text{Ga}_{0.72}\text{N}_{0.025}\text{As}_{0.975}$ sample studied by TEM in this chapter, in order to work out phenomena that are typically ob-

served at InGaNaNs infrared emitters. The red PL spectrum in Fig. 5.1 has been recorded at the as-grown sample, whereas the black one stems from its thermally annealed counterpart. The fact that room-temperature PL can be achieved is encouraging on the one hand, but PL peak width and -intensity of the red curve must be optimised on the other hand. To this end, the sample was annealed at 670°C, which obviously improves spectral width and intensity of the PL peak drastically. However, the black spectrum is significantly shifted by about 65 nm to smaller wavelengths. This behaviour has been observed by many groups [16, 144, 18, 23, 15], and is even in quantitative agreement with systematic studies of the blue shift in dependence on annealing temperature performed by Klar et al. [16]. This implies that studying structural changes for the present sample reveals characteristic processes in InGaNaNs. In particular, we conclude from Fig. 5.1 that epitaxy of an InGaNaNs sample intended for a certain spectral application must comprise a blue shift of several tens of meV induced by post-growth annealing. Consequently, it would be necessary to further raise the amount of nitrogen, which is given a limit by the miscibility gap. In summary, it is desirable from the application point of view to understand microscopic processes that take place during annealing, such as changes in local stoichiometry.

In methodical respect, lattice strain and contrast are in principle accessible by TEM. Both quantities may be measured locally in a single high-resolution TEM image, and both are sensitive to chemical composition in InGaNaNs. However, in addition to the complexity of electron scattering at the specimen as outlined in chapter 2, nonlinear imaging theory predicts contributions of all Bragg scattered beams to a single diffractogram reflection, making quantitative analysis difficult. An exception occurs if the image is formed solely by diffracted beams whose reciprocal lattice vectors are linearly independent. The simplest case is dark field imaging using the chemically sensitive 200 beam, but due to Abbe's theory, strain measurement is impossible then. For this reason, Grillo et al. [2] merge contrast and strain information from different images acquired under different specimen tilts. Inclusion of the primary beam overcomes this problem, as was shown by Müller et al. [7] (see also chapter 4), who measured both indium and nitrogen content using a combination of strain state and composition evaluation by lattice fringe analysis (CELFA) [34]. Unfortunately, this technique is based on the interference of beams 200 and 000, prohibiting the evaluation of strain near $x \approx 0.15$, where the 200 structure factor vanishes. This chapter therefore introduces a three-beam imaging technique that allows for dual compositional mapping of, e.g., indium and nitrogen content, at atomic scale. Both compositions are extracted from a single TEM lattice fringe image based on the interference of 000, 220 and 020. In this way, it is assured that strain, being measured from the local 220 fringe distances, is simultaneously present at nulls of the 020 fringe intensity, which in turn provides the chemically sensitive signal as a second source of information.

At first sight, the presented three-beam technique looks like a superposition of CELFA and strain state approaches as traditionally applied, but at least three aspects require special attention. First, an objective aperture is to be designed that transmits beams 000, 220 and 020. Second, it was pointed out in section 2.6.4 that Huang scattering must be accounted for in dilute nitride alloys, which is especially true for beam incidence near a low-index zone axis. It is obvious that, contrary to two-beam techniques [34, 145], recording both 220 and 020 fringes cannot be accomplished in a systematic row geometry. Hence, the third problem is finding optimised three-beam imaging conditions which minimise the dependence of measured concentrations on (usually inaccurately known) specimen thickness.

Table 5.1:	Name	x	y	Growth technique	Note
Summary of main characteristics for the four $\text{In}_x\text{Ga}_{1-x}\text{N}_y\text{As}_{1-y}$ samples.	Sample I	0.08	0.03	MOVPE	As-grown
	Sample II	0.08	0.02	MOVPE	As-grown
	Sample III a	0.28	0.025	MBE	Annealed
	Sample III b	0.28	0.025	MBE	As-grown

This chapter is organised as follows: First, the three-beam method is described in section 5.3, including a brief outline of nonlinear imaging theory, finding of optimised imaging conditions and example reference data. In section 5.4 the method is applied to structures with compositions below the null of the 020 structure factor. Finally, annealing effects on the $\text{In}_{0.28}\text{Ga}_{0.72}\text{N}_{0.025}\text{As}_{0.975}$ sample are studied and interpreted in terms of its PL spectra in Fig. 5.1 in section 5.5. This chapter ends with a detailed discussion and essential conclusions in sections 5.6 and 5.7.

5.2 Experimental

A 15 nm thick lattice-matched quantum well with nominal composition $\text{In}_{0.08}\text{Ga}_{0.92}\text{N}_{0.03}\text{As}_{0.97}$, being a typical setup for InGaNAs solar cell structures, was grown by metal organic vapour phase epitaxy (MOVPE). We refer to this structure as sample I whose composition has been studied before in chapter 4 and Ref. [7]. It therefore helps to verify the three-beam approach for composition mapping presented here. Moreover, a 15 nm thick quantum well with nominal composition $\text{In}_{0.08}\text{Ga}_{0.92}\text{N}_{0.02}\text{As}_{0.98}$ was grown by MOVPE and studied by the three-beam method, in order to investigate also a strained structure in the low-indium regime. This sample is called sample II in this chapter. Nominal compositions of samples I and II are based on calibration samples, which have been characterised using X-ray diffraction measurements and corresponding dynamical simulations for multiple quantum well structures.

A 7 nm thick quantum well with nominal composition $\text{In}_{0.28}\text{Ga}_{0.72}\text{N}_{0.025}\text{As}_{0.975}$, being a typical setup for InGaNAs laser structures, was grown by molecular beam epitaxy (MBE). It is referred to as sample III in the following. Part of this sample was treated by thermal annealing at 670°C for 15 minutes in N_2 atmosphere. When dealing with comparison of the annealed and the as-grown part, the former is referred to by sample III a and the latter by sample III b.

Cross-sectional TEM specimens have been prepared conventionally in zone axis [001] by first mechanical grinding and second argon ion polishing using a Gatan precision ion polishing system operating at angles of $\pm(3 - 5^\circ)$ and an energy of 3.5 keV. An FEI Titan 80/300 TEM facility, equipped with a corrector for the spherical aberration of the objective lens, operated at 300 kV, has been used for all TEM measurements. All images have been recorded on a $2K \times 2K$ CCD camera. An L-shaped objective aperture consisting of two $12.5 \mu\text{m} \times 25 \mu\text{m}$ rectangles oriented by 90° was etched into a 7 μm thick platinum foil using an FEI Nova 200 NanoLab focused ion beam facility.

Main characteristics of all $\text{In}_x\text{Ga}_{1-x}\text{N}_y\text{As}_{1-y}$ samples are summarised in table 5.1.

The room-temperature near-infrared PL spectra of samples III a and b shown in Fig. 5.1 have been dispersed using a 46 cm monochromator equipped with a 600 lines/mm grating and detected by a thermoelectrically cooled InGaAs detector using a lock-in technique. A laser diode emitting at a wavelength of 670 nm with a power of about 200 mW was used for excitation.

5.3 Description of the method

5.3.1 Nonlinear imaging

Following the book of Rosenauer [146], we first examine the coherent transfer of a specimen exit wave function $\Psi(\mathbf{r})$ through a lens for plane wave illumination along the optical axis of the TEM. Initially, the exit wave must be convoluted with the point spread function $P(\mathbf{r})$ to obtain the wave function in the image plane. Since only image intensity $I(\mathbf{r})$ is physically observable, this function must be multiplied with its complex conjugate. Finally, the image intensity is to be Fourier transformed in order to analyse the impact of the imaging process on diffractogram reflections. The diffractogram is thus given by

$$I(\mathbf{q}) = \mathcal{F}[I](\mathbf{q}) = \mathcal{F} \left\{ \underbrace{\mathcal{F}^{-1} [\Psi(\mathbf{q}) P(\mathbf{q})] (\mathbf{r}) \cdot \{\mathcal{F}^{-1} [\Psi(\mathbf{q}) P(\mathbf{q})] (\mathbf{r})\}^*}_{\text{Image intensity } I(\mathbf{r})} \right\} (\mathbf{q}) \quad , \quad (5.1)$$

where $\Psi(\mathbf{q}) = \mathcal{F}[\Psi](\mathbf{q})$ and $P(\mathbf{q}) = \mathcal{F}[P](\mathbf{q})$ are Fourier transforms. In Eq. (5.1), use of the convolution theorem was made, leading to a multiplication of the Fourier transformed exit wave with the coherent transfer function $P(\mathbf{q})$. Note that all vectors in Eq. (5.1) lie in one plane perpendicular to the optical axis, so that essentially two-dimensional Fourier transforms are involved.

Let us restrict the analysis on the contribution of Bragg scattered beams. Then, Fourier transform of Eq. (2.42), inserted into Eq. (5.1), leads to

$$\begin{aligned} I(\mathbf{q}) &= \mathcal{F} \left\{ \sum_{\mathbf{g}} \Psi_{\mathbf{g}} P(\mathbf{g}) e^{2\pi i \mathbf{g} \mathbf{r}} \cdot \sum_{\mathbf{h}} \Psi_{\mathbf{h}}^* P^*(\mathbf{h}) e^{-2\pi i \mathbf{h} \mathbf{r}} \right\} (\mathbf{q}) \\ &= \mathcal{F} \left\{ \sum_{\mathbf{g}} \sum_{\mathbf{h}} \Psi_{\mathbf{g}} P(\mathbf{g}) \cdot \Psi_{\mathbf{h}}^* P^*(\mathbf{h}) e^{-2\pi i (\mathbf{h} - \mathbf{g}) \mathbf{r}} \right\} (\mathbf{q}) \\ &= \sum_{\mathbf{g}} \sum_{\mathbf{h}} \int \Psi_{\mathbf{g}} P(\mathbf{g}) \cdot \Psi_{\mathbf{h}}^* P^*(\mathbf{h}) e^{-2\pi i (\mathbf{h} - \mathbf{g} + \mathbf{q}) \mathbf{r}} d^2 \mathbf{r} \\ &= \sum_{\mathbf{g}} \sum_{\mathbf{h}} \Psi_{\mathbf{g}} P(\mathbf{g}) \cdot \Psi_{\mathbf{h}}^* P^*(\mathbf{h}) \cdot \delta(\mathbf{h} - \mathbf{g} + \mathbf{q}) \end{aligned} \quad (5.2)$$

with reciprocal lattice vectors \mathbf{g} and \mathbf{h} . From Eq. (5.2) it becomes obvious that it is in general not only the amplitude of a single Bragg beam that determines a certain diffractogram reflection, but all differences $\mathbf{g}' = \mathbf{g} - \mathbf{h}$. Hence, reflection \mathbf{g}' in the diffractogram reads

$$I(\mathbf{g}') = \sum_{\mathbf{h}} \Psi_{\mathbf{h} + \mathbf{g}'} P(\mathbf{h} + \mathbf{g}') \cdot \Psi_{\mathbf{h}}^* P^*(\mathbf{h}) \quad . \quad (5.3)$$

The coherent transfer function $P(\mathbf{q})$ is a product of a pupil function $A(\mathbf{q})$, being one inside and zero outside an objective aperture, and a phase factor $e^{i\chi(\mathbf{q})}$. Considering spherical aberration, defined by the length C_S , and defocus, given by the length Δf , the function $\chi(\mathbf{q}) = \chi(q)$ is rotationally symmetric and reads

$$\chi(q) = \frac{\pi}{2} C_S \lambda^3 q^4 + \pi \Delta f \lambda q^2 \quad . \quad (5.4)$$

It was pointed out by Ishizuka in 1980 [147] that Eq. (5.3) must be modified further in order to take into account effects of spatial and temporal coherence. The former is determined by the finite size of the electron source and causes primary electrons to travel at an angular distribution with respect to the optical axis, even if the condenser is aligned for parallel illumination. The latter is characterised by the width of the energy spectrum of the primary electrons and fluctuations of the objective lens current. In summary, spatial and temporal coherence is accounted for by two additional factors E_S and E_T , respectively, and Eq. (5.3) becomes [146]

$$I(\mathbf{g}') = \sum_{\mathbf{h}} \Psi_{\mathbf{h}+\mathbf{g}'} \Psi_{\mathbf{h}}^* \cdot \underbrace{P(\mathbf{h} + \mathbf{g}') P^*(\mathbf{h}) \cdot e^{-\frac{1}{2} \frac{\alpha^2}{\lambda^2} [\nabla\chi(\mathbf{h}+\mathbf{g}') - \nabla\chi(\mathbf{h})]^2}}_{E_S} \cdot \underbrace{e^{-\frac{1}{2} \pi^2 \lambda^2 \Delta^2 [(\mathbf{h}+\mathbf{g}')^2 - \mathbf{h}^2]^2}}_{E_T} \quad (5.5)$$

$T_{\mathbf{h}+\mathbf{g}',\mathbf{h}}(\Delta f, \alpha, \Delta)$

with the transmission cross coefficients $T_{\mathbf{h}+\mathbf{g}',\mathbf{h}}(\Delta f, \alpha, \Delta)$. The parameter α denotes the full width at half maximum of, e.g., Gaussian statistics of the angular distribution of the primary electron wave vectors, whereas all effects of temporal coherence are carried by the effective focus spread parameter Δ .

To stress the importance of contrast transfer in the framework of nonlinear imaging, the consequences of Eq. (5.5) on diffractogram reflections of interest in this chapter are studied in Fig. 5.2. The three curves in each subfigure correspond to different objective apertures, that is, a different number of beams that are used for imaging. The simplest case corresponds to two-beam imaging, where either 220 (first row) or 020 (second row) interfere with 000, which is represented by the black circles. Here, no nonlinear imaging artefacts are observed, meaning that this curve can easily be calculated from the diffracted beam amplitudes, aberrations and coherence parameters. In case of the red graphs, the additional beam 220 passes through the objective aperture. Here, nonlinearity causes the 200 reflection to appear in the diffractogram due to the interference of 020 with 220. Note that this is not a marginal effect since, depending on specimen thickness, the 200 amplitude is approximately half as large as the amplitude of 020, although this beam had not been included by the objective aperture. However, both amplitudes and phases of beams 220 and 020 remain unchanged in comparison to two-beam imaging. Hence, nonlinear effects can be eliminated by Fourier filtering (i.e. deleting the ± 200 reflection in the diffractogram), yielding a 220 and an 020 fringe image as formed by two-beam imaging at the same time. Finally, the blue curve in Fig. 5.2 depicts the case where an objective aperture is used that transmits all Bragg beams up to a spatial frequency of 15 nm^{-1} . Obviously this has drastic consequences for both amplitudes and phases of diffractogram reflections. Coupling among all transmitted beams results in a complicated thickness dependence of the amplitudes of all reflections shown, although the thickness dependence of the diffracted beams themselves is much weaker, as depicted in, e.g., Figs. 2.6 and 2.9. Due to symmetry, 020 and 200 plots are equivalent. It is also important to notice that the 220 phase is a continuous function in the two- and three-beam cases, whereas the blue curve exhibits phase jumps of π , impeding, e.g., measurement of strain from lattice fringes in the presence of thickness gradients. However, instead of (or in addition to) thickness gradients, composition gradients govern diffracted amplitudes and phases in compositional analysis, which qualitatively cause similar effects.

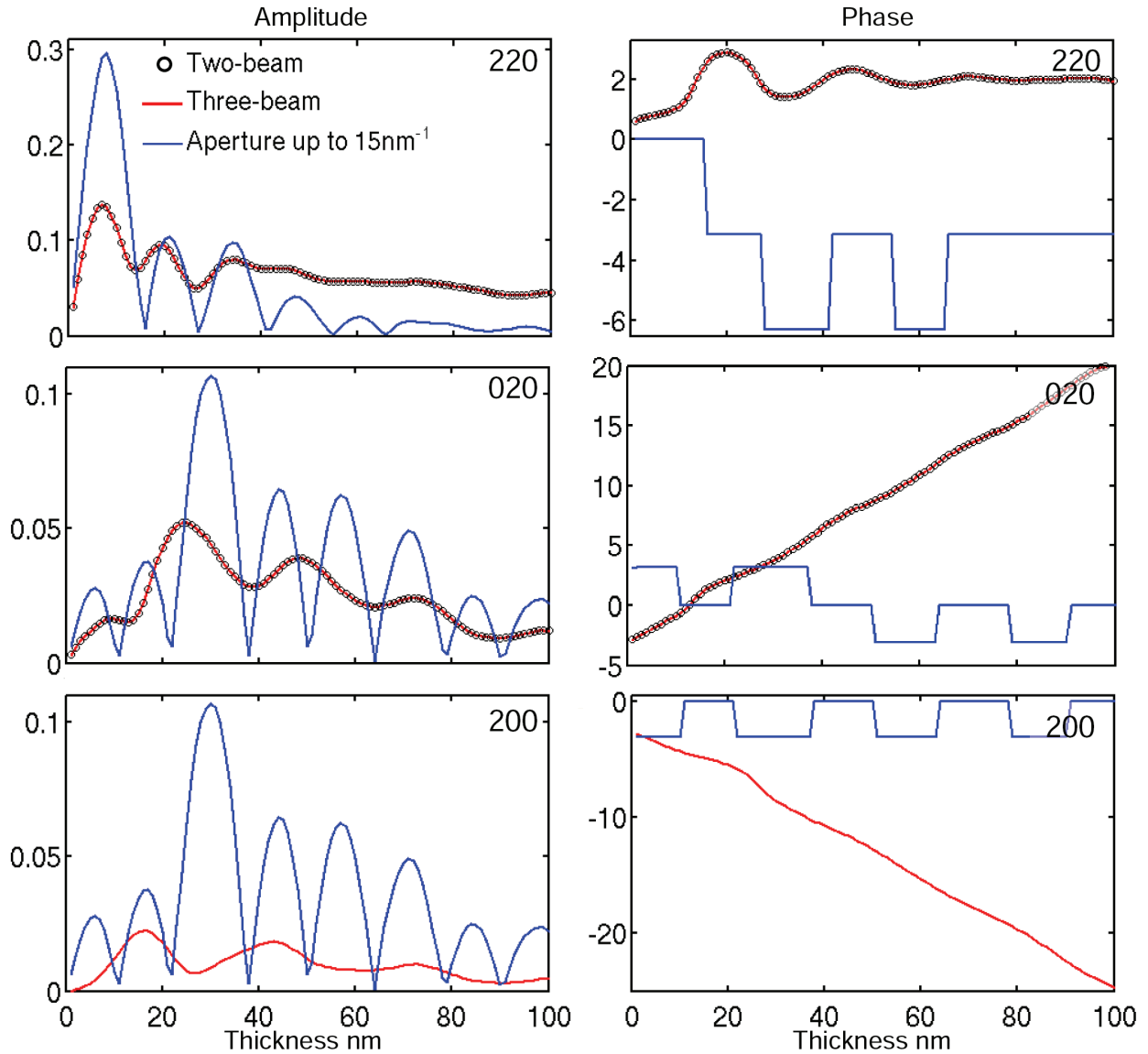


Figure 5.2: Thickness dependence of amplitudes and phases of selected diffractogram reflections calculated with the Bloch4TEM [37] software using Eq. (5.5). Parameters for nonlinear incoherent imaging have been chosen as follows: $C_S = 0.5\text{ mm}$, $\alpha = 0.3\text{ mrad}$, $\Delta = 5\text{ nm}$, and $\Delta f = -31\text{ nm}$ (Scherzer defocus). Incidence of 300 kV electrons was along [001] in GaAs.

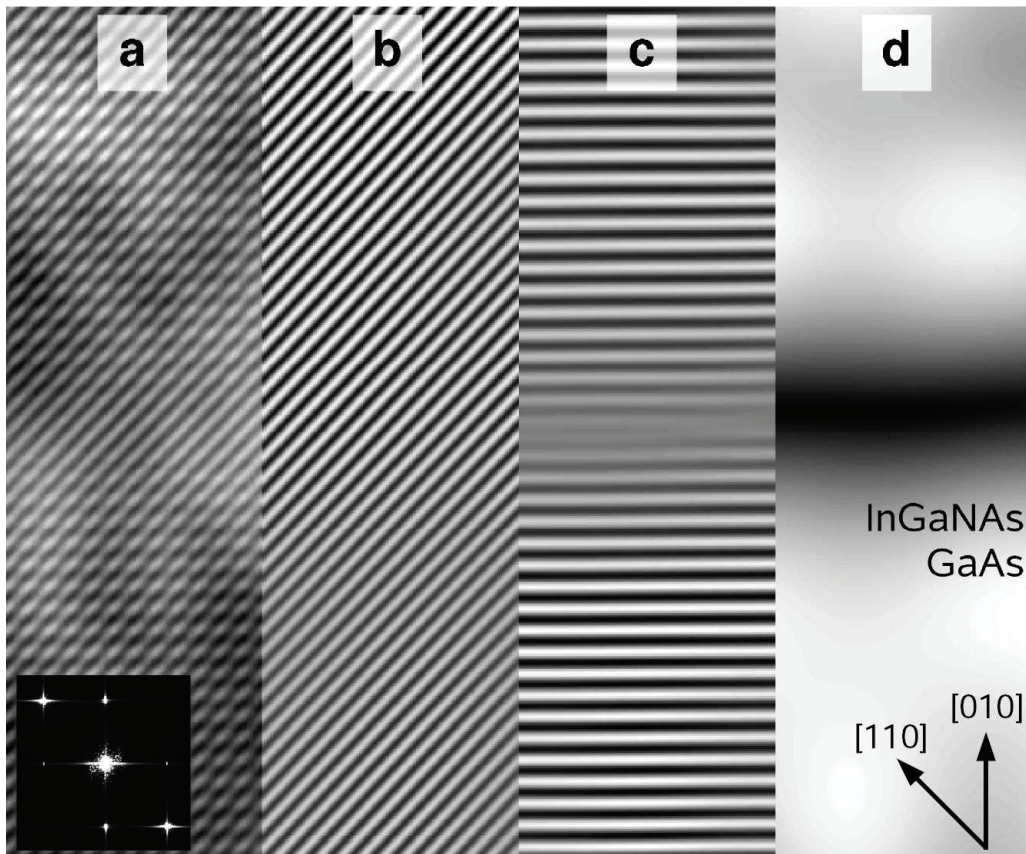


Figure 5.3: Decomposition of an experimental three-beam image (a) acquired near zone axis [001] with a Laue circle centre at (4.200). Via Fourier filtering, 220 and 020 fringe images (b,c) are obtained by keeping the primary beam and a circular area around the respective reflection in the diffractogram, shown as inset in (a). The 020 fringe amplitude obtained by keeping only frequencies close to the 020 reflection in the diffractogram and inverse Fourier transformation is shown in part (d), where also the GaAs/ $\text{In}_{0.28}\text{Ga}_{0.72}\text{N}_{0.025}\text{As}_{0.975}$ interface is marked. Contrast has been adjusted for better visibility.

5.3.2 Three-beam imaging

In order to measure strain from 220 and chemically sensitive contrast from 020 lattice fringes, an objective aperture is preferable that transmits the beams $\mathbf{g}_1 = (000)$, $\mathbf{g}_2 = (020)$ and $\mathbf{g}_3 = (220)$. In the frame of nonlinear imaging theory outlined in section 5.3.1, the image intensity at position \mathbf{r} reads

$$\begin{aligned}
 I(\mathbf{r}) = & A_1^2 + A_2^2 + A_3^2 + \\
 & 2A_1A_2T_{12} \cos(2\pi\mathbf{g}_2\mathbf{r} - \phi_{12} - \varphi_{12}) + \\
 & 2A_1A_3T_{13} \cos(2\pi\mathbf{g}_3\mathbf{r} - \phi_{13} - \varphi_{13}) + \\
 & 2A_2A_3T_{23} \cos[2\pi(\mathbf{g}_2 - \mathbf{g}_3)\mathbf{r} + \phi_{23} + \varphi_{23}] \quad .
 \end{aligned}
 \tag{5.6}$$

In Eq. (5.6), $\Psi_{\mathbf{g}_n} = A_n \exp(i\varphi_n)$ is the amplitude of diffracted beam \mathbf{g}_n , $\varphi_{nm} = \varphi_n - \varphi_m$ is the phase difference between beams $\mathbf{g}_n, \mathbf{g}_m$, and $T_{nm} \exp(i\phi_{nm})$ is the corresponding transmission cross coefficient. The first two cosine terms in Eq. (5.6) express conventional two-beam images, i.e. interference of one diffracted with the primary beam. The last summand, however, originates from nonlinear imaging and causes additional diffractogram

reflections at $\pm(200)$, as was seen in Fig. 5.2. Thus, 020 and 220 fringes are not affected by nonlinear imaging, so that the three-beam image can be decomposed into conventional two-beam fringe images by Fourier filtering, which was already observed in the simulations depicted in Fig. 5.2.

Figure 5.3 (a) depicts an experimental noise-filtered three-beam image containing an interface between $\text{In}_x\text{Ga}_{1-x}\text{N}_y\text{As}_{1-y}$ and GaAs in the centre. The superposition of 020 and 220 fringes is clearly visible in both image and diffractogram bottom left. However, the latter depicts also weak $\pm(200)$ reflections, although only beams (000), (020) and (220) were selected by the L-shaped objective aperture. The advantage to include the (220) beam becomes obvious in Fig. 5.3 (b-d): At certain concentrations (x,y), the 020 structure factor becomes zero and changes sign, resulting in nearly vanishing 020 fringes and a phase shift of half a period as depicted in Fig. 5.3 (c) and (d). In contrast, the amplitude of the 220 fringes in Fig. 5.3 (b) is nearly constant throughout the interface, allowing for strain measurement in the whole region.

The term *strain* requires some attention since it not only refers to the distortion of a bulk InGaNAAs cell in terms of the relaxed cell dimensions as in chapter 4, but also because it is measured along [110] direction. In practice, elasticity theory as described in section 4.3 is applied to calculate the lattice parameter in growth direction as a function of composition. Then, the result is normalised to the lattice parameter of the GaAs substrate. As growth is along [010] here, the 020 fringe distance can be used to access this relative lattice parameter, which is denoted by $\varepsilon_{[010]}$ in the following. However, 45° rotation of the 220 fringes with respect to growth direction [010] induces a conversion factor

$$\varepsilon_{[010]} = \frac{\varepsilon_{[110]}}{\sqrt{2 - \varepsilon_{[110]}^2}} \quad (5.7)$$

in order to calculate $\varepsilon_{[010]}$ in growth direction from the measured quantity $\varepsilon_{[110]}$.

Equation (5.7) requires precise measurement of the local fringe distances, because small errors for $\varepsilon_{[110]}$ translate to considerably larger errors for $\varepsilon_{[010]}$. For example, a fluctuation of $\Delta\varepsilon_{[110]} = 0.01$ yields $\Delta\varepsilon_{[010]} = 0.02$. In practice, a Wiener noise filter is applied to the 220 fringe image, before detecting preliminary maxima positions by searching for pixels with highest intensity on each fringe. After that, local cosines are fitted at each maximum, yielding positions with subpixel accuracy. Then, $\varepsilon_{[010]}$ is obtained by application of Eq. (5.7) to local distances along [110] between adjacent maxima, normalised to the mean distance in a GaAs reference region. Note that a cosine is the exact representation of the image intensity according to Eq. (5.6).

Concerning evaluation of 020 fringe amplitude, we proceed as follows [7, 34]: In the diffractogram, spatial frequencies around the 020 reflection are isolated, which yields the local 020 fringe amplitude after inverse Fourier transform. Regions of known composition, usually GaAs buffer layers, are used for a two-dimensional polynomial surface fit, yielding the expected signal for pure GaAs throughout the whole image, to which the 020 fringe amplitude is normalised. This normalised 020 amplitude a_N , defined by

$$a_N(\mathbf{r}, \mathbf{c}, t, x, y) = \frac{A_1(\mathbf{r}, \mathbf{c}, t, x, y) \cdot A_2(\mathbf{r}, \mathbf{c}, t, x, y)}{A_1(\mathbf{r}, \mathbf{c}, t, 0, 0) \cdot A_2(\mathbf{r}, \mathbf{c}, t, 0, 0)}, \quad (5.8)$$

does in general not only depend on compositions x and y at position \mathbf{r} (chemical sensitivity) but also on specimen thickness t and specimen orientation \mathbf{c} , measured in terms of the position of the Laue circle centre. Since the specimen thickness is usually inaccurately known, section 5.3.3 deals with the derivation of orientations \mathbf{c} being robust against this

error. For this reason, the dependence on \mathbf{c} is explicitly written here, whereas it was omitted in Eq. (4.7) because optimised imaging conditions were known.

Finally, each point \mathbf{r} in the image can be assigned a concentration pair (x,y) by comparison of $\varepsilon_{[010]}$ and $a_N(\mathbf{r}, \mathbf{c}, t, x, y)$ with their simulated counterparts, similar to section 4.3. Whereas concentration-dependent strain reference data can be calculated using Vegard's rule in combination with elasticity theory, care must be taken for the simulation of a_N because the method relies on significant presence of both the 020 and the 220 beams. This can only be achieved by small specimen tilts with respect to zone axis [001]. This in turn causes strong dynamical effects on beam amplitudes and phases in Eq. (5.6), which will be analysed in section 5.3.3.

5.3.3 Simulation of reference data and optimised imaging conditions

Composition-dependent lattice parameters have been calculated exploiting elasticity theory as described in section 4.3 using parameters of table 2.1. Strain relaxation along the specimen surface normal was accounted for by the relaxation parameter r , which was set to represent an infinitely thin ($r = 0$), intermediately thick ($r = 0.5$) and an infinitely thick ($r = 1$) specimen, according to Eq. (4.5). Using these results, $50 \times 50 \times 50$ $\text{In}_x\text{Ga}_{1-x}\text{N}_y\text{As}_{1-y}$ supercells have been generated for the composition ranges $x \in \{0, 0.02, \dots, 1\}$ and $y \in \{0, 0.01, \dots, 0.07\}$. Indium and nitrogen atoms have been placed randomly at the metal- and nonmetal sublattice, respectively. Valence force field (VFF) relaxation has been performed as described in section 2.6.2 and Ref. [32] for each of these cells to obtain static atomic displacements (SAD). Structure factors have then been derived from the VFF-relaxed supercells as explained in Ref. [7] and chapter 4 in combination with modified atomic scattering amplitudes (MASA) defined in Eq. (2.31). The compositional dependence of the MASA for the 020 reflection and $r = 0.5$ is shown in Fig. 2.5. Furthermore, we have seen in sections 2.6.3 and 2.6.4 that Huang scattering losses in Bragg scattered beams, due to SAD, must be taken into account. According to section 2.6.4 and Ref. [134], this was included via additional absorptive form factors, derived from SAD statistics. The program Bloch4TEM [37] was used to simulate a_N as defined in Eq. (5.8).

Before turning towards explicit reference amplitudes used for the present experiments, let us consider the dependence of a_N on specimen thickness as a function of specimen tilt \mathbf{c} as expressed by Eq. (5.8). This was studied via Bloch wave simulations of pendellösung plots for various specimen orientations, assuming an $\text{In}_{0.08}\text{Ga}_{0.92}\text{N}_{0.03}\text{As}_{0.97}$ crystal. In practice, the beam is usually focused slightly to concentrate illumination on the specimen area of interest. This was accounted for by averaging a_N over several incidences according to a beam convergence of 1.5 mrad, which was measured from the reflection disc size in a diffraction pattern. To present results in a compact manner, the standard deviation $\sigma_t(\mathbf{c})$ of the thickness dependence $a_N(t = [0 \dots 100 \text{ nm}])$ was calculated for each orientation $\mathbf{c} = (hk0)$. In order to study the relevance of $\sigma_t(\mathbf{c})$ in view of the magnitude of a_N itself, it was divided by the respective normalised amplitude at 1 nm thickness, which in principle represents a_N in kinematic approximation. The function $\sigma_t(\mathbf{c})/a_N(1 \text{ nm})$ is mapped in reciprocal space in dependence on h and k in Fig. 5.4.

As expected, orientations close to zone axis in the left quarter of Fig. 5.4 exhibit comparably strong thickness dependence with $\sigma_t(\mathbf{c})/a_N(1 \text{ nm}) \in [0.1 \dots 0.25]$. This means that the uncertainty of a_N due to unknown specimen thickness is up to 25% of the signal

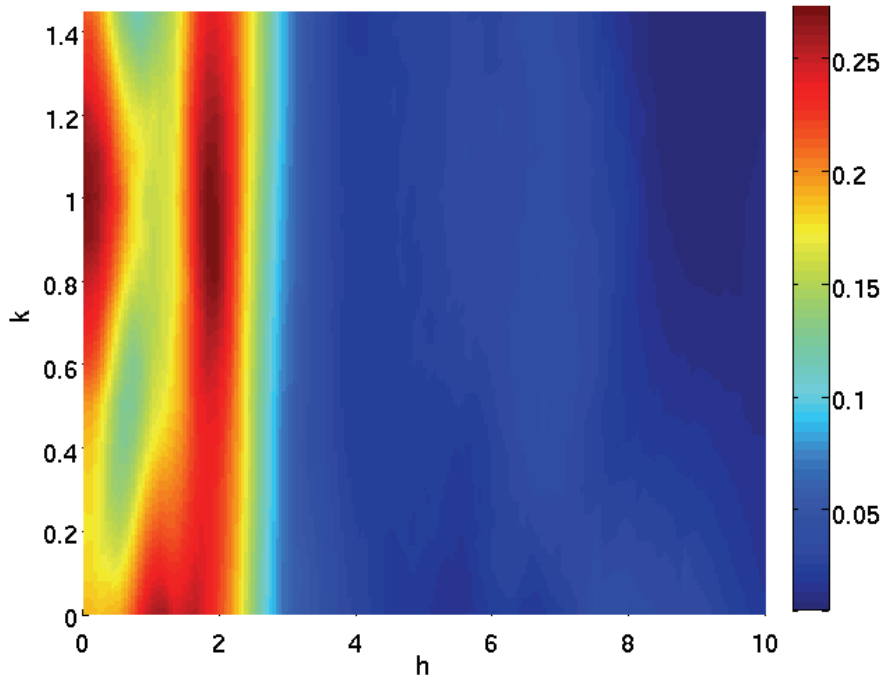


Figure 5.4: On the thickness dependence of $a_N(\mathbf{c} = (hk0), t, x = 0.08, y = 0.03)$ as a function of specimen tilt. The standard deviation $\sigma_t(h, k)$ derived from thickness characteristics of $a_N(t)$ was normalised to $a_N(1 \text{ nm})$ and is depicted colour-coded, showing that tilts with $h > 3$ significantly minimise dependence on thickness.

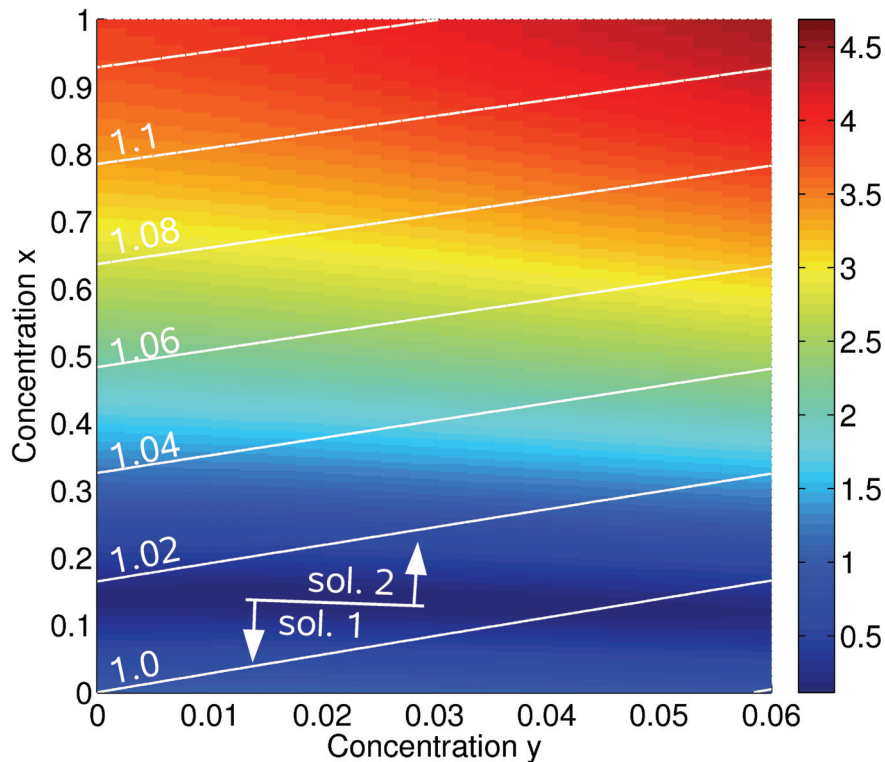


Figure 5.5: Reference values for $\varepsilon_{[010]}$ (white isolines) and relative 020 fringe amplitude a_N as a function of indium concentration x and nitrogen concentration y for a Laue circle centre $\mathbf{c} = (4.200)$ and for a thickness of 30 nm. Bonding and SAD are accounted for as proposed by Müller et al. [7], except for the additional absorptive form factor due to SAD diffuse losses dealt with in section 2.6.4 and Ref. [134].

itself. Towards $h \approx 3$, the ratio $\sigma_t(\mathbf{c})/a_N(1 \text{ nm})$ rapidly drops below 0.05 which is due to the fact that the excitation of the relatively strong ± 400 reflections becomes very weak. For $h > 3$, $\sigma_t(\mathbf{c})/a_N(1 \text{ nm})$ first passes a minimum around $h \approx 5$ and then slightly increases again towards $h = 10$. Furthermore, the thickness dependence is rather independent of tilt k for $h > 3$, so that the error due to a slight misalignment in experiment is low. However, in order to achieve significant 220 fringes and passably small thickness dependence of $a_N(t)$, a Laue circle centre $\mathbf{c} = (4.200)$ was set in all experiments and simulations of reference amplitudes according to Eq. (5.8). Here, the uncertainty of a_N due to unknown specimen thickness is only around 2% of a_N itself.

In general, it is of course not only necessary to additionally study $\sigma_t(\mathbf{c})$ as a function of composition but also to translate the error due to inaccurately known specimen thickness to absolute errors for the concentrations x and y . For reasons of brevity, this issue is alternatively addressed explicitly for each measured composition map in sections 5.4 and 5.5, where experimental profiles are presented by giving composition ranges for the indium- and nitrogen content resulting from different assumptions for the specimen thickness.

As an example, Fig. 5.5 depicts a_N obtained from Bloch wave simulations for a thickness of 30 nm as a colour-coded map, together with reference values for the relative fringe distance $\varepsilon_{[010]}$ as white isolines. Note that, except for the tilt setting and the fact that absorption due to Huang scattering was taken into account here, the reference data in Fig. 5.5 appears completely analogous to former work (see chapter 4 and Ref. [7]), to which the reader is referred to for details on bonding, VFF relaxation and strain reference data. Another important difference is the magnitude of the normalised amplitude here, being nearly twice as large in the maximum, compared to using a Laue circle centre of $\mathbf{c} = (20 \ 1.5 \ 0)$ [7].

However, each point in a three-beam image as depicted in Fig. 5.3 can be assigned an amplitude/strain pair that corresponds to at most two indium/nitrogen composition pairs, separated by the dark blue valley as indicated in Fig. 5.5. Nevertheless this ambiguity is not critical since both solutions can be well separated in experiment as Fig. 5.3 (d) shows.

Let us finally pick up the impact of additional absorptive form factors for Huang scattering for the imaging condition just found. To this end, the STEMsim software [33] was used to perform frozen lattice multislice simulations of pendellösung plots, analogous to section 2.6.4, but assuming $\mathbf{c} = (4.200)$ here. In particular, tilt was accomplished by modified Fresnel propagation as defined in Eq. (2.50) and compositions were chosen to be $x = 0.3$ and $y = 0.02$, which is close to the nominal content of sample III. Lateral extension of the VFF-relaxed supercell was 10×10 Bravais cells. For each of the 20 supercells with identical composition but different spatial distribution of indium and nitrogen, the frozen lattice result was averaged over 10 thermal displacement configurations. Additionally, Bloch wave [37] simulations were carried out, in which Huang scattering was neglected or included via absorptive potentials [75], respectively. In this case, structure factors and SAD statistics have been derived from the same cells as used for the frozen lattice multislice simulations. A comparison between the three approaches is shown in Fig. 5.6 for the 200 reflection. As expected from the exact zone axis case in Fig. 2.9, the blue curve shows that neglect of Huang scattering losses leads to a too large beam amplitude, or, equivalently, to an underestimation of damping with increasing specimen thickness. In contrast, the Bloch wave simulation including additional absorptive form factors (red graph) exhibits improved consistency with the black frozen lattice result. Nevertheless the agreement is not perfect which can be explained by the fact that Huang scattering occurs at definite positions in the crystal where SAD are large. This is translated to a

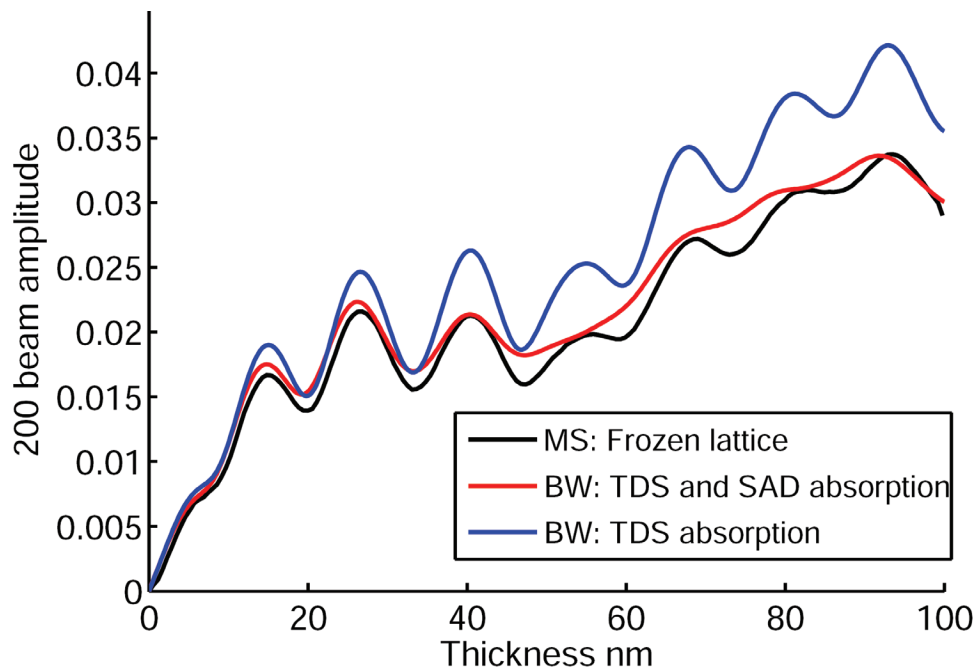


Figure 5.6: Pendellösung plots for the 020 beam in $\text{In}_{0.3}\text{Ga}_{0.7}\text{N}_{0.02}\text{As}_{0.98}$ with the Laue circle centre at (4.200). *Black*: Frozen lattice multislice (MS) simulation. *Red*: Bloch wave (BW) simulation with thermal diffuse and SAD absorption [75]. *Blue*: Conventional BW simulation with thermal diffuse absorption only.

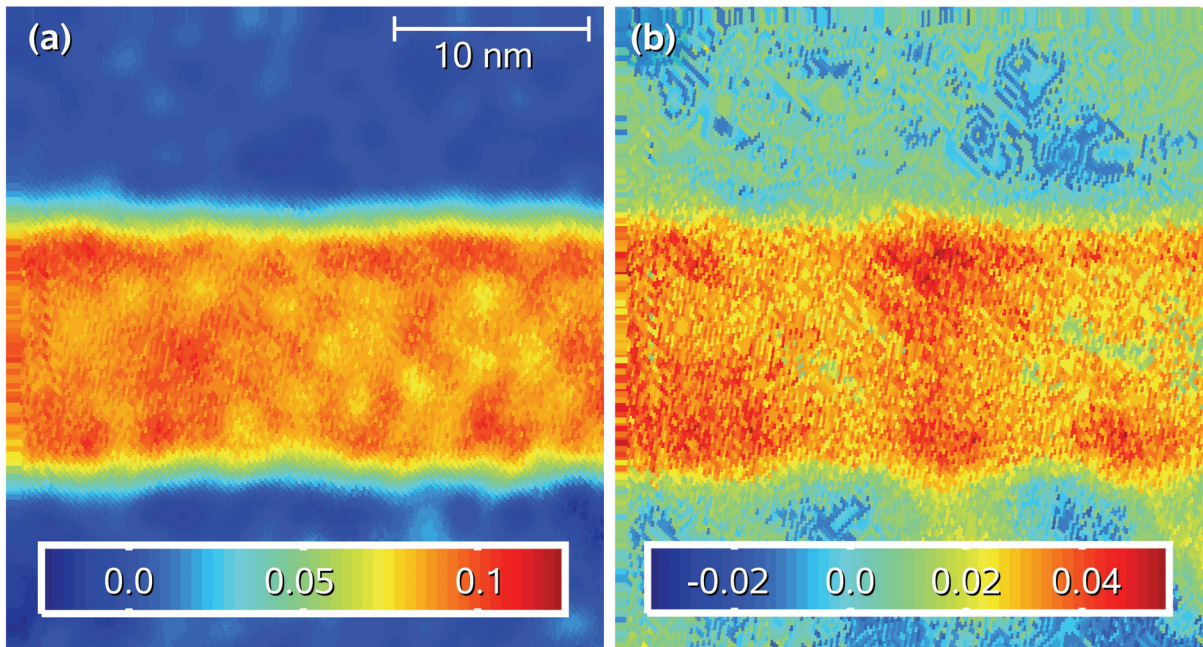


Figure 5.7: Concentration evaluation yielding (a) local indium- and (b) local nitrogen distribution for sample I exemplarily for a thickness of 30 nm.

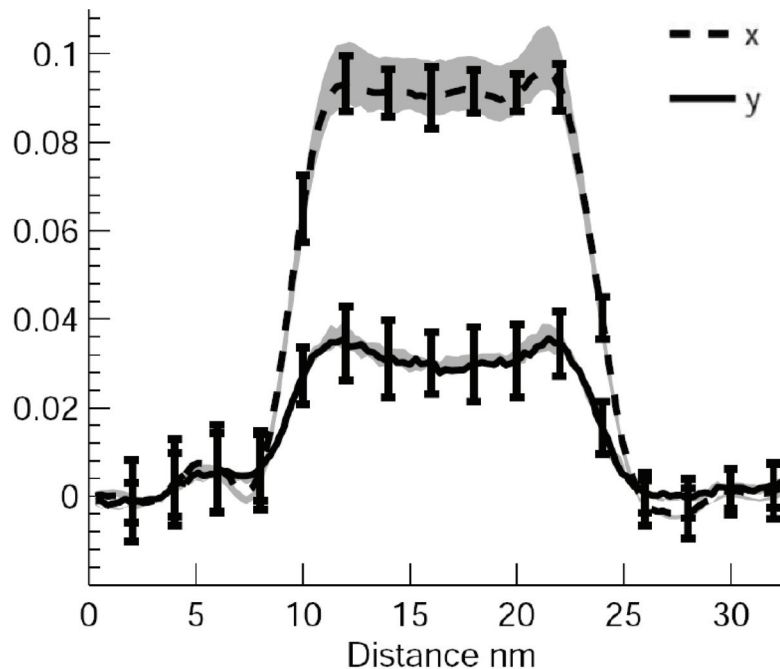


Figure 5.8: Concentration profiles for the indium content x and the nitrogen content y of sample I, obtained by averaging horizontally in (Fig. 5.7 a, b). Error bars are drawn each 2 nm only and indicate statistical fluctuations, the grey corridor is a measure of error due to inaccurate knowledge of the specimen thickness.

continuous, mean absorption in the Bloch wave approach, so that we expect mainly the damping envelopes to be well represented, as was already discussed in section 2.7.3. In summary, we conclude that it is necessary to take into account Huang scattering losses for the present imaging condition with the Laue circle centre at $\mathbf{c} = (4.200)$, whereas no significant influence has been observed for the systematic row case in chapter 4 and Ref. [7].

5.4 Results for the low-indium regime

As a first evaluation, results for a lattice-matched InGaNAs layer in sample I, being a typical setup for solar cell applications, are presented. These results are of particular interest from the methodological point of view, because consistency with compositional analysis of this sample using different TEM methods [7] (see also chapter 4), or X-ray diffraction and bandgap measurements [15] for a sample grown under the same conditions may be checked.

Figure 5.7 depicts local distributions of indium (part a) and nitrogen (part b) which have been obtained from three-beam imaging as described in section 5.3.2. At this stage, we will not go into details of strain and amplitude maps, but interpret results as to the maps derived by two-beam imaging in Fig. 4.9. Concerning quantum well height, homogeneity and mean values of both compositions, results of both chapters are in good agreement. However, statistical composition fluctuations are slightly larger here due to more imprecise strain measurement owing to the conversion factor in Eq. (5.7).

As mentioned in section 5.3.3, it is necessary to analyse the dependence of compositional analysis on specimen thickness. To this end, a series of composition maps has

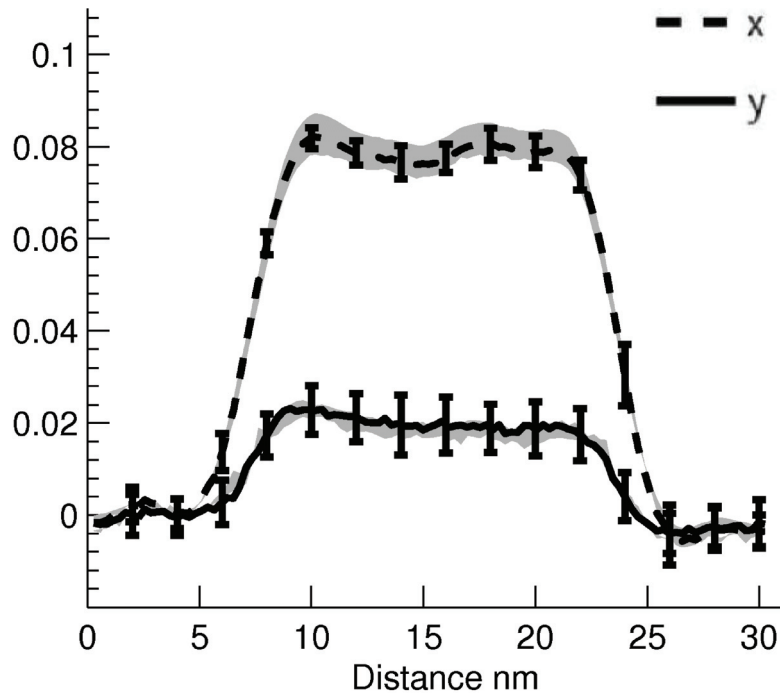


Figure 5.9: Concentration profiles for the indium content x and the nitrogen content y of sample II. Error bars are drawn each 2 nm only and indicate statistical fluctuations, the grey corridor is a measure of error due to inaccurate knowledge of the specimen thickness.

been calculated analogously to Fig. 5.7, assuming thicknesses between 10 nm and 80 nm in steps of 5 nm. For each thickness, compositions have been averaged horizontally over the full maps in Fig. 5.7 to obtain an upper and a lower limit for the error induced by insufficient knowledge of the specimen thickness. Figure 5.8 shows the profiles for intermediate thickness of 30 nm from Fig. 5.7 as black curves. The grey corridors mark the composition ranges in which all profiles fall. Furthermore, errorbars in Fig. 5.8 correspond to the standard deviations in horizontal direction in Fig. 5.7. These lateral compositional fluctuations stay below ± 0.01 and are independent of the magnitude of x and y . In contrast, the grey corridor, in which all results between thicknesses of 10 and 80 nm fall, widens to diameters of $\Delta x \approx 0.012$ with increasing composition. However, a mean indium composition $\bar{x} = 0.088 \pm 0.01$ and a mean nitrogen content $\bar{y} = 0.03 \pm 0.01$ can be assigned to sample I from Fig. 5.8. Finally, the nitrogen profile exhibits marginal enrichment of this element at the layer interfaces, which nevertheless ranges inside the error bars. Whether this is indeed a physical effect or an artefact of, e.g., the measurement of local fringe distances, will be discussed in section 5.6.

Let us finally turn towards sample II, which differs from sample I only in the nitrogen flux during growth, having been calibrated to result in a nominal nitrogen content $y = 0.02$. In contrast to sample I, where the relative fringe distance $\varepsilon_{[010]}$ takes values of approximately 1.0 throughout the whole quantum well, the InGaNaNs layer in sample II is compressively strained laterally, so that $\varepsilon_{[010]} \approx 1.005$ in growth direction. In complete analogy to sample I, composition maps have been determined from a three-beam image assuming thicknesses between 10 nm and 80 nm. Figure 5.9 depicts the resulting composition profiles, together with both thickness and statistical errors as in Fig. 5.8. The indium profile exhibits a mean concentration of $\bar{x} = 0.079 \pm 0.006$, which is nearly one percent less than the mean indium content in sample I. However, the nitrogen profile

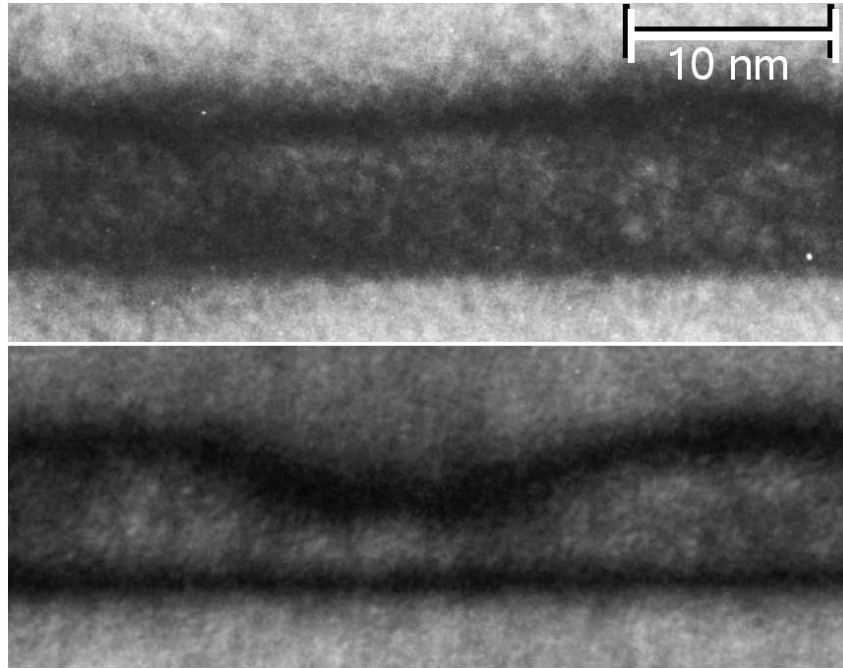


Figure 5.10: 020 dark field overview images of samples III a (annealed, top) and III b (as-grown, bottom) which qualitatively show the effect of thermal annealing on layer morphology which roughly follows the null of the 020 structure factor. Both images were taken off-zone with a Laue circle centre at (2010).

with $\bar{y} = 0.020 \pm 0.008$ shows that the intended composition is indeed reached. Although the indium profiles of Figs. 5.8 and 5.9 agree as to the mean indium content within the error margins, it seems that incorporation of indium during growth is not independent of the nitrogen flux, stressing the importance of dual compositional mapping without, e.g., a ternary standard.

5.5 Annealing effects in $\text{In}_{0.28}\text{Ga}_{0.72}\text{N}_{0.025}\text{As}_{0.975}$

To get an impression of annealing effects on structural changes in an InGaNaS layer, Fig. 5.10 contains TEM darkfield images of samples III a (annealed, top) and III b (as-grown, bottom). Before annealing, clear evidence for island formation on a wetting layer is observed as in the Stranski-Krastanow growth mode. After annealing, homogenisation of layer thickness is found. A more quantitative result for the local indium and nitrogen distributions will now be derived using the three-beam method.

Before turning towards elemental distributions, evaluation of normalised fringe distance $\varepsilon_{[010]}$ and -contrast is exemplified using sample III a in order to show that strain data is present throughout the whole quantum well. Parts of the local distance and amplitude maps, having been derived from a TEM three-beam image as explained in section 5.3.2, are depicted in Fig. 5.11. Each pixel on the left corresponds to one local result for $\varepsilon_{[010]}$, clearly exhibiting GaAs buffer layers with $\varepsilon_{[010]} \approx 1.0$ and a strained InGaNaS layer with a thickness of about 10 nm with $\varepsilon_{[010]} \approx 1.025$ in the maximum. The right hand side of Fig. 5.11 shows the normalised amplitude a_N for the same specimen region. Here, two different regimes appear according to indium contents below and above the intensity valley in Fig. 5.5. Note that precise data for $\varepsilon_{[010]}$ is available also where a_N

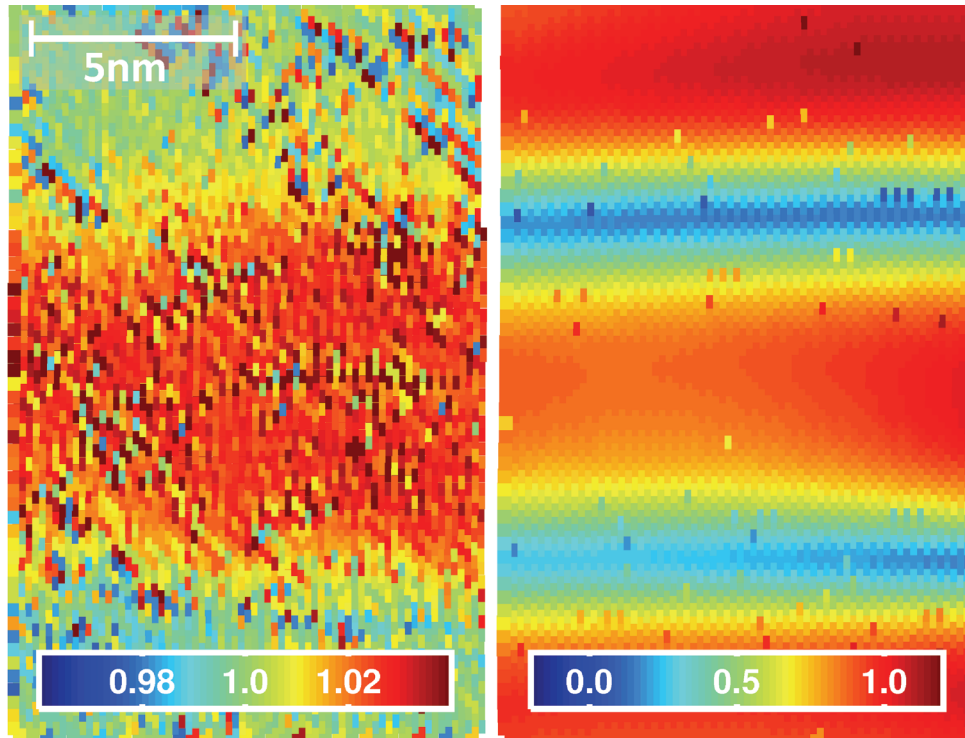


Figure 5.11: Experimental maps for the local fringe distance (normalised to GaAs) $\varepsilon_{[010]}$ (left) and chemically sensitive fringe amplitude a_N (right) for sample III a. Both maps have been extracted from the same three-beam TEM image by evaluation of local 220 fringe distances and Eq. (5.7), and the 020 fringe amplitude.

nearly vanishes.

Comparison with reference data as described in section 5.3 for thicknesses between 10 and 80 nm and sub-division of the TEM image in high- and low-indium sections yields local distributions of indium and nitrogen which are shown in Fig. 5.12 (a,b) exemplarily for a specimen thickness of 30 nm. To allow for composition fluctuations around zero in the GaAs buffer layers due to statistical errors in measurements of local fringe distances and normalised amplitudes, the reference data was extrapolated down to concentrations of -0.05 . Both maps in Fig. 5.12 reveal a more or less homogeneous layer thickness and -stoichiometry in lateral direction with $x \in [0 \dots 0.28]$ and $y \in [0 \dots 0.03]$, respectively. However, a slight indium enrichment of 0.03 appears at the left and right edge of Fig. 5.12 (a).

The lateral homogeneity motivates an analysis of characteristic features on the basis of concentration profiles presented in Fig. 5.12 (c), which originate from lateral averages over the full widths in parts (a) (dashed line) and (b) (solid line), respectively. For indium, a symmetric, Gaussian-shaped profile is observed with a maximum of $x = 0.27$. In contrast, the nitrogen profile is shifted by about 2 nm in growth direction, leading to slight enrichment up to $y = 0.03$ in the upper half of the quantum well.

As in section 5.4, Fig. 5.12 (c) contains two types of error displayed in form of error bars and a grey corridor, respectively. The former corresponds to the standard deviation derived from the full lateral averages in the two-dimensional elemental maps in Fig. 5.12 (a,b). For better visibility, this error is drawn only each two nanometres. The latter error results from elemental maps for which different specimen thicknesses were assumed. In this respect, the grey area indicates the concentration range derived from

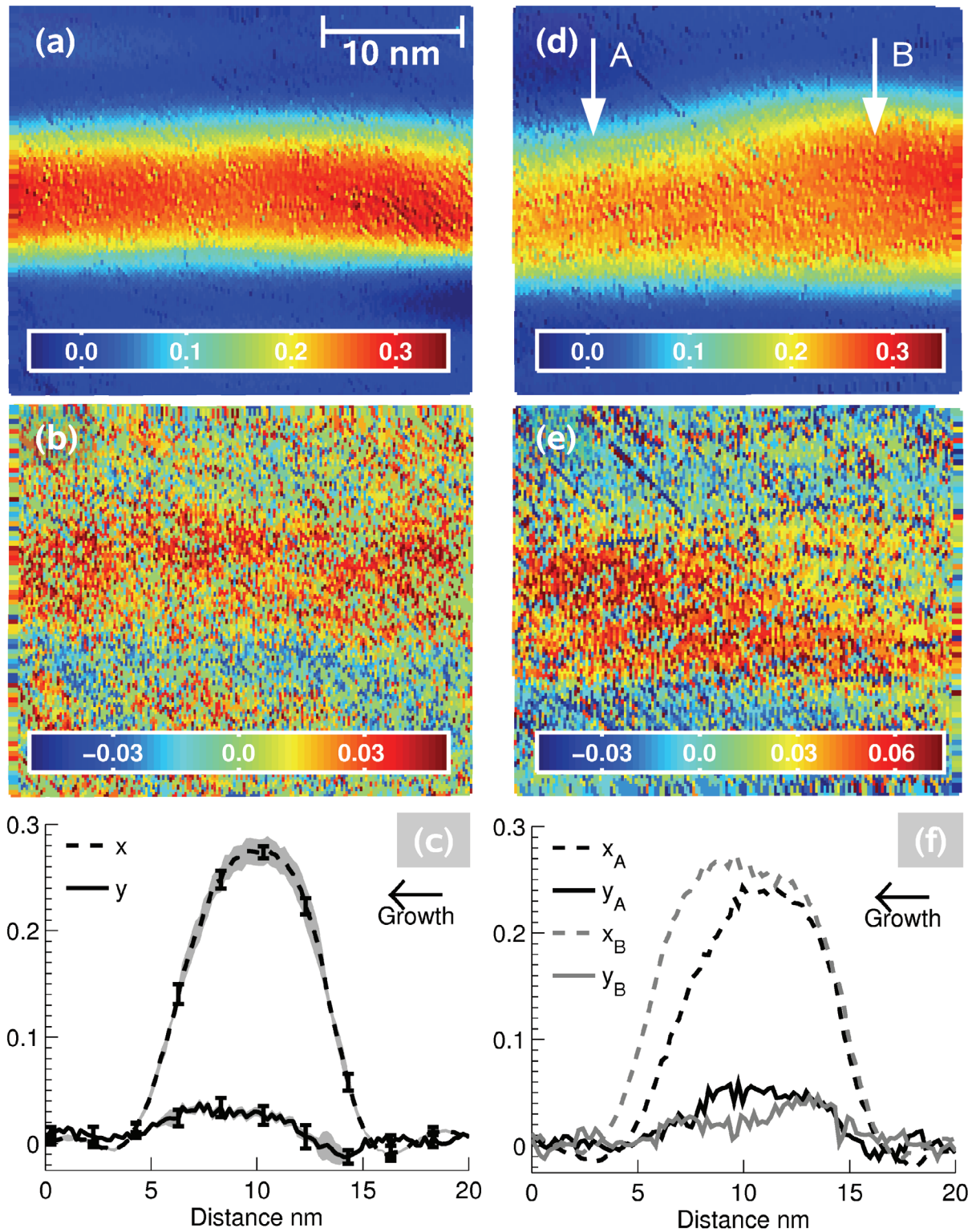


Figure 5.12: Concentration evaluation for sample III. Figure parts (a-c) correspond to the annealed sample III a, whereas parts (d-f) belong to the as-grown sample III b. At the top (a,d), the local distribution of indium is mapped, in the middle (b,e) we see the local distribution of nitrogen. Figure part (c) shows composition profiles obtained by averaging horizontally in (a,b). Error bars indicate statistical fluctuations, the grey corridor is a measure of error due to inaccurate knowledge of the specimen thickness. Part (f) summarises four composition profiles taken at paths indicated in (d). In all evaluations, a relaxation parameter $r = 0.5$ was assumed which corresponds to intermediate specimen thickness.

profiles corresponding to specimen thicknesses between 10 and 80 nm in steps of 5 nm. Thus it is a direct measure of the error induced by inaccurately known specimen thickness. Whereas the statistical error (black bars) takes nearly constant values of ± 0.01 and is widely independent of x , y and the atomic species, the imprecision due to unknown specimen thickness mostly affects the indium measurement. It significantly depends on the magnitude of x , resulting in a maximum absolute error of ± 0.01 in the quantum well centre.

As to structural changes during annealing it is instructive to compare sample III a with its as-grown counterpart III b whose composition maps are depicted in Fig. 5.12 (d,e). Regarding the indium distribution in Fig. 5.12 (d), lateral fluctuations become evident, especially towards the upper third of the layer. Besides this morphologic separation into wetting layer and island regions, a slight indium enrichment of 0.03 – 0.05 appears inside the island. In contrast, the nitrogen distribution in Fig. 5.12 (e), follows an opposite trend: Being inhomogeneous as well, nitrogen preferably occupies the region outside the island with concentrations up to $y \approx 0.06$, dropping to $y \approx 0.02$ inside the island.

Because of the inhomogeneity of the InGaNA_s layer, Fig. 5.12 (f) shows two pairs of profiles A and B, having been derived from lateral averages in the respective regions labelled in figure part (d). Here, error bars have been omitted to point out profile shape. However, thickness errors are comparable to those in Fig. 5.12 (c), whereas statistical fluctuations are slightly larger due to the narrow areas for averaging. As expected, indium profiles $x_{A,B}$ exhibit fluctuations of about 2.5 nm for the layer thickness and differ in maximum indium amounts by about 0.04. Compared to the symmetric indium profile for sample III a, especially the profile for x_A is asymmetric: After gradual increase, the indium content saturates to a maximum in the upper half of the layer and then decreases rapidly.

The nitrogen profiles $y_{A,B}$ in Fig. 5.12 (f) differ significantly in shape and reveal different nitrogen contents as mentioned above. However, y_A shows up a maximum amount of about 0.05. The profile is not only symmetric with respect to the centre of the wetting layer, but also in phase with profile x_A . Concerning the grey curve y_B , slight nitrogen enrichment up to $y_B = 0.05$ at incipient layer formation is observed which decays to about 0.02 during further growth and increasing indium content as expressed by profile x_B .

5.6 Discussion

5.6.1 Composition mapping

The three-beam method presented here is in principle a consequent combination of strain state analysis and composition evaluation by lattice fringe analysis (CELFA [34]) and is of low experimental effort, provided that an aperture is available which suppresses nonlinear imaging artefacts on the 220 and 020 diffractogram reflections. In contrast to systematic row techniques [2, 148, 34, 7], the error of inaccurately known specimen thickness becomes significant, so that indication of concentration-dependent corridors, which contain solutions for physically plausible thicknesses, should be part of final concentration profiles. Nevertheless one should keep in mind that, even though the corridor in Fig. 5.12 (c) corresponds to a thickness interval of 70 nm, errors for nitrogen are negligible and those for indium do not exceed ± 0.01 . However, comparison of Figs. 5.12 (a-c) with 5.12 (d-f) clearly shows that qualitative observations as to the correlation of indium and nitrogen distributions, or as to the shape of the layer, are not influenced by this error.

A similar argument holds for a last source of error, on which few attention has been spent until here. In section 4.3, a relaxation parameter r was introduced in order to account for strain relaxation along the specimen surface normals. For the analysis of lattice-matched InGaNAs in chapter 4 and section 5.4, the choice of r is not critical, but for $\text{In}_{0.28}\text{Ga}_{0.72}\text{N}_{0.025}\text{As}_{0.975}$ in section 5.5, the impact of zone axis relaxation was checked. To this end, strain reference data for an infinitely thin ($r = 0$) and an infinitely thick ($r = 1$) specimen was used to re-evaluate the composition maps of sample III a. For a thin specimen, the lattice parameter in growth direction decreases in the InGaNAs layer, so that a higher amount of indium or a lower amount of nitrogen is needed to produce the same relative fringe distance, compared to a thick specimen. However, the isolines of the normalised fringe amplitude a_N in Fig. 5.5 are widely independent of r and proceed nearly horizontally. Therefore, a change in position and angle of the isolines for $\varepsilon_{[010]}$ mainly alters the result for nitrogen. In particular, the assumption of a thin specimen leads to a maximum nitrogen content of 0.019 in the profile of Fig. 5.12 (c), whereas a maximum content of 0.033 is found for a thick specimen. As to the maximum indium content, the choice of r leads to changes of $\Delta x \approx 0.01$, meaning that the relative error induced by unknown relaxation along zone axis is negligible here, compared to the nitrogen profiles. However, it must be noticed that neither $r = 0$ nor $r = 1$ are realistic assumptions, because for very low thicknesses, the 020 intensity would have been too weak for the evaluation of a_N on the one hand, whereas identification of single islands, being separated by approximately only 20 nm according to Fig. 5.10, is unfeasible for thick specimens on the other hand.

In methodological respect, introduction of a new approach should meet two criteria: First, compared to previously reported techniques, application to the same samples must reproduce former reliable results. Second, it should extend applicability of existing TEM methods [2, 3, 7]. Concerning the first argument, it was verified in section 5.4 that mean indium- and nitrogen contents agree well with independently found results: For sample I, two-beam imaging under systematic row conditions yielded $\bar{x} = 0.08 \pm 0.01$, $\bar{y} = 0.03 \pm 0.005$ for the mean concentrations in chapter 4 and Ref. [7]. Additionally, bandgap measurements and X-ray diffraction applied to a sample grown under the same conditions confirmed this composition [15]. As to different TEM composition quantification techniques, three main arguments are worth mentioning: First, the present approach works standardless in a sense that no ternary quantum well is needed as reference as it is the case in studies of Litvinov et al. [3]. Especially the assumption can be dropped that indium incorporation during growth does not depend on that of nitrogen. Indeed, the indium content of sample II was found to be slightly lower than in sample I in this chapter. This trend is additionally confirmed by a previous study [7] in chapter 4, where the indium content of a ternary InGaAs layer was also found to be slightly lower than that of sample I. Although this is a marginal effect here because differences in indium compositions are below 0.01, this effect is not unexpected because incorporation of nitrogen reduces strain and hence facilitates indium incorporation. Second, the present method is not limited anymore to concentrations far-off the phase jump, or, equivalently, significant presence of the 020 fringes. This extends single-image compositional analysis to the important field of InGaNAs laser structures. Third, it becomes obvious from section 5.5 that an analysis of composition fluctuations relies on knowledge of both strain and chemical contrast for each lattice point which can hardly be assured by superposition of a systematic row dark field and a zone axis high-resolution TEM image [2, 148]. Of course this procedure is less critical for InGaNAs layers having homogeneous composition

laterally. However, a three-beam approach has been proposed already before to solve this problem [2, 7].

5.6.2 Annealing effects

Investigation of compositional fluctuations by TEM must critically be analysed with respect to specimen thickness, because measured quantities are a superposition of sample properties in zone axis direction. Nevertheless it is obvious that the island observed in Fig. 5.12 (d-f) is indeed the image of a single island. If the specimen was much thicker than the mean distance between islands, being 20–30 nm according to Fig. 5.10, a blurred layer with homogeneous thickness would be observed. If so, the observation of an InGaNAs layer with homogeneous thickness after annealing in Fig. 5.12 (a-c) could be due to this effect. However, then the 020 fringe intensity would not vanish at the upper interface because, at some specimen depth, an area with pure GaAs would exist which violates the continuity condition for the transition between the two possible solutions according to Fig. 5.5. For thick regions of the as-grown sample III b this effect was indeed observed.

In short, it is observed here that annealing changes long-range order of both indium and nitrogen. This results in a homogenisation of the nitrogen distribution and symmetric indium concentration profiles. In particular, thermal annealing caused a dissolution of islands, which leads to a nearly homogeneously thick InGaNAs layer. This observation suggests that the increase of PL intensity by a factor of 20 and the spectral shift of about 60 meV to higher energies is due to a long-range homogenisation of stoichiometry in the present case. From the experimental point of view, presence of nitrogen fluctuations in as-grown InGaNAs is controversially discussed in literature. For example, Albrecht et al. [144] found indium fluctuations of ± 0.05 on a length scale of 20 nm but homogeneous nitrogen content. In contrast, Herrera et al. [149] additionally report on nitrogen modulations, resulting in uncoupled indium-rich and nitrogen-rich regions. Common to these analyses is the underlying darkfield imaging technique using, e.g., the 220 reflection. In this respect, simultaneous evaluation of both strain and chemical sensitive contrast at identical specimen positions is a requirement to clarify this issue. Thus, present results tend to confirm findings of Herrera et al. [149] who interpret composition modulations and decoupling of nitrogen and indium profiles in the framework of spinodal decomposition. However, it is important to keep in mind that characteristics of the InGaNAs layer are highly dependent on growth conditions which differ among research groups.

Photoluminescence spectra from Fig. 5.1 exhibit characteristic annealing behaviour, since a blue shift of about 60 meV has also been found by Klar et al. [16] for the same annealing temperature. However, Klar et al. found no evidence for compositional fluctuations even in the as-grown sample. Consequently this group interprets annealing effects in terms of preferential coordination of nearest neighbours, that is, an affinity to form In-N bonds instead of Ga-N bonds, as has frequently been reported in conjunction with thermal annealing [16, 22, 150, 148, 21, 151]. In this work, direct observation of the dissolution of compositional modulations during thermal annealing implies that the change in PL is due to homogenisation of stoichiometry. Since Klar et al. used MOVPE, whereas sample III in this work was grown by MBE, one tends to assign different annealing mechanisms to both epitaxial techniques. In fact, there is no contradiction between both explanations, because annealing might also have caused preferential nearest neighbour configurations here. In this respect, Fig. 5.12 implies that a dissolution of nitrogen- and indium-rich regions in favour of a more homogeneous layer ought to be accompanied by an increase

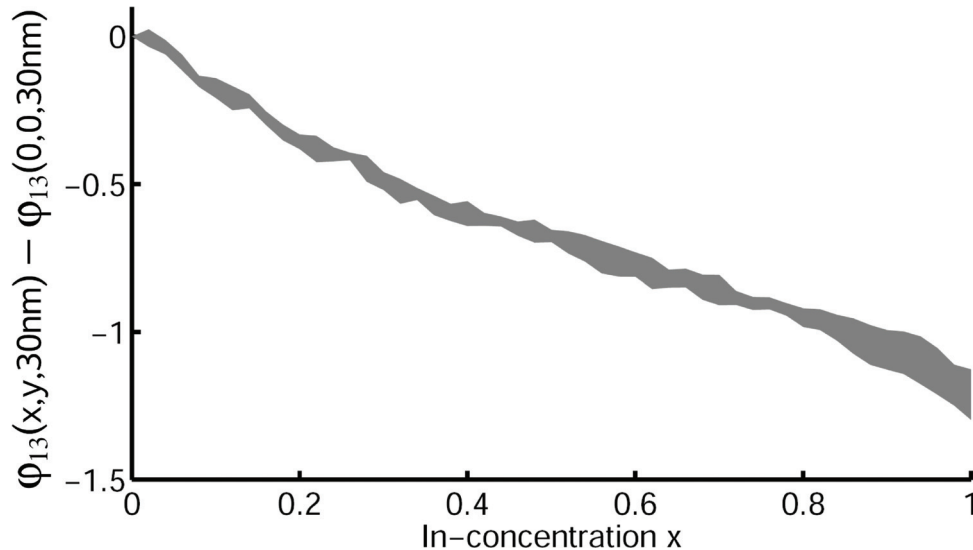


Figure 5.13: Simulation of the 220 fringe phase dependence on In-content x and nitrogen content y (grey corridor) according to Eq. (5.6). Constant specimen thickness of 30 nm was assumed. The influence of φ_{13} on composition measurement at interfaces is estimated in the text.

of the frequency of In-N bonds.

In the strict sense, structure factors for random alloys, which determine all simulations in this work, should be modified to take into account preferential bond configurations. So far, the effect on composition maps is considered to be small with respect to experimental errors, so that observations of long-range structural changes remain unchanged. Furthermore, both high-resolution and dark field TEM provide only indirect access to study preferential nearest neighbour configurations. Instead, it is advisable to make combined use of TEM and, e.g., extended X-ray absorption fine structure investigations, which are not available for the samples investigated here but left as a future task.

Additionally, literature offers various findings for the impact of annealing on the nitrogen profile. Grillo et al. [2] deduce strong nitrogen enrichment at the well edges, confirmed by later studies of Albrecht et al. [148] with the same method, where additional diffusion out of the quantum well is found and assigned to the blue shift of PL peaks. Contrary, Volz et al. observed no annealing effect on nitrogen profiles in InGaNaNs [4]. One common result of these groups and the present work is that annealing leads to lateral homogenisation of the nitrogen content, although profiles themselves differ a lot. According to Fig. 5.12 (c), a tendency of nitrogen to diffuse out of the well in growth direction may be derived from the fact that both profiles are not centred around the same position, but this must be considered a minor effect here, which is not responsible for the change in PL. Concerning the indium concentration profile, the Gaussian shape observed here after annealing in principle agrees with previous reports [148].

We finally pick up the evaluation of the local fringe distances at interfaces. Equation (5.6) contains a phase φ_{nm} which determines the position of intensity maxima in addition to the local lattice constant and aberrations. This phase is only constant in the absence of composition gradients, which in turn means that composition gradients may simulate strain where is none. This chemical shift depends on compositions x and y , thickness and magnitude of the gradient which makes a comprehensive study difficult. Nonetheless, to get an impression of the consequences for the measurement of the normalised fringe distance, the influence of this chemical shift on composition quanti-

cation for a specimen thickness of 30 nm is estimated exemplarily. For the whole indium concentration range, Fig. 5.13 depicts the dependence of φ_{13} on x , whereas the grey corridor represents the dependence on nitrogen content $y \in [0 \dots 0.05]$. Obviously φ_{13} is dominated by the dependence on x , which is almost linear. From that we can roughly estimate the error for measured compositions as follows. For a fictitious sharp interface between GaAs and InAs, φ_{13} changes about 1.5 rad, which makes the 220 fringe at the interface appear at a position that is shifted by about 25% of the native 220 fringe distance. Since the interface is sharp, this corresponds to an indium concentration gradient of about 2.5/nm. In contrast, present composition profiles exhibit gradients of less than $0.3/(5 \text{ nm}) = 0.06/\text{nm}$. Consequently, as φ_{13} proceeds linear, we expect the real chemical shift to be only $0.06/2.5 = 0.024$ of that for a sharp GaAs/InAs interface. In terms of strain state analysis based on the detection of 220 fringe positions, the present gradient causes the fringes to be displaced by 1.2 pm from the position determined solely by the geometric phase. By comparison of the resulting (erroneous) normalised fringe distance $\varepsilon_{[010]}$ with Fig. 5.5, this can cause nitrogen contents to be wrong by $\Delta y \approx \pm 0.015$. This error is expected to be present in many profiles, for example nitrogen enrichment at well edges in Fig. 5.8 or negative nitrogen contents in Fig. 5.12 (c) might be attributed to this artefact. Note that this effect is observed only in presence of composition gradients and should especially be taken into account when comparing with the work of Albrecht et al. [144, 148] and Grillo et al. [2], where M-shaped nitrogen profiles have been found in InGaNAs quantum wells.

5.7 Summary and conclusions

A method for the measurement of strain and contrast in quaternary InGaNAs was introduced, which allows for simultaneous quantification of indium- and nitrogen content. The technique exploits one high-resolution TEM micrograph formed by three beams, being not coupled with respect to nonlinear imaging, of which a brief theoretical review was given. Bloch wave simulations of reference beam amplitudes included the finding of optimised imaging conditions and account for absorption ascribed to Huang scattering at static atomic displacements (SAD), as well as chemical bonding and the influence of SAD (found by valence force field (VFF) relaxation) on structure factors. Application of the three-beam method to an $\text{In}_{0.28}\text{Ga}_{0.72}\text{N}_{0.025}\text{As}_{0.975}$ quantum layer before and after thermal annealing has shown that annealing caused a dissolution of indium- and nitrogen-rich regions in favour of a homogeneous layer with Gaussian-shaped indium profile. In addition, recorded room-temperature photoluminescence exhibits a blue shift of about 60 meV and an increase by a factor of 20 after annealing, for which the observed structural changes were made responsible.

In this chapter, method and application took equal part, so that the latter was restricted to one as-grown and one annealed structure. From the significant redistribution of impurity atoms of all species on length scales of 10 nm, it can be concluded that interpretation of PL spectra solely in the context of nearest neighbour configurations can be insufficient. However, detailed understanding of structural transitions as a function of annealing conditions, such as temperature or pressure, and correlation to optical properties and growth conditions, is left as a future task.

As the three-beam method falls in the category of conventional high-resolution TEM without explicit need for advanced equipment such as imaging correctors, it is easy to apply, provided that a proper objective aperture for three-beam imaging is available. In

principle, the same holds for the simulation of reference data, since Bloch wave simulations can be performed on desktop computers. This even holds if bonding and SAD are to be included since MASA and VFF provide efficient but accurate approximations, respectively. In that respect, absorptive form factors for SAD scattering included here are not only of academical interest but may also affect concentration profiles more or less strongly, depending on the amount of nitrogen and imaging conditions.

Chapter 6

Comprehensive discussion

In retrospect, a detailed discussion was part of each chapter, which entitles us to focus on categorising the results of this thesis and to draw connections to related topics in the field of TEM in the present, final chapter. This thesis is intended to document work on electron structure factors and quaternary composition quantification in such a way that scientists eventually may follow up this work directly. In this respect, prospects for possible future effort are sketched in section 6.2.

6.1 Discussion of the present work

A substantial part of the preceding chapters falls into the category of *methodical work* concerning the two operation modes of a TEM, diffraction and imaging. Another important component consists of application and verification of *theoretical models* for electron scattering factors in the presence of bonding and static disorder. As a third category, we have the *experimental results* for structure factors and chemical compositions. Let us briefly think about the impact of this interplay between several disciplines.

Measurement of the 200 structure factor for GaAs using, e.g., parallel beam electron diffraction (PBED), yields a single value. In principle, this already allows us to correctly simulate bonding in GaAs for TEM applications. However, it is the comparison with modified atomic scattering amplitudes (MASA) obtained from density functional theory (DFT) that is of even more interest than the numerical result itself, because it verifies a model. This is an important point since it enables us to calculate and model structure factors for a variety of materials reliably. Please note that theoretical modelling is not primarily intended to save effort, that is, to replace an experiment by calculations. The main advantage is the applicability to problems not accessible by experiment. In particular, experimental determination of the 200 structure factors was limited to the arsenic crystals GaAs and InAs in chapter 3, because high-quality cubic bulk crystals of the nitrides GaN and InN are not (yet) available. However, as both results for the arsenic crystals agree well with the MASA concept, we conclude that MASAs most likely describe bonding correctly also in GaN and InN crystals. In this way, at least reliable benchmarks for the binary constituents of InGaNAs are obtained, being fundamental for composition quantification in quaternary alloys.

Regarding publications of atomic scattering amplitudes (ASA) for isolated atoms, numerous groups have been concerned with their parameterisation. However, it is surprising that parameterised scattering data accounting for electron redistributions due to chemical bonding is hardly available, except for selected MASA [9, 72], although

DFT is a comfortable way for the inclusion of bonding since many years. Nonetheless, the importance of this issue is permanently stressed from the experimental point of view [117, 6, 152, 121, 153, 50, 49, 51, 154, 127, 126]. One consequence is that most (commercial) TEM simulation programs do not allow for the inclusion of bonding, so that experimental composition quantification frequently disregards this effect. However, we have seen in chapter 4 that the isolated atom approximation can lead to a relative error of 25% for the indium content.

Above, the interconnection of the preceding chapters with each other had to be stressed because each chapter was designed as a stand-alone report. In addition, there are some important connections to further TEM disciplines as well. The PBED refinement method has been applied primarily to low-order structure factor measurement, but as a by-product it allows for a determination of accurate Debye-Waller factors. These are central quantities in scanning TEM (STEM) image simulations. In particular, models for the temperature dependence of Debye-Waller factors have been introduced [81, 155], which are to be verified preferably by PBED as exemplified in chapter 3. However, in view of STEM composition quantification, the impact of a reliable treatment of thermal and static disorder must be seen to be at least comparable to the impact of low-order structure factors on composition measurement using conventional TEM. Reliability studies of valence force field calculations of SAD in chapter 4 are thus of comparable importance to Debye-Waller factor verification. Furthermore, as mentioned in the introduction, recent methodical development in the field of quantitative STEM is promising with respect to quaternary composition evaluation in InGaNAs. The most attractive approaches either evaluate lattice strain and high-angle annular dark field (HAADF) contrast simultaneously or exploit the typical angular dependence of the HAADF signal on composition by using several STEM images taken with different acceptance angles of the HAADF detector [140, 156, 157]. However, any STEM approach first ought to compare with independently found results, such as composition maps measured by the three-beam method in chapter 5 of this thesis.

In all chapters where TEM experiments were involved, the reader might have noticed that an aberration corrected Titan 80/300 facility had been used. To some extent it may therefore be surprising that the three-beam imaging method has been developed, which not explicitly exploits the capability of this machine. In particular, tuning the aberration corrector to negative values of the spherical aberration constant has been shown [158] to be a possibility for direct structural imaging, that is, interpreting high resolution TEM contrast directly in terms of atomic positions. Additionally, aberration correction facilitates the retrieval of both amplitude and phase of the specimen exit wave function from a series of images taken at different defoci [159]. Common to the two techniques is that they successfully apply to extremely thin specimens with thicknesses of a few nanometres only. Concerning InGaAs diluted with small amounts of nitrogen (below 3%), the question arises whether a specimen of less than 10 Bravais cells in thickness contains a statistically representative portion. As the comparably weak chemically sensitive 200 beam owns significant intensity only for considerably larger thicknesses of a few tens of nanometres, taking advantage of chemical sensitivity is difficult in addition. In contrast, two- and three-beam imaging as presented in chapters 4 and 5 does neither demand advanced methods for sample preparation, nor expensive aberration corrected microscopes, nor capable computing facilities or commercial software for reference data simulation. Analogous arguments in principle hold for PBED refinements.

6.2 Prospects

Whereas ternary and quaternary compounds have been subject to theoretical studies and composition mapping, PBED and CBED structure factor measurement is currently stalled at binary crystals. The advantage in this case is that stoichiometry is known. However, it would be very interesting to investigate the composition dependence of the 200 structure factor experimentally by PBED and/or convergent beam electron diffraction (CBED). The extension of structure factor measurements to quaternary InGaNAs, or at least ternary InGaAs and GaNAs alloys, definitely poses a future challenge, because then the effect of static atomic displacements (SAD) interferes with that of bonding.

It was pointed out in section 6.1 that quantitative STEM requires accurate Debye-Waller factors. With respect to composition quantification, it is thus also interesting to investigate the thermal movement of impurity atoms in a host lattice. The main question is whether it is sufficient to derive a Debye-Waller factor for, e.g., atomic species in InGaAs, from Vegard's rule [102], or if composition dependence behaves nonlinear.

Modified atomic scattering amplitudes have so far been published for use in very special context. In particular, only MASA for the 200 reflections of selected ternary zinc blende alloys are available to the TEM community [9, 72] as mentioned above. Since dependence of MASA on lattice parameters is almost linear, parameterisation requires only a few parameters, so that a publication of *all* low-order structure factors affected by bonding as a function of lattice parameters suggests itself. Up to now, this has only been implemented in the Bloch4TEM [37] software for InGaNAs, InGaN_P and MgZnSeTe.

Moreover, it is important to find a model for the inclusion of MASA in frozen lattice multislice simulations. This means that a projected potential for a slightly disturbed translational symmetry of the crystal must be derived. This might either be done in real space by putting together patches of atomic potentials under the requirement that the transition between the patches must be continuous, or it can be done in reciprocal space by varying the lattice parameter slightly.

As to the question of annealing effects on structural and optical properties in InGaNAs, this work was limited to one sample application to show that long-range homogenisation of both indium and nitrogen composition is one important process. Especially the dependence on annealing temperature is still left as an important future task. Nevertheless this work provides a consistent picture of scattering factors, reference data simulation and composition quantification in InGaNAs, which can easily be transferred to further zincblende material systems. For example, near-infrared laser diodes based on $\text{In}_x\text{Ga}_{1-x}\text{N}_y\text{P}_{1-y}$ or distributed Bragg reflectors based on alternating $\text{Mg}_x\text{Zn}_{1-x}\text{Se}_y\text{Te}_{1-y}$ layers are fields of active research, to name a few.

List of acronyms

APW	Augmented plane waves
ASA	Atomic scattering amplitudes
BK	Bird and King
BW	Bloch wave
CBED	Convergent beam electron diffraction
CCD	Charge coupled device
CELFA	Composition evaluation by lattice fringe analysis
COLC	Centre of Laue circle
DALI	Digital analysis of lattice images [software]
DFT	Density functional theory
EDX	Energy dispersive X-ray [analysis]
EELS	Electron energy loss spectroscopy
ELSTRU	[Acronym built from ELection and STRUcture, software]
FOLZ	First order Laue zone
GGA	Generalised gradient approximation
GIF	Gatan imaging filter
GOF	Goodness of fit
GREED	Graphical extraction/reduction of electron diffraction data [software]
HAADF	High angle annular dark field
HOLZ	Higher order Laue zone
HRTEM	High resolution transmission electron microscopy
LAPW	Linearised augmented plane waves
LDA	Local density approximation
LO/lo	Local orbitals
MASA	Modified atomic scattering amplitudes
MBE	Molecular beam epitaxy
MBFIT	Many beam dynamical simulations and least-squares fitting [software]
MOVPE	Metal organic vapour phase epitaxy
MS	Multislice
MSLS	Multislice least-squares
PBED	Parallel beam electron diffraction
PL	Photoluminescence
SAD	Static atomic displacements
SAED	Selected area electron diffraction
STEM	Scanning transmission electron microscopy
TDS	Thermal diffuse scattering
TEM	Transmission electron microscopy
VFF	Valence force field
WK	Weickenmeier and Kohl
ZOLZ	Zero order Laue zone

Bibliography

- [1] P. Blaha, K. Schwarz, and J. Luitz G. K. H. Madsen, D. Kvasnicka. *Wien2k, An Augmented Plane Wave + Local Orbitals Program for calculating crystal properties*. Number ISBN 3-9501031-1-2. Technische Universität Wien, Austria, 2001.
- [2] V. Grillo, M. Albrecht, T. Remmele, H. P. Strunk, A. Yu. Egorov, and H. Riechert. Simultaneous experimental evaluation of In and N concentrations in InGaAsN quantum wells. *Journal of Applied Physics*, 90(8):3792–3798, 2001.
- [3] D. Litvinov, D. Gerthsen, A. Rosenauer, M. Hetterich, A. Grau, Ph. Gilet, and L. Grenouillet. Determination of the nitrogen distribution in InGaAsN/GaAs quantum wells by transmission electron microscopy. *Applied Physics Letters*, 85:3743–3745, 2004.
- [4] K. Volz, T. Torunski, O. Rubel, W. Stolz, P. Kruse, D. Gerthsen, M. Schowalter, and A. Rosenauer. Annealing effects on the nanoscale indium and nitrogen distribution in Ga(NAs) and (GaIn)(NAs) quantum wells. *Journal of Applied Physics*, 102(8):083504, 2007.
- [5] Knut Müller, Marco Schowalter, Jacob Jansen, Kenji Tsuda, John Titantah, Dirk Lamoen, and Andreas Rosenauer. Refinement of the 200 structure factor for GaAs using parallel and convergent beam electron nanodiffraction data. *Ultramicroscopy*, 109:802–814, 2009.
- [6] J. M. Zuo, J. C. H. Spence, and M. O’Keeffe. Bonding in GaAs. *Phys. Rev. Lett.*, 61(3):353–356, Jul 1988.
- [7] Knut Müller, Marco Schowalter, Andreas Rosenauer, Oleg Rubel, and Kerstin Volz. Effect of bonding and static atomic displacements on composition quantification in $\text{In}_x\text{Ga}_{1-x}\text{N}_y\text{As}_{1-y}$. *Phys. Rev. B*, 81(7):075315, Feb 2010.
- [8] Frank Glas. The effect of the static atomic displacements on the structure factors of weak reflections in cubic semiconductor alloys. *Philosophical Magazine*, 84(20):2055–2074, 2004.
- [9] A. Rosenauer, M. Schowalter, F. Glas, and D. Lamoen. First-principles calculations of 002 structure factors for electron scattering in strained $\text{In}_x\text{Ga}_{1-x}\text{As}$. *Physical Review B*, 72:085326, August 2005.
- [10] Jörg Neugebauer and Chris G. Van de Walle. Electronic structure and phase stability of $\text{GaAs}_{1-x}\text{N}_x$ alloys. *Phys. Rev. B*, 51(16):10568–10571, Apr 1995.
- [11] I. Vurgaftman, J. R. Meyer, and L. R. Ram-Mohan. Band parameters for III–V compound semiconductors and their alloys. *Journal of Applied Physics*, 89(11):5815–5875, 2001.
- [12] Markus Weyers and Michio Sato. Growth of GaAsN alloys by low-pressure metalorganic chemical vapor deposition using plasma-cracked NH_3 . *Applied Physics Letters*, 62(12):1396–1398, 1993.
- [13] M. Kondow, T. Kitatani, M. C. Larson, K. Nakahara, K. Uomi, and H. Inoue. Gas-source MBE of GaInNAs for long-wavelength laser diodes. *Journal of Crystal Growth*, 188(1-4):255–259, 1998.
- [14] M. Hetterich, M. D. Dawson, A. Yu. Egorov, D. Bernklau, and H. Riechert. Electronic states and band alignment in GaInNAs/GaAs quantum-well structures with low nitrogen content. *Applied Physics Letters*, 76:1030, 2000.
- [15] K. Volz, W. Stolz, J. Teubert, P. J. Klar, W. Heimbrodt, F. Dimroth, C. Baur,

- and A. W. Bett. *Dilute III/V Nitride Semiconductors and Material Systems*, chapter Doping, electrical properties and solar cell application of GaInNAs, pages 369–404. Springer Berlin, Heidelberg, 2008.
- [16] P. J. Klar, H. Grüning, J. Koch, S. Schäfer, K. Volz, W. Stolz, W. Heimbrod, A. M. Kamal Saadi, A. Lindsay, and E. P. O’Reilly. (Ga, In)(N, As)-fine structure of the band gap due to nearest-neighbor configurations of the isovalent nitrogen. *Phys. Rev. B*, 64(12):121203, Sep 2001.
- [17] H.S. Djie, D.-N. Wang, B.S. Ooi, J.C.M. Hwang, X.-M. Fang, Y. Wu, J.M. Fastenau, and W.K. Liu. Emission wavelength trimming of self-assembled InGaAs/GaAs quantum dots with GaAs/AlGaAs superlattices by rapid thermal annealing. *Thin Solid Films*, 515(10):4344–4347, 2007. The Third International Conference on Materials for Advanced Technologies (ICMAT 2005); Symposium J - III - V Semiconductors for Microelectronic and Optoelectronic Applications - ICMAT 2005 - Symposium J.
- [18] J.-Y. Duboz, J. A. Gupta, Z. R. Wasilewski, J. Ramsey, R. L. Williams, G. C. Aers, B. J. Riel, and G. I. Sproule. Band-gap energy of $\text{In}_x\text{Ga}_{1-x}\text{N}_y\text{As}_{1-y}$ as a function of N content. *Phys. Rev. B*, 66(8):085313, Aug 2002.
- [19] A. Pomarico, M. Lomascolo, R. Cingolani, A. Yu Egorov, and H. Riechert. Effects of thermal annealing on the optical properties of InGaNAs/GaAs multiple quantum wells. *Semiconductor Science and Technology*, 17(2):145, 2002.
- [20] Kwiseon Kim and Alex Zunger. Spatial Correlations in GaInAsN Alloys and their Effects on Band-Gap Enhancement and Electron Localization. *Phys. Rev. Lett.*, 86(12):2609–2612, Mar 2001.
- [21] Arndt Jenichen, Cornelia Engler, Gunnar Leibiger, and Volker Gottschalch. Growth and annealing of GaInAsN: density-functional calculations on the reactions of surface and bulk structures. *Surface Science*, 574(2-3):144–152, 2005.
- [22] O. Rubel, K. Volz, T. Torunski, S. D. Baranovskii, F. Grosse, and W. Stolz. Columnar [001]-oriented nitrogen order in Ga(NAs) and (GaIn)(NAs) alloys. *Applied Physics Letters*, 85(24):5908–5910, 2004.
- [23] C. S. Peng, E. M. Pavelescu, T. Jouhti, J. Konttinen, and M. Pessa. Diffusion at the interfaces of InGaNAs/GaAs quantum wells. *Solid-State Electronics*, 47(3):431–435, 2003.
- [24] R. P. Burgner, M. M. Disko, and P. R. Swann. *EELS Atlas*. Gatan, Inc., 1983.
- [25] J. Verbeeck and S. Van Aert. Model based quantification of EELS spectra. *Ultramicroscopy*, 101:207–224, 2004.
- [26] James M. LeBeau and Susanne Stemmer. Experimental quantification of annular dark-field images in scanning transmission electron microscopy. *Ultramicroscopy*, 108:1653–1658, 2008.
- [27] V. Grillo, E. Carlino, and F. Glas. Influence of the static atomic displacement on atomic resolution Z-contrast imaging. *Physical Review B*, 77:054103, 2008.
- [28] Andreas Rosenauer, Katharina Gries, Knut Müller, Angelika Pretorius, Marco Schowalter, Adrian Avramescu, Karl Engl, and Stephan Lutgen. Measurement of specimen thickness and composition in $\text{Al}_x\text{Ga}_{1-x}\text{N}/\text{GaN}$ using high-angle annular dark field images. *Ultramicroscopy*, 109(9):1171–1182, 2009.
- [29] Tim Grieb, Knut Müller, Oleg Rubel, Rafael Fritz, Claas Glostein, Nils Neugebohrn, Marco Schowalter, Kerstin Volz, and Andreas Rosenauer. Determination of Nitrogen Concentration in Dilute GaNAs by STEM HAADF Z-Contrast Imaging. In *Microscopy*

- of semiconducting materials, Cambridge (UK) [Submitted as a talk], 2011.*
- [30] Tim Grieb, Knut Müller, Oleg Rubel, Rafael Fritz, Claas Glostein, Nils Neugebohrn, Marco Schowalter, Kerstin Volz, and Andreas Rosenauer. Determination of Nitrogen Concentration in Dilute GaNAs by STEM HAADF Z-Contrast Imaging and improved STEM-HAADF strain state analysis. *In preparation for submission to Ultramicroscopy*, 2011.
- [31] P. N. Keating. Effect of Invariance Requirements on the Elastic Strain Energy of Crystals with Application to the Diamond Structure. *Phys. Rev.*, 145(2):637–645, May 1966.
- [32] O. Rubel, I. Németh, W. Stolz, and K. Volz. Modeling the compositional dependence of electron diffraction in dilute GaAs- and GaP-based compound semiconductors. *Physical Review B (Condensed Matter and Materials Physics)*, 78(7):075207, 2008.
- [33] Andreas Rosenauer and Marco Schowalter. STEMSIM—a new software tool for simulation of STEM HAADF Z-contrast imaging. In A. G. Cullis and P. A. Midgley, editors, *Springer Proceedings in Physics*, volume 120, pages 169–172. Springer, 2007.
- [34] A. Rosenauer, U. Fischer, D. Gerthsen, and A. Förster. Composition evaluation by lattice fringe analysis. *Ultramicroscopy*, 72:121–133, 1998.
- [35] A. Rosenauer, S. Kaiser, T. Reisinger, J. Zweck, W. Gebhardt, and D. Gerthsen. Digital analysis of high resolution transmission electron microscopy lattice images. *Optik*, 102:63–69, 1996.
- [36] Hans Bethe. Theorie der Beugung von Elektronen an Kristallen. *Annalen der Physik*, 87:55–129, 1928.
- [37] Knut Müller. *Bloch4TEM* simulation software (MATLAB). Simulation and refinement of Electron diffraction data as well as Simulation of high-resolution TEM images including bonding and static atomic displacements. Availability: please see webpage <http://www.ifp.uni-bremen.de> at the software subpage of the Electron microscopy group at Bremen University and/or contact mueller@ifp.uni-bremen.de, Development 2007–2010.
- [38] Marc de Graef. *Introduction to Conventional Transmission Electron Microscopy*. Cambridge University Press, first edition, 2003.
- [39] J. M. Cowley and A. F. Moodie. The scattering of electrons by atoms and crystals. I. A new theoretical approach. *Acta Crystallographica*, 10(10):609–619, Oct 1957.
- [40] K. Ishizuka and N. Uyeda. A new theoretical and practical approach to the multislice method. *Acta Crystallographica Section A*, 33(5):740–749, Sep 1977.
- [41] D. van Dyck. Fast computational procedures for the simulation of structure images in complex or disordered crystals: a new approach. *Journal of Microscopy*, 119:141, 1980.
- [42] D. van Dyck and W. Coene. The real space method for dynamical electron diffraction calculations in high resolution electron microscopy: I. Principles of the method. *Ultramicroscopy*, 15(1-2):29–40, 1984.
- [43] W. Coene and D. van Dyck. The real space method for dynamical electron diffraction calculations in high resolution electron microscopy: II. Critical analysis of the dependency on the input parameters. *Ultramicroscopy*, 15(1-2):41–50, 1984.
- [44] W. Coene and D. van Dyck. The real space method for dynamical electron diffraction calculations in high resolution electron microscopy: III. A computational algorithm for

- the electron propagation with its practical applications. *Ultramicroscopy*, 15(4):287–300, 1984.
- [45] A. J. F. Metherell. Diffraction of electrons by perfect crystals. In U. Valdre and E. Ruedl, editors, *Electron Microscopy in Materials Science*, volume 2 of *Course of Int. School of Electron Microscopy*, pages 397–552. CEC, Bruxelles, 1975.
- [46] J. M. Zuo and A. L. Weickenmeier. On the beam selection and convergence in the Bloch-wave method. *Ultramicroscopy*, 57:375–383, March 1995.
- [47] J. C. H. Spence and J. M. Zuo. *Electron Microdiffraction*. Plenum Press New York, 1992.
- [48] J. C. H. Spence. Quantitative Electron Microdiffraction. *Journal of Electron Microscopy (Tokyo)*, 45(1):19–26, 1996.
- [49] J. C. H. Spence. Direct Inversion of Dynamical Electron Diffraction Patterns to Structure Factors. *Acta Crystallographica Section A*, 54:7–18, 1998.
- [50] K. Tsuda and M. Tanaka. Refinement of crystal structure parameters using convergent-beam electron diffraction: the low-temperature phase of SrTiO₃. *Acta Crystallographica Section A*, 51(1):7–19, Jan 1995.
- [51] Kenji Tsuda and Michiyoshi Tanaka. Refinement of crystal structural parameters using two-dimensional energy-filtered CBED patterns. *Acta Crystallographica Section A*, 55(5):939–954, Sep 1999.
- [52] Z. L. Wang. Dynamical theories of dark-field imaging using diffusely scattered electrons in STEM and TEM. *Acta Crystallographica Section A*, 51(4):569–585, Jul 1995.
- [53] Hide Yoshioka. Effect of Inelastic Waves on Electron Diffraction. *Journal of the Physical Society of Japan*, 12(6):618–628, 1957.
- [54] C. R. Hall and P. B. Hirsch. Effect of Thermal Diffuse Scattering on Propagation of High Energy Electrons Through Crystals. *Proceedings of the Royal Society of London. Series A. Mathematical and Physical Sciences*, 286(1405):158–177, 1965.
- [55] C. R. Hall. The scattering of high energy electrons by the thermal vibrations of crystals. *Philosophical Magazine*, 12:815–826, 1965.
- [56] R. W. James. *The crystalline state II: The optical principles of the diffraction of X-rays*. G. Bell and Sons Ltd. London, 3rd edition, 1962.
- [57] Andreas Rosenauer, Marco Schowalter, John T. Titantah, and Dirk Lamoen. An emission-potential multislice approximation to simulate thermal diffuse scattering in high-resolution transmission electron microscopy. *Ultramicroscopy*, 108(12):1504–1513, 2008.
- [58] K. Huang. X-Ray Reflexions from Dilute Solid Solutions. *Proceedings of the Royal Society of London. Series A. Mathematical and Physical Sciences*, 190(1020):102–117, 1947.
- [59] John M. Cowley. *Diffraction physics*. North-Holland personal library. Elsevier, Amsterdam, 3rd rev. edition, 1995.
- [60] Frank H. Stillinger and Thomas A. Weber. Computer simulation of local order in condensed phases of silicon. *Phys. Rev. B*, 31(8):5262–5271, Apr 1985.
- [61] P. N. Keating. Relationship between the Macroscopic and Microscopic Theory of Crystal Elasticity. I. Primitive Crystals. *Phys. Rev.*, 152(2):774–779, Dec 1966.
- [62] P. Hohenberg and W. Kohn. Inhomogeneous electron gas. *Physical Review*, 136(3B):B864–B871, Nov 1964.

- [63] W. Kohn and L. J. Sham. Self-consistent equations including exchange and correlation effects. *Phys. Rev.*, 140(4A):A1133–A1138, Nov 1965.
- [64] Michael Springborg. *Methods of electronic-structure calculations: From Molecules to Solids*. Wiley series in theoretical chemistry. John Wiley & Sons, Chichester, 2000.
- [65] S. Cottenier. *Density Functional Theory and the Family of (L)APW-methods: a step-by-step introduction*. Instituut voor Kern- en Stralingsfysica (IKS), Katholieke Universiteit Leuven, Celestijnenlaan 200 D, B-3001 Leuven, Belgium, August 2004. ISBN 90-807215-1-4.
- [66] Peter Blaha, Karlheinz Schwarz, Georg Madsen, Dieter Kvasnicka, and Joachim Luitz. *WIEN2K. An augmented Plane Wave Plus Local Orbitals Program for Calculating Crystal Properties*. Universität Wien, Getreidemarkt 9/156, A-1060 Wien, Austria, June 2002.
- [67] P. Blaha, K. Schwarz, P. Sorantin, and S.B. Trickey. Full-potential, linearized augmented plane wave programs for crystalline systems. *Computer Physics Communications*, 59(2):399–415, 1990.
- [68] Max Petersen, Frank Wagner, Lars Hufnagel, Matthias Scheffler, Peter Blaha, and Karlheinz Schwarz. Improving the efficiency of fp-lapw calculations. *Computer Physics Communications*, 126(3):294–309, 2000.
- [69] K. Schwarz, P. Blaha, and G. K. H. Madsen. Electronic structure calculations of solids using the wien2k package for material sciences. *Computer Physics Communications*, 147(1-2):71–76, 2002.
- [70] J. T. Titantah, D. Lamoen, M. Schowalter, and A. Rosenauer. Bond length variation in $\text{Ga}_{1-x}\text{In}_x\text{As}$ crystals from the Tersoff potential. *Journal of Applied Physics*, 101(12):123508, 2007.
- [71] J. T. Titantah, D. Lamoen, M. Schowalter, and A. Rosenauer. Modified atomic scattering amplitudes and size effects on the 002 and 220 electron structure factors of multiple $\text{Ga}_{1-x}\text{In}_x\text{As}/\text{GaAs}$ quantum wells. *Journal of Applied Physics*, 105(8):084310, 2009.
- [72] Marco Schowalter, Knut Müller, and Andreas Rosenauer. Scattering amplitudes and static atomic correction factors for the composition sensitive 002 reflection in sphalerite ternary III-V and II-VI semiconductors. *Acta Crystallographica Section A*, 2011.
- [73] L.-M. Peng, G. Ren, S. L. Dudarev, and M. J. Whelan. Debye-Waller Factors and Absorptive Scattering Factors of Elemental Crystals. *Acta Crystallographica A*, 52:456–470, January 1996.
- [74] L.-M. Peng, G. Ren, S. L. Dudarev, and M. J. Whelan. Robust Parameterization of Elastic and Absorptive Electron Atomic Scattering Factors. *Acta Crystallographica Section A*, 52(2):257–276, Mar 1996.
- [75] A. Weickenmeier and H. Kohl. Computation of absorptive form factors for high-energy electron diffraction. *Acta Crystallographica Section A*, 47(5):590–597, Sep 1991.
- [76] D. M. Bird. Absorption in high-energy electron diffraction from non-centrosymmetric crystals. *Acta Crystallographica Section A*, 46(3):208–214, Mar 1990.
- [77] D. M. Bird and Q. A. King. Absorptive form factors for high-energy electron diffraction. *Acta Crystallographica Section A*, 46(3):202–208, Mar 1990.
- [78] P. A. Doyle and P. S. Turner. Relativistic Hartree-Fock X-ray and Electron Scattering Factors. *Acta Crystallographica A*, 24:390–397, 1968.
- [79] John S. Reid. Debye-Waller Factors of Zinc-Blende-Structure Materials - A Lattice

- Dynamical Comparison. *Acta Crystallographica A*, 39:1–13, 1983.
- [80] H. X. Gao and L.-M. Peng. Parameterization of the temperature dependence of the Debye-Waller factors. *Acta Crystallographica A*, 55:926–932, April 1999.
- [81] M. Schowalter, A. Rosenauer, J. T. Titantah, and D. Lamoen. Computation and parametrization of the temperature dependence of Debye–Waller factors for group IV, III–V and II–VI semiconductors. *Acta Crystallographica Section A*, 65(1):5–17, Jan 2009.
- [82] M. Schowalter, A. Rosenauer, J. T. Titantah, and D. Lamoen. Temperature-dependent Debye–Waller factors for semiconductors with the wurtzite-type structure. *Acta Crystallographica Section A*, 65(3):227–231, May 2009.
- [83] W. Qian, J. C. H. Spence, and J. M. Zuo. Transmission low-energy electron diffraction (TLEED) and its application to the low-voltage point-projection microscope. *Acta Crystallographica Section A*, 49(3):436–445, May 1993.
- [84] M. A. Coulthard. A relativistic Hartree-Fock atomic field calculation. *Proceedings of the Physical Society*, 91(1):44, 1967.
- [85] 56 contributors. *International Tables for Crystallography*, volume C. Springer Netherlands, 2nd edition, 2004.
- [86] 35 contributors. *International Tables for Crystallography*, volume B. Kluwer Academic Publishers, 2nd edition, 2006.
- [87] A. Bravais. Mémoire sur les systèmes formés par les points distribués régulièrement sur un plan ou dans l’espace. *Journal de l’Ecole Polytechnique*, 33:1–128, 1850.
- [88] L. H. Thomas. The calculation of atomic fields. *Mathematical Proceedings of the Cambridge Philosophical Society*, 23:542–548, 1926.
- [89] E. Fermi. Un metodo statistico per la determinazione di alcune priorieta dell’atome. *Rend. Accad. Naz. Lincei*, 6:602–607, 1927.
- [90] M. Leszczynski, A. Kulik, and P. Ciepielewski. Lattice Parameters of GaInP/GaAs Epi-Layers at Temperatures 77 to 752 K. *Physica Status Solidi Section A*, 119:495–502, 1990.
- [91] K. Parlinski, Z. Q. Li, and Y. Kawazoe. First-Principles Determination of the Soft Mode in Cubic ZrO₂. *Phys. Rev. Lett.*, 78(21):4063–4066, May 1997.
- [92] Gilbert N. Lewis. The atom and the molecule. *Journal of the American Chemical Society*, 38:762–785, 1916.
- [93] G. M. Brown. Symmetry relations among structure factors. *Acta Crystallographica Section B*, 27(8):1675–1676, Aug 1971.
- [94] H. A. Ferwerda, B. J. Hoenders, and C. H. Slump. Fully relativistic treatment of electron-optical image formation based on the Dirac equation. *Optica Acta*, 33(2):145–157, 1986.
- [95] L. J. Allen, S. D. Findlay, M. P. Oxley, and C. J. Rossouw. Lattice-resolution contrast from a focused coherent electron probe. Part I. *Ultramicroscopy*, 96:47–63, 2003.
- [96] S. D. Findlay, L. J. Allen, M. P. Oxley, and C. J. Rossouw. Lattice-resolution contrast from a focused coherent electron probe. Part II. *Ultramicroscopy*, 96:65–81, 2003.
- [97] D. Van Dyck. Is the frozen phonon model adequate to describe inelastic phonon scattering? *Ultramicroscopy*, 109:677–682, 2009.
- [98] Z. L. Wang. The ‘Frozen-Lattice’ Approach for Incoherent Phonon Excitation in Electron Scattering. How Accurate Is It? *Acta Crystallographica Section A*, 54(4):460–

- 467, Jul 1998.
- [99] L.-M. Peng. Electron Scattering Factors of Ions and their Parameterization. *Acta Crystallographica Section A*, 54(4):481–485, Jul 1998.
- [100] A. L. Weickenmeier and H. Kohl. The Influence of Anisotropic Thermal Vibrations on Absorptive Form Factors for High-Energy Electron Diffraction. *Acta Crystallographica Section A*, 54(3):283–289, May 1998.
- [101] Z. L. Wang. *Elastic and inelastic scattering in electron diffraction and imaging*. Plenum Press, New York, 1995.
- [102] L. Vegard. Die Konstitution der Mischkristalle und die Raumfüllung der Atome. *Zeitschrift für Physik A Hadrons and Nuclei*, 5:17–26, 1921. 10.1007/BF01349680.
- [103] José Luís Martins and Alex Zunger. Bond lengths around isovalent impurities and in semiconductor solid solutions. *Phys. Rev. B*, 30(10):6217–6220, Nov 1984.
- [104] W. Cochran and G. Kartha. Scattering of X-rays by defect structures. II. An extension of the theory. *Acta Crystallographica*, 9(11):941–943, Nov 1956.
- [105] D. Porezag, Th. Frauenheim, Th. Köhler, G. Seifert, and R. Kaschner. Construction of tight-binding-like potentials on the basis of density-functional theory: Application to carbon. *Phys. Rev. B*, 51(19):12947–12957, May 1995.
- [106] B. Deng and L. D. Marks. Theoretical structure factors for selected oxides and their effects in high-resolution electron-microscope (HREM) images. *Acta Crystallographica Section A*, 62(3):208–216, May 2006.
- [107] Bin Deng, Laurence D. Marks, and James M. Rondinelli. Charge defects glowing in the dark. *Ultramicroscopy*, 107(4-5):374–381, 2007.
- [108] James Ciston, Sarah J. Haigh, Judy S. Kim, Angus I. Kirkland, and Laurence D. Marks. Optimized conditions for direct imaging of bonding charge density in electron microscopy. *arxiv/cond-mat.mtrl-sci*, 2010.
- [109] Knut Müller, Marco Schowalter, Andreas Rosenauer, Jacob Jansen, Kenji Tsuda, John Titantah, and Dirk Lamoen. Refinement of chemically sensitive structure factors using parallel and convergent beam electron nanodiffraction. *Journal of Physics: Conference Series*, 209(1):012025, 2010.
- [110] J. Stahn, M. Möhle, and U. Pietsch. Comparison of Experimental and Theoretical Structure Amplitudes and Valence Charge Densities of GaAs. *Acta Crystallographica B*, 54:231–239, 1998.
- [111] Kerstin Volz, Torsten Torunski, Bernardette Kunert, Oleg Rubel, Siegfried Nau, Stefan Reinhard, and Wolfgang Stolz. Specific structural and compositional properties of (GaIn)(NAs) and their influence on optoelectronic device performance. *Journal of Crystal Growth*, 272(1-4):739–747, 2004. The Twelfth International Conference on Metalorganic Vapor Phase Epitaxy.
- [112] F. Glas. Correlated static atomic displacements and transmission-electron-microscopy contrast in compositionally homogeneous disordered alloys. *Physical Review B*, 51(2):825–839, January 1995.
- [113] Michael Lehmann and Hannes Lichte. Is there a Stobbs-Factor in Off-axis Electron Holography? In *Microscopy and Microanalysis (Suppl. 3: Proceedings)*, volume 9, pages 46–47, 2003.
- [114] Yoichiro Ogata, Kenji Tsuda, and Michiyoshi Tanaka. Determination of the electrostatic potential and electron density of silicon using convergent-beam electron diffraction. *Acta Crystallographica Section A*, 64(5):587–597, Sep 2008.

- [115] J. Jansen, D. Tang, H. W. Zandbergen, and H. Schenk. MSLS, a Least-Squares Procedure for Accurate Crystal Structure Refinement from Dynamical Electron Diffraction Patterns. *Acta Crystallographica Section A*, 54(1):91–101, Jan 1998.
- [116] J. Jansen, H. W. Zandbergen, and M. T. Otten. The effect of inelastic scattering on crystal structure refinement from electron diffraction patterns recorded under almost parallel illumination. *Ultramicroscopy*, 98:165–172, 2004.
- [117] K. Gjønnes, J. Gjønnes, J. Zuo, and J. C. H. Spence. Two-beam features in electron diffraction patterns – application to refinement of low-order structure factors in GaAs. *Acta Crystallographica Section A*, 44(6):810–820, Nov 1988.
- [118] U. Pietsch and N. K. Hansen. A critical review of the experimental valence charge density of GaAs. *Acta Crystallographica Section B*, 52(4):596–604, Aug 1996.
- [119] J M Zuo. Measurements of electron densities in solids: a real-space view of electronic structure and bonding in inorganic crystals. *Reports on Progress in Physics*, 67(11):2053, 2004.
- [120] J. M. Cowley, C. J. Humphreys, E. G. Bithell, J. Barry, M. J. Carr, C. E. Lyman, B. K. Vainshtein, B. B. Zvyagin, A. S. Avilov, J. A. Eades, J. C. H. Spence, and Istvan Hargittai. *Electron Diffraction Techniques*, volume 1 of *IUCr Monographs on Crystallography*. Oxford University Press, 1992.
- [121] J. C. H. Spence. On the accurate measurement of structure-factor amplitudes and phases by electron diffraction. *Acta Crystallographica Section A*, 49(2):231–260, Mar 1993.
- [122] J. S. Lally, C. J. Humphreys, A. J. F. Metherell, and R. M. Fisher. The critical voltage effect in high voltage electron microscopy. *Philosophical Magazine*, 25:321–343, 1972.
- [123] R. Uyeda. Dynamical effects in high-voltage electron diffraction. *Acta Crystallographica Section A*, 24(1):175–181, Jan 1968.
- [124] P. Goodman and G. Lehmpfuhl. Electron diffraction study of MgO $h00$ -systematic interactions. *Acta Crystallographica*, 22(1):14–24, Jan 1967.
- [125] J. M. Zuo and J. C. H. Spence. Automated structure factor refinement from convergent-beam patterns. *Ultramicroscopy*, 35:185–196, June 1991.
- [126] B. Jiang, J. M. Zuo, D. Holec, C. J. Humphreys, M. Spackman, and J. C. H. Spence. Combined structure-factor phase measurement and theoretical calculations for mapping of chemical bonds in GaN. *Acta Crystallographica Section A*, 66(4):446–450, Jul 2010.
- [127] K. Tsuda, D. Morikawa, Y. Watanabe, S. Ohtani, and T. Arima. Direct observation of orbital ordering in the spinel oxide FeCr_2O_4 through electrostatic potential using convergent-beam electron diffraction. *Phys. Rev. B*, 81(18):180102, May 2010.
- [128] J. Taftø and J. C. H. Spence. A simple method for the determination of structure-factor phase relationships and crystal polarity using electron diffraction. *Journal of Applied Crystallography*, 15(1):60–64, Feb 1982.
- [129] Jeremy Kepner and Stan Ahalt. MatlabMPI. *Journal of Parallel and Distributed Computing*, 64(8):997–1005, 2004.
- [130] Masakazu Ichikawa and Kazunobu Hayakawa. Generalized Bethe Potential in Reflection Electron Diffraction. *Journal of the Physical Society of Japan*, 42(6):1957–1964, 1977.
- [131] S Figge, T Aschenbrenner, C Kruse, G Kunert, M Schowalter, A Rosenauer, and

- D Hommel. A structural investigation of highly ordered catalyst- and mask-free GaN nanorods. *Nanotechnology*, 22(2):025603, 2011.
- [132] James E. Bernard and Alex Zunger. Bonding charge density in GaAs. *Phys. Rev. Lett.*, 62(19):2328, May 1989.
- [133] J. M. Zuo, J. C. H. Spence, and M. O’Keeffe. Zuo, Spence, and O’Keeffe reply. *Phys. Rev. Lett.*, 62(19):2329, May 1989.
- [134] Knut Müller, Marco Schowalter, Andreas Rosenauer, Dongzhi M. Hu, Daniel Schaadt, Michael Hetterich, Philippe Gilet, Oleg Rubel, Rafael Fritz, and Kerstin Volz. Atomic scale annealing effects on InGaNAs studied by TEM three-beam imaging. *Submitted to Physical review B*.
- [135] Georg Joos. *Lehrbuch der Theoretischen Physik*. Aula-Verlag, 1989. 15. Auflage.
- [136] Woldemar Voigt. *Lehrbuch der Kristallphysik (mit Ausschluß der Kristalloptik)*. Teubners Sammlung von Lehrbüchern auf dem Gebiete der mathematischen Wissenschaften mit Einschluß ihrer Anwendungen; 34. Teubner, Leipzig, 1910.
- [137] K. Tillmann, M. Lentzen, and R. Rosenfeld. Impact of column bending in high-resolution transmission electron microscopy on the strain evaluation of GaAs/InAs/GaAs heterostructures. *Ultramicroscopy*, 83(1-2):111–128, 2000.
- [138] M. M. J. Treacy and J. M. Gibson. The effects of elastic relaxation on transmission electron microscopy studies of thinned composition-modulated materials. *Journal of Vacuum Science & Technology B: Microelectronics and Nanometer Structures*, 4(6):1458–1466, 1986.
- [139] V. Grillo. The effect of surface strain relaxation on HAADF imaging. *Ultramicroscopy*, 109(12):1453–1464, 2009.
- [140] Vincenzo Grillo. Personal communication, 2009–2011.
- [141] G. Patriarche, L. Largeau, J.-C. Harmand, and D. Gollub. Morphology and composition of highly strained InGaAs and InGaAsN layers grown on GaAs substrate. *Applied Physics Letters*, 84(2):203–205, 2004.
- [142] Fang-I. Lai, S. Y. Kuo, J. S. Wang, R. S. Hsiao, H. C. Kuo, J. Chi, S. C. Wang, H. S. Wang, C. T. Liang, and Y. F. Chen. Temperature-dependent optical properties of $\text{In}_{0.34}\text{Ga}_{0.66}\text{As}_{1-x}\text{N}_x/\text{GaAs}$ single quantum well with high nitrogen content for application grown by molecular beam epitaxy. *Journal of Crystal Growth*, 291(1):27–33, 2006.
- [143] M. Kondow, T. Kitatani, S. Nakatsuka, M.C. Larson, K. Nakahara, Y. Yazawa, M. Okai, and K. Uomi. GaInNAs: a novel material for long-wavelength semiconductor lasers. *Selected Topics in Quantum Electronics, IEEE Journal of*, 3(3):719–730, June 1997.
- [144] M. Albrecht, V. Grillo, T. Remmele, H. P. Strunk, A. Yu. Egorov, Gh. Dumitras, H. Riechert, A. Kaschner, R. Heitz, and A. Hoffmann. Effect of annealing on the In and N distribution in InGaAsN quantum wells. *Applied Physics Letters*, 81(15):2719–2721, 2002.
- [145] A. Rosenauer, D. Gerthsen, and V. Potin. Strain state analysis of InGaN/GaN – sources of error and optimized imaging conditions. *Physica Status Solidi A*, 203(1):176–184, January 2006.
- [146] Andreas Rosenauer. *Transmission Electron Microscopy of Semiconductor Nanostructures*. Springer, 2003.
- [147] Kazuo Ishizuka. Contrast transfer of crystal images in TEM. *Ultramicroscopy*,

- 5(1-3):55–65, 1980.
- [148] M. Albrecht, H. Abu-Farsakh, T. Remmele, L. Geelhaar, H. Riechert, and J. Neugebauer. Compositional correlation and anticorrelation in quaternary alloys: Competition between bulk thermodynamics and surface kinetics. *Phys. Rev. Lett.*, 99(20):206103, Nov 2007.
- [149] M. Herrera, D. Gonzalez, M. Hopkinson, M. Gutierrez, P. Navaretti, H. Y. Liu, and R. Garcia. Composition modulation in GaInNAs quantum wells: Comparison of experiment and theory. *Journal of Applied Physics*, 97(7):073705, 2005.
- [150] O. Rubel, B. Kunert, S. D. Baranovskii, F. Grosse, K. Volz, and W. Stolz. Model of annealing-induced short-range order effects in (GaIn)(NP) alloys. *Phys. Rev. B*, 74(19):195206, Nov 2006.
- [151] K. Volz, T. Torunski, O. Rubel, and W. Stolz. Direct structural evidence of the change in N-III bonding in (GaIn)(NAs) before and after thermal annealing. *Journal of Applied Physics*, 104(5):053504, 2008.
- [152] J. M. Zuo, J. C. H. Spence, J. Downs, and J. Mayer. Measurement of individual structure-factor phases with tenth-degree accuracy: the 00.2 reflection in BeO studied by electron and X-ray diffraction. *Acta Crystallographica Section A*, 49(3):422–429, May 1993.
- [153] C. Deininger, G. Necker, and J. Mayer. Determination of structure factors, lattice strains and acceleration voltage by energy-filtered convergent beam electron diffraction. *Ultramicroscopy*, 54:15–30, 1994.
- [154] Kenji Tsuda, Yoichiro Ogata, Kazunari Takagi, Takuya Hashimoto, and Michiyoshi Tanaka. Refinement of crystal structural parameters and charge density using convergent-beam electron diffraction – the rhombohedral phase of LaCrO₃. *Acta Crystallographica Section A*, 58(6):514–525, Nov 2002.
- [155] M. Schowalter, A. Rosenauer, J. T. Titantah, and D. Lamoen. Calculation of Debye-Waller temperature factors for GaAs. *Journal of Physics: Conference Series*, 209:012025, 2010.
- [156] Vincenzo Grillo, Frank Glas, Knut Müller, and Andreas Rosenauer. Simulation of STEM-HAADF microscopy images for the chemical quantification in InGaAsN alloys. In *Transnational Access Meeting (TAM), Helsinki (Finland) [Poster presentation]*, 2010.
- [157] Vincenzo Grillo, Knut Müller, C. Frigeri, Kerstin Volz, Frank Glas, and Andreas Rosenauer. Strain, composition and disorder in ADF imaging of semiconductors. In *Microscopy of semiconducting materials, Cambridge (UK) [Invited talk]*, 2011.
- [158] C. L. Jia, M. Lentzen, and K. Urban. Atomic-Resolution Imaging of Oxygen in Perovskite Ceramics. *Science*, 299:870–873, 2003.
- [159] W. M. J. Coene, A. Thust, M. Op de Beeck, and D. van Dyck. Maximum-likelihood method for focus-variation image reconstruction in high resolution transmission electron microscopy. 64:109–135, 1996.

Selected publications

- [A1] Knut Müller, Marco Schowalter, Andreas Rosenauer, Oleg Rubel, and Kerstin Volz. Effect of bonding and static atomic displacements on composition quantification in $\text{In}_x\text{Ga}_{1-x}\text{N}_y\text{As}_{1-y}$. *Phys. Rev. B*, 81(7):075315, Feb 2010.
- [A2] Knut Müller, Marco Schowalter, Jacob Jansen, Kenji Tsuda, John Titantah, Dirk Lamoen, and Andreas Rosenauer. Refinement of the 200 structure factor for GaAs using parallel and convergent beam electron nanodiffraction data. *Ultramicroscopy*, 109:802–814, 2009.
- [A3] Knut Müller, Marco Schowalter, Andreas Rosenauer, Jacob Jansen, Kenji Tsuda, John Titantah, and Dirk Lamoen. Refinement of chemically sensitive structure factors using parallel and convergent beam electron nanodiffraction. *Journal of Physics: Conference Series*, 209(1):012025, 2010.
- [A4] Andreas Rosenauer, Katharina Gries, Knut Müller, Angelika Pretorius, Marco Schowalter, Adrian Avramescu, Karl Engl, and Stephan Lutgen. Measurement of specimen thickness and composition in $\text{Al}_x\text{Ga}_{1-x}\text{N}/\text{GaN}$ using high-angle annular dark field images. *Ultramicroscopy*, 109(9):1171–1182, 2009.
- [A5] Andreas Rosenauer, Katharina Gries, Knut Müller, Marco Schowalter, Angelika Pretorius, Adrian Avramescu, Karl Engl, and Stephan Lutgen. Measurement of composition profiles in III-nitrides by quantitative scanning transmission electron microscopy. *Journal of Physics: Conference Series*, 209(1):012009, 2010.
- [A6] Stephan Figge, Timo Aschenbrenner, Carsten Kruse, Gerd Kunert, Marco Schowalter, Andreas Rosenauer, and Detlef Hommel. A structural investigation of highly ordered catalyst- and mask-free GaN nanorods. *Nanotechnology*, 22(2):025603, 2011.
- [A7] Angelika Pretorius, Knut Müller, Tomohiro Yamaguchi, Roland Kröger, Detlef Hommel, and Andreas Rosenauer. Concentration evaluation in nanometre-sized InGaN islands using transmission electron microscopy. In A. G. Cullis and P. A. Midgley, editors, *Microscopy of Semiconducting Materials 2007*, volume 120 of *Springer Proceedings Physics*, pages 17–20. Springer Netherlands, 2008.
- [A8] J. K. Dash, A. Rath, R. R. Juluri, P. Santhana Raman, K. Müller, A. Rosenauer, and P. V. Satyam. DC heating induced shape transformation of Ge structures on ultra clean Si (5 5 12) surfaces. *Journal of Physics: Condensed matter*, 23:135002, 2011.
- [A9] Angelika Pretorius, Knut Müller, Roland Kröger, Detlef Hommel, Andreas Rosenauer, and Tomohiro Yamaguchi. Concentration measurement in free-standing InGaN nano-islands with transmission electron microscopy. *Microscopy and Microanalysis*, 13 (Suppl. 03):312–313, 2007.
- [A10] Patrick Sonström, Johannes Birkenstock, Yulia Borchert, Laura Schilinsky, Peter Behrend, Katharina Gries, Knut Müller, Andreas Rosenauer, and Marcus Bäumer. Nanostructured Praseodymium Oxide: Correlation between phase transitions and catalytic activity. *ChemCatChem*, 2:694–704, 2010.

Notes: Ref. [A1] contains most of the results in chapter 4. Ref. [A2] contains the development of the PBED method and the measurement of the 200 structure factor of GaAs, and the comparison with CBED refinements of chapter 3. Ref. [A3] contains the CBED measurement of the 200 structure factor of GaAs and the PBED measurement for GaAs and InAs. Measurement of polarity in Ref. [A6] using CBED has been done by Dr. Marco Schowalter and the author in equal parts. Ab-initio structure factors for wurtzite-GaN in reference [A6] have been calculated by the author by DFT (WIEN2K [1]).

Danksagung

Hätte man lediglich alles im Literaturverzeichnis aufgeführte Wissen mit den während der letzten drei Jahre zur Verfügung stehenden modernen Labor- und Rechenkapazitäten gepaart, so wäre dies dennoch ein schwieriger Ausgangspunkt für diese Arbeit gewesen. Ihr Gelingen verdankt sie zu einem wesentlichen Teil stetigem Interesse und fortwährender Unterstützung weiterer Personen, denen ich auf dieser letzten Seite danken möchte.

Mein Dank gilt Prof. Dr. Andreas Rosenauer, der nicht nur diese Arbeit mit selbstbestimmter Schwerpunktsetzung ermöglichte, sondern sie auch stets als Motivator und Ansprechpartner bereichert hat.

Ich danke Prof. Dr. Dagmar Gerthsen für die Begutachtung dieser Arbeit.

Ich danke Dr. Marco Schowalter für sein Interesse an meiner Arbeit, viele anregende Diskussionen und für die Selbstverständlichkeit, mit der er seine Kompetenz weitergab.

Bedanken möchte ich mich weiterhin bei meinen Zimmergenossen Thorsten Mehrstens und Katharina Gries für die angenehme Atmosphäre. Mit Katharina verbinden mich nun einige Jahre einträchtiger Kollegialität. Einträchtig, das trifft den Punkt.

Allen weiteren Mitgliedern der AG Rosenauer, Oliver Oppermann, Oliver Walter, Annegret Ebert, Kristian Frank, Tim Grieb, Stephanie Bley, Alexander Würfel und Prof. Dr. Satyam Parlapalli danke ich für die nette Atmosphäre und Zusammenarbeit.

Prof. Dr. Kenji Tsuda danke ich für die engagierte Einarbeitung in die konvergente Elektronenbeugung, sein Programm MBFIT und seine Hilfsbereitschaft. Ich danke auch allen Mitgliedern seiner Arbeitsgruppe an der Tohoku Universität dafür, mich während meines Besuchs in Japan so freundlich aufgenommen zu haben.

Mein Dank gilt Jouk Jansen für seine Hilfsbereitschaft in Sachen paralleler Elektronenbeugung und für die Bereitstellung der ELSTRU software.

Prof. Dr. Kerstin Volz danke ich für die fruchtbare Zusammenarbeit. Ganz besonders danke ich für das Überlassen der MOVPE Proben, ohne die der experimentelle Teil dieser Arbeit so nicht möglich gewesen wäre. Vielen Dank auch an Rafael Fritz für seine Kooperation.

Gleiches gilt für die Zusammenarbeit mit Dr. Daniel Schaadt, Dr. Dongzhi Hu und Dr. Michael Hetterich vom Karlsruhe Institute of Technology und Dr. Philippe Gilet vom CEA-LETI Grenoble. Danke für die MBE Proben, das PL Spektrum in Fig. 5.1 und die gute Zusammenarbeit.

Dr. Oleg Rubel hat mir freundlicherweise sein Programm zur Minimierung der Verzerrungsenergie mittels empirischer Potentiale überlassen. Vielen Dank dafür!

Mein Dank gilt außerdem Thorsten Mehrstens, Robert Imlau, Dennis Zillmann, sowie Claas Gloistein und Nils Neugebohrn, die während ihrer Diplom-/Master- bzw. Bachelorzeit wichtige Beiträge zu dieser Arbeit geleistet haben.

Ich danke Dr. Mathias Palm vom Institut für Umweltphysik der Uni Bremen für sein Engagement bei der PL-Spektroskopie am FTIR im Observatorium auf dem Dach der Uni.

Gleichermaßen möchte ich mich bei Dr. Jan-Peter Richters für die Einweisung in die Absorptionsmessungen und sein Interesse daran bedanken.

Eine wichtige Hilfe und Anlaufstelle war außerdem das Physics International Postgraduate Programme (PIP) der Universität Bremen, das durch Exkursionen und finanzielle Unterstützung von Tagungsteilnahmen und der Reise nach Japan diese Doktorarbeit bereicherte.

Ich danke der DFG für die finanzielle Unterstützung im Rahmen der Projekte (RO-2057/4) und (SCHO 1196/3).

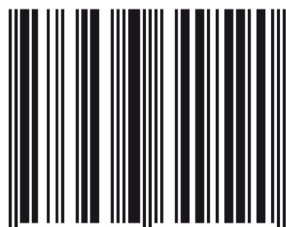
Dafür, mich in vielen Jahren des Studiums in jeder Hinsicht unterstützt, gefördert und motiviert, sowie den Tellerrand jenseits von $E = mc^3$ gelegt zu haben, danke ich meinen Eltern.

In hohem Maße hat sich diese Arbeit über das universitäre Leben hinaus in den privaten und familiären Bereich erstreckt. Dafür, immer Verständnis gehabt und Rückhalt gegeben zu haben, Motivationsquelle und einfach da zu sein, widme ich den Schluß dieser Arbeit meiner geliebten Familie

Liv und Conny Caspary.

mbvberlin
mensch und buch verlag | 2011

38,00 Euro
ISBN: 978 3 86664 959 0



9 783866 649590 >